

# POLITECNICO DI TORINO

Collegio di Ingegneria Chimica e dei Materiali

**Master of Science Course  
in Materials Engineering**

Master of Science Thesis

## **PLA/PHBH compounding by twin-screw extrusion: simulation-based evaluation of the processing parameters**



### **Tutors**

prof. Alberto Frache  
prof. Rossella Arrigo

### **Candidate**

Andrea Basolo

March 2021



## Summary

<b>1. Riassunto della tesi</b> .....	1
<b>2. Introduction</b> .....	19
<b>3. Theoretical fundamentals</b> .....	21
3.1. <i>Thermodynamic considerations</i> .....	21
3.2. <i>Rheological considerations</i> .....	23
3.3. <i>Morphology development</i> .....	23
3.4. <i>The model of Vergnes and Delamare</i> .....	28
3.4.1. Modelling of coalescence and breakup phenomena .....	29
3.4.2. Modelling of morphologic variation along the extruder .....	30
3.5. <i>Devices used in melt extrusion</i> .....	31
3.6. <i>PLA-based blends</i> .....	34
3.6.1. PLA-PHBH blends .....	35
3.6.2. Mechanical properties of PLA-PHBH blends .....	38
3.6.3. Biodegradability of PLA-PHBH blends.....	39
<b>4. Simulations with Ludovic</b> .....	41
4.1. <i>The software</i> .....	41
4.2. <i>Working principles</i> .....	41
4.2.1. Melt behaviour modelling .....	41
4.2.2. Geometrical modelling of the extruder.....	43
4.2.3. Mechanical model for the screw and the die.....	44
4.2.4. Thermal model for the screw and the die.....	47
4.2.5. The computation process.....	49
4.3. <i>Setting of the simulations</i> .....	49
4.3.1. “Extruder” tab – Definition of the geometry .....	49
4.3.2. “Product” tab – Characterisation of the materials .....	51
4.3.3. “Process” tab – Definition of the working parameters .....	54
4.4. <i>Setting of the Design of Experiment (DoE)</i> .....	56

<b>5. DoE results analysis</b> .....	59
5.1. <i>Case status</i> .....	59
5.2. <i>Residence Time Distribution (RTD)</i> .....	60
5.3. <i>Temperature</i> .....	62
5.4. <i>Shear rate</i> .....	63
5.5. <i>Viscosity</i> .....	65
5.6. <i>Torque</i> .....	66
5.7. <i>Effect of the composition</i> .....	67
5.8. <i>Conclusions about the DoE results</i> .....	71
<b>6. Analysis of the simulations</b> .....	73
6.1. <i>RTD</i> .....	73
6.2. <i>Temperature</i> .....	76
6.3. <i>Local and Total Residence Times</i> .....	79
6.4. <i>Shear rate</i> .....	82
6.5. <i>Viscosity</i> .....	83
6.6. <i>Application of Vergnes and Delamare's model to this case study</i> .....	86
6.7. <i>Effect of the screw speed on the simulations run with the profile 3</i> .....	92
6.8. <i>Comparison of the computed results with SEM micrographs</i> .....	98
6.9. <i>Effect of the mixing law for the polymers</i> .....	101
6.10. <i>Conclusions</i> .....	102
<b>7. List of symbols</b> .....	105
<b>8. References</b> .....	107
<b>9. Instruments employed in the present work</b> .....	111
<b>10. Breve manuale di Ludovic</b> .....	113
<b>Acknowledgements</b> .....	127

# 1. Riassunto della tesi

## 1.1. Introduzione

Negli ultimi vent'anni l'inquinamento da materie plastiche è diventato un argomento di grande preoccupazione, soprattutto a causa del loro uso nel settore degli imballaggi. La vita utile di tali imballaggi è generalmente molto breve, soprattutto se destinati a contenere cibi e bevande, comportando quindi la produzione giornaliera di tonnellate di rifiuti. Nonostante i grandi sforzi fatti per mettere in piedi una filiera in grado di avviare a riciclo per lo meno le materie plastiche di uso più comune, ancora oggi una quota considerevole di questi rifiuti è ancora destinata a discariche più o meno legali o ad operazioni di valorizzazione energetica. Questo comporta un impatto ambientale per nulla trascurabile, oltre che il consumo di risorse non rinnovabili al fine di produrre i precursori chimici per la sintesi dei polimeri più usati nel campo del packaging (poliolefine e PET su tutti). Una possibile soluzione oggetto di studi attenti negli ultimi anni è la produzione di materie plastiche biodegradabili a partire da risorse rinnovabili, come ad esempio l'acido polilattico (PLA), derivato dall'amido di mais, o la famiglia dei poliidrossialcanoati (PHA), utilizzati come riserva di energia da varie famiglie di batteri. Si tratta in entrambi i casi di polimeri termoplastici che però, allo stato attuale, hanno caratteristiche meccaniche piuttosto scarse, soprattutto se paragonati a PP e PET, e risultano anche più difficili da processare. In particolare, il PLA è fragile, ha bassi valori di Heat Deflection Temperature, cristallizza lentamente e ha scarse proprietà barriera. Tra i PHA, il più comune (in ragione della più facile reperibilità sul mercato) è il poli(3-idrossibutirrato) (PHB) che è rigido a causa dell'elevata cristallinità ed è difficile da trasformare a causa della sensibilità alle alte temperature. Per risolvere il problema dell'eccessiva rigidità del PHB, l'azienda giapponese Kaneka ha sviluppato il poli(3-idrossibutirrato-co-3-idrossiesanoato) (PHBH), un copolimero la cui struttura irregolare lo rende più flessibile.

Al fine di realizzare un materiale biodegradabile idoneo per il settore degli imballaggi a partire da risorse rinnovabili, la soluzione più semplice ed economica è la realizzazione di blend polimerici. Infatti, combinando opportunamente due polimeri è possibile compensare reciprocamente gli svantaggi dei singoli componenti. Ad esempio, unendo il PLA, fragile, con il PHBH più flessibile è possibile ottenere un materiale con proprietà intermedie a costi contenuti, anche in virtù della sempre più facile reperibilità dei componenti del blend. Tuttavia, molto spesso l'individuazione della migliore composizione è effettuata con un processo empirico in cui si va a realizzare fisicamente il blend con un estrusore bivate per poi valutarne le caratteristiche finali. Questo allunga decisamente i tempi di sviluppo anche perché, oltre che la composizione in grado di garantire le migliori performances, è necessario individuare il profilo vite che permette di ottenere la migliore microstruttura finale. Infatti, il PHBH non è miscibile con il PLA, motivo per cui è assolutamente necessario avere un controllo sulla morfologia del blend, in quanto questa ha un effetto determinante sulla proprietà del materiale. Per semplificare e velocizzare questo processo di selezione, sono stati sviluppati alcuni software in grado di fornire, a partire dai parametri di processo, dati relativi all'evoluzione di varie grandezze lungo l'asse della vite. In questo modo è possibile effettuare previsioni sulle condizioni operative più adatte per ottenere determinate proprietà del materiale.

Il programma usato in questo lavoro è Ludovic, che è in grado di simulare il processo di estrusione in condizioni stazionarie nella sola direzione parallela all'asse della vite. Per questi motivi, le operazioni di calcolo sono assai veloci (qualche decina di secondi) e possono essere svolte anche da un comune personal computer.

## 1.2. Modellizzazione del processo di compounding

L'estrusore oggetto delle simulazioni è un Leistritz ZSE 18 HP a viti corotanti con cilindri aventi diametro interno di 18 mm e distanza tra gli assi delle viti di 15 mm. La macchina, adatta principalmente ad applicazioni di laboratorio, è costituita da 8 segmenti riscaldati lunghi 80 mm (numerati progressivamente nella direzione del die) con aperture a metà del primo e del quarto che permettono l'ingresso dei polimeri e della carica minerale, se necessaria. Un'ulteriore apertura sul penultimo elemento permette il degasaggio del fuso. La filiera è costituita da quattro elementi modellizzati sotto forma di cilindri con diverse lunghezze e diametri. Il modulo all'interfaccia con il cilindro è termoregolato a 180°C.

Si è simulato il processo di compounding con tre differenti profili vite (Figura 1.1), identificati con i numeri da 1 a 3. In particolare, il primo blocco di masticazione (dove il polimero fonde) è in comune per le tre viti, mentre la parte che segue distingue i vari profili. Il numero 1 possiede un breve blocco di masticazione all'incirca a metà della sua lunghezza e una sequenza di elementi masticatori poco prima del die. Il profilo 2 è caratterizzato solamente da una seconda lunga sequenza di elementi masticatori prima della filiera, mentre sulla vite 3 sono montate due ulteriori sezioni di masticazione, una al centro e una verso il die. con un Al termine della sequenza centrale di masticazione è montato un elemento di retroflusso.

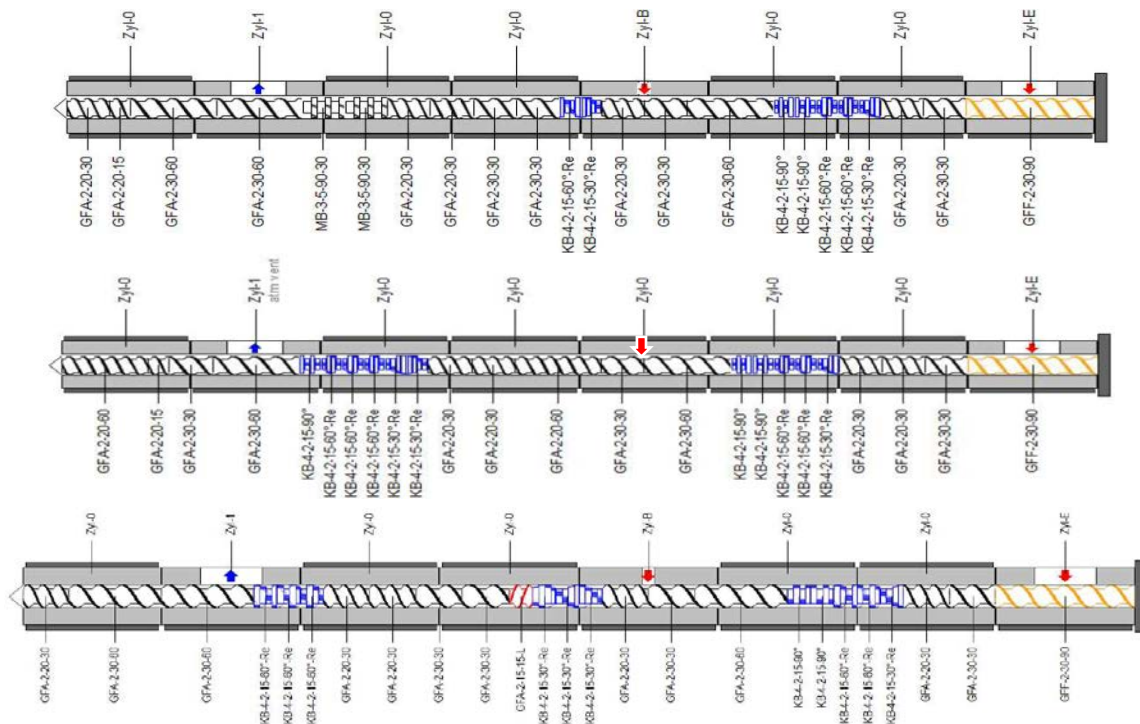


Figura 1.1 - Profili vite impiegati nelle simulazioni, numerati, dall'alto verso il basso, da 1 a 3

I polimeri che costituiscono il blend sono PLA (Ingeo Biopolymer 3251D) e PHBH (Kaneka X151A). I dati relativi a calore specifico, densità e conducibilità termica del solido e del fuso, oltre che le temperature e le entalpie di fusione, sono stati ricavati a partire dalle schede tecniche, da prove di laboratorio tramite DSC e, quando necessario, consultando la letteratura scientifica esistente. La loro viscosità è stata determinata attraverso prove di laboratorio con un reometro del tipo piatto-cono e i dati relativi sono stati caricati nel software come insieme di punti (Set of Points, SoP). Un certo numero di simulazioni prevedeva l'aggiunta di una carica minerale composta principalmente da bentonite (Cloisite 5) per cui è stato necessario definire, oltre alle proprietà termiche elencate in precedenza, anche il fattore di forma L/D. Questi materiali,

opportunamente combinati secondo precise percentuali in peso, formano la cosiddetta *Recipe*, che specifica quali materiali e in quale quantità sono presenti nelle diverse sezioni dell'estrusore. In particolare, nelle simulazioni si è utilizzato un blend 70/30 wt. % rispettivamente di PLA e PHBH con una portata di 3 kg/h. Ove necessario, la Cloisite è stata aggiunta con una percentuale in peso del 5% (incrementando la portata a 3,15 kg/h) dopo un'asciugatura in forno a 80°C per 5 ore. La viscosità del blend è stata calcolata con una legge di tipo lineare, pur nella consapevolezza del fatto che le sue componenti non sono miscibili. L'effetto dell'aggiunta di Cloisite sulla viscosità del fuso è stato valutato con la relazione (1.1) proposta Maron e Pierce, una versione semplificata della legge di Krieger-Dougherty.

$$\eta = \frac{\eta_{pol}}{[1 - (\Phi/\Phi_m)]^2} \quad (1.1)$$

Il processo di compounding è stato simulato impostando la velocità di rotazione della vite a 400 rpm. Dopo un affinamento basato sui dati forniti da una termocoppia montata sull'elemento riscaldato del die nel processo reale, per il coefficiente di scambio termico tra cilindro e ambiente circostante è stato scelto il valore di 2500 W/m<sup>2</sup>K. Lo stesso valore per quanto riguarda la filiera è stato settato a 500 W/m<sup>2</sup>K come suggerito dal manuale di Ludovic per uno scambio termico di media entità.

Il profilo di temperatura è riportato nella Tabella 1.1 dove è anche possibile osservare che nelle simulazioni in cui non si aggiunge la carica minerale, l'apertura da cui entrerebbe la Cloisite non viene chiusa ed è quindi considerata come un degasaggio.

**Tabella 1.1** - Profilo di temperatura usato in tutte le simulazioni. Si noti l'apertura sull'elemento 4, che in base alla composizione del blend agisce da alimentazione (▼) o degasaggio (▲).

	▼		▼ / ▲		▲				
Element number	1	2	3	4	5	6	7	8	
Temperature (°C)	170	175	180	180	185	185	190	190	<b>Die</b>

A partire da questi dati sono state lanciate le simulazioni, in cui il software calcola le varie grandezze muovendosi dal die verso la tramoggia. Di particolare interesse è la temperatura, il cui profilo lungo l'asse della vite è ricostruito a partire da un valore casuale in corrispondenza della filiera. Se il dato calcolato in corrispondenza del primo elemento non di trasporto incontrato dai pellet di polimero corrisponde alla temperatura di fusione del PLA (più alta di quella del PHBH) e se a monte di tale elemento si registra un aumento di pressione, la simulazione viene interrotta e i risultati vengono mostrati all'utente. Se ciò non avviene, la temperatura in corrispondenza del die viene variata e si ricalcolano i valori lungo la vite finché le condizioni per la convergenza non sono rispettate.

### 1.2.1. DoE

Qualora si desiderasse analizzare l'andamento di determinate grandezze al variare di uno o più parametri definiti dall'utente senza la necessità di lanciare manualmente un numero elevato di simulazioni, è possibile usare lo strumento *Design of Experiments* (DoE). In particolare, a partire dalle impostazioni di una simulazione preesistente, Ludovic permette scegliere fino a due *Primary Parameters*, che variano in maniera indipendente all'interno di intervalli definiti dall'utente secondo un numero di step che può essere scelto liberamente. È anche possibile selezionare fino a 12 *Secondary Parameters* (dipendenti), i quali variano sì entro intervalli definiti dall'utente, ma secondo un numero di step che è lo stesso della grandezza indipendente a cui sono legati.

In questo lavoro lo strumento del DoE è stato utilizzato al fine di individuare eventuali combinazioni di velocità di rotazione e portata in grado di assicurare particolari performance nello sviluppo di una morfologia finale con domini di PHBH e lamelle di Cloisite (se presenti) ben dispersi nel volume del materiale. Inoltre, i risultati sono stati impiegati allo scopo di valutare l'affidabilità delle previsioni fornite da Ludovic in merito al blend di biopolimeri. A partire da simulazioni esistenti con portata di 3 kg/h (3,15 in caso di aggiunta della Cloisite) e velocità di rotazione di 400 rpm, si sono fatti variare i parametri negli intervalli riportati in Tabella 1.2. Si noti come per i *Secondary Parameters* non è specificato un numero di step, in quanto quest'ultimo è uguale a quello scelto per la variabile indipendente a cui sono collegati.

Allo scopo di valutare l'efficacia del software nel fornire previsioni affidabili, per il coefficiente di scambio termico sono stati usati i valori di 1000 e 2500 W/m<sup>2</sup>K.

**Tabella 1.2** - Impostazioni dei DoE nel caso in cui non è prevista l'aggiunta della carica minerale. Si noti come i valori limite delle variabili dipendenti siano stati scelti in modo da rispettare le proporzioni osservate nelle simulazioni di partenza.

	<b>Tipo di variabile</b>	<b>Valore iniziale</b>	<b>Valore finale</b>	<b>Numero di step</b>
<b>Velocità di rotazione</b>	Indipendente	50 rpm	600 rpm	12
<b>Portata (Zona 1)</b>	Indipendente	1 kg/h	5 kg/h	5
<b>Portata (Zona 2)</b>	Dipendente dalla portata della zona 1	0,993 kg/h	4,967 kg/h	-
<b>Portata (Zona 3)</b>	Dipendente dalla portata della zona 1	0,983 kg/h	4,917 kg/h	-

Le grandezze che si è scelto di analizzare sono:

- *Case Status*
- Minimo dell'RTD (s)
- Varianza dell'RTD
- Temperatura massima (°C)
- Shear rate massimo (s<sup>-1</sup>)
- Viscosità massima (Pa·s)
- Coppia (N·m)
- Media dell'RTD (s)
- Temperatura media (°C)
- Shear rate medio (s<sup>-1</sup>)
- Viscosità media (Pa·s)
- Viscosità minima (Pa·s)

### 1.3. *Analisi dei risultati ottenuti con le prove DoE*

Per quanto riguarda la convergenza delle simulazioni che non prevedono l'aggiunta della carica minerale, si è osservato tramite il parametro *Case Status* che non è possibile processare con successo il blend polimerico a 50 rpm o con portate inferiori a 2 kg/h, qualunque sia il profilo vite. Questo comportamento è stato attribuito alla minore quantità di calore immagazzinato nel fuso a portate più basse e alla riduzione di temperatura conseguente ad un transito più lento nell'estrusore a bassi rpm. In questo modo il PLA solidifica prima di raggiungere la filiera o all'interno di essa. L'ipotesi sembrerebbe confermata dall'ulteriore riduzione dell'intervallo in cui è possibile effettuare il compounding quando il coefficiente di scambio termico del cilindro è portato da 1000 a 2500 W/m<sup>2</sup>K. L'aggiunta di Cloisite permette di operare anche con portate di 2 kg/h (ma solo per elevate velocità di rotazione) in quanto l'aumento di viscosità che ne consegue fa sì che una quota maggiore di energia meccanica sia trasformata in calore e che quindi la massa fusa si raffreddi di meno. In generale, quindi, il blend può essere ottenuto più facilmente con una combinazione di portate e velocità di rotazione più alte.

Per quanto riguarda la distribuzione dei tempi di residenza (RTD), i trend osservati sono, anche in questo caso, uguali per tutti i profili vite. In particolare, i minimi e le medie delle distribuzioni decrescono per portate e velocità di rotazione maggiori siccome in entrambi i casi quantità maggiori di materiale passano attraverso la macchina nell'unità di tempo. Il leggero spostamento delle distribuzioni verso tempi più brevi quando lo scambio termico nel cilindro è maggiore è stato interpretato in termini di viscosità. Si è infatti supposto che una fluidità del fuso lievemente più bassa, possa rendere più efficace il suo spostamento in direzione del die. Quest'ultima considerazione sembra confermata anche dai risultati ottenuti in seguito all'aggiunta della carica minerale, che aumenta la viscosità complessiva. Si è anche concluso che le lamelle di Cloisite, le quali non fondono alle temperature di processo, possano forzare il polimero fuso a muoversi nella direzione del flusso.

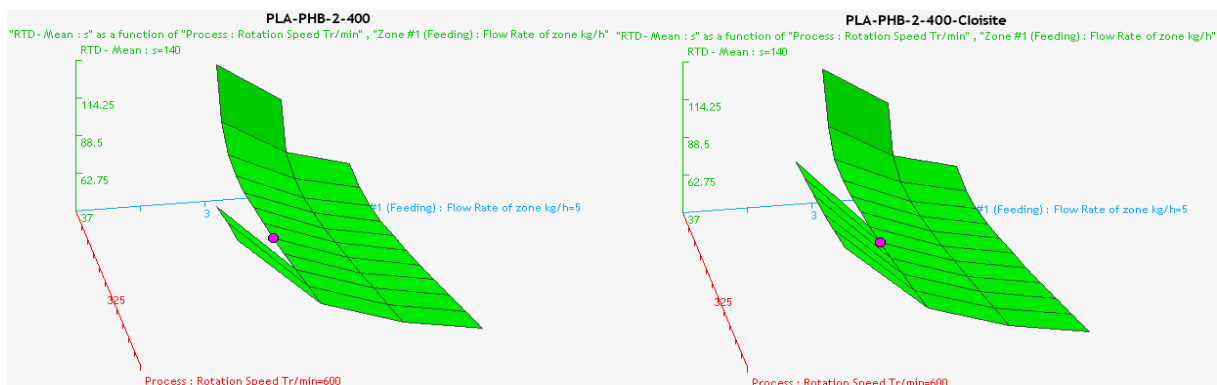


**Figura 1.2** - Valori medi delle RTD a 1000 W/m<sup>2</sup>K in presenza (destra) o assenza (sinistra) di Cloisite.

Analizzando la varianza delle curve RTD, si è notato che portate e velocità di rotazione maggiori risultano in distribuzioni maggiormente schiacciate verso tempi più brevi. Anche questo fenomeno è una conseguenza della maggiore velocità di trasferimento del materiale e dovrebbe permettere un controllo più accurato sul processo. Infatti, siccome i fenomeni di coalescenza e rottura dei domini di fase dispersa dipendono dal tempo trascorso dal blend in determinate sezioni dell'estrusore, se una maggiore frazione di fuso impiega tempi simili per passare attraverso la macchina ci si può aspettare una morfologia finale più uniforme.

Per quanto riguarda la temperatura media, è possibile osservare che gli andamenti sono i medesimi per i diversi profili vite. In particolare, questo parametro aumenta con la velocità di rotazione, mentre rimane sostanzialmente costante con la portata (anche se valori leggermente superiori si riscontrano per portate più grandi). Lo stesso vale per la temperatura massima, importante in quanto permette di avere il controllo sulla degradazione dei polimeri, anche se l'aumento con la velocità di rotazione è più marcato rispetto al caso precedente. In entrambi i casi l'aggiunta di Cloisite causa una traslazione delle superfici verso valori più alti, ma senza variarne in modo sostanziale la forma. Al contrario, l'aumento del coefficiente di scambio termico nel cilindro fa sì che le stesse superfici si spostino verso il basso. L'effetto della velocità di rotazione (e quindi dello shear rate) e quello dell'aggiunta del filler minerale, che aumenta la viscosità, sono una conseguenza della dissipazione di energia meccanica, la quale segue la relazione

$$\dot{W} = \eta \dot{\gamma}^2 \quad (1.2)$$

dove  $\dot{W}$  è la potenza dissipata,  $\eta$  la viscosità del fuso e  $\dot{\gamma}$  lo shear rate.

Nell'eq. (1.2) non compare la portata e questo spiega la sostanziale indipendenza della temperatura dalla portata. Inoltre, in letteratura è riportato che se da una parte, a parità di

temperatura, un minore volume di fuso comporta una maggiore densità di energia, dall'altra è maggiore anche il rapporto superficie/volume, che è determinante per lo scambio termico.

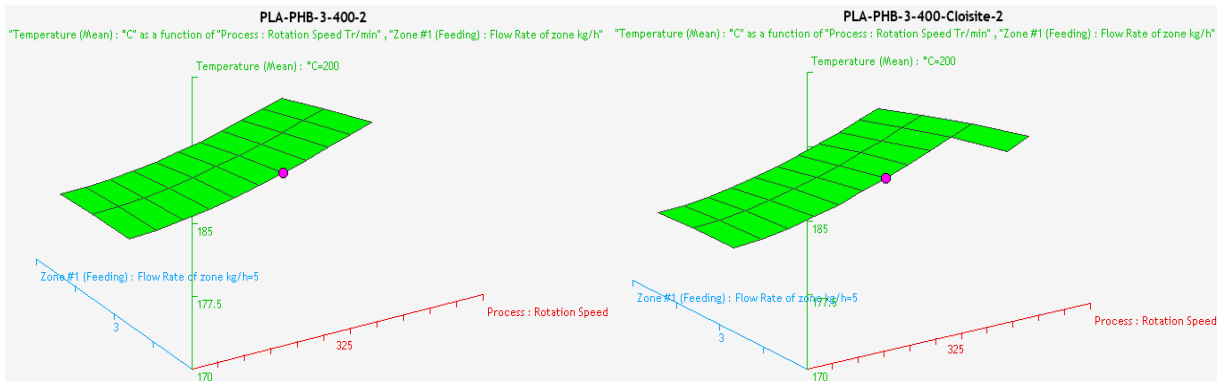


**Figura 1.3** - Andamento della temperatura media al variare di portata e velocità di rotazione delle viti in presenza (destra) e assenza (sinistra) di Cloisite. Il coefficiente di scambio termico nel cilindro è pari a 2500 W/m<sup>2</sup>K in entrambi i casi.

Lo shear rate viene calcolato a partire dai parametri geometrici della vite, attraverso i quali si ottiene il valore  $\dot{\gamma}_0$  secondo la formula:

$$\dot{\gamma}_0 = \omega \frac{R_2}{H} \quad (1.3)$$

dove  $\omega$  è la velocità angolare,  $R_2$  il raggio esterno e  $H$  l'altezza dei canali in cui passa il fuso. Successivamente, il risultato viene corretto sulla base delle condizioni locali di flusso, ma dall'analisi dei risultati si è determinato che questa correzione influisce solo marginalmente sul risultato finale (si nota solo un leggero aumento al crescere della portata). In definitiva, tra i parametri studiati solo la velocità di rotazione influisce sul valore della velocità di taglio, mentre lo scambio termico e l'aggiunta di filler non comportano variazioni apprezzabili. Per quanto riguarda lo shear rate medio, i valori più alti si registrano con il profilo 3, mentre con il numero 2, che possiede due soli blocchi di masticazione, si ottengono quelli più bassi. Le differenze risultano più marcate ad elevati regimi di rotazione, mentre ai bassi rpm i valori sono simili. Per quanto riguarda la velocità di taglio massima, le superfici relative ai profili 1 e 2 sono sovrapponibili, siccome  $\dot{\gamma}_{max}$  è registrata in corrispondenza di elementi masticatori comuni ad entrambe le configurazioni. Con il profilo 3 si ottengono risultati numericamente maggiori siccome su di esso è montato un modulo di retro-flusso a cui corrispondono shear rate superiori.

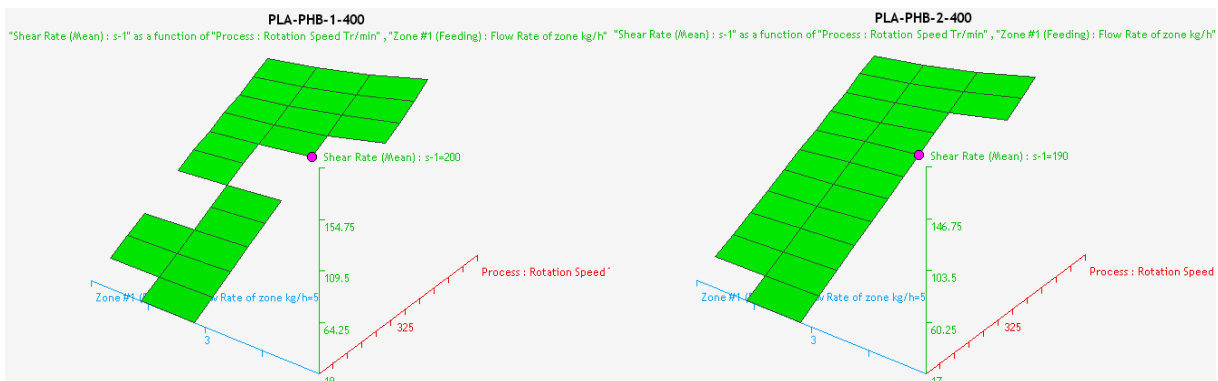


**Figura 1.4** - Andamento dello shear rate medio al variare di portata e velocità di rotazione con i profili vite 1 (sinistra) e 2 (destra).

Per quanto riguarda la viscosità, i valori massimo e minimo sono risultati di scarsa utilità siccome vengono calcolati analizzando i dati relativi all'intera macchina. Infatti, nel primo tratto dell'estrusore, dove il polimero è ancora presente in forma di pellet solidi, Ludovic restituisce un valore di 0 Pa·s, mentre le viscosità più alte sono registrate all'interno del die durante la solidificazione della massa fusa. Per questo motivo, i DoE restituiscono una viscosità minima di 0 Pa·s indipendentemente dalle condizioni di processo, mentre i massimi non sono rappresentativi di quanto accade nel cilindro, ovvero dove si ha effettivamente lo sviluppo della morfologia finale del blend. L'unica quantità effettivamente interessante è la viscosità media, che, seppur condizionata da quanto avviene alle due estremità della macchina, permette di analizzare gli effetti di velocità di rotazione, portata, scambio termico e aggiunta del filler. Proprio a causa del condizionamento di cui si è appena detto, si è concluso che avrebbe poco senso classificare i profili vite in base alle viscosità medie ottenibili con essi.

In generale, velocità di rotazione (e shear rate) superiori risultano in una riduzione della viscosità, che invece aumenta in seguito all'aggiunta di Cloisite o per scambi termici più efficienti nel cilindro. L'effetto di una maggiore portata è stato attribuito all'aumento di temperatura che ne consegue. Questo comporta una riduzione di  $\eta_{media}$  che, stando ai risultati del DoE, è piuttosto marcata e quindi non rispecchia la crescita solo lieve della temperatura. Siccome lo stesso è stato osservato anche nei risultati relativi a  $\eta_{max}$ , è possibile che tale risultato sia influenzato in maniera significativa da quanto accade nel die e che quindi i dati siano almeno parzialmente alterati.

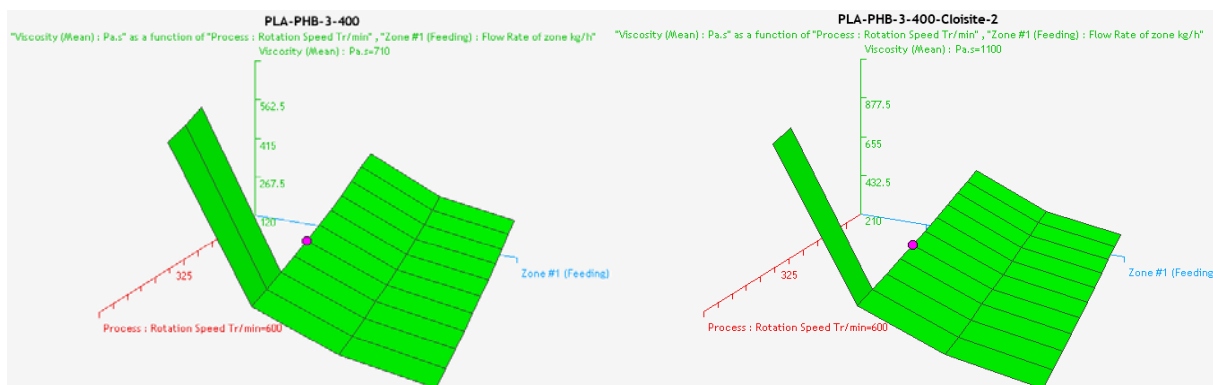


**Figura 1.5** - Viscosità media per il profilo vite 3 in funzione di velocità di rotazione e portata in presenza (destra) e assenza (sinistra) di filler. Lo scambio termico nel cilindro è pari a 2500 W/m<sup>2</sup>K.

La coppia viene calcolata secondo l'equazione

$$Tq = \frac{E_{mat} \cdot Q}{2\Omega} \quad (1.4)$$

dove  $E_{mat}$  è l'energia persa per dissipazione viscosa, trasporto e fusione da una massa unitaria di materiale,  $Q$  la portata e  $\Omega$  la frequenza di rotazione. Di conseguenza, si ottengono valori maggiori per portate superiori e, soprattutto ai bassi regimi di rotazione, in seguito all'aggiunta di Cloisite. Quest'ultima azione comporta infatti sia un leggero incremento della portata, sia un aumento della quantità di energia meccanica convertita in calore a causa della viscosità superiore. Aumentando la velocità di rotazione,  $Tq$  diminuisce a causa di una maggiore frequenza  $\Omega$ . Inoltre, i maggiori shear rate che ne conseguono possono provocare un abbassamento della viscosità del fuso e quindi della dissipazione viscosa (e di  $E_{mat}$ ).

Quando la vite ruota più lentamente, l'effetto di uno scambio termico più efficace è praticamente insignificante, mentre ciò non è più valido a velocità superiori. Questo comportamento è stato spiegato in termini di  $E_{mat}$  e in particolare della quota legata alla conversione di energia meccanica in calore, quantificata dall'eq. (1.2). Infatti, nel primo caso l'aumento di viscosità conseguente al

raffreddamento più efficace del fuso è bilanciato dalla riduzione dello shear rate, mentre questo equilibrio non esiste più sopra i 300 rpm, dove è l'effetto di un maggiore  $\dot{\gamma}$  ad avere la meglio. Di conseguenza, anche la coppia aumenta leggermente ad elevati regimi di rotazione.

### 1.3.1. Effetto della composizione

Siccome Ludovic non permette di impostare dei DoE variando la composizione del blend, la valutazione dell'effetto che questo parametro ha sulla distribuzione dei tempi di residenza e su temperatura, viscosità e shear rate è stata effettuata elaborando e mettendo insieme con MS Excel i risultati di singole simulazioni. Questo procedimento è risultato piuttosto dispendioso in termini di tempo, perciò si è scelto di operare con un coefficiente di scambio termico nel cilindro pari a  $2500 \text{ W/m}^2\text{K}$  e di utilizzare il solo profilo vite 3 in presenza di Cloisite. La velocità è stata impostata a 200, 400 e 550 rpm.

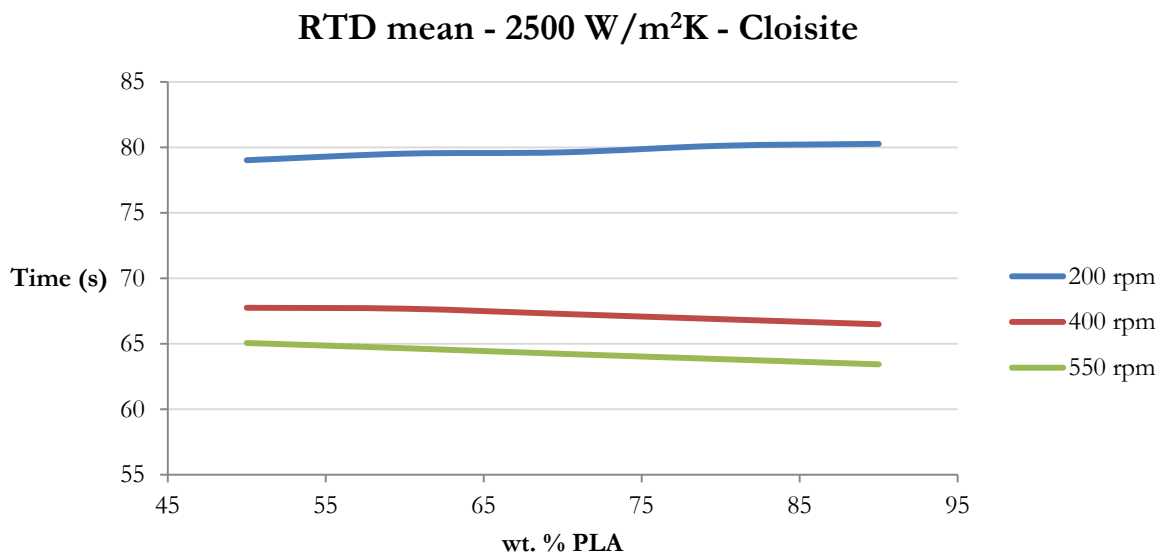


**Figura 1.6** - Variazione dei valori medi delle distribuzioni dei tempi di residenza al variare della composizione.

Per quanto riguarda la distribuzione dei tempi di residenza, si è osservato che aumentando la concentrazione di PHBH i valori minimo e medio (Figura 1.6) delle curve rimangono sostanzialmente invariati. A 400 e 550 rpm, l'ampiezza calcolata a mezza altezza decresce all'aumentare della concentrazione di PLA, mentre resta sostanzialmente invariata a 200 rpm. In letteratura è riportato che una RTD più ampia è indice di una migliore miscelazione distributiva, perciò, secondo quanto descritto dai risultati delle simulazioni, si può concludere che la composizione del blend influisce su tale aspetto solo ad alte velocità di rotazione. Tuttavia, è bene ricordare che distribuzioni più ampie possono favorire in misura maggiore eventuali fenomeni di coalescenza.

I valori medi della temperatura (Figura 1.7) sono stati calcolati a partire dai dati riferiti al solo cilindro ed è possibile osservare una loro diminuzione per maggiori quantitativi di PLA e velocità di rotazione inferiori. Anche in questo caso gli andamenti sono stati messi in relazione con la dissipazione di energia meccanica, dipendente da shear rate (legato alla velocità di rotazione) e viscosità, che è più bassa con minori quantitativi di PHBH.

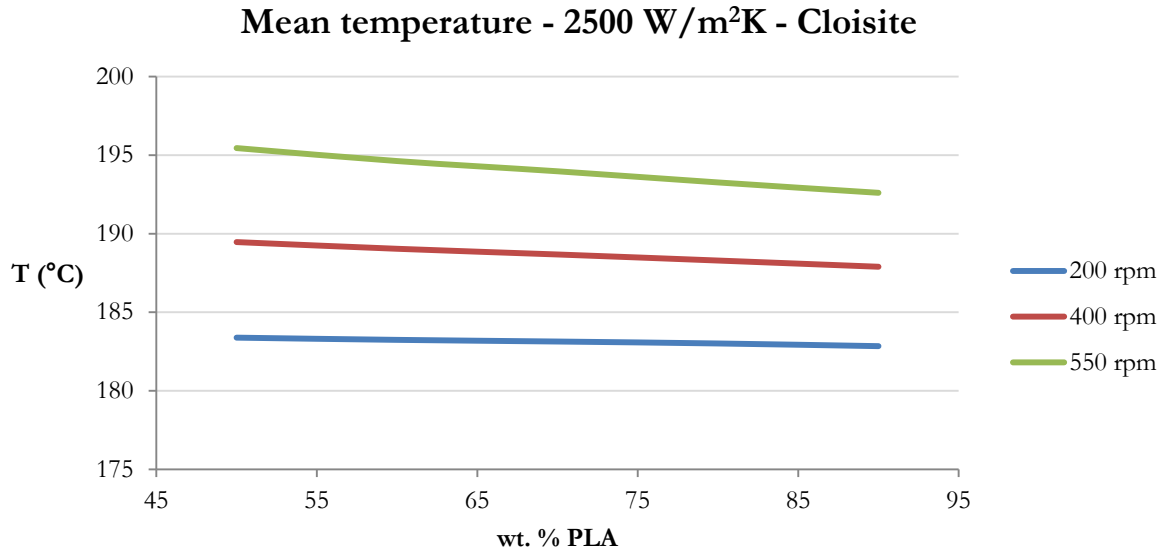


**Figura 1.7** - Variazione dei valori medi di temperatura al variare della composizione.

Viscosità e shear rate medi sono stati ottenuti escludendo dal calcolo la parte iniziale della vite, dove Ludovic restituisce valori nulli per le due grandezze, e il die. Come detto in precedenza, in quest'ultima parte dell'estrusore i risultati sono calcolati tramite un modello approssimato e sono generalmente molto maggiori di quelli riscontrati nel cilindro, con il rischio di falsare le medie in maniera significativa. Come prevedibile, lo shear rate non dipende dalla composizione del blend, mentre la viscosità (Figura 1.8) varia in maniera lineare al variare delle percentuali dei componenti polimerici, siccome si è scelto di descrivere  $\eta_{blend}$  con una legge di questo tipo.

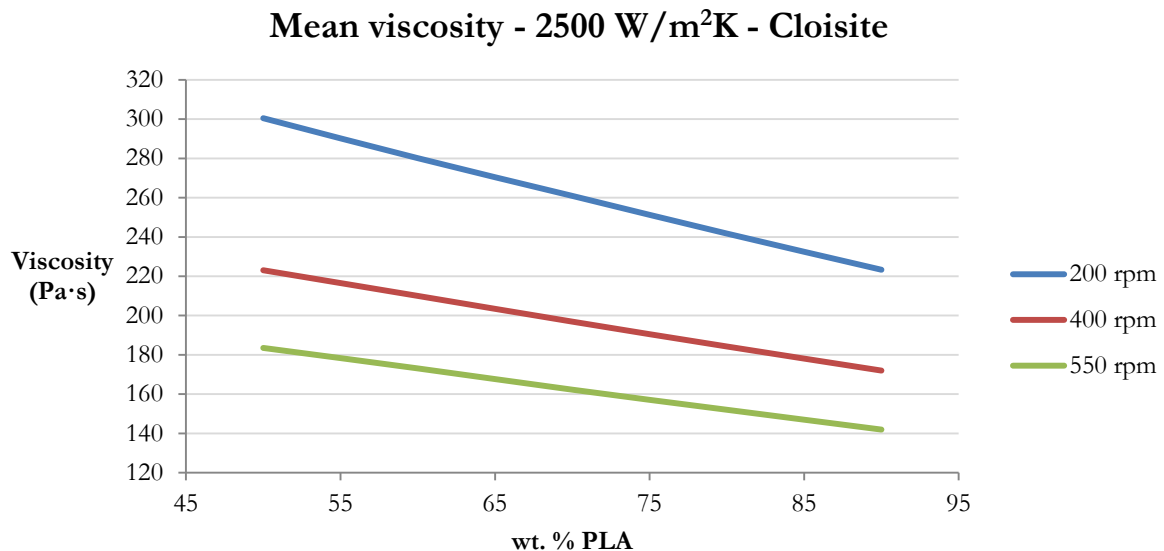


**Figura 1.8** - Variazione dei valori medi di viscosità al variare della composizione.

#### 1.4. Analisi dei risultati ottenuti con le simulazioni

Una volta verificata l'affidabilità di Ludovic nel fornire previsioni su quanto accade all'interno dell'estrusore, si è provveduto a simulare gli andamenti lungo l'asse della vite di alcune delle

grandezze osservate in precedenza per blend 70 wt. % PLA/ 30 wt. % PHBH processati a 400 rpm con portate di 3 kg/h (3,15 se è aggiunta la Cloisite). In questo modo è stato possibile uno studio più approfondito dell'effetto che un particolare profilo ha nella determinazione della morfologia finale.

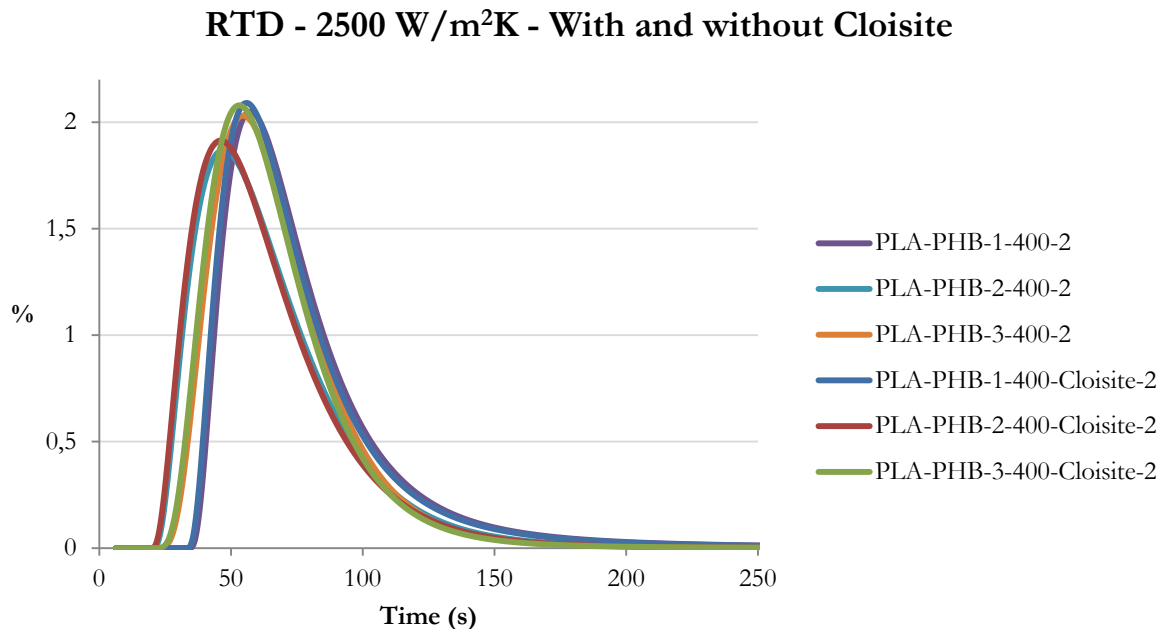


**Figura 1.9** - Distribuzioni dei tempi di residenza per le simulazioni a 400 rpm con e senza Cloisite.

Analizzando le distribuzioni dei tempi di residenza (Figura 1.9) si è osservato che il profilo vite 2, il quale possiede un numero minore di segmenti di masticazione, porta all'ottenimento di valori minimi e medi più bassi. Al contrario, con la configurazione numero 1, dotata di un elemento di miscelazione, sposta la curva verso destra e fa sì che questa presenti una "coda" più marcata per tempi più lunghi. La vite 3, dotata di un elemento di retro-flusso, è stata considerata come il giusto compromesso tra la necessità di disperdere finemente nel volume del PLA i noduli di PHBH e quella di evitare la coalescenza di questi ultimi. Entrambi i fenomeni, infatti, dipendono dal tempo che il fuso trascorre in determinate parti dell'estrusore. In seguito all'aggiunta di Cloisite si è notata una leggera traslazione delle distribuzioni verso tempi più brevi, una conseguenza dei leggeri aumenti di viscosità e portata.

Per quanto riguarda i profili della temperatura (Figura 1.10), si è notato che gli aumenti di tale grandezza in corrispondenza del primo blocco di masticazione (comune a tutti i profili vite) sono esattamente identici e le curve possono essere sovrapposte. Con la vite 2 si ottengono dapprima le temperature più basse, ma poi, nel secondo lungo segmento di masticazione, i valori diventano i più alti fatti registrare dalle simulazioni. Le configurazioni 1 e 3 garantiscono invece un andamento più regolare, fatto di riscaldamenti meno intensi negli elementi che restringono il flusso, seguiti da raffreddamenti nei segmenti di trasporto. Quando la Cloisite è aggiunta, i profili di temperatura sono "stirati" verso l'alto siccome negli elementi di masticazione la dissipazione viscosa è maggiore. Si nota inoltre una diminuzione di temperatura nel punto in cui il filler a temperatura ambiente entra nella macchina, causando un raffreddamento della massa fusa. Utilizzando la vite 3, questo raffreddamento è immediatamente compensato dall'azione del blocco di masticazione e retro-flusso.

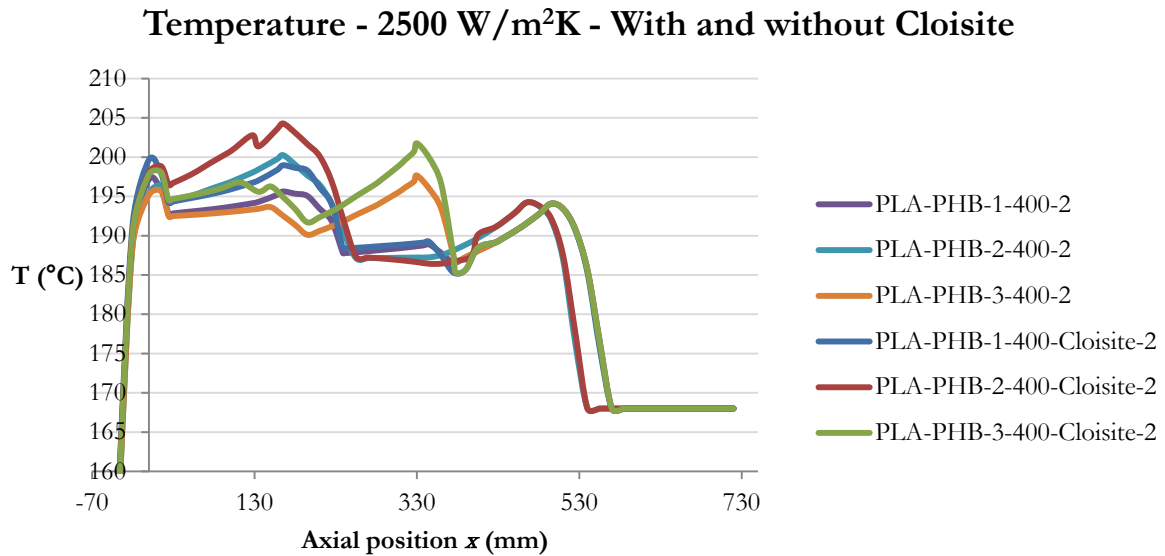


**Figura 1.10** - Profili di temperatura per le simulazioni a 400 rpm con e senza Cloisite. L'origine dell'asse  $x$  è posizionata all'interfaccia tra cilindro e die.

L'analisi dei tempi di residenza locali (LRT) ha dimostrato come i valori di tale parametro siano gli stessi per uno stesso tipo di elemento della vite. In particolare, il transito attraverso gli elementi di trasporto è più veloce rispetto a quello nei blocchi masticatori, a sua volta più veloce del passaggio attraverso un modulo di retro-flusso. Gli elementi che richiedono più tempo in assoluto ad essere attraversati sono quelli di miscelazione utilizzati sul profilo 1. Ciò spiega anche le osservazioni riportate in precedenza in merito alla RTD. L'aggiunta di Cloisite causa un leggero abbassamento dei LRT.

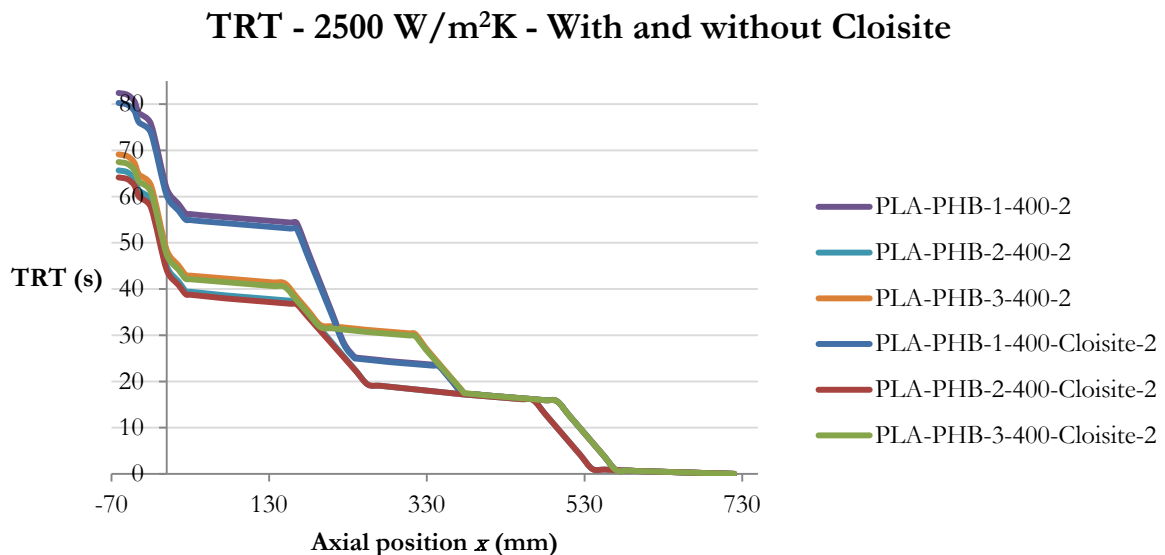


**Figura 1.11** - Evoluzione dei tempi di residenza totali a 400 rpm con e senza Cloisite. L'origine dell'asse  $x$  è posizionata all'interfaccia tra cilindro e die.

Osservando i profili del tempo di residenza totale (TRT, Figura 1.11) si può studiare l'andamento di  $RTD_{mean}$  al variare della coordinata assiale, che permette di apprezzare come utilizzando i profili identificati da numeri dispari il fuso sia obbligato a trascorrere un tempo maggiore all'interno di elementi che restringono il flusso. In questo modo dovrebbe essere garantita una migliore miscelazione dispersiva e distributiva sia del polimero disperso che della carica minerale.

I valori assunti dallo shear rate dipendono esclusivamente dal tipo di elemento montato sulla vite. In particolare, agli elementi di trasporto corrispondono le velocità di taglio più basse, mentre quelle più alte sono prerogativa del blocco di retro-flusso. Risultati leggermente inferiori sono calcolati in corrispondenza dei segmenti di masticazione e miscelazione. Come prevedibile, l'aggiunta di Cloisite non modifica la forma dei diagrammi. Ancora una volta, la vite 3 è stata identificata come quella in grado di assicurare migliori performance dal punto di vista della morfologia, siccome il fuso è sottoposto a shear rate più alti in maniera uniforme lungo tutta la lunghezza della macchina. La presenza di elementi che restringono il flusso immediatamente dopo il punto di ingresso della carica minerale nei profili 1 e 3 dovrebbe anche portare ad una dispersione e una distribuzione più efficace della carica minerale.

Nei profili di viscosità (Figura 1.12) si è osservato come questa grandezza aumenti nei segmenti di trasporto, per poi diminuire in corrispondenza dei blocchi di masticazione, miscelazione o retroflusso a causa dell'effetto combinato di shear rate e aumento della temperatura. Ancora una volta, il profilo 2 mostra una variazione piuttosto brusca all'incirca a 2/3 della vite, con  $\eta_{blend}$  che passa dai valori massimi osservati nei profili a quelli minimi (favorendo maggiormente i fenomeni di coalescenza) per effetto del secondo lungo blocco di masticazione. Al contrario, impiegando le configurazioni identificate dai numeri dispari i risultati si assestano su valori intermedi. Ciò, unito alla diminuzione di viscosità per effetto dei blocchi di masticazione posizionati appena dopo il punto da cui è aggiunta la Cloisite, permette di ottenere una morfologia finale con gocce di PHBH e, se presenti, lamelle di argilla finemente disperse e ben distribuite in tutto il volume. La presenza del filler, in accordo con la legge di Maron e Pierce, causa una traslazione delle curve verso viscosità maggiori.

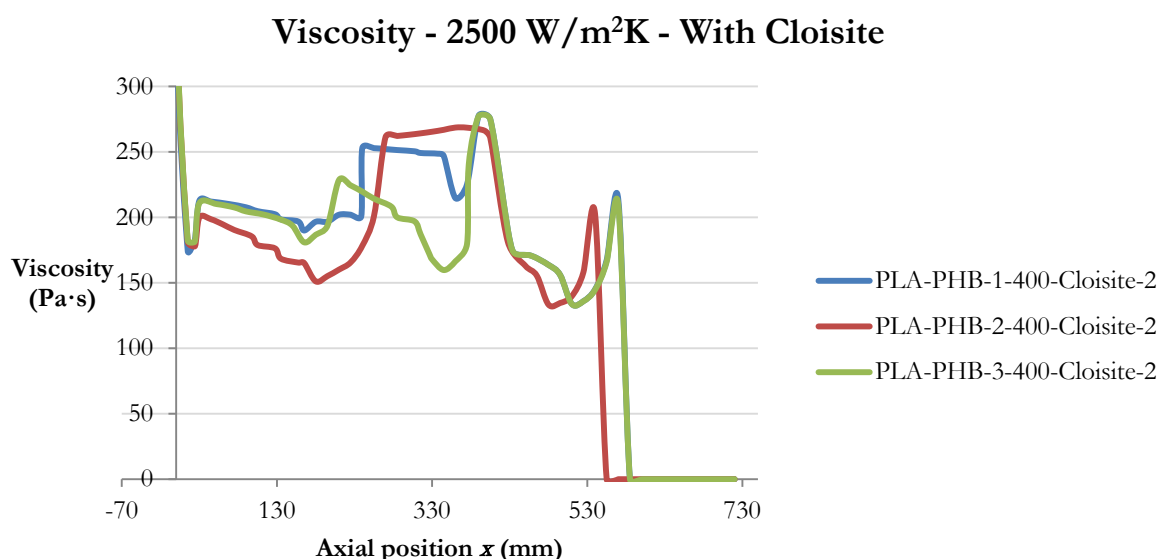


**Figura 1.12** - Evoluzione della viscosità a 400 rpm con e senza Cloisite.

Da quanto visto finora, il profilo vite 3 dovrebbe portare alla migliore morfologia finale sia quando la Cloisite è aggiunta, sia quando non lo è. Per confermare tale ipotesi, si è provato ad

applicare il modello proposto da Vergnes e Delamare ai risultati ottenuti con Ludovic. Questo modello è stato impiegato con successo nello studio della morfologia di blend a base poliolefinica e perciò si è provato a valutare se potesse risultare altrettanto efficace nel caso di un bio-blend immiscibile. Molte sono state le assunzioni e le semplificazioni (prima tra tutte quella di considerare tutti i domini di PHBH con la stessa taglia), perciò lo scopo di tali calcoli è stato principalmente quello di studiare gli andamenti, piuttosto che l'individuazione di valori numerici precisi. Il modello ha sostanzialmente confermato quanto ipotizzato in precedenza, indicando il profilo 3 come quello in grado di produrre la morfologia più soddisfacente (si veda Figura 1.13).

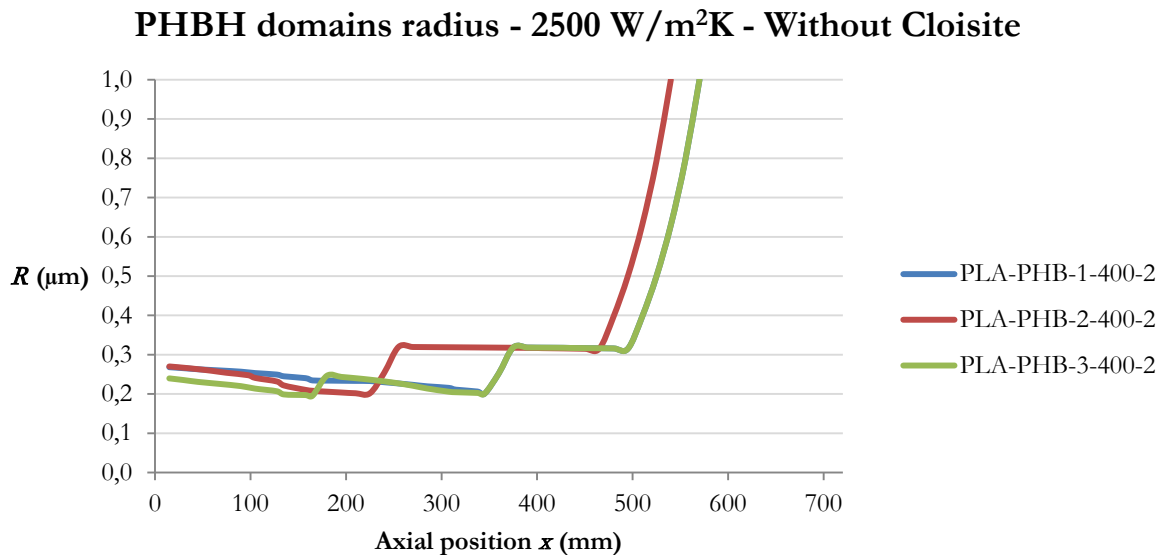


**Figura 1.13** - Evoluzione delle dimensioni dei domini di PHBH lungo la vite per le simulazioni che non prevedono l'aggiunta di Cloisite.

Opportune correzioni, basate sul fatto che alcuni parametri chiave provengono dalla letteratura scientifica e non da osservazioni sperimentali, hanno permesso di individuare il profilo 2 come quello che invece risulta meno efficace nella rottura dei domini più grandi di PHBH. Sostanzialmente le stesse osservazioni sono state fatte in merito alle simulazioni che prevedono l'aggiunta di filler. In quest'ultimo caso la taglia finale dei noduli di fase dispersa è inferiore.

#### 1.4.1. Effetto della velocità di rotazione

Una volta individuato il profilo vite 3 come quello in grado di assicurare la morfologia finale più soddisfacente, sono state effettuate tre simulazioni in presenza di Cloisite lasciando invariate tutte le impostazioni, eccetto la velocità di rotazione delle viti. Questa è stata impostata dapprima a 200, poi a 400 e successivamente a 550 rpm in modo da analizzare l'effetto di tale parametro sul processo di compounding in presenza di filler.

Si è osservato che l'aumento della velocità di rotazione causa lo spostamento delle curve RTD verso tempi più brevi, insieme con un loro "schiacciamento", entrambi giustificabili con il fatto che un maggiore numero di rotazioni al minuto risulta in una maggiore velocità di traslazione orizzontale (Figura 1.14). Questo spostamento appare più marcato passando da 200 a 400 rpm, mentre a 550 rpm la differenza è decisamente meno evidente.

### RTD - 2500 W/m<sup>2</sup>K - Cloisite

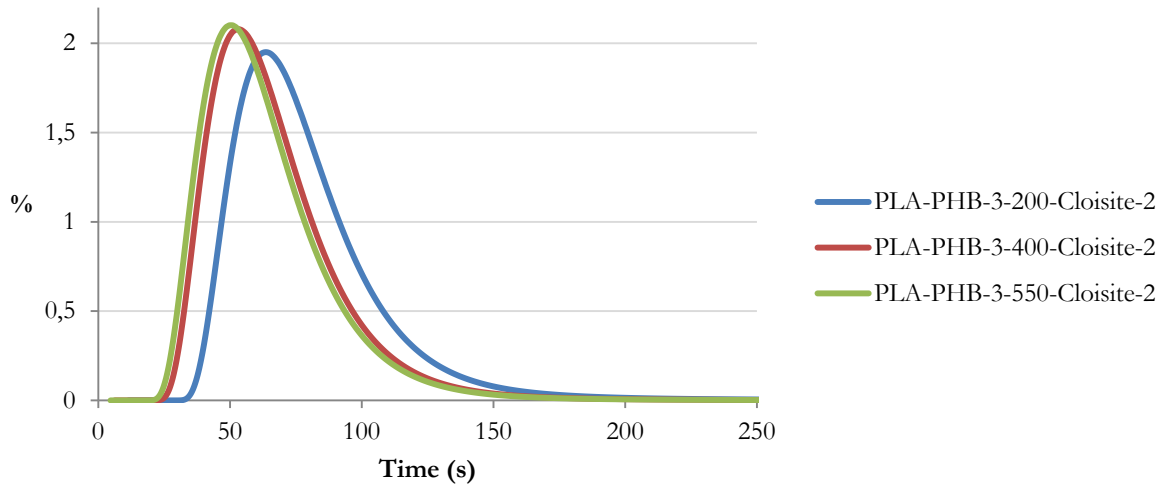


**Figura 1.14** - Distribuzioni dei tempi di residenza al variare della velocità di rotazione. I dati sono riferiti al profilo 3 ed al blend è aggiunta la Cloisite.

L'analisi dei diagrammi relativi ai tempi di residenza locali e totali dimostra come la differenza tra le RTD dipenda principalmente dai diversi tempi necessari ad attraversare le sezioni di trasporto (più lunghi ai bassi rpm). Infatti, la forma dei diagrammi LRT in corrispondenza degli elementi che restringono il flusso non varia. Questo può essere imputato al fatto che in tali elementi il tempo di residenza è calcolato esclusivamente sulla base di portata e volume libero.

A velocità di rotazione superiori corrispondono maggiori shear rate. Questo significa che sarà maggiore anche la temperatura del fuso a causa della dissipazione di energia meccanica. L'effetto combinato di questi due parametri fa sì che la viscosità diminuisca se aumenta il numero di giri che le viti compiono ogni minuto.

### PHBH domains radius - 2500 W/m<sup>2</sup>K - Cloisite

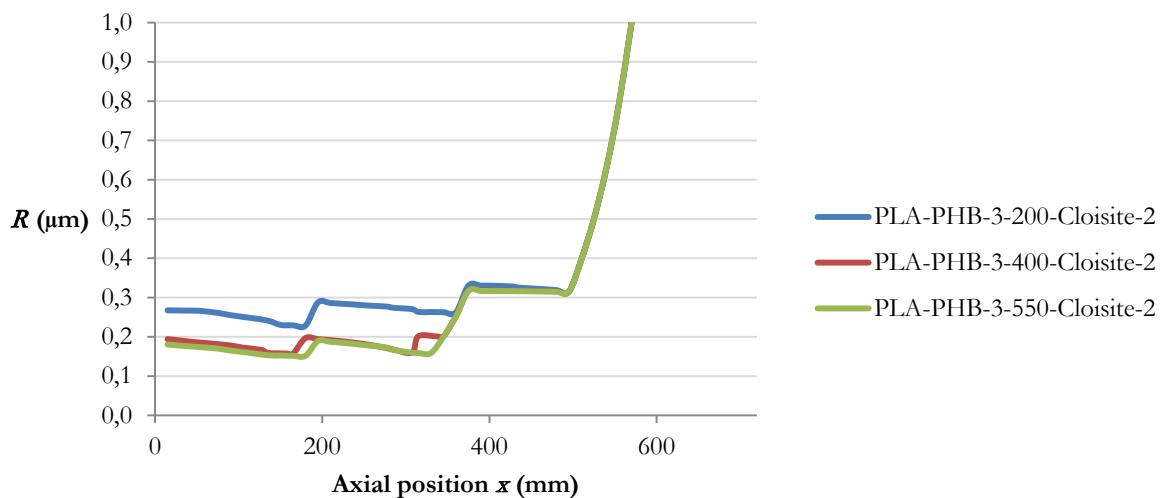


**Figura 1.15** - Evoluzione delle dimensioni dei domini di PHBH lungo la vite al variare della velocità di rotazione. Le simulazioni prevedono l'aggiunta della carica minerale.

Sulla base delle valutazioni effettuate in precedenza, si è concluso che i migliori risultati sono ottenuti quando la vite ruota più velocemente. È però necessario tenere in considerazione che questo significa il raggiungimento di temperature maggiori, le quali possono provocare la degradazione del polimero. Queste assunzioni sono confermate dall'analisi dei trend restituiti in seguito all'elaborazione dei risultati secondo il modello di Vergnes e Delamare (Figura 1.15). Tale modello conferma tra l'altro che la diminuzione di viscosità registrata a 400 e 550 rpm aumenta la probabilità di andare incontro a fenomeni di coalescenza, che sono però ampiamente compensati dalla rottura dei domini di PHBH, più efficace per maggiori velocità di taglio.

#### 1.4.2. Confronto delle previsioni con micrografie SEM

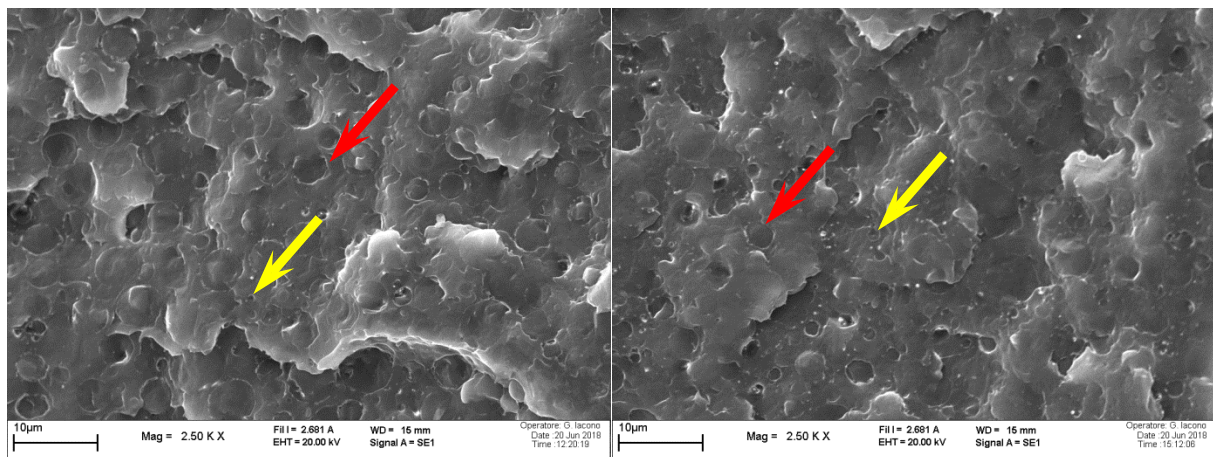


**Figura 1.16** - Micrografie SEM del blend PLA/PHBH 70/30 ottenuto a 400 rpm senza l'aggiunta di Cloisite con i profili vite 1 (sinistra) e 2 (destra). Le frecce rosse indicano i domini di PHBH più grandi, quelle gialle i noduli più piccoli.

Siccome le simulazioni sono state effettuate simulando il processo di compounding effettuato utilizzando un estrusore realmente esistente, per confermare i risultati si è proceduto all'osservazione delle micrografie SEM di blend 70 wt.% PLA/30 wt.% PHBH ottenuti a 400 rpm. In particolare, in assenza di Cloisite (Figura 1.16) con il profilo vite 1 si ottengono noduli di PHBH di grandi dimensioni ( $R \approx 1,5 \mu\text{m}$ ) affiancati da altri più piccoli ( $R \approx 0,6-0,7 \mu\text{m}$ ) ben distribuiti nel volume del blend. Lo stesso si osserva con la configurazione numero 2, ma in questo caso se da una parte i domini più grandi hanno dimensioni inferiori ( $1,4 \mu\text{m}$ ), quelli più piccoli hanno un volume leggermente maggiore ( $R \approx 0,8-0,9 \mu\text{m}$ ). Tuttavia, con quest'ultima vite la miscelazione distributiva risulta meno soddisfacente, in quanto è minore il tempo trascorso dal fuso all'interno degli elementi masticatori.

Osservando le micrografie dei campioni ottenuti aggiungendo la carica minerale (Figura 1.17) è possibile notare come la morfologia sia radicalmente differente, con noduli di PHBH molto più piccoli e caratterizzati da una distribuzione dimensionale molto stretta. Come previsto, i risultati migliori ( $R \approx 0,3-0,4 \mu\text{m}$ ) sono stati ottenuti con i profili vite 1 e 3, in particolare con quest'ultimo. La configurazione 2, invece, porta a domini di PHBH più grandi. Se da una parte le previsioni effettuate sulla base dei risultati ottenuti con Ludovic e con il modello di Vergnes e Delamare sono state confermate dalle analisi al SEM, dall'altra le micrografie dei blend in cui è stata aggiunta la Cloisite mostrano un importante limite di entrambi gli strumenti. Infatti, le differenze tra i profili ottenuti in presenza o in assenza del filler non permettono di accorgersi dell'effetto fondamentale che le lamine di argilla hanno sullo sviluppo della morfologia finale. Tali lamine, infatti, vanno a posizionarsi all'interfaccia tra i due polimeri riducendo la tensione interfacciale, e

quindi la taglia dei domini di polimero disperso. Si tratta cioè di un fenomeno di natura chimica che Ludovic, il quale valuta solo parametri fisici, non è in grado di considerare. Lo stesso può dirsi per il modello di Vergnes e Delamare, in cui si è ipotizzato che l'azione del filler riguardasse esclusivamente la viscosità delle due fasi polimeriche.

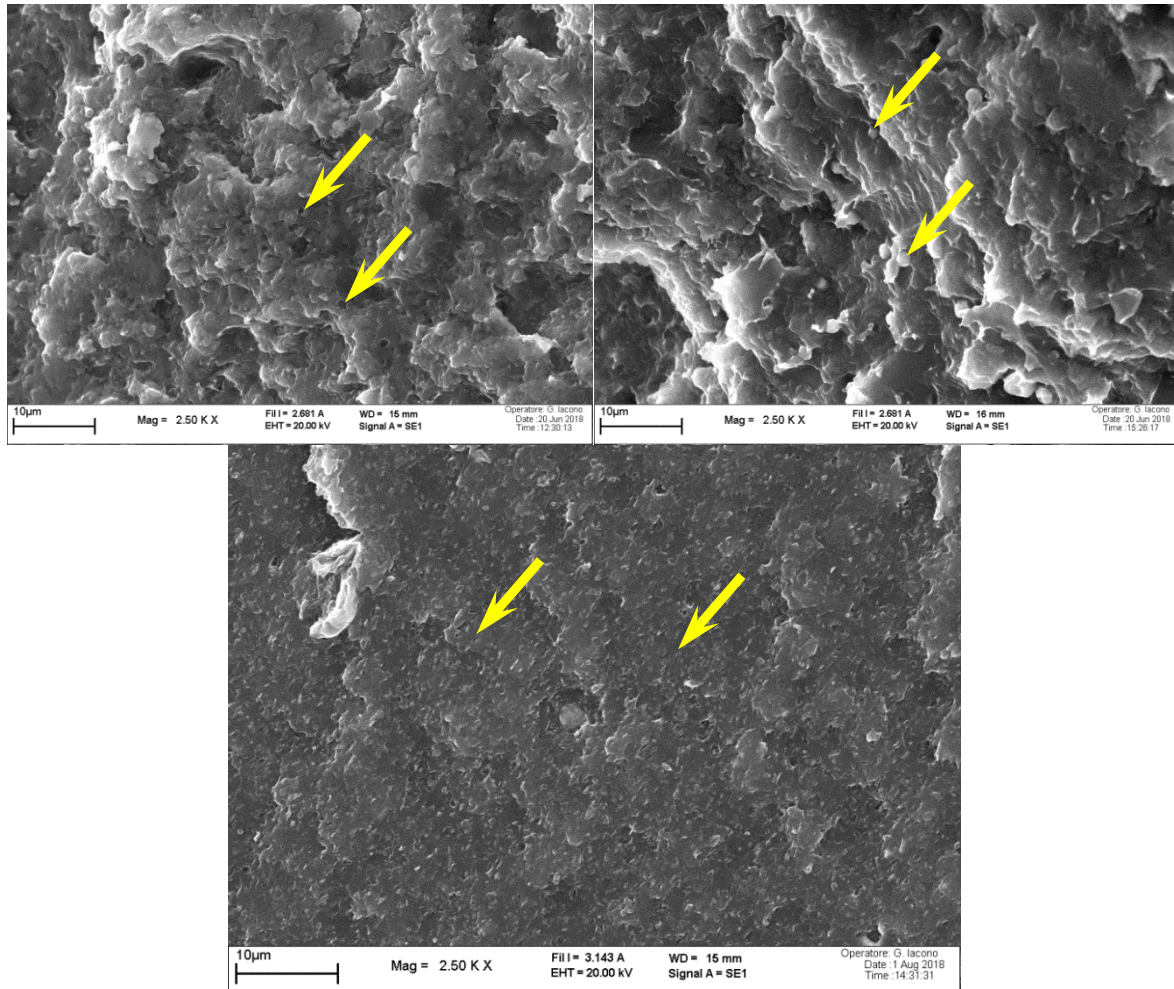


**Figura 1.17** - Micrografie SEM del blend PLA/PHBH 70/30 ottenuto a 400 rpm con aggiunta di Cloisite usando i profili vite 1 (in alto a sinistra), 2 (in alto a destra) e 3 (in basso). Sono indicati i domini di PHBH.

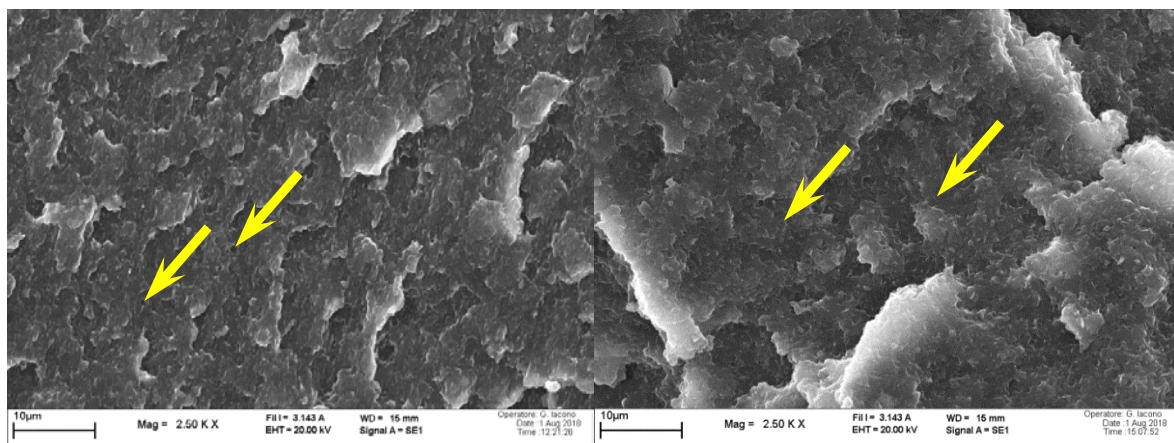


**Figura 1.18** - Micrografie SEM del blend PLA/PHBH 70/30 ottenuto a 250 rpm (sinistra) e 550 rpm (destra) con l'aggiunta di Cloisite usando il profilo vite 3. Le frecce gialle indicano i domini di PHBH.

Come previsto, aumentando la velocità di rotazione delle viti si riduce progressivamente la taglia dei domini di polimero, tanto che a 550 rpm ed in seguito all'aggiunta di Cloisite tali domini risultano praticamente indistinguibili (Figura 1.18).

### *1.5. Conclusioni*

Ludovic si è rivelato un valido aiuto nell'indirizzare la scelta delle migliori condizioni di processo per il processo di compounding, permettendo di selezionare il profilo vite in grado di portare ad una morfologia più soddisfacente e il regime di rotazione più adatto. La veridicità di tali previsioni, data inizialmente per assodata in seguito all'analisi dei risultati dei DoE, è stata poi sostanzialmente confermata dall'osservazione delle micrografie ottenute al SEM. Il modello proposto da Vergnes e Delamare, pur con tutti i limiti derivanti dal grande numero di semplificazioni che sono state fatte per applicarlo ai risultati ottenuti con Ludovic, si è dimostrato un ulteriore valido aiuto nella selezione del migliore profilo vite. Un'applicazione più rigorosa e ragionata del modello potrebbe permettere, in un prossimo futuro, di simulare con un buon grado di precisione anche la morfologia finale che si ottiene in seguito al compounding.



## 2. Introduction

In the last twenty years, plastic pollution has become a matter of great concern due to the massive use of polymers in disposable packaging applications. Since the service life of those objects is generally short, especially when they have to contain food, tons of waste are produced every day, with a considerable fraction that is still dispatched to landfills (although this percentage decreases every year). This issue implies a gradual consumption of oil supplies, because the most common materials employed in this field are polyolefins and polyethylene terephthalate (PET) synthesized from fossil resources. The final products are characterized by a low cost and good mechanical characteristics, but they result in a positive carbon footprint and require hundreds of years to be biodegraded.

Since recycling does not solve all the problems, due to some drawbacks related to the energy consumption and to the progressive degradation of the macromolecules in each re-processing step, many efforts have been made in order to produce large quantities of bio-based and biodegradable polymers that can be employed in the packaging industry. Unfortunately, the most common employed bioplastics, such as polylactic acid (PLA) produced from starch and polyhydroxyalkanoates (PHA) used as an energy supply by numerous microorganisms, show poor mechanical properties coupled with poor processability. Nowadays, chemical industries are able to supply large quantities (thousands of tons per year) of PLA at a competitive price, while the market of PHA is expanding because of the progressive increase in production capability, thanks to new plants in Asia and in the USA that will be able to quadruple the productivity in 2021 with regards to 2016<sup>[1]</sup>. Therefore, an effective solution could be the production of biopolymers-based blends in order to reciprocally compensate the drawbacks of each component.

At industrial scale, blending is performed in twin-screw extruders when both the polymers are in the molten state, but the identification of the best processing conditions, such as the optimal screw speed or feeding rate, is usually done by a trial and error approach. It means that long times are required in order to find a suitable screw profile. Moreover, an error means the necessity of disassemble the extruder to clean up the solidified polymer from the barrel and the screw before proceeding to further experiments. This forced break is highly time consuming and so should, obviously, be avoided.

A solution, whose feasibility for the case of the PLA-PHBH blend is studied later on, can be found in the use of Ludovic, a software especially designed to simulate the extrusion process. In fact, it has been pointed out by many studies as a valid help in the search for the optimal processing conditions<sup>[2],[3],[4]</sup>. The present work starts from a theoretical introduction of the topic with an overview on the thermodynamics of polymeric blends, followed by a section in which some considerations about the rheology are discussed. In fact, the final morphology depends mainly on the miscibility of the substances that constitute the system (determined by thermodynamics) along with the ratio between the viscosity of the minor and of the major component. Therefore, it can be said that these first two sections are preparatory to the following one, where the mechanisms for coalescence and breakup of a polymeric particle inside a melt are studied. In order to apply the various theories to extrusion, with the aim of predicting the morphology after compounding, a model proposed by the researchers Bruno Vergnes and Laurent Delamare is reported<sup>[5]</sup>. In fact, this model is very useful to understand what is happening along the screw, owing to a detailed mathematical description. Then, after a deepening on the functioning of twin-screw extruders, an overview on the existing PLA-based bio-blends with a

brief description of their characteristics introduces a more in-depth analysis of the properties of the PLA-PHBH blend.

A further chapter is devoted to the description of the software Ludovic, starting from a general description of how it organizes the simulations, followed by a deepening on the principles used for the calculation. Attention is put especially on the mathematical modelling of the elements constituting the screw and on the iterative process employed in order to get the results. The section that follows can instead be thought as the equivalent of the “Experimental” part of laboratory researches, since it reports the settings entered in order to correctly simulate the behaviour of the bio-based blend. The same is reported also for what concerns the Design of Experiments (DoEs), which basically consist in the repetition of a single simulation coupled with the simultaneous variation of two selected independent parameters inside a defined range. So, the results of the DoEs (commented in the fourth chapter of this work) can be shown as surfaces, whose height along the  $z$ -axis is a function of the independent variables cited before, reported on the  $x$  and  $y$ -axis. This representation and, in general, the DoE instrument enable to evaluate the reliability of the predictions returned by Ludovic. Maxima and minima of the surfaces can also point out specific configurations and settings of the extruder that can lead to a blend with particular properties.

The simulations are commented and compared in the fifth chapter, paying more attention to the Residence Time Distribution (RTD) data and to the curves of temperature, residence time, shear rate and viscosity plotted as a function of the axial position along the screw. This part is the core of the work, where the performances of the different profiles in the development of a satisfying morphology are evaluated, both in presence and in absence of the filler (Cloisite 5). The results of the simulations are employed to apply the model of Vergnes and Delamare, in order to aid the above-mentioned selection. After the individuation of the screw configuration that leads to the best final morphology, some simulations with different rotation speeds have been conducted with the aim of evaluating also the effect of this variable. Finally, the SEM micrographs of PLA-PHBH specimens compounded employing the same processing parameters used for the simulations are analysed, showing a satisfying accordance with the predictions.

### 3. Theoretical fundamentals

#### 3.1. Thermodynamic considerations

To mix polymers, it is necessary a negative value of the Gibbs free energy for mixing, that is

$$\Delta G_m < 0 \quad (3.1)$$

with  $\Delta G_m$  defined as

$$\Delta G_m = \Delta H_m - T\Delta S_m \quad (3.2)$$

where  $\Delta H_m$  and  $\Delta S_m$  are respectively the enthalpy and the entropy of mixing. In most of the cases  $\Delta H_m$  is positive while  $\Delta S_m$  is practically zero<sup>[6]</sup>, meaning that it is quite unusual to find a couple of miscible polymers. Using Flory and Huggins theories and the equation (3.2), Coleman<sup>[6],[7]</sup> derived the following relationship:

$$\frac{\Delta G_m}{RT} = \left[ \frac{\Phi_A}{N_A} \ln \Phi_A + \frac{\Phi_B}{N_B} \ln \Phi_B \right] + \chi \Phi_A \Phi_B \left( \frac{\Delta G_H}{RT} \right) \quad (3.3)$$

in which  $R$  is the gas constant,  $T$  the temperature (Kelvin),  $\Phi_A$  and  $\Phi_B$  the volume fractions of the two components,  $N_A$  and  $N_B$  their polymerization degrees,  $\chi$  an interaction parameter (the Flory-Huggins one) and  $\Delta G_H$  a free energy related to specific interactions between polymers.

Since in general  $N_A$  and  $N_B$  are large values, the term in square brackets, related to the combinatory entropy, is substantially zero and so to determine if two polymers are miscible or not the Flory-Huggins parameter becomes really important. This parameter measures the density of cohesive energy (it is its square root) or, in other words, the energy per unit volume required to remove a molecule from a liquid or a solid.  $\chi$  contains contributions of polar and non-polar interactions and it can be calculated by using the equation (3.4)<sup>[6]</sup>

$$\chi = \frac{V_{ref}}{RT} [\delta_A - \delta_B]^2 \quad (3.4)$$

where  $V_{ref}$  is a reference volume (the molar volume of the solvent), while  $\delta_A$  and  $\delta_B$  are the solubility parameters of polymers A and B respectively. It must be noted that the difference between these two quantities is squared, so  $\chi$  will always assume positive values, meaning that the miscibility depends on the term  $\Delta G_H/RT$ , which is negative if specific interactions are present.

What is reported above clearly shows that two polymers with similar solubility parameters have higher compatibility, but only if it is possible to establish specific interactions. As an example, the PP/PE blends are immiscible also if the solubility parameters are highly similar, since there are no specific interactions, but just weak dispersive forces.

Starting from what has been described before, Coleman has defined a critical value of  $\Delta\delta$  under which, dependently on the type of the polymers involved (and so on the intensity of specific interactions), miscibility can be attained. Those values are reported in Table 3.1.

Looking one more time to the PP/PE blends, since there are only dispersive forces  $\Delta\delta$  must be less than 0,1, but in this case the difference in solubility parameters is higher, explaining why the two polymers are not miscible. This approach can be useful in the first instance, but it has a disadvantage due to the fact that exact values of  $\delta$  are determined exclusively for those substances showing physical interactions only. In fact, every attempt to calculate them indirectly for systems interacting through hydrogen bonds or highly polar interactions leads to results with greater uncertainty that are, on a practical point of view, substantially useless<sup>[6]</sup>.

**Table 3.1** - Examples of interactions that can be found in a blend with the corresponding values of  $\Delta\delta_{critical}^{[6],[7]}$ .

Intensity of the interaction	Blend example	$\Delta\delta_{critical}$ (Hildebrands, $cal^{1/2}/cm^{3/2}$ )
Dispersive forces	PBD-PE	<0,1
Dipole-dipole	PMMA-PEO	0,5
Weak	PVC-BAN	1
Weak to moderate	SAN-PMMA	1,5
Moderate	PC-Poliestere	2
Moderate to strong	Nylon-PEO	2,5
Strong	PVPh-PVAc	3
Very strong	PMMA-PEO	>3

If miscibility is assessed from a thermodynamic point of view, the properties show a linear variation with the concentration of the dispersed component, as it is shown in Figure 3.1. Moreover, the material has only one glass transition temperature, that generally lies in the range between the ones of the two polymers, and it is transparent because no scattering phenomena take place, due to the absence of small domains of the minor component, which are typical of immiscible blends. In this last case, significant deviations from the linear trend are observed because the properties are strictly related to the morphology, and so to the processing conditions, for a specific composition of the blend.

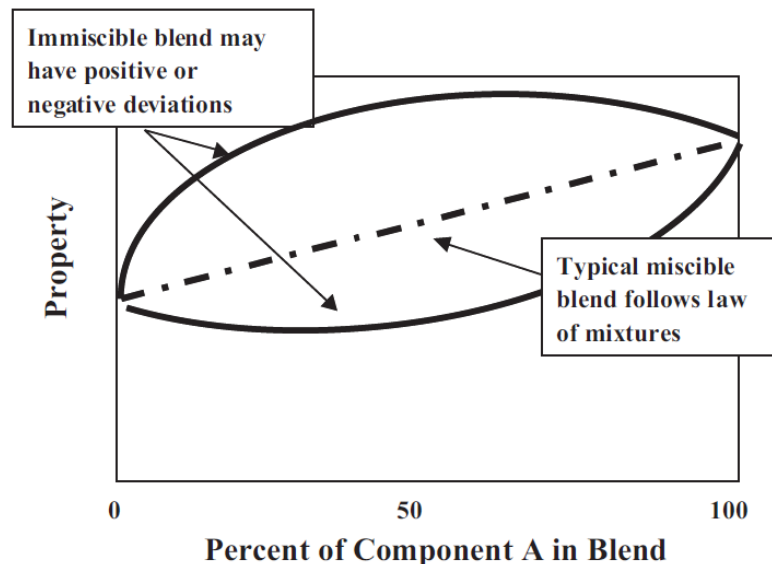


**Figure 3.1** - Variation of a certain property in a blend depending on the percentage of the A component. The behaviour of miscible and immiscible blends is plotted with dashed and continuous lines, respectively. Reproduced from [6].

In literature it is not so rare the use of the word “compatibility” to describe the interactions between two polymers in a blend when they are not completely miscible, while “miscibility” is used in the case it is assessed over the entire range of possible compositions. This approach is not really correct because while the second term describes a specific and well defined situation (two

polymers are miscible if they form a unique phase at any temperature and composition), the same cannot be said while talking of “compatibility”, so its use results more subjective and sometimes quite unclear<sup>[6]</sup>.

### 3.2. Rheological considerations

Miscible blends are quite easy to be characterized from a rheological point of view, because a simple logarithmic relationship (3.5) can be used

$$\log(\eta_{blend}) = X_A \log(\eta_A) + X_B \log(\eta_B) \quad (3.5)$$

in which  $X_A$  and  $X_B$  are the mass fractions of the two components, while  $\eta_A$  and  $\eta_B$  are the viscosities of both the polymers. The same formula is effective also if the viscosity  $\eta$  (Pa·s) is substituted with the *MFI* (g/10 min). Some studies have observed positive deviations of the model from experimental results, but, due to its simplicity, it can be used at least as a first approximation.

With immiscible blends the situation is more complicated, sometimes also in the case they are produced by using compatibilizers. In fact, the typical (for polymers) time-temperature superposition loses its validity, since the two components have generally a different behaviour. For the same reason, also the mixing rule of eq. (3.5) is no longer useful<sup>[6]</sup>.

In the case of polymer blends containing a certain amount of solid particles, also their presence must be taken into account since a rigid filler dispersed into a polymer usually raise the polymer viscosity by hindering the regular flow of the melt. One more time, the non-Newtonian nature of the fluid together with general morphology, size distribution and agglomeration make the attempt to write an effective mathematical relationship more difficult. Also the morphology developed by the minor component must be taken into account while working with immiscible blends.

For a single polymer with a dispersed mineral filler, the equation (3.6) proposed by Krieger-Dougherty<sup>[8]</sup> can be used to calculate the viscosity of the system.

$$\eta = \frac{\eta_{pol}}{[1 - (\Phi/\Phi_m)]^{-[\eta]\Phi_m}} \quad (3.6)$$

$\eta_{pol}$  is the polymer viscosity,  $\Phi$  the volume fraction of dispersed phase,  $[\eta]$  the intrinsic viscosity and  $\Phi_m$  an empirical parameter. This last one is the maximum volume fraction at which the flow can occur and accounts for the shape of the particles constituting the filler. In fact, it decreases at higher aspect ratios (the ratio between larger and smaller dimension), while it increases, for the same morphology, if size distribution is not uniform. It must be noted that this particular equation, but also the majority of the other models relating viscosity and filler concentration, does not consider the possibility that the additives used to improve polymer/filler adhesion at the interface can further increase the viscosity of the material. As an example, if the polymers contain functional groups, they can react and lead to the formation of crosslinks, enhancing the viscosity of the system in this way.

A simplified version of the above equation is proposed by Maron and Pierce (3.7)<sup>[8]</sup>.

$$\eta = \frac{\eta_{pol}}{[1 - (\Phi/\Phi_m)]^2} \quad (3.7)$$

### 3.3. Morphology development

Due to the fact that a couple of polymers is miscible only in rare cases, most of the blends show a multiphasic structure characterized by a high interfacial tension and a low adhesion between the

phases. Therefore, it is clear the importance of secondary interactions and morphology in the determination of the final properties of the blend, that can be tuned to reach an optimum. In particular, it is necessary that the interfacial tension of the dispersed phase (present in less amount) allows the formation of droplets small enough to guarantee the homogeneity at a macroscopic level, and that the adhesion lets the component to withstand stresses and deformation without disrupting the initial morphology.

The behaviour of a single droplet of Newtonian fluid inside another Newtonian fluid is currently well understood. In particular, it depends on the interfacial tension, that holds together the droplet, and on the force exerted by the surrounding fluid, which has the tendency to disrupt it. The more alike the two substances are, the lower will be the interfacial tension and so the droplet shows a greater difficulty to remain intact. This explains why it is useful to put in relation  $\Gamma_{12}$  at first with the surface tension (easy to measure) and, after that, with the solubility parameters. Starting from Good and Girifalco equation (3.8)<sup>[6]</sup>

$$\Gamma_{12} = \Gamma_1 + \Gamma_2 - 2\varphi\sqrt{\Gamma_1\Gamma_2} \quad (3.8)$$

where  $\Gamma_{12}$  is the interfacial tension between polymers, whose surface tensions are  $\Gamma_1$  and  $\Gamma_2$ , and  $\varphi$  is an interaction parameter ranging, according to the values reported by Wu<sup>[9]</sup> about several couples of substances, between 0,79 and 0,98.

Since surface tension can be related to the solubility parameter  $\delta_1$  and to the density  $\rho_1$  using the following equation<sup>[6]</sup>:

$$\Gamma_1 = 0,2575 \frac{\delta_1}{\sqrt[3]{\rho_1}} \quad (3.9)$$

By putting together (3.8) and (3.9) and considering a density for the polymer of about 1 g/mL and  $\varphi=1$ , it can be got

$$\Gamma_{12} \cong 0,26(\delta_1 - \delta_2)^2 \quad (3.10)$$

This relationship (3.10) reports what has been explained by words before, in fact the more solubility parameters are similar, and so the more the two substances are similar, the lower will be the interfacial tension.

The stress field surrounding the droplet is able to exert on it a drag force which, approximating its section to a square with sides equal to the radius  $a$ , is

$$F_{drag} \sim \eta_c \dot{\gamma} a^2 \quad (3.11)$$

where  $\eta_c$  is the viscosity of the continuous phase and  $\dot{\gamma}$  the shear rate<sup>[6]</sup>. It must be noted that  $\eta_c \dot{\gamma}$  quantifies the shear stress imposed to the droplet.

Having defined these two forces that work on opposite directions (one holds the droplet together, while the other tends to disrupt it) it is possible to write a formula to calculate the capillary number  $Ca$  (3.12)<sup>[6],[10]</sup>

$$Ca = \frac{F_{drag}}{F_{interfacial}} = \frac{\eta_c \dot{\gamma} D_d}{2\Gamma_{12}} \quad (3.12)$$

with  $D_d$  diameter of the droplet. Over a critical value of  $Ca$  the droplet is disrupted because the external force overcomes the one that keeps it intact. According to Taylor, in a Newtonian fluid the value of  $Ca_{critical}$  depends over the ratio between the viscosity of the droplet and the one of the surrounding continuous phase  $\eta_d/\eta_c$ .

In a simple shear flow,  $Ca_{critical}$  reaches a minimum for viscosity ratios next to 1. On the other side, in an elongational flow a simple decrease of this parameter with the increase of  $\eta_d/\eta_c$  is

observed<sup>[10]</sup>. Those trends are resumed in Figure 3.2, where it is possible to note the greater effectiveness of the elongational flow in reducing the diameter of the droplet. In fact, keeping constant the viscosity ratio, the critical capillary number is always lower, pointing out the lower forces needed to break the dispersed phase.

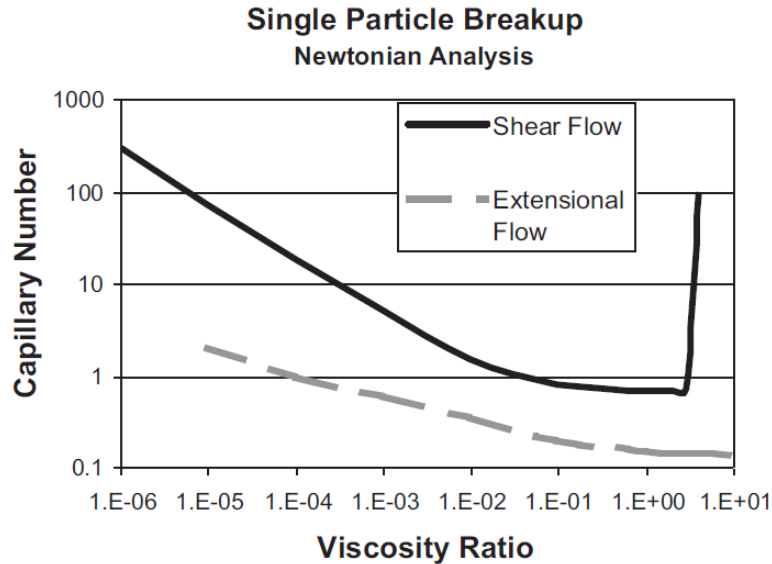


**Figure 3.2** - Critical capillary number  $Ca_{critical}$  as a function of the viscosity ratio in a shear (continuous line) or elongational flow (dashed line). Reproduced from [6].

The rapid increase of  $Ca_{critical}$  for viscosity ratios slightly higher than 1 shows the impossibility to break the droplet under shear flow when  $\eta_d/\eta_c > 3,5$ . This problem is not encountered in the case of elongational flow, explaining why the more common twin-screw extruders have a co-rotating configuration in order to maximize this kind of stresses.

Eq. (3.12) can be re-written in order to isolate the droplet diameter (3.13).

$$D_d = \frac{2\Gamma_{12}Ca_{critical}}{\eta_c\dot{\gamma}} \quad (3.13)$$

In this way, it is possible to observe that in order to reduce the diameter of the dispersed phase (because generally this is the objective) many paths can be followed. In particular, it is possible to:

- reduce  $\Gamma_{12}$ , for example by using compatibilizers;
- reduce  $Ca_{critical}$  by properly adjusting  $\eta_d/\eta_c$  according to what is observed in Figure 3.2;
- raise  $\eta_c$ ;
- raise  $\dot{\gamma}$ ;
- use mixing apparatus able to exert high elongational stresses.

If the situation for Newtonian fluids is currently clear and well understood, the same cannot be said for polymeric blends. In fact, resins show viscosity values that decrease by increasing the shear rate, that is they are shear-thinning fluids. Another element to be considered is the melt elasticity, characterized by the difference between the first and the second normal stresses difference. Many models use the conservative module to take into account this phenomenon, but the assumption has been proved to be correct only at low shear rates, where  $G'$  is actually proportional to this difference, while it causes an underestimation of the elasticity for higher values of  $\dot{\gamma}$ .

Elastic forces help in holding together the droplets, so if these droplets are more elastic than the surrounding fluid an increase in  $Ca_{critical}$  is registered. It leads to greater difficulties in dispersive mixing, with the discontinuous phase showing larger mean dimensions. On the contrary, a higher elasticity of the matrix results in higher drag forces, which help in disrupting the droplets. If in general the trends are clear, there is a lack of precise and reliable mathematical models and the existing theories are more or less effective in dependence of the boundary conditions.

Furthermore, it must be taken into account also the fact that droplets breakup usually happens due to different mechanisms with respect to the ones proposed for Newtonian fluids (like Taylor instability). Actually, under particular conditions those mechanisms have been observed also in the case of non-Newtonian fluids, but in general the droplets become elongated in a direction perpendicular to the flow. In this way their extremities are located in zones characterized by different velocities, causing the breakup<sup>[6]</sup>.

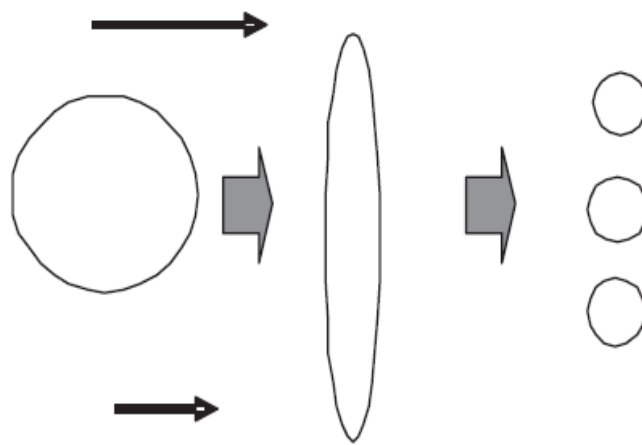


**Figure 3.3** - Breakup mechanism of a non-Newtonian droplet in a fluid. Reproduced from [6].

Another complication comes when trying to extend a model that studies the behaviour of a single droplet to the case of systems where the minor component is present in percentages higher than 1%, since coalescence is more likely to happen and leads to droplets with final dimensions greater than what expected according to the models. Shi<sup>[11]</sup> has observed that the ideal conditions for disrupting a single droplet (high shear rates and lower viscosity of the dispersed phase) at the same time promote coalescence. Using compatibilizers the phenomenon can be prevented, because these substances are able to create a shell on droplets' surfaces, that undergo reciprocal repulsion in this way.

Due to what is explained above, it has been experimentally observed that if the concentration of the dispersed phase is increased, at a certain point it becomes the continuous phase. It is something clearly not astonishing, so it is more interesting to look at the variations in the morphology of the system. For example, taking a HDPE/PS blend as an example (the two polymers are not miscible) and analysing what is reported in Figure 3.4, it can be observed that, under the particular operating conditions employed, PS constitutes the matrix of the system up to concentrations of about 70% (and not 50% as it could be expected). Moreover, PS has initially a spherical shape that, due to coalescence, becomes fibrillar if its concentration is raised. A further increase of the presence of PS leads to a co-continuous structure when its percentage is near to the one at which phase inversion is observed. In Figure 3.4 it is also interesting to see the effect of compatibilizers (dashed line) in the development of a morphology with smaller PS domains because SEBS are able to inhibit, at least partially, the coalescence<sup>[6]</sup>.

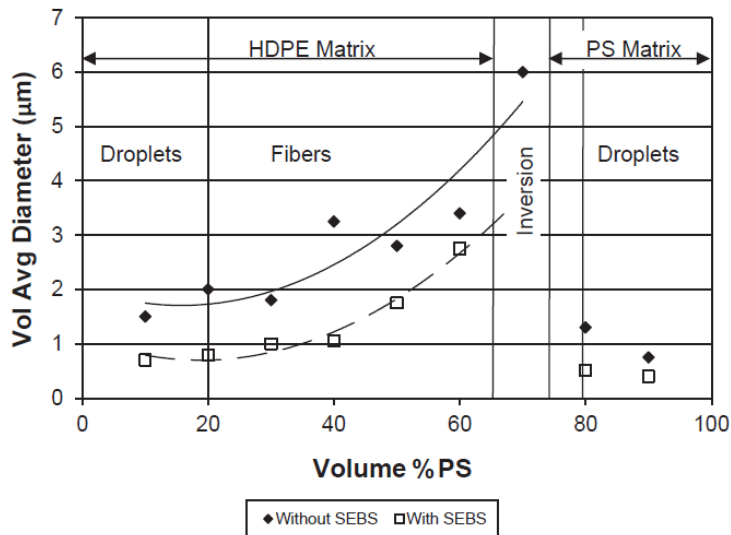


**Figure 3.4** - Morphology of a HDPE/PS blend as a function of the volume percentage of polystyrene. Please note that the inversion occurs at about 70 vol. %. Reproduced from [6].

In particular, a co-continuous morphology of two immiscible polymers is achieved when the system shows the coexistence of continuous structures (in the three dimensions) within the same volume. Two definitions for co-continuous blends have been proposed, whose differences are graphically explained in Figure 3.5. The first one considers the blend as a system where the two polymers form two different and complementary reversed (antitropic) networks without interruptions. It happens for a composition range about  $\Phi_{PI}$ , called the phase inversion point.

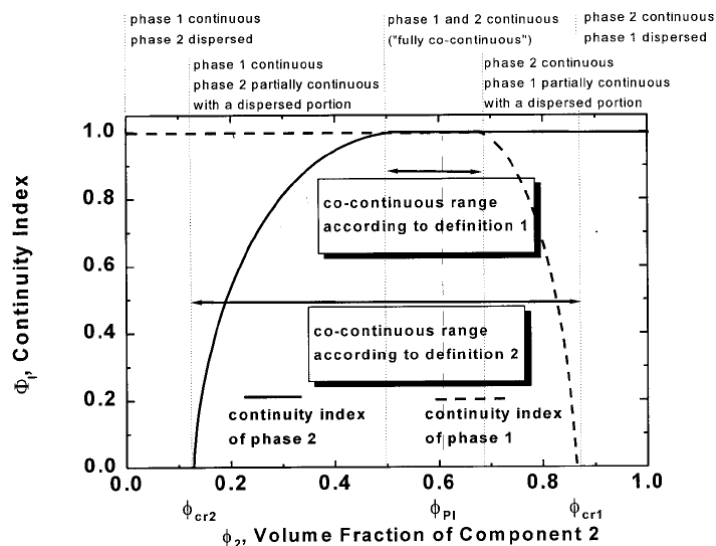


**Figure 3.5** - Difference between the two definitions for the co-continuous morphology in a polymer blend. Reproduced from [12].

The second definition, proposed by Utracki, is based on the concept of percolation threshold, so a co-continuous morphology is attained if the two components of the blend form at least two structures (one for each polymer) that span over the whole volume. Since a certain percentage of macromolecules is initially excluded from these continuous networks, a continuity index  $\Phi_c$  is needed together with the critical volume fraction  $\Phi_{cr}$ , at which percolation is got, to completely describe the system. The first definition is the most used in the literature and can be considered a

special case of the second one, with both the components having a  $\Phi_I$  equal to 1. The co-continuous structure is transient because it tends to evolve to a more stable one with lower surface energy. Then, it is necessary to kinetically inhibit this evolution with a rapid quenching, in order to preserve the morphology by crystallization or vitrification<sup>[12]</sup>.

To develop a co-continuous structure from a polymer melt in a shear field, the most effective condition is achieved when the ratio of the viscosities and the one of the volume fractions are equal or, in other words, when

$$\frac{\Phi_{1,PI}}{\Phi_{2,PI}} \cong \frac{\eta_1}{\eta_2} \quad (3.14)$$

In fact, equal volume fractions maximise the opportunity to maintain connectivity (there is not a component present in minor amount), but generally the viscosities are not the same for the two polymers. Since the component with lower viscosity tends to be continuous, because in this way it maximises the energy dissipation in the flow field, to compensate this phenomenon it is necessary to increase to the same extent the weight percentage of the other polymer, leading in this way to the above equation (3.14). To correctly describe what is happening in the system, it is of great importance the correct choice of the conditions in which the viscosity is measured; to this aim, some researchers have proposed to substitute the viscosity ratio with the torque ratio, since blending generally takes place in twin-screw extruders or similar machines. Moreover, due to the fact that the equation describes a system containing non-Newtonian fluids, significant deviations can be observed, especially for viscosity ratios higher than 1. Anyway, the great simplicity of the relationship makes it useful especially as a first approximation.

Other problems can arise in the attempt to model the behaviour of the dispersed polymeric phase inside the machines commonly used for compounding operations, like twin-screw extruders. These devices are in fact characterized by complex stress fields, resulting generally from the superposition of shear and elongational stresses, and shear rates that change significantly along the axial direction. Due to that, in the past it has been proposed to measure  $Ca_{critical}$  as a function of viscosity for the specific machine, rather than try to write a complex model.

As briefly stated before, some uncertainty exists also about what kind of viscosity values have to be used in the calculation of  $\eta_d/\eta_c$ , because the temperature changes along the screw. In fact, this ratio varies of several orders of magnitude in the path from the feeder to the die, since the dependence between  $\eta$  and the temperature is not the same for the two polymers. In the case of a blend, some studies report that zero shear viscosity must be used, while others are more favourable to employ the viscosity at a shear rate that is significant for the process. Due to the fact that the droplet is broken up by the stress field surrounding it, which is constant along the interface in the steady-state (but the same cannot be said for the shear rate), it can be thought to determine  $\eta_d/\eta_c$  at a constant stress value which is representative for the process. The results calculated with the various methods can significantly change, adding more and more complexity to the attempts of writing a reliable model<sup>[12]</sup>.

### 3.4. *The model of Vergnes and Delamare*

Taking into account the difficulties of writing an effective model, the researchers Laurent Delamare and Bruno Vergnes have revised a study published in 1992 by Shi and Utracki<sup>[11]</sup>, in order to provide mathematical relationships able to describe the development of the final morphology of a blend after compounding. In particular, their work is based on the quantification of the probability for coalescence and breakup to happen inside an extruder<sup>[5]</sup>.

### 3.4.1. Modelling of coalescence and breakup phenomena

With reference to the capillary number and to its influence on the final morphology, the study reports that:

- If  $Ca < Ca_{critical}$  the droplet is deformed, but does not break.
- If  $Ca_{critical} < Ca < 2Ca_{critical}$  two identical droplets are formed due to instability phenomena. This does not happen immediately, but it requires a certain time that depends on the initial diameter, the interfacial tension and the viscosity ratio. Vergnes and Delamare propose the following relationship:

$$t_b = \frac{2t_b^* Ca}{\dot{\gamma}} \quad (3.15)$$

where  $\dot{\gamma}$  is the shear rate,  $t_b$  is the time required for breakup and  $t_b^*$  is a dimensionless constant that depends only on  $\eta_a/\eta_c$ . Longer times are required for higher capillary numbers, while more intense shear rates speed up the phenomenon.

- If  $Ca > 2Ca_{critical}$  the minor phase accommodates the deformation of the matrix, elongating to create fibrils. These fibrils will breakup, if their diameter is lower than a critical empirical value  $d^*$ , due to capillary instability phenomena that follow the stop of the flow. In this case the required time is quantified by eq. (3.16)

$$t_b = \frac{2\eta_c R_0}{\Omega_m \Gamma_{12}} \ln \left( \sqrt{\frac{2R_0}{3\alpha_0}} \right) \quad (3.16)$$

where  $R_0$  is the initial diameter of the fibrils,  $\alpha_0$  the amplitude of the deformation and  $\Omega_m$  another function of the viscosity ratio.

The researchers repeatedly point out that the final model is developed from assumptions referred to Newtonian fluids, so it could result partially inaccurate due to the higher stability of viscoelastic non-Newtonian fluids. At the same time, they recognise the lack in the existing literature of valuable and complete theoretical models referred to the examined case.

The collision of two droplets inside the flow can lead to larger final diameters due to coalescence. This phenomenon starts to be perceptible already with concentrations slightly higher than 0,5 wt. %, so it is necessary to properly describe it in the model. In particular, Vergnes and Delamare report the conclusions of Elmendorp and Van der Vegt<sup>[13]</sup> for what concerns the collision of two spherical nodules under shear stress. In this last study, coalescence is considered as the result of two subsequent steps, particularly:

- The collision of two nodules, whose frequency can be calculated by the relationship (3.17)

$$C = \frac{8\dot{\gamma}\Phi}{\pi} \quad (3.17)$$

where  $\dot{\gamma}$  is the shear rate and  $\Phi$  the volume fraction of dispersed phase. The probability for collision to happen is instead quantified as

$$P_{col} = \exp \left( \frac{-\pi}{8\dot{\gamma}\Phi t_{loc}} \right) = \exp \left( -\frac{1}{C t_{loc}} \right) \quad (3.18)$$

with  $t_{loc}$  residence time in the considered sub-element, like the C-chamber. Inside the totally-filled elements (kneading, backflow)  $t_{loc}$  is obtained by simply dividing the volume by the flow rate, while in the partially-filled elements it depends on the screw speed.

- The expulsion of the liquid film. The probability for this phenomenon to happen depends on the mobility of the interface, in turn related to the viscosity ratio. In particular, if  $\eta_d/\eta_c \gg 1$  the interface is mobile, while it is immobile when  $\eta_d/\eta_c \ll 1$ . Three different cases can be distinguished, each with a particular formula to quantify the probability of eliminating the liquid film. For immobile interfaces

$$P_{exp} = \exp \left[ -\frac{9}{8} \left( \frac{R}{b^*} \right)^2 Ca^2 \right] \quad (3.19)$$

while for partially mobile interfaces it is valid the relationship

$$P_{exp} = \exp \left[ -\frac{\sqrt{3}}{4} \left( \frac{R}{b^*} \right) \frac{\eta_d}{\eta_c} Ca^{\frac{3}{2}} \right] \quad (3.20)$$

Finally, with immobile interfaces

$$P_{exp} = \exp \left[ -\frac{3}{2} \ln \left( \frac{R}{b^*} \right) Ca \right] \quad (3.21)$$

In the formulas reported above,  $R$  is the radius of the dispersed nodule, while  $b^*$  is the critical thickness needed to have the breakage of the film, defined as

$$b^* = \left( \frac{10^{-20} R}{8\pi\Gamma_{12}} \right)^{\frac{1}{3}} \quad (3.22)$$

The probability to have coalescence  $P_{coal}$  is the product of  $P_{col}$  and  $P_{exp}$  and by knowing it the final dimension of the new droplet can be obtained. Basing on volume conservation, the following relation can be obtained:

$$R^* = R \left( \frac{2}{2 - P_{coal}} \right)^{\frac{1}{3}} \quad (3.23)$$

### 3.4.2. Modelling of morphologic variation along the extruder

Once coalescence and breakup mechanisms have been defined, some assumptions must be done to define when, where and why these phenomena happen inside the extruder.

Since the model proposed before describes what happens to nodular droplets, the analysis can only be referred to the case in which the concentration of the minor component is quite low because it would not be effective with co-continuous morphologies. Starting from this assumption, it can be assumed that the rheological behaviour of the system substantially reflects the one of the matrix, described by Vergnes and Delamare with Carreau-Yasuda law.

The study does not provide an analysis of melting and a quite drastic hypothesis is done, considering that this process fully happens in correspondence of the first restricting element (kneading, mixing or back-flow), so the computation starts there. It is necessary to define the dimension of the dispersed phase  $D_0$  in this region, that can be likely be estimated in the range 1-10  $\mu\text{m}$ .

Vergnes and Delamare subdivide the screw in “strong” and “weak” zones that have a different effect over the final morphology. In particular, the “strong” zones are always filled and the pressure is over the atmospheric one, with complex flows and high shear rates. Here it is valid what has been stated before about the relationships between capillary number and droplets breakup, that happens only if  $Ca > Ca_{critical}$ . In a “strong” element two identical droplets are formed starting from a bigger one if  $Ca_{critical} < Ca < 2Ca_{critical}$  and the local residence time  $t_{loc}$  is

lower than  $t_b$ , while ellipsoidal fibrils are produced if  $Ca > 2Ca_{critical}$ . These fibrils are characterized by a length  $L$  equal to

$$L = D\gamma \quad (3.24)$$

and a diameter  $B$  calculated by the following equation:

$$B = D\gamma^{\frac{1}{2}} \quad (3.25)$$

In both cases  $D$  is the diameter of the starting droplet, while  $\gamma$  is the shear deformation obtained by multiplying shear rate and residence time ( $\gamma = \dot{\gamma}t_{loc}$ ). If  $B$  is lower than a critical value  $d^*$ , the fibril breaks and originates, in the case the viscosity ratio is near the unity (like it happens in the study), spherical nodules of diameter  $2d^*$ . If the viscosity ratio is different, the final diameters is determined by the wavelength of the disturbance. Spherical nodules large enough can originate new fibrils and so new droplets with a smaller diameter than the starting one.

“Weak” zones present low shear rates and they are subjected to atmospheric pressure. In these sections only the breakup of fibrils, previously formed in “strong” zones, can happen if the residence time is large enough to allow that.

Coalescence can instead be assessed in both “strong” and “weak” zones (because it does not require the application of large stresses) and the probability for it to happen is quite high, since generally the content of dispersed polymer is remarkable.

The model described above is valid to study, apart monodisperse systems, also the evolution of a specific size distribution of the droplets defined by the user. Analysing the results, larger mean dimensions are assessed in the second situation, since  $d^*$  is larger. The observed trends are the same both for monodisperse systems and for each class of polydisperse ones.

In the section dedicated to the discussion of the results, Delamare and Vergnes point out in particular the initial diameter of the minor component  $D_0$  (or its size distribution) and the critical diameter of the fibrils  $d^*$  as fundamental to determine the morphology of the blend. Moreover, it is interesting to note also the important effect of the feed rate: in fact, by increasing it, the residence time diminishes and so does also the time available for the droplets to breakup (they will have a larger diameter). Finally, the screw speed is more difficult to correlate to the final properties because faster rotations lower the residence time, but on the other hand there is an increase of the shear rate and so a variation of the viscosity ratio<sup>[5]</sup>.

### 3.5. Devices used in melt extrusion

At industrial scale, polymers are compounded in the molten state with the aim of adding mineral reinforcements, plasticizers, lubricants or other polymers. This is necessary since chemical facilities provide only neat polymer, eventually with the presence of UV stabilizers in order to minimize degradation during transport.

Compounding is carried up with the use of extruders, which are characterized by the presence of one or two screws mounted inside a barrel with one or more hoppers, used to bring the raw material inside the machine, and degassing holes. The barrel ends with a die that gives the material its final shape. Single-screw extruders show lower performances, but also lower costs, so they are generally employed when the concentration of the additive is of few percentage points in weight, as it happens for example with dyes, plasticizers, stabilizers and lubricants. Twin screw extruders are instead more expensive, but they ensure better performances, especially with highly concentrated added components (mineral or organic). As it can be understood from the name of the machine, it is equipped with two equal screws that rotate in the same direction (co-rotating configuration) or in opposite ones (counter-rotating configuration).

The aim of compounding is to ensure a homogeneous distribution of the additive (extensive or distributive mixing) coupled with the disruption of its particles or droplets in order to increase the extent of the interfacial surface (intensive or dispersive mixing). Distribution is attained through the re-orientation of the flow by screw elements, while dispersion depends on the local stresses. In particular, in a simple shear flow the additive is disrupted only if a critical value  $\tau_{critical}$  is reached, but this type of stress field is not so effective, since after the shear deformation the distance between two contiguous particles changes only slightly. Better results are achieved exploiting the elongational flow, but it has been observed that after a 10-times elongation its effect is drastically reduced. It means the necessity of re-orienting the particles if it is necessary to further reduce their size. Inside an extruder the actual deformation results from the superposition of shear and elongational stresses. The above considerations explain why a co-rotating and intermeshing twin-screw extruder (like the one used in the present work) is the most effective to ensure the correct mixing of two molten polymers in order to produce a blend, due to the high concentrations of the minor component. In fact, this configuration is able to provide the highest possible elongational deformation and to multiply the shear stresses undergone by the polymers thanks to the combination of two parallel screws.

This last type of extruder is constituted by a heated barrel with an 8-shaped section that houses the screws, which are assembled using different modules put on a ribbed core, allowing to obtain the most suitable profile for a specific application. This machine is starve-fed, meaning that the feeding operation relies on an external system also capable of pre-mix the pellets of the various polymers with a proper ratio. It implies that the feed rate is not related to the screw speed, as it happens in single-screw extruders that are flood-fed. The modules cited before can be divided into:

- *Screw (transport) elements* (Figure 3.6), similar to the screws commonly used for the extrusion of finished products (like tubes, rods or slabs) with the significant difference of the core diameter, that does not vary. On the contrary, the pitch varies between different modules, since a larger one is characterized by lower residence time and transport efficiency, but it is needed in a degassing zone because there must not be overpressure in this section of the apparatus. It is also more suitable to transfer the solid grains of polymer from the hopper during the melting step. Smaller pitches are instead required to pump the melt through the kneading or mixing elements, which restrict the flow.

*Back-flow elements* are special modules with a reverse helical thread that can be employed if it is necessary to increase the residence time in a particular section of the screw, like a kneading one, with the aim of improving mixing.

Screw elements are designated according to the subsequent codification

*GFX-Number of thread starts-Pitch (mm)-Length of the element*

with X=F for an element that is not able to self-clean and X=A for a self-cleaning one. Back-flow elements are distinguished by the suffix Re (or L, that stands for left handed, since threads are generally right handed).



**Figure 3.6** - A couple of conveying elements. It can be observed the ribbed shape of the core.

- *Kneading elements* (Figure 3.7) are constituted by a sequence of bilobal or trilobal discs put aside with a certain staggering angle (commonly 30°, 60° or 90°), so they have an helicodal shape although they do not show any thread. A single element presents a certain number of discs shifted with the same angle, while the kneading block of a screw is the result of the juxtaposition of many elements, with increasing angles moving from the hopper to the die. This last configuration provides a pressure gradient able to transfer the melt downstream, since a single module is not able to ensure axial flow. These modules have the task of providing melting, thanks to the high shear rate coupled with the effect of the heated barrels, but also extensive and intensive mixing because the clearance between two lobes is very small (far less than 1 mm), so the melt is forced to pass through a narrow slot that provides the necessary elongational flow<sup>[14]</sup>. The subsequent code, similar to the one used to identify screw elements, is employed for the designation of kneading elements

*KBX-Number of thread starts (mm)-Length of the element (mm)-Staggering angle (°)-Suffix*

Where X stands for the number of discs, while the suffix is RE for a positive transport and LI for a negative one. If the staggering angle is 90° no suffix is added.



**Figure 3.7** - A couple of kneading blocks.

- *Mixing elements* (Figure 3.8A) are used to re-orientate the flow, in order to get distributive mixing or to improve the intensive mixing provided by kneading elements. They are substantially screw elements with slits cut on the threaded edges following a helical path, so the most important geometrical parameters are the ones already reported for the transport modules, with the addition of the number of slits.
- *TME elements* (Figure 3.8B) are particular mixing elements made by a sequence of circular discs with two different diameters and a certain number of slits milled through the bigger ones. The resulting pins modify the velocity profile inside the flow during the rotation of the screw.

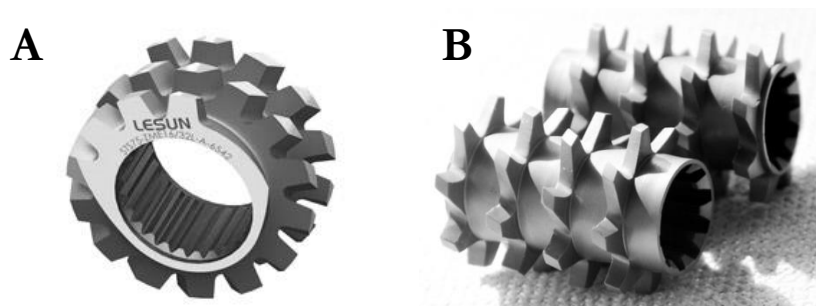


**Figure 3.8** - Comparison between a conventional mixing element (A) and a TME one (B).

### 3.6. PLA-based blends

Due to the high concern about plastic pollution and to the more and more shortage of petroleum reserves, resulting in progressively high costs of the feedstocks, currently there is a big challenge in the development of bio-based and biodegradable materials. One of the most exploited polymers in this field is polylactide (PLA), that currently is largely synthesised (thousands of tons per year) starting from corn and maize starch, which are renewable resources<sup>[15]</sup>. These raw materials are converted into lactic acid, that exists in two different stereo-isomers (L and D), and this last substance is then polymerized. Thanks to the high stereoregularity of the chains, pure poly(L-lactide) and poly(D-lactide) are both semi-crystalline<sup>[16]</sup>. PLA is maybe the most promising substitute for plastics derived from fossil resources, since its values of tensile strength and elastic modules are very similar to those of polymers commonly used in the packaging industry<sup>[17]</sup>. As previously stated in the introduction, a massive use of bio-based polymers, with the aim of replacing the petrochemical-based ones for this application, could solve the problem of the huge production of plastic wastes that need to be recycled. Moreover, a copolymer of lactide and glycol acid is also biocompatible and it has been approved by the American Food and Drug Administration (FDA) as a carrier for controlled drug release<sup>[18]</sup>. Unfortunately, polylactide (Figure 3.9) has some drawbacks, because it is brittle (this regards both the amorphous and semi-crystalline forms) and it is characterized by slow crystallization rates, low HDT and poor barrier properties<sup>[1],[16],[17],[18]</sup>.

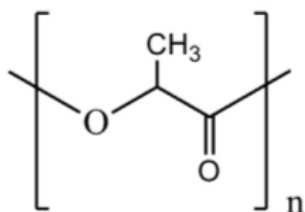


**Figure 3.9** - Chemical structure of polylactide.

In order to solve these problems, the copolymerization of lactide monomers with other ones is a possibility that leads to good results, thanks to the modifications introduced along the polymer chain. Another effective solution is melt blending, which is preferred by industries thanks to its higher practicality and flexibility, since the properties can be tuned by simply adjusting the weight ratio of the components. In the literature, many examples of blends where PLA is the major constituent can be found. For the dispersed polymeric phase have been used, among the others, starch<sup>[18]</sup>, poly( $\epsilon$ -caprolactone) (PCL)<sup>[19]</sup>, poly(ethylene glycol) (PEG)<sup>[20]</sup>, and poly(3-hydroxybutyrate) (PHB)<sup>[1],[15],[16],[17],[21]</sup>.

PLA-starch blends are produced in order to reduce costs and to increase biodegradability. Moreover, PLA is hydrophobic and water resistant, while starch is hydrophilic and sensitive to water. From a mechanical point of view, tensile strength and elongation at break decrease with increasing starch content and the resulting blend is brittle, so, to balance this drawback, low molecular weight plasticizers like glycerol are required for most of the applications. It has also been observed that a starch content above 5 wt. % increases the rate and the enthalpy of crystallization, since its granules act as a nucleating agent<sup>[18]</sup>.

The addition of 20 wt. % PCL to PDLA causes a slight increase of elastic modulus, yield strength and break strength, but higher concentrations of the minor component result in a progressive decrease of those properties. Elongation at break reaches its maximum at 40 wt. % PCL. The addition of a surfactant (since the blend is immiscible) causes a further decrease of the mechanical properties, but increases elongation<sup>[19]</sup>.

PEG with  $M_w$  in the range 1000-20000 g/mol blended with PLA can be employed as a carrier for the controlled release of bio-active substances, since it can undergo enzymatic degradation, which is faster and more effective for higher PEG contents. DSC analysis on the blend show miscibility or, at least, partial miscibility in the amorphous region, depending on the concentration of poly(ethylene glycol). A considerable drop of 30% in tensile strength is observed after the addition of 10 wt. % PEG and similar trends are registered for what concerns the values of yield strength for both the 70/30 and 30/70 blends. This behaviour is imputed to the higher mobility of the macromolecules, resulting from the low  $T_g$  of PEG, that imparts flexibility to the final material. The addition of this polymer results also in a decrease of the elastic modulus, although a slight increase of it (coupled with a decrease of the elongation at break equal to 3%) is shown after the addition of 70 wt. % poly(ethylene glycol).

### 3.6.1. PLA-PHBH blends

PHB is part of the larger family of poly(hydroxycanoate)s (PHAs), polyesters synthesised as an energy reserve by several Gram-positive and Gram-negative bacteria through controlled fermentation. As a response to the shortage of some elements like phosphorous and nitrogen, if large quantities of carbon are available, those bacteria can accumulate up to 60-80% of their weight in PHA to prevent starvation<sup>[1]</sup>. Among PHAs, poly(3-hydroxybutyrate) (PHB) is the most common and the most studied polymer, thanks to the progressively improved production capability of new plants located in Asia and in the USA. PHB is obtained through the digestion of oils and fats by bacteria belonging to the *Aeromonas* family and it is rigid and stiff, since it has a high level of crystallinity with quite large spherulites. To overcome these last problems, a different polymer, poly(3-hydroxybutyrate-co-3-hydroxyhexanoate) (PHBH), has been developed in Japan by Kaneka Corporation. PHBH (Figure 3.10) is a stereoregular copolyester characterized by randomly distributed 3-hydroxyhexanoate (3H) monomers intercalating the 3-hydroxybutyrate (3HB) backbone. 3H forms a short branch on the side of the polymeric chain that acts as a defect able to interrupt the regularity of the copolymer and so to partially hinder crystallinity and to lower the melting temperature  $T_m$ <sup>[15]</sup>. It means that PHBH is more flexible and ductile than PHB. Then, the copolymer is more suitable to be blended with PLA in order to get a material with superior properties and to overcome the problems related to the use of neat polylactide in several applications. As explained many times before, blending is a faster and less expensive way to improve the overall characteristics of the material if compared with the development of a brand new polymer with a different chemistry.

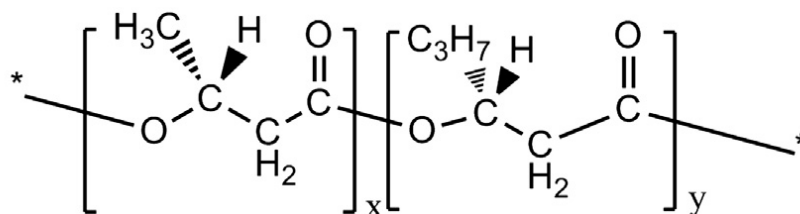


Figure 3.10 - Chemical structure of PHBH.

Obviously, also the miscibility of the two components in the system must be assessed, because of its great influence on the final properties of the blend. In fact, as previously explained, they are strongly related to the morphology when the polymers are immiscible<sup>[22]</sup>.

Although many studies about PLA-PHB blends can be found in the literature, the same cannot be said for those blends in which the copolymer is blended with polylactide. Since this work has the aim of assessing the ability of the Ludovic software to simulate the melt blending of PLA and

PHBH, it has been preferred to focus on this particular blend. The consideration reported in the subsequent paragraphs mainly follow the conclusions of Lim *et al.*<sup>[15]</sup>, since their work has been appreciated for its completeness and because the materials and the techniques used are practically the same employed to conduct this work.

In particular, Lim conducted a study on Ingeo™ 2003D PLA to evaluate the effect of incorporating different amounts of Kaneka Aonilex® PHBH by direct melt compounding in a twin roll counterrotating mixer. Data from the supplier report a D-isomer content in the PLA of 4,3%, while its  $M_w$  is 210000 g/mol with a polydispersity of 1,74. As far as PHBH is concerned, the 3H content is about 11 mol %,  $M_w$  is equal to 1388000 g/mol and the polydispersity is about 2. Before compounding with various weight ratios at 180°C and 100 rpm, the two polymers are dried at 60°C overnight since they are sensitive to hydrolysis at the high temperatures. After compounding, specimens are produced by compression molding in a hydraulic press for 5 minutes at 180°C and 6000 psi.

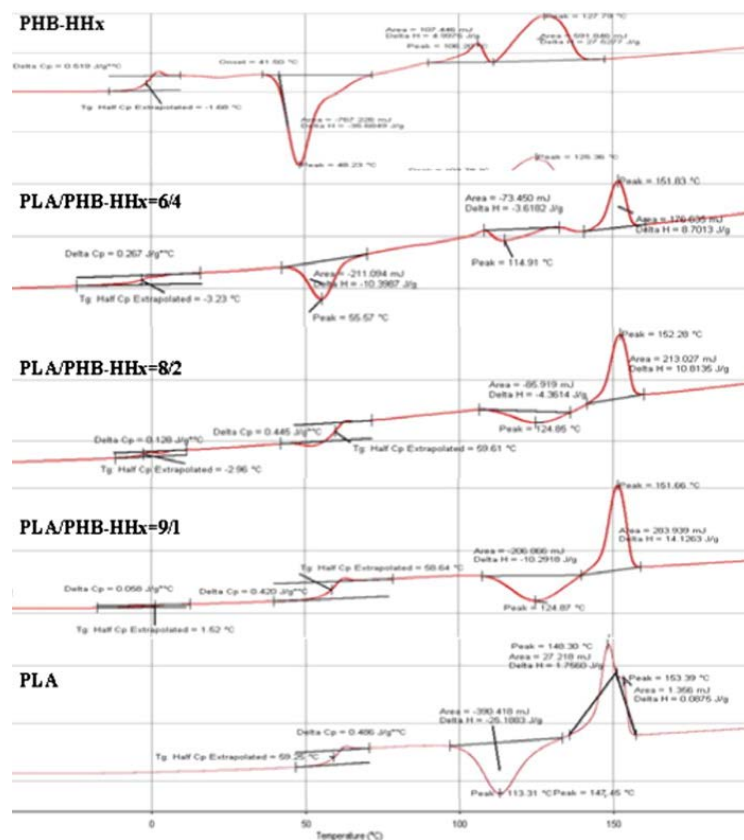


**Figure 3.11** - DSC plots for PLA-PHBH blends with different compositions and for the neat polymers. Reproduced from [15].

DSC analysis on the second heating ramp have been conducted on the neat PLA and PHBH and over the PLA/PHBH blends with weight ratios of 90/10, 80/20 and 60/40. These results show that PHBH crystallizes at about 50°C and melts in the range 100-130°C, while PLA has a crystallization peak at 113°C and melts around 150°C. The glass transition temperatures  $T_g$  are -2°C and 60°C for PHBH and PLA, respectively. Starting from these observations, the consequences of the compounding operations can be studied. In particular, the blends show well defined glass transitions temperature peaks located at -2°C and 60°C, so this, in addition to the absence of a considerable lowering of the melting point, reveals the immiscibility of the two polymers. This is confirmed also by the AFM analysis, employed to assess phase separation from

the measurements of roughness, that is higher if the weight percentage of PHBH increases. The addition of PHBH causes also the appearance of two crystallization peaks in the thermogram which correspond to the same ones of the neat polymers, so the blend can be classified as semicrystalline/semicrystalline. It worth noting that the peak related to the crystallisation of PLA shifts to higher temperatures while the heat of melting decreases, proving a restriction to the chain mobility and the lower crystallization rate of this polymer caused by PHBH. In fact, the long chains of the copolymer can affect the entanglement of PLA. The same effect is observed for what concerns the effect of PLA on PHBH, since a positive shift of the crystallization peak of the copolyester is also observed at 60/40 weight ratio. The DSC diagrams are reported in Figure 3.11.

DMA analysis show a decrease in the storage modulus (and so a reduction of stiffness) for the blend. In fact, since stiffness is related to the stored elastic energy, the restriction to the PLA chain mobility caused by PHBH lowers the stored elastic energy and so the modulus. Moreover, the copolyester is also able to hinder the crystallization of PLA as explained before. For what concerns the loss modulus, a peak emerges at about 20°C with increasing the PHBH content and this is attributed to the poor miscibility of the two polymers. It is also interesting to observe that the peak corresponding to the glass transition temperature of PLA does not shift, excluding a plastic action of PHBH. This is an advantage and means not only an improved behaviour of the blend at higher temperatures, but also that the flexibility is a consequence of the innate ductility and to the ability of hindering crystallization shown by PHBH. Moreover, the height of the  $\tan \delta$  peak decreases if the copolyester weight percentage is increased, pointing out one more time the inhibition effect of PHBH on the mobility of PLA chains.

DMA and DSC analysis prove that PLA and PHBH are not miscible, but also the possibility of a slight compatibility has been investigated through the study of IR absorption spectra of the polymers and of the blends near the C-O-C peak (see Figure 3.12). In fact, since the vibrational frequency of a functional group is related to the force constant and to the mass of the bonded atoms, any interaction with other functional groups (like the carbonyl one) results in a decrease of this force constant and so in a shift of the peak to lower wavenumbers.

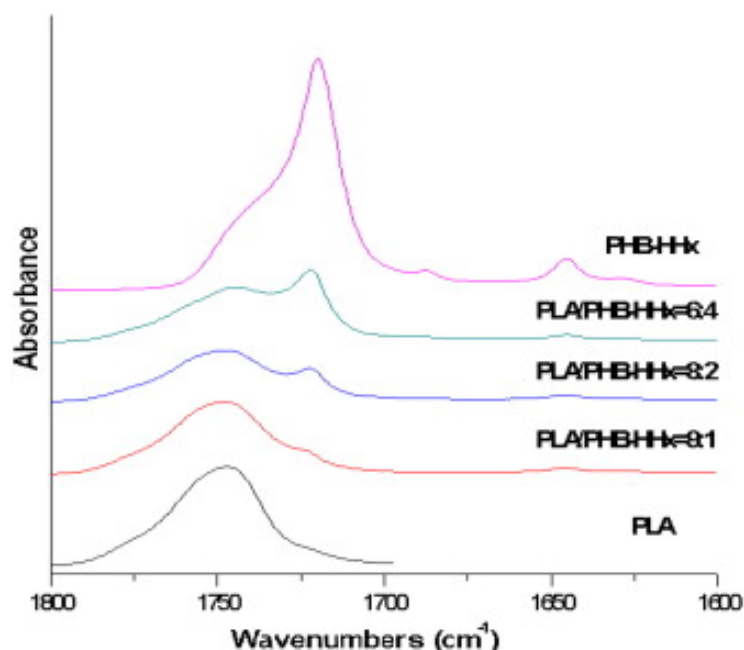


**Figure 3.12** - Carbonyl-stretching region of the IR absorption spectrum for different compositions of the PLA/PHBH blend. The specimens were crystallized at 30°C after melting. Reproduced from [15].

No evidences of that have been found, since the IR spectra of the blends are practically the sum of the ones corresponding to the neat polymers. The only difference is the presence of two new peaks related to crystallized PHBH, since the specimens were subjected to this treatment at 30°C after melting. Crystallization has been investigated analysing the stretching vibration corresponding to the C=O group for the two polymers. PLA shows a peak at 1750 cm<sup>-1</sup>, while the one of PHBH is divided into two sub-peaks located in the interval between 1740 and 1723 cm<sup>-1</sup> (corresponding to the carbonyl groups of amorphous and crystalline PHBH, respectively). Observing the IR spectra of the blends, it can be noted that the peak at 1750 cm<sup>-1</sup> does not shift, while the peak of crystalline PHBH increases its height if the concentration of this polymer does the same. This has been explained with the greater ease of crystallization for what concerns PHBH, that forms phase separated domains embedded in a PLA matrix.

The same analysis has been carried out over specimens crystallized at 130°C, so at higher temperatures than the  $T_m$  of PHBH. The peak at 1750 cm<sup>-1</sup> of PLA does not shift, while a broad one at 1740 cm<sup>-1</sup>, corresponding to amorphous PHBH, shifts to lower wavenumbers. Some studies have reported the existence of C-H-O hydrogen bonds between CH<sub>3</sub> and C=O groups in PLA-polyhydroxyalkanoates blends, but the observation of the C-H stretch peak shows that nothing changes with the increase of PHBH concentration. It leads to the conclusion that if hydrogen bonds are present between the two components of the blend, they are too weak to be considered as significant.

### 3.6.2. Mechanical properties of PLA-PHBH blends

Mechanical properties have been tested at room temperatures on dumbbell specimens with a crosshead speed of 10 mm/min. The results from 10 successful measurements were then averaged.

Neat PLA fails as soon as its yield strength is overcome due to strain softening that is not compensated by an adequate strain hardening. Strain softening can cause strain localization and the build-up of multiaxial stresses, which result in void nucleation if these stresses are not properly delocalized. Voids then lead to cracks in the matrix and so to brittle failure. The addition of 20 wt. % PHBH results instead in neck growth and strain hardening, so the ductility of the blend is significantly higher. Measured data are reported in Table 3.2.

**Table 3.2** - Mechanical properties of PLA, PHBH and some of their blends<sup>[15]</sup>.

	Tensile strength (MPa)	Young modulus (MPa)	Toughness (MPa)	Elongation at break (%)
<b>PLA</b>	62,2	1603	3,2	3,6
<b>90% PLA/10% PHBH</b>	54,1	1416	4,0	7,6
<b>80% PLA/20% PHBH</b>	45,3	1265	68,7	113,1
<b>60% PLA/40% PHBH</b>	40,1	1093	20,4	37,6
<b>PHBH</b>	21,6	309	160,6	524,8

The effect of PHBH is quite impressive, since only a small decrease of tensile strength and Young modulus is observed, but at the same time toughness and elongation at break increase significantly. These trends can be observed especially for the 80/20 blend, while the mechanical properties of the 60/40 one are quite worse. Since the maximum toughness is reached with small

and well distributed PHBH domains (able to dissipate tensile energy), the low mechanical properties of the 60/40 blend can be explained with the greater size of the dispersed nodules. As confirmed by SEM analysis, this phenomenon is linked to coalescence, that is more likely to happen with higher concentrations of the copolyester. Moreover, these analysis show that the interface between PLA and PHBH in the 80/20 blend is quite vague (maybe because PHBH is miscible with the low weight fraction of PLA macromolecules), meaning that phase separation is not absolute and so the final characteristics are improved. For what concerns the 90/10 blend, the values of toughness and elongation at break can be explained with the low concentration of the dispersed phase. Other studies about PLA/PHB blends report that toughness is further improved if a compatibilizer is used, since this property strongly depends on the ability of transferring mechanical energy from the PLA matrix to the dispersed PHB and to the dimensions of the dispersed domains<sup>[17],[23]</sup>.

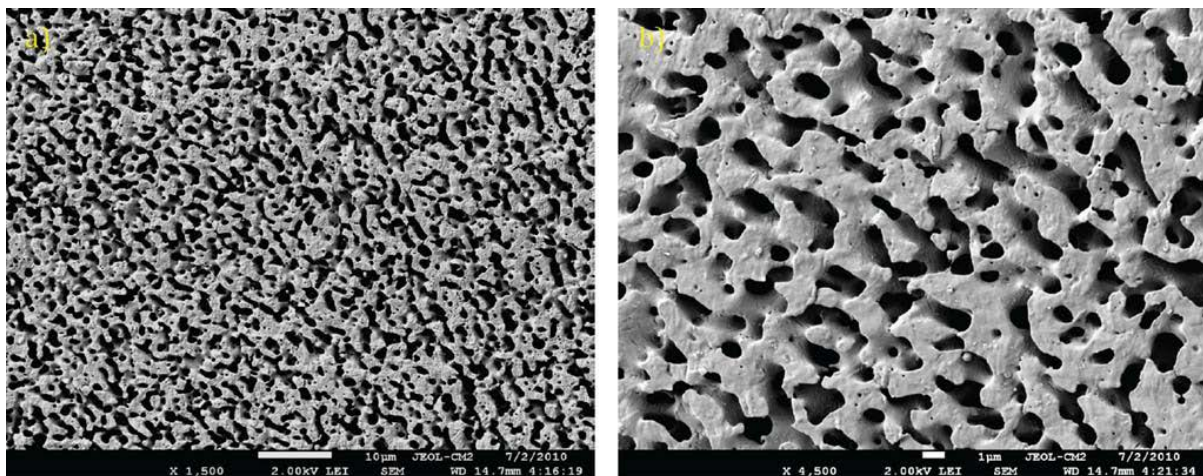


**Figure 3.13** - Co-continuous morphology of a 50/50 PLA/PHB blend. Reproduced from [24]

Since a possibility for the employment of the blend is based on the production of a co-continuous morphology, its characteristics are reported below. Unfortunately, in the literature studies about this particular morphology are not available for what concerns the PLA/PHBH blends, so the analysis reported here is referred to the PLA/PHB ones. The specimens observed with a scanning electron microscope are prepared by melt blending and then subjected to solvent extraction with chloroform in order to remove PLA. Since the weight percentage at which co-continuity is attained strongly depends on the viscosity ratio of the two polymers, it must be noted that the study whose conclusions are reported here contains interesting micrographs of various bio-based blends, but few information about the processing conditions is provided. For a 50/50 PLA/PHB blend, the obtained morphology is reported in Figure 3.13<sup>[24]</sup>.

The small dimensions of the PLA domains (in black since the polymer has been extracted) and the quite large interfacial area lead to the conclusion that good mechanical properties should be expected. By selectively filling one of the two polymers when the morphology is co-continuous, a conductive path can be created through the material with a smaller expense of filler.

### 3.6.3. Biodegradability of PLA-PHBH blends

Also biodegradation has not yet been investigated for blends containing PHBH, so the results reported here are once again referred to PLA/PHB ones. This is done since the chemistry is quite similar and so should be also the degradation operated by micro-organisms.

In particular, after a soil burial test conducted at room temperature with multi-purpose compost, an initial weight increment is observed and it is attributed to water absorption by both PLA and PHB (greater for the second one). After an induction time of 14 weeks for 50/50 and 25/75 PLA/PHB blends (only 8 for neat PHB) a strong decrease in weight is observed. For the 75/25 PLA/PHB blend the loss is less drastic and requires an induction time of 23 weeks. All the tested samples, except for neat PLA, have signs of degradation and discoloration whose intensity increases with the percentage of PHB and with the exposure time. SEM micrographs after 50 weeks show that biodegradation occurs in both PLA and PHB whatever the concentration is. These images point out also that PHB is mainly eroded by enzymes starting from the surface and moving to the core, while the degradation of PLA takes place at the same time in the whole sample.

It can be concluded that the feasibility of biodegradation at room temperature does not depend on the composition, but so does the time required by the process. In fact, the higher water uptake obtained with the addition of PHB is thought to be the responsible of the faster nonenzymatic (and temperature dependent) hydrolysis of PLA<sup>[25]</sup>.

## 4. Simulations with Ludovic

### 4.1. *The software*

Ludovic has been released under a proprietary licence by SC-Consultants in order to provide a global thermo-mechanical analysis of compounding inside a twin-screw extruder. It returns a 1-D description under stationary conditions of the material behaviour along the screw and inside the die. Obviously, the analysis in only one dimension and the limitation of working in stationary conditions lower the precision of the results; however, this software is an useful tool since it makes possible to foresee what happens inside the machine in a short time. The calculation requires in fact only few seconds and can be accomplished also with a common laptop. It is a great advantage on a laboratory or industrial scale, since it allows to rapidly compare many screw configurations with different temperature profiles or rotation speeds and so to identify the best solutions without the necessity of physically conduct the experiment. As a comparison, a more detailed 3-D unstationary local analysis can be conducted with XimeX, another software developed by SC-Consultants, but it requires about 10 hours to be completed and, at least, a highly expensive 16-core microprocessor.

Ludovic requires the definition of various operating parameters (detailed information are given later) and after the calculation it reports data about energy consumption, residence time distribution and many other quantities, like temperature, pressure, viscosity and so on, as a function of time or of the axial distance from the die. Data can be exported as a .xls file which can be elaborated and compared with the results of other simulations, although this last operation is made possible also by a specific tool provided by the software itself. Using the settings of a specific simulation, it is also possible to define a Design of Experiment (DoE), which basically consists in the automatized repetition of that simulation by progressively varying one or two independent parameters defined by the user. This procedure allows to find the conditions needed to reach certain desired values without the necessity to proceed by attempts, that is a more time-consuming approach which does not ensure to achieve the goal.

A certain number of simulations with their linked DoEs, characterized for example by the same objective or by similar parameters, can be grouped into a project, while many projects constitute a database. This kind of organization allows managing hundreds of different simulations and the developers recommend to use it, since automatic backup operations are simplified in this way

The version of the software described in the following sections is the 7.0.

### 4.2. *Working principles*

In this section the mathematical relationships used by the software to simulate the twin-screw extrusion are reported. All the information comes from Ludovic User's Manual<sup>[26]</sup>.

#### 4.2.1. Melt behaviour modelling

To proper describe the flow of the melt, it is necessary to characterize its rheological behaviour. Usually, thermoplastic polymers show a pseudo-plastic behaviour known as shear thinning, meaning that the viscosity (calculated as the ratio between the shear stress and the shear rate) decreases with increasing the shear rate following a linear trend on a  $\log \eta$  ( $\log \dot{\gamma}$ ) chart. Moreover, at low values of  $\dot{\gamma}$  the melt behaves as a Newtonian fluid, showing constant viscosity.

The dependence of the viscosity on the shear rate can be modelled by entering a certain number of parameters required by the following analytical relationships:

- power law

$$\eta = K\dot{\gamma}^{m-1} \quad (4.1)$$

where  $m$  is an index that accounts for the pseudo-plasticity and  $K$  the consistency of the material;

- Carreau-Yasuda law

$$\eta = \frac{\tau_0}{\dot{\gamma}} + \eta_0[1 + (\lambda\dot{\gamma})^a]^{\frac{m-1}{a}} \quad (4.2)$$

$\tau_0$  is the yield stress,  $\eta_0$  the zero-shear viscosity,  $\lambda$  the relaxation time and  $a$  a parameter that characterizes the transition between the Newtonian plateau and the power law section of the chart.

These equations can be adjusted to account for the effect of the temperature using an Arrhenius-like relationship or a Williams-Landell-Ferry one. In particular, when the melt behaviour is described by a power law, a  $K(T)$  function is defined, while if the model of Carreau-Yasuda is employed, it is necessary to determine  $\eta(T)$  and  $\lambda(T)$ . Also in this case the user has to enter some parameters depending on the chosen type of adjustment.

The rheological behaviour of the molten polymer can also be defined through an analytical law defined by the user, or by a Set of Points (SoP) in the form  $\eta(T, \dot{\gamma}, x)$ . This last possibility allows to directly input experimental data.

To properly simulate the blending operations it is necessary to specify the most appropriate polymer-polymer mixing law that the software has to use for the computation. The choice is between the logarithmic equation (3.5), and the following relationships:

- linear relationship

$$\eta_{blend} = \sum_{i=1}^{i=n} \eta_i X_i \quad (4.3)$$

where  $n$  is the number of components, while  $\eta_i$  and  $X_i$  are respectively the local viscosities and the volume fractions of each of these components;

- harmonic relationship

$$\ln \eta_{blend} = \sum_{i=1}^{i=n} \ln \eta_i X_i \quad (4.4)$$

If a mineral filler is dispersed in the melt, its viscosity is calculated using the equation derived by Krieger-Dougherty (3.6). Ludovic gives the possibility to manually define the values of  $\Phi_m$  and  $[\eta]\Phi_m$  or, as an alternative, to use the simplified relationship proposed by Maron and Pierce. In this last case  $[\eta]\Phi_m$  it is assumed to be equal to 2 and  $\Phi_m$  is automatically computed by the software on the basis of the aspect ratio of the dispersed mineral particles.

A similar law is needed also to compute the viscosity in the melting zone, where the polymer is progressively converted from solid pellets into the liquid phase. The fluidity of the material decreases due to the presence of a certain solid volume fraction  $\Phi$ , that accounts for the material which has not been molten yet. The increase in viscosity is modelled by Ludovic through the following relationship:

$$\eta = \eta_{liq}(1 + \alpha\Phi)^\beta \quad (4.5)$$

The software assumes the empirical parameters  $\alpha$  and  $\beta$  as equal to -1,11 and -0,508, respectively. These default values enable to employ the melting model for solid fractions up to 85%.

#### 4.2.2. Geometrical modelling of the extruder

Ludovic is designed to model the flow inside the extruder under stationary conditions, but, due to the rotation of the screws, it is not possible to find a reference in which the flow is stationary. This problem is solved using a simplified approach that considers the screws as fixed, with the barrel turning around them. It is also assumed that locally the melt is isothermal, incompressible, Newtonian and the effect of gravity is neglected. The flow is then described in one or two dimensions, depending on the type of element, employing cylindrical coordinates. The software automatically defines, according to the geometry of the screw and of the die, some elementary domains where pressure and temperature drops are computed.

The volume available for the flow is calculated starting from three main parameters, that are:

- the inner radius of the barrel  $R$ ;
- the centreline distance or, in other words, the distance between the screw axis  $C_L$ ;
- the leakage between the screw and the barrel  $\delta$ .

For screws with two flights, the cross-section of the extruder is shown in Figure 4.1.

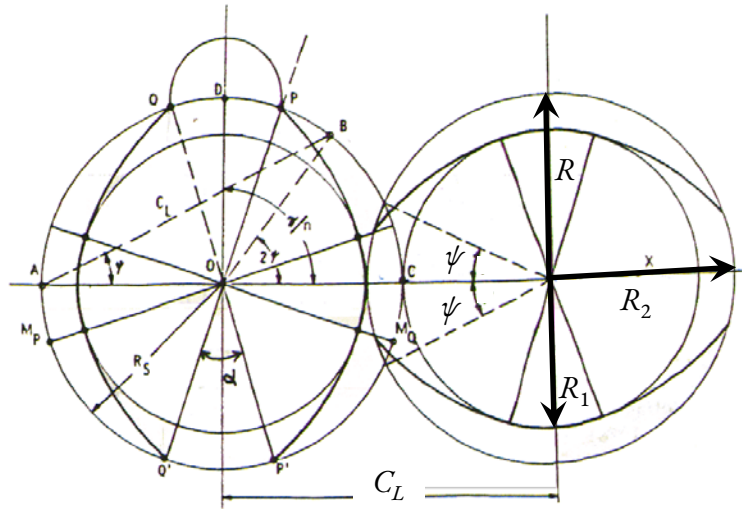


**Figure 4.1** - Cross-section of a twin-screw extruder as modelled by Ludovic. Both the screws have two flights and the leakage is not represented. Reproduced from [26].

Using the parameters reported above, it is possible to calculate other useful quantities like

- inner ( $R_1$ ) and outer ( $R_2$ ) radii of the screws

$$R_1 = C_L - R_2 \quad (4.6)$$

$$R_2 = R - \delta \quad (4.7)$$

- intermeshing angle  $\psi$

$$\psi = \arccos\left(\frac{C_L}{2R_2}\right) \quad (4.8)$$

- transverse section of the barrel

$$S_B = 2(\pi - \psi)R^2 + C_L R \sin\psi \quad (4.9)$$

In this way, the cross-section area where the melt can flow freely ( $S_F$ ) is derived from by subtracting the cross-section area of each screw  $S_s$  from  $S_B$ , that is

$$S_F = S_B - 2S_s \quad (4.10)$$

As it can be seen in Figure 4.1, the flights of the screws cause the formation of a certain number of channels with similar flow conditions and, if the presence of the leakage  $\delta$  is ignored, they can be considered as independent one from the other. The number of those channels  $m$  can be calculated using the relationship

$$m = 2n \left(1 - \frac{\psi}{\pi}\right) \quad (4.11)$$

where  $n$  is the number of flights.

The cross-section of a channel is semi-circular, so its height depends on an angle that varies from 0 to  $2\psi$ . The resulting equation is unnecessarily complex, so, to speed up the computation, this cross-section is approximated to a rectangular one (see Figure 4.2) and then the results are adjusted using a proper shape factor that accounts for the simplifying assumption. In particular, the height of the channels  $H$  is simply calculated as

$$H = R_2 - R_1 \quad (4.12)$$

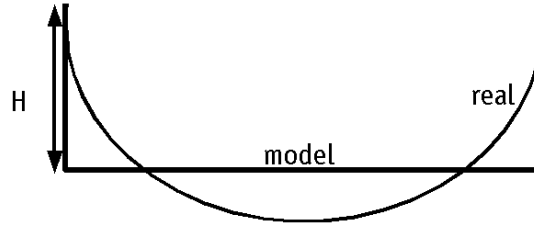


**Figure 4.2** - Comparison between the cross-sections of the real channel and the modelled one. The difference is taken into account through a proper shape factor. Reproduced from [26].

#### 4.2.3. Mechanical model for the screw and the die

To describe the flow inside the channels of the screw in terms of velocity and pressure, Ludovic uses a system of cylindrical coordinates where the axial one ( $x$ ) coincides with the screw axis. The velocity components in the three directions are considered independent from  $x$  and the flow along the radius is neglected, so

$$v_x = v_x(r, \theta) \quad (4.13)$$

$$v_\theta = v_\theta(r, \theta) \quad (4.14)$$

$$v_r = 0 \quad (4.15)$$

$$p = p(x, r, \theta) \quad (4.16)$$

A polymer melt is a viscous fluid, so the software is normally set for operating with the sticky condition at the wall, meaning that the velocity is equal to zero on the internal radius of the screw  $R_1$ . Sliding can however be considered through the definition of two factors  $\alpha$  and  $\beta$ , that account for this phenomenon on the surfaces of the screw and of the barrel, respectively.

Since the radial velocity component is neglected, the velocity profile inside the channels of a left- or right-handed conveying element (that is symmetrical due to revolution symmetry), is described with a 2-D model. After the definition of the velocity field, the shear rate, initialized to a value  $\dot{\gamma}_0$  equal to the ratio between  $R_2$  and  $H$  times the angular velocity  $\omega$ , is computed by the combination of axial and angular velocity gradients. Viscosity is then updated according to the analytical law or to the SoP provided by the user. The local residence time is computed using the equation

$$Rt = \frac{VF_r}{Q} \quad (4.17)$$

where  $V$  is the free volume,  $F_r$  the local filling ratio (equal to 1 in a completely filled element) and  $Q$  the volumetric flow rate.

What is reported above does not concern the intermeshing zone, since in this part of the extruder the shear rate is provided by the reciprocal movement of the screw and not by the wall of the barrel. To model this section of the extruder, the geometry is approximated to a portion of tube with thickness  $H$  where

$$v_x = 0 \quad (4.18)$$

$$v_\theta = v_\theta(r) \quad (4.19)$$

$$v_r = 0 \quad (4.20)$$

Kneading discs are considered as fully-filled elements, meaning that the whole free volume is occupied by the melt. For the purposes of calculation it is assumed that the flow through them is determined by the pressure drop along the  $x$ -axis and that the element has a great width, so  $dH/d\theta \ll 1$ . This allows to neglect the dependence of  $v_\theta$  on the angular coordinate, so the velocity field  $u$  has the following form:

$$u = f(v_x, v_\theta(r), 0) \quad (4.21)$$

The tangential velocity field is computed using the Navier-Stokes equations with the following boundary conditions:

$$v_x(R_1) = 0 \quad (4.22)$$

$$v_\theta(R_1) = 0 \quad (4.23)$$

$$v_x(R_2) = 0 \quad (4.24)$$

$$v_\theta(R_2) = R_2\omega \quad (4.25)$$

The tangential pressure profile is calculated using numerical integration on a single channel with an iterative process that is stopped as the condition  $p(\theta_e)=p(\theta_s)$  (see Figure 4.3) is reached. This condition imposes that the pressure in two simmetrical points of the module must be the same. In parallel, also the circumferential flow rate  $Q_\theta$  is evaluated starting from an approximated value that allows the evaluation of the  $dp/d\theta$  gradient. If the condition mentioned before is not respected, the value of  $Q_\theta$  is updated until the computation converges.

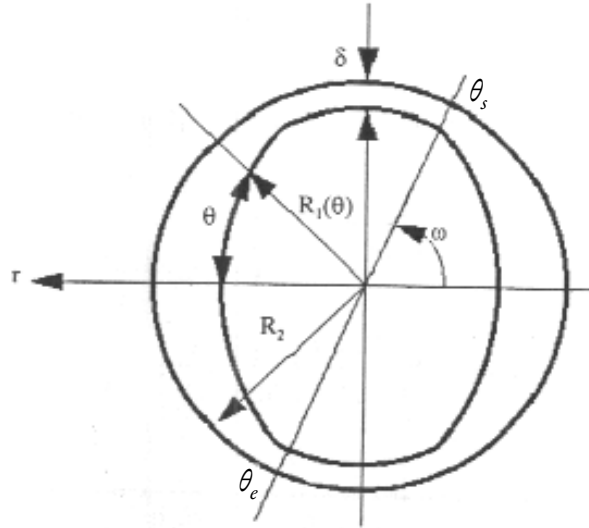


**Figure 4.3** - Cross-section of a kneading element.  $\theta_s$  and  $\theta_e$  are put in evidence. Reproduced from [26].

For what concerns the axial flow in a kneading block, it must be noted that a single element is not able to perform it, so many lobed discs are put together with a determined staggering angle  $\alpha_m$  in order to obtain an axial pressure gradient that grants the transport towards the die. The axial flow rate is computed using one more time the Navier-Stokes equations over the whole element, putting as a condition the axial and transverse flow rate balance for each elementary volume that constitute the channels. This condition can be written as

$$Q_{i-1,j}^\theta + Q_{i,j-1}^x = Q_{i,j}^\theta + Q_{i,j}^x \quad (4.26)$$

where the  $i - 1$  and  $i$  indexes identify two adjacent volumes in the transverse direction, while  $j - 1$  and  $j$  are related to the volumes along the screw axis. Since kneading blocks are completely filled elements, the local residence time is

$$Rt = \frac{V}{Q} \quad (4.27)$$

Finally, a TME mixing element (Figure 4.4) is described by subdividing it into a sequence of ring elements (where the flow is computed using the Navier-Stokes equations) and slit elements. The throughput of each one of them is then halved. In particular, the flow inside a slit element is the superposition of an axial one through the slots and a transverse one. Their flow rates are the sum of two terms related to a pressure-driven flow and to a shear one.

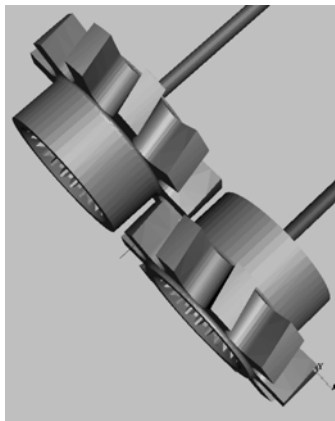


**Figure 4.4** - A couple of TME mixing elements. Reproduced from [26].

To correctly evaluate the flow inside the die, the numerical resolution of derivative equations is needed also for simple geometries. To overcome this problem, Ludovic employs a simplified 1D method that returns only global values. Moreover, the fluid is considered Newtonian, isothermal, incompressible and an equivalent viscosity is defined. In this way, it is possible to calculate the mean shear rate and the temperature at die exit. It is also assumed that only the axial velocity exists (neglecting the other components), that the flow does not depend on time and the effect of gravity is not taken into account.

In this way, for a tube-shaped element the pressure drop is

$$\Delta p = \frac{8\eta LQ}{\pi R_{eq}^4} \quad (4.28)$$

with  $R_{eq}$  an  $L$  d equivalent radius and length of the element, respectively.  $Q$  is the flow rate.

To consider the shear thinning behaviour of the melt, if it is possible to determine the pseudo-plasticity coefficient  $m$ , the shear rate is computed as

$$\dot{\gamma} = 2 \frac{1 + 3m}{1 + 2m} \frac{Q}{\pi R_{eq}^3} \quad (4.29)$$

When the viscosity law is defined by the user,  $m$  cannot be derived by Ludovic, so it is assumed as equal to 1.

#### 4.2.4. Thermal model for the screw and the die

The temperature profile along the screw and the die is the result of different phenomena that contemporarily occur inside the extruder. In fact, heat is lost through conduction in the barrel, in the die and, possibly, in the screw, but at the same time mechanical energy is turned into thermal one due to viscous dissipation. Since Ludovic gives the possibility to simulate reactive extrusion (an endo- or exothermic process) and to use microwaves as a source of thermal energy, also their effect must be taken into account.

The software calculates the temperature difference between two adjacent elements as a sum of the various contributions related to the phenomena described above. This approach allows to apply the melting model only to a very localized part of the extruder. Moreover, the model does not depend on the type of modules constituting the screw (conveying, kneading or mixing block) and it can be written as

$$\Delta T = \Delta T_{cond} + \Delta T_{mec} + \Delta T_{kin} + \Delta T_{mw} + \Delta T_{melt} \quad (4.30)$$

The heat flux related to conduction can be described in terms of heat transfer coefficients related to the screw ( $h_s$ ) and the barrel ( $h_b$ ) or on the basis of the correspondent Nusselt numbers  $Nu_s$  and  $Nu_b$ . The relationship that links the two quantities is

$$Nu = h \frac{(R_2 - R_1)}{k} \quad (4.31)$$

with  $k$  thermal conductivity of the polymer. Once the couple of values  $h_s$  and  $h_b$  (or  $Nu_s$  and  $Nu_b$ ) is known, it is in fact possible to derive the thermal power exchanged with the thermo-regulation system of the extruder employing the equation (4.32)

$$\dot{Q} = h_s (T_s - \bar{T}) S_s + h_b (T_b - \bar{T}) S_b \quad (4.32)$$

where  $S_s$  and  $S_b$  are the heat exchange surfaces with, respectively, the screw and the barrel,  $\bar{T}$  the mean temperature of the material (considered as isothermal inside an elementary volume), while  $T_s$  and  $T_b$  are the temperatures imposed by the regulation system. After the calculation of  $\dot{Q}$ , the

heat capacity  $C_p$  and the volumetric flow rate  $Q_v$  are employed, along with the density  $\rho$ , to calculate the temperature variation caused by conduction. The relationship which is employed is the following one:

$$\Delta T_{cond} = \frac{\dot{Q}}{\rho C_p Q_v} \quad (4.33)$$

The thermal power related to the dissipation of mechanical energy ( $\dot{W}$ ) is determined as follows:

$$\dot{W} = \eta \dot{\gamma}^2 \quad (4.34)$$

If  $\dot{W}$  is known,  $\Delta T_{mec}$  is computed with eq. (4.33) by substituting  $\dot{Q}$  with  $\dot{W}$ .

In the melting zone it must be introduced also an additional term  $\Delta T_{melt}$ , which accounts for the liquid/solid thermal transfer. In particular,

$$\Delta T_{melt} = \frac{\Delta t}{\rho_l C_{p,l}} \left[ \frac{3\Phi}{R} b_s (T_{sol} - T_{liq}) \right] \quad (4.35)$$

with  $\rho_l$  density and  $C_{p,l}$  heat capacity of the molten polymer,  $R$  size of the solid particles,  $b_s$  thermal transfer coefficient,  $T_{sol}$  and  $T_{liq}$  temperature of the two phases.  $T_{sol}$  is calculated through an energy balance over a sphere of radius  $R$  that initially is isothermal ( $T=T_{sol,0}$ ), while at the time  $t$  its surface is at temperature  $T_f$ . The value of  $R$  changes with time depending on the heat transfer between the liquid and the solid phases  $b_s(T_{sol} - T_{liq})$ , the melting enthalpy  $\Delta H_{melt}$  and the energy variation of the solid phase  $C_{p,s}(T_{melt} - T_{sol})$ . The resulting relationship is

$$\frac{dR}{dt} = \frac{b_s (T_{sol} - T_{liq})}{\rho_s [C_{p,s} (T_{melt} - T_{sol}) + \Delta H_{melt}]} \quad (4.36)$$

where  $\rho_s$  is the density of the solid phase.

In order to avoid of excessively weighing down the work, the terms describing the temperature drops due to reactive extrusion and microwaves will not be analysed, since in the simulations reported in this work the polymers do not chemically react and the heat is provided only by the electrical resistances mounted on the barrel.

If an intermediate feeding or a degassing section is employed in the simulation, the temperature computation before and after the opening is performed taking into account the principle of energy conservation. It means that

$$Q_d C_{p,d} T_d = Q_f C_{p,f} T_f + Q_u C_{p,u} T_u \quad (4.37)$$

where the subscript  $d$  stands for “downstream”,  $u$  for “upstream” and  $f$  identifies the flow coming from the feeding (or degassing) section. The equation can be rewritten in terms of the downstream temperature  $T_d$  as

$$T_d = \frac{Q_f C_{p,f} T_f + Q_u C_{p,u} T_u}{Q_d C_{p,d}} \quad (4.38)$$

To derive the temperature profile, the die is treated in the same way as a generic screw element. It means that the model reported above is applied also in this part of the extruder, with no differences for what concerns the various equations.

#### 4.2.5. The computation process

It is now time to explain how all the considerations explained above are used by Ludovic to define the profiles of temperature, pressure, viscosity and so on along the screw and in the die. The user has to build the screw profile by putting together the different modules after the definition of their geometrical parameters. The same operations are done for what concerns the die. It is also required to enter the temperature profile of the barrel and the characteristics (specific heat, density and thermal conductivity) of the polymers and of the possible mineral fillers. Ludovic requires also the choice of the polymer/polymer and polymer/filler mixing laws and the values of the thermal exchange coefficients (or Nusselt numbers).

Since the section of the screw below the hopper is not completely filled, it is not possible to directly calculate the pressure in this part of the extruder. The approach used is then to start the computation from the die and then moving back to the feeder. In particular, starting from an arbitrary exit temperature in the die (set by default at 150°C, but adjustable if necessary), its profile is determined. In parallel also the other quantities are evaluated. Although the melting point can be imposed by the user, Ludovic considers that the melting takes place in the first restrictive and always filled element. To validate the results of the simulation, the computed temperature in correspondence of the first element that narrows the flow is compared with  $T_{melt}$  of the polymer (with the highest value in case of more than one polymers). If they do not match, the simulation is restarted until convergence is reached.

### 4.3. Setting of the simulations

#### 4.3.1. “Extruder” tab – Definition of the geometry

A simulation with Ludovic starts by defining the geometry of the extruder in the “Extruder” tab. The apparatus employed in the present work is a Leistritz ZSE 18 HP, with a barrel diameter of 18 mm and a centreline (distance between the screws) of 15 mm, while the measured leakage between the pitches of the thread and the barrel is of 0,1 mm. The small dimensions make this extruder suitable for research applications, since satisfying data can be obtained without the need of great amounts of raw material.

The barrel is constituted by 8 elements, progressively numbered starting from the hopper, whose length is 90 mm. The polymer is loaded in the middle of the first element, while the mineral filler enters in the machine from an opening in the fourth one. Finally, another opening in the seventh element allows degassing. For those simulations that do not require the inclusion of the filler, also its feeding hole is considered as a vent.

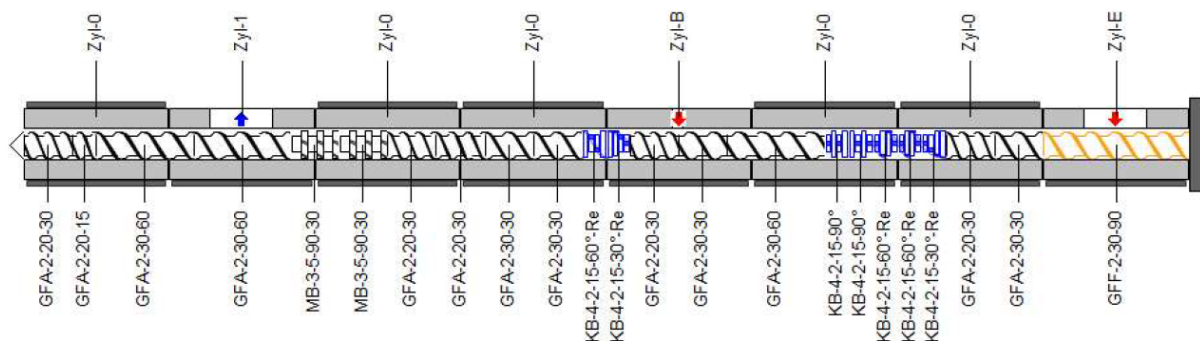


Figure 4.5 - Screw profile 1.

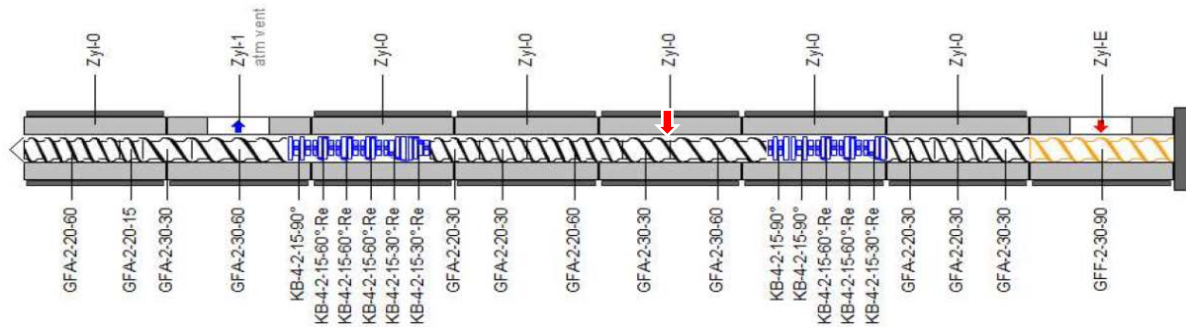


Figure 4.6 – Screw profile 2.

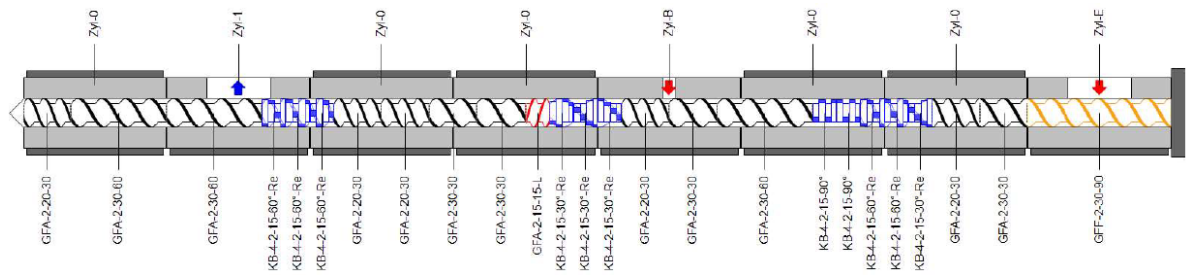


Figure 4.7 - Screw profile 3.

Three screw profiles reported in Figure 4.5, Figure 4.6 and Figure 4.7 have been tested. In all the cases, the polymers melt in the first kneading section, constituted by the same sequence of modules with increasing staggering angles of 30, 60 and 90 degrees. From this point on, significant differences can be noted for the various profiles. In fact, on the screw named “BioPolymer\_Blend\_1” two kneading elements with angles of 30° and 60° are mounted just after the feeding of the mineral filler, while two TME mixing blocks are exploited to enhance dispersive mixing before the vent. The screw “BioPolymer\_Blend\_3” has a similar configuration, but the second kneading block (nearer to the feeding of the filler if compared to the same one of the profile 1) has a staggering angle of 30° and its lower effectiveness is compensated by a back-flow module, while the final mixing section is substituted by a sequence of 90° kneading blocks. Finally, the screw “BioPolymer\_Blend\_2” is equipped with a longer kneading section before the degassing hole, but only conveying elements are employed just after the mineral filler is loaded. Although almost all the geometrical parameters of the elements can be derived from their codes, some values had to be directly measured. The resulting data are resumed in Table 4.1.

Table 4.1 - Measured parameters of kneading and mixing elements.

Kneading elements (KB-...)	
Leakage between two parallel discs	0,2 mm
TKD elements (MB-3-5-90-30)	
Total length	30 mm
Number and shape of the slits	5, rectangular
Slit width	5,5 mm
Slit height	2 mm
Twist angle	-30°

The real die has been modelled as a sequence of pipe elements. In particular, the first one is constituted by two intermeshing cylinders with the same diameter of the barrel, while in the last one the pipes run one parallel to the other, without intermeshing. In the remaining elements a single cylinder is present. The dimensions have been directly measured with the aid of a calliper and are resumed in Table 4.2 (the modules are progressively numbered starting from the interface with the barrel). The overall geometry is shown in Figure 4.8, where it can be appreciated the increase of the diameter in correspondence of the third element, employed to account for the flanged shape of the junction.

**Table 4.2** - Measured dimensions of the die. The element number 5 is the most external one.

Number of the element	Diameter (mm)	Length (mm)	Notes
1	18	20	Two intermeshing cylinders
2	12	15	-
3	20	6	Flanged junction
4	12	9	-
5	4	11	Two non-intermeshing cylinders

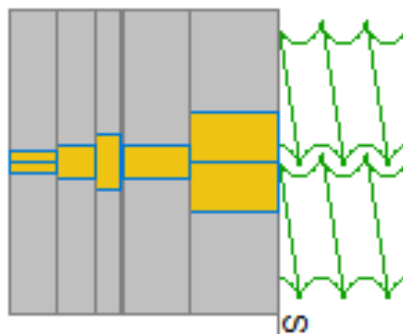


**Figure 4.8** - Profile of the die.

#### 4.3.2. “Product” tab – Characterisation of the materials

This tab is intended to enter the characteristics of the polymers and of the possible mineral fillers, as well as to define the so called “Recipes”. These “Recipes” specify which materials are present in the different sections of the extruder, their mass (or volume) fractions and the mixing laws that will be used for the computation.

As far as the characteristics of the polymer are concerned, Ludovic requires heat capacity, density and thermal conductivity for both the solid and the liquid phases. Besides, the melting temperature and the enthalpy have to be quantified. In another tab (“Viscosity”) the rheology of the material is described through an analytical law or by a SoP.

The PLA used in this work, Ingeo Biopolymer 3251D provided by NatureWorks LLC. (USA), is intended for injection molding applications. Its technical datasheet reports only the density of the solid phase and the melting temperature  $T_m$ . This means it is necessary to search for the other data in the literature or to derive them from DSC measures. Since the heat capacity calculated from experimental data was not in accordance with the results found in the literature, only the melting enthalpy is derived from the DSC plot using the *TA Universal Analysis* software. The resulting data are reported in Table 4.3.

The density of the liquid phase at 180°C has been obtained with the Tait equation, calculated for a Ingeo 3001D PLA (similar to 3251D) by Mahmood et al<sup>[28]</sup>. The temperature  $T$  has to be entered in °C.

$$\rho = \frac{1}{0,766 \cdot e^{(9,6372 \cdot 10^{-4} T)}} \quad (4.39)$$

**Table 4.3 - Thermal characteristics of PLA.**

<b>PLA - Ingeo Biopolymer 3251D</b>	
<b>Heat capacity (solid phase)</b>	1314 J/kg·K ( $RT$ ) <sup>[29]</sup>
<b>Density (solid phase)</b>	1240 kg/m <sup>3</sup> ( $RT$ ) <sup>[30]</sup>
<b>Thermal conductivity (solid phase)</b>	0,111 W/m·K ( $T=48,4^{\circ}\text{C}$ ) <sup>[31]</sup>
<b>Heat capacity (liquid phase)</b>	2140 J/kg·K ( $T=177^{\circ}\text{C}$ ) <sup>[29]</sup>
<b>Density (liquid phase)</b>	1098 kg/m <sup>3</sup> ( $T=180^{\circ}\text{C}$ ) <sup>[28],[31]</sup>
<b>Thermal conductivity (liquid phase)</b>	0,195 W/m·K <sup>[31]</sup>
<b>Melting temperature</b>	168°C <sup>[30]</sup>
<b>Melting enthalpy</b>	40,42 KJ/Kg

As far as PHBH (X151A provided by Kaneka Corporation, Japan) is concerned, the heat capacity has been derived as the ratio between the heat flow, obtained from the DSC plot, and the heating rate of the same test, equal to 10°C/min. The DSC plot is used also to derive the melting enthalpy by integrating the corresponding double endothermic peak. The technical datasheet provides the values of melting temperature and density of the solid phase, while the other quantities have to be found in the literature. Unfortunately PHBH is less studied than PHB, so some quantities are approximated as equal in the solid and liquid phase, due to the lack of reliable information. All these data are listed in Table 4.4.

**Table 4.4 - Thermal characteristics of PHBH.**

<b>PHBH – Kaneka X151A</b>	
<b>Heat capacity (solid phase)</b>	1407 J/kg·K ( $RT$ )
<b>Density (solid phase)</b>	1190 kg/m <sup>3</sup> ( $RT$ ) <sup>[32]</sup>
<b>Thermal conductivity (solid phase)</b>	0,260 W/m·K <sup>[33]</sup>
<b>Heat capacity (liquid phase)</b>	1447 J/kg·K ( $T=180^{\circ}\text{C}$ )
<b>Density (liquid phase)</b>	1190 kg/m <sup>3</sup> <sup>[32]</sup>
<b>Thermal conductivity (liquid phase)</b>	0,260 W/m·K <sup>[33]</sup>
<b>Melting temperature</b>	126°C <sup>[32]</sup>
<b>Melting enthalpy</b>	28,37 KJ/Kg

The viscosity has been defined through a Set of Points based on experimental data measured with a parallel plate rheometer. In particular, each polymer has been tested at three different

temperatures in the same frequency range of 0,1-100 rad/s. Since both PLA and PHBH are neat polymers with regular macromolecular architecture, they follow the Cox-Merz rule, assessing the equivalence of the complex viscosity (obtained through oscillatory measurements) and the shear viscosity as a function of frequency and shear rate, respectively. For this reason, the data coming from oscillatory shear tests were used to model the rheological behaviour of the materials. The plots in Figure 4.9 show the flow curves of the two polymers.

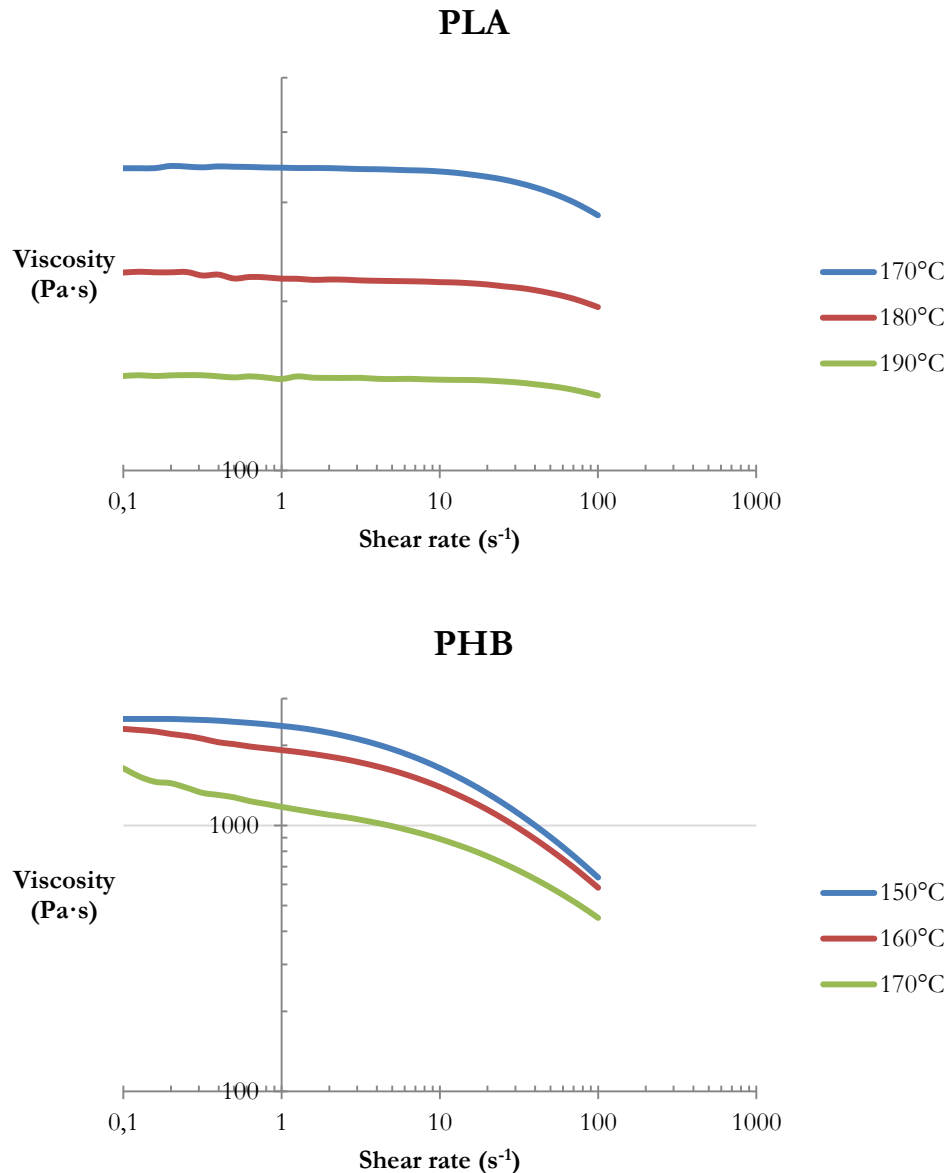


**Figure 4.9** - Viscosity of PLA (3251D) and PHBH (X151A) as a function of temperature and shear rate.

The mineral filler does not melt at the temperatures commonly reached inside the extruder, so to define them only the values of heat capacity, density and thermal conductivity for the solid state are required. In addition, it is also necessary to enter the shape coefficient, calculated as the ratio between the length and the diameter of the particles. In this work Cloisite 5, provided by BYK (Germany), has been used after a drying step in oven for 5 hours at 80°C. The filler consists of a bis(hydrogenated tallow alkyl)dimethyl sodic salt used as a counterion in a bentonite natural structure. Its density is obtained from the technical datasheet, while the other values have been

derived from the existing literature. For what concerns the shape coefficient, it must be noted that Ludovic allows to enter a value only in the range 1-30, because the software is designed to work mainly with glass fibres as fillers. Since Cloisite is a clay, the maximum value of 30 has been employed on the advice of the developer, although it is evidently quite far from the reality (a ratio of at least 100 would be more likely). Data for Cloisite 5 are resumed in Table 4.5.

**Table 4.5** - Thermal characteristics of the mineral filler.

Cloisite 5	
Heat capacity (oven-dry)	650 J/kg·K <sup>[34]</sup>
Density	1770 kg/m <sup>3</sup> <sup>[35]</sup>
Thermal conductivity (oven-dry)	0,68 W/m·K <sup>[34]</sup>
Shape coefficient, L/D	30

After the characterisation of the employed materials, it is necessary to define the Recipe or, in other words, to define the composition of the blend and the mixing laws that have to be used for the computation.

In this work, a blend containing 70 wt. % PLA and 30 wt. % PHBH has been studied. Furthermore, the effect of the addition of 5 wt. % Cloisite has been investigated. The polymer/polymer mixing law has been considered as linear, although the substances are not miscible. This choice is justified by the small difference between the values of  $\eta_{PLA}$  and  $\eta_{PHB}$  at the operating conditions. For the simulations which involve the use of the mineral filler, the chosen polymer/filler mixing law is the one proposed by Maron and Pierce. The “Recipe” window of Ludovic, where all these data are entered, is shown in Figure 4.10.

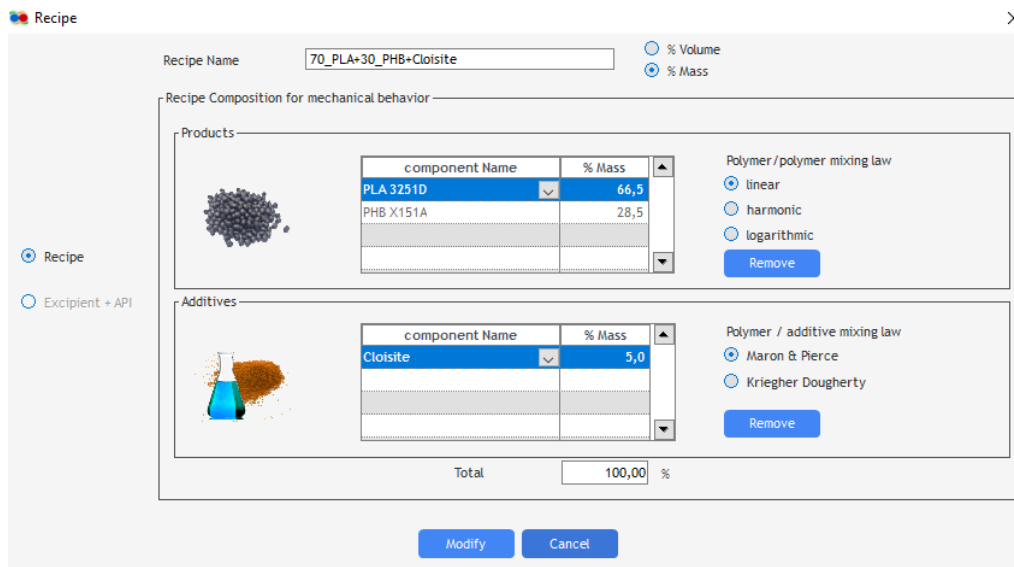


**Figure 4.10** – Ludovic "Recipe" window.

#### 4.3.3. “Process” tab – Definition of the working parameters

The purpose of the “Process” tab (Figure 4.11) is to specify the operating conditions of the extruder, whose geometry has been previously determined, and which materials are present in the

various sections of the apparatus. The rotation speed is set at 400 rpm, while, according to the instructions of the user's manual and since the screw is not heated, its temperature is left unchanged to the default value of 0°C.

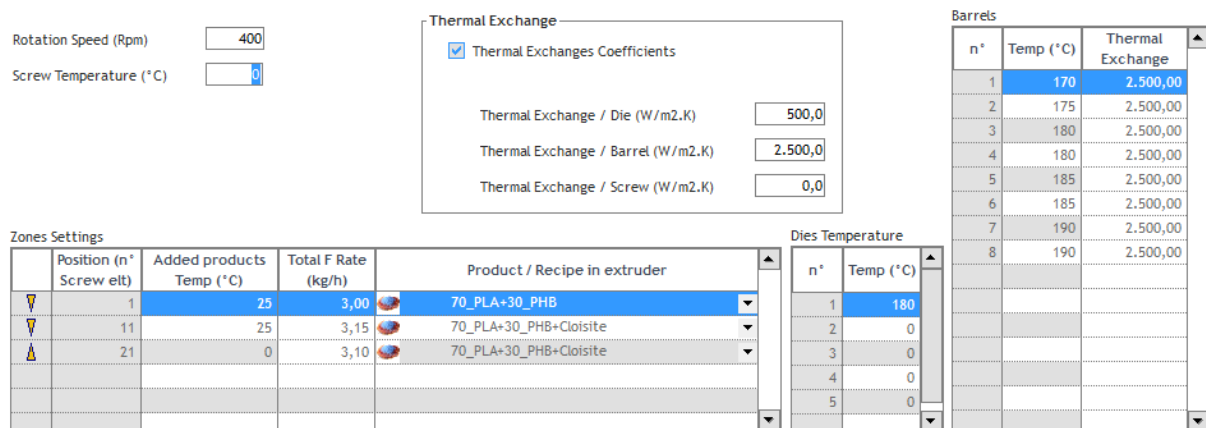


Figure 4.11 - Ludovic "Process" tab.

In the “Zones settings” tab of the window, the type of substances and their flow rates in the various section of the extruder are defined. This tab is also used to specify the temperature of what is progressively loaded inside the machine. The degassing action of the venting holes is taken into account by a decrease of the flow rate. For all the simulations run without Cloisite, the data entered in the “Zones settings” tab are listed in Table 4.6.

Table 4.6 - Configuration employed for the simulations without the addition of Cloisite.

	Position (barrel element)	Added product temperature (°C)	Total flow rate (kg/h)	Product/Recipe in the extruder
<b>Feeding (polymers)</b>	1	25	3,00	70 wt. % PLA – 30 wt. % PHB
<b>Degassing</b>	3	-	2,98	70 wt. % PLA - 30 wt. % PHB
<b>Degassing</b>	7	-	2,95	70 wt. % PLA -30 wt. % PHB

While, for the simulations that employ the mineral filler, the same data are reported in Table 4.7.

Table 4.7 - Configuration employed for the simulations with the addition of Cloisite.

	Position (barrel element)	Added product temperature (°C)	Total flow rate (kg/h)	Product/Recipe in the extruder
<b>Feeding (polymers)</b>	1	25	3,00	70 wt. % PLA - 30 wt. % PHB
<b>Feeding (Cloisite 5)</b>	3	25	3,15	70 wt. % PLA - 30 wt. % PHB + Cloisite
<b>Degassing</b>	7	-	3,10	70 wt. % PLA - 30 wt. % PHB + Cloisite

From the tables above, it is possible to observe that a same opening (the one in the middle of the third element of the barrel) acts alternatively as a vent or as the feeding of the filler. These settings result from the necessity of simulating a real experiment, in which the system that loads Cloisite is connected to that hole, which has not been plugged while compounding the blend without the clay. Then, the gases were allowed to leave the extruder from there, leading to the choice of modelling the opening as a normal degassing zone.

The thermal exchange has been quantified using the thermal exchange coefficients  $h_{barrel}$ ,  $h_{die}$  and  $h_{screw}$ . This last parameter has been neglected, since the screw is not thermoregulated, while the ones concerning the barrel and the die have been initially set, respectively, to 1000 and 500 W/m<sup>2</sup>K. These numbers, suggested by the developers in case of good and medium exchange, respectively, have been adopted after a tuning stage in which several simulations did not converge if higher values were employed for  $h_{die}$ . Once the simulations have been run, it has become clear that the computed temperature in correspondence of the first element of the die was far from the reality, if compared to the data measured with a thermocouple (185°C). The Advanced Control Interface (ACI) provided by Ludovic has been employed to reach the desired temperature in that particular point. Then,  $h_{barrel}$  has been modified to 2500 W/m<sup>2</sup>K for all the elements of the barrel, a value that is surely overestimated but necessary to have convergence between the computed results and the experimental ones.

The temperature profile of the barrel, entered in the “Barrel” section, is reported in Table 4.8. Please remember that the elements are numbered starting from the hopper and moving through the die.

**Table 4.8** - Temperature profile of the extruder. ▼ denotes a feeding zone, while ▲ stands for a degassing section.

	▼		▼/▲		▲			
Element number	1	2	3	4	5	6	7	8
Temperature (°C)	170	175	180	180	185	185	190	190

Finally, the “Dies Temperature” tab is necessary to specify the temperatures of the elements constituting the die. In the present work, only the first element (the one nearest to the screw, where the thermocouple is housed) is heated up to 180°C, while the others do not possess a thermoregulation system. Their temperature is then set to 0°C.

At this point, it is possible to launch the simulation through the “Compute” button of the “Execute” tab, where all the parameters are left unchanged to the default values. Ludovic returns the residence time distribution (RTD), the energy distribution, the  $f(x)$  plots of several quantities and the  $f(t)$  plots of temperature, pressure, shear rate and free volume.

#### 4.4. Setting of the Design of Experiment (DoE)

A DoE can be run starting from an existing simulation. It is at first necessary to define the quantities that will be varied and the related ranges. In the “Parameters Selection” tab (Figure 4.12), a distinction is made between primary (independent) and secondary (dependent) parameters. In fact, the first ones can change their value with a number of steps that is defined by the user, while for the second ones the number of steps is the same value entered for the quantity to which they are linked.

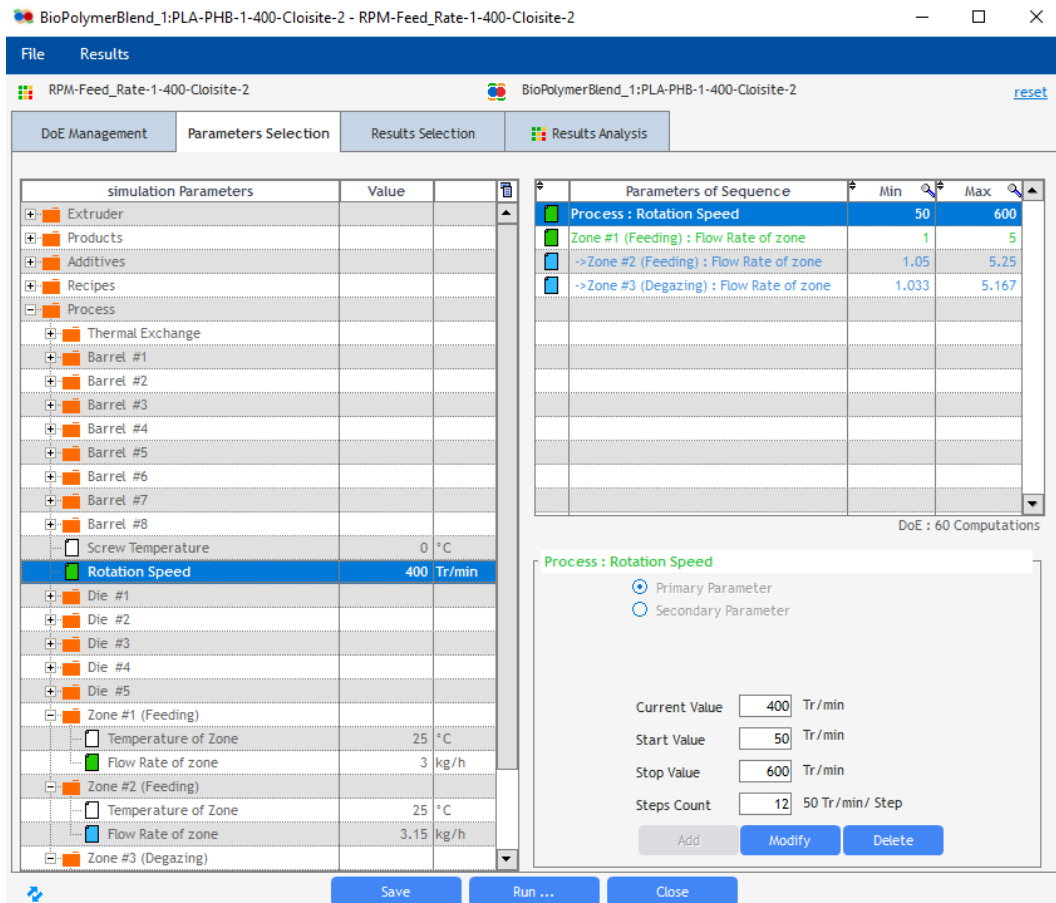


Figure 4.12 - DoE "Parameters Selection" tab.

In this work the DoEs are employed to analyse the feasibility of compounding under different working conditions. In particular, the effect of various combinations of rotation speed, defined as primary parameter, and flow rate have been evaluated. Besides, the flow rate in correspondence of the first zone of the extruder is considered as a primary parameter, while the same quantity in the other zones is proportional to the value set for the first section and so it must be considered as a secondary parameter. The data entered for all the DoEs (if Cloisite is not added) are reported in Table 4.9.

Table 4.9 - Settings of a DoE based on a simulation that does not include the addition of Cloisite.

	Type of the parameter	Start value	Stop value	Steps count
Rotation speed	Primary	50 rpm	600 rpm	12
Flow rate (Zone 1)	Primary	1 kg/h	5 kg/h	5
Flow rate (Zone 2)	Secondary (linked to the flow rate of the first zone)	0,993 kg/h	4,967 kg/h	-
Flow rate (Zone 3)	Secondary (linked to the flow rate of the first zone)	0,983 kg/h	4,917 kg/h	-

If the simulation is run with the addition of Cloisite, the correspondent parameters are reported in Table 4.10.

**Table 4.10** - Settings of a DoE based on a simulation that includes the addition of Cloisite.

	Type of the parameter	Start value	Stop value	Steps count
<b>Rotation speed</b>	Primary	50 rpm	600 rpm	12
<b>Flow rate (Zone 1)</b>	Primary	1 kg/h	5 kg/h	5
<b>Flow rate (Zone 2)</b>	Secondary (linked to the flow rate of the first zone)	1,05 kg/h	5,25 kg/h	-
<b>Flow rate (Zone 3)</b>	Secondary (linked to the flow rate of the first zone)	1,033 kg/h	5,167 kg/h	-

In the “Results Selection” tab, the results of interest are chosen. The quantities that vary along the screw (for which it is possible to trace a  $f(x)$  plot) are returned in the form of their maximum, minimum or average values. It is also possible to get the computed data in a specific point of the screw. The “Case status” parameter, always present between the results, reveals if a simulation run under specific condition converges.

For the purposes of this research, the following quantities have been selected:

- Case status
- Torque (N·m)
- RTD min (s)
- RTD mean (s)
- RTD variance
- Mean temperature (°C)
- Maximum temperature (°C)
- Mean shear rate ( $s^{-1}$ )
- Maximum shear rate ( $s^{-1}$ )
- Mean viscosity (Pa·s)
- Maximum viscosity (Pa·s)
- Minimum viscosity (Pa·s)

It is now possible to run the DoE through the “Run” button in the bottom of the window. According to the settings reported in Table 4.10, 60 simulations take place.

Finally, in the “Results Analysis” tab, the computed data are shown as surfaces in a 3-D space (“Graphical Analysis” sub-tab) or listed in a table (“Results Data” sub-tab).

## 5. DoE results analysis

Before examining the results of the simulations, it is necessary to assess the reliability of the predictions made by Ludovic. This is done with an analysis of what is returned by the DoEs, in order to verify if they are in accordance with the current knowledge about polymer processing.

The simulations used to start the DoEs are named with the following codification:

PLA-BHB-Number of the screw profile-Screw speed (rpm)-Cloisite-2

If it is present the attribute “-Cloisite” the DoE is run employing the mineral filler, while the suffix “-2” identifies those Design of Experiments that have the thermal exchange coefficient of the barrel set at 2500 W/m<sup>2</sup>K (otherwise its value is equal to 1000 W/m<sup>2</sup>K).

### 5.1. Case status

The first parameter taken into account is “Case status”, that reports if the simulations in the DoE converge and, so, to understand which are the range of settings that can be employed to process the materials. In particular, “Case status” is equal to 1 in case of convergence.

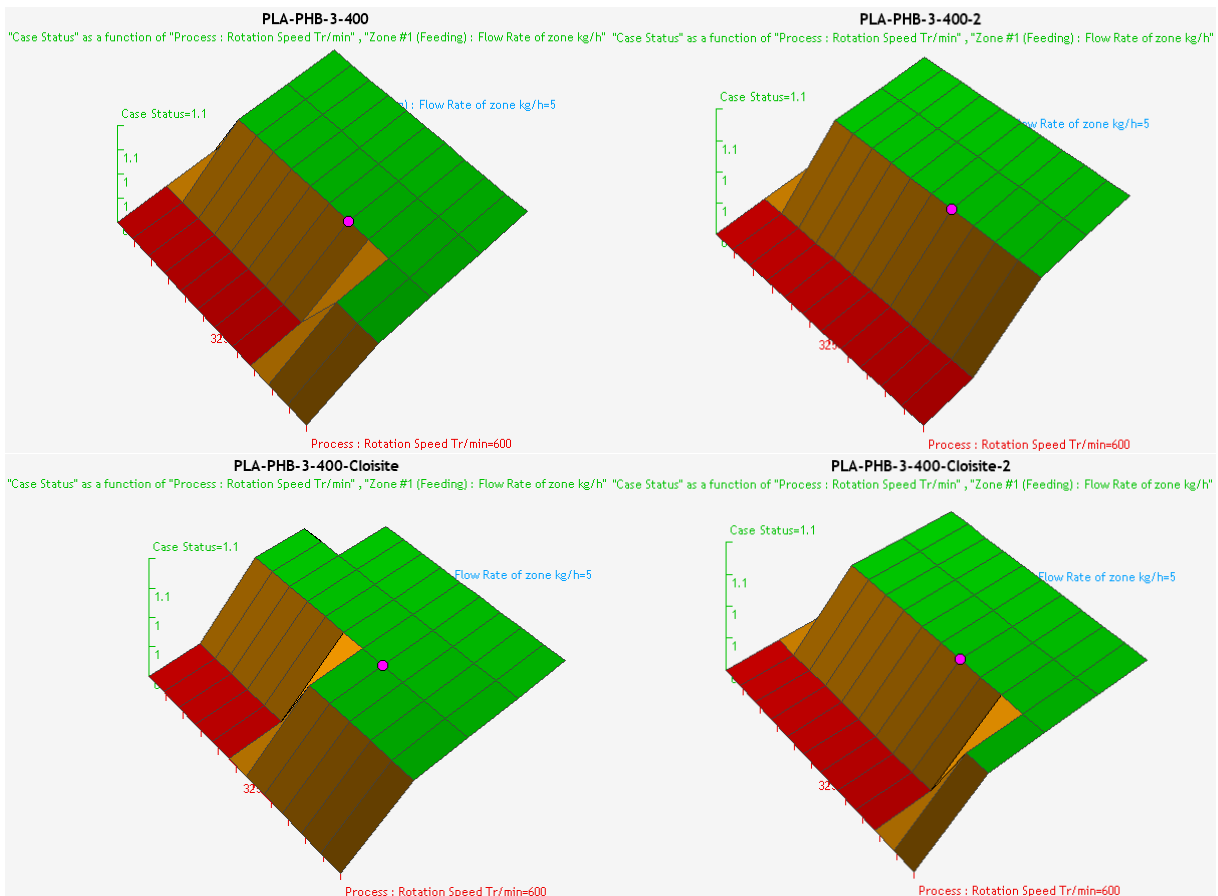


Figure 5.1 - DoEs "Case Status" results for the screw profile 3.

Regarding all the screw configurations, it is possible to note that the simulations run with the neat polymers (top of Figure 5.1) at a flow rate of 1 kg/h do not converge. The same can be observed for the majority of the simulations in which the rotation speed is set at 50 rpm. Moreover, a higher thermal exchange coefficient in the barrel decreases the number of simulations for which the computation is successful, since it becomes completely impossible to blend the polymers at a flow rate of 2 kg/h with any rotation speed. This happens because, due to the more effective heat exchange coupled with the lower quantity of molten polymer, the temperature of the melt drops below the melting temperature of PLA, causing its solidification in the barrel.

Looking at all the DoEs involving the use of Cloisite (bottom of Figure 5.1), the situation is similar to what is described before, but it is worth noting that for a flow rate of 2 kg/h a higher number of simulations reaches convergence. In particular, it happens also when the thermal exchange coefficient is set at 2500 W/m<sup>2</sup>K for rotation speeds of 550 and 600 rpm (only at 600 rpm for the screw profile 1). This behaviour can be attributed to the presence of a mineral filler, since it increases the viscosity and so the amount of mechanical energy turned into heat that, according to eq. (4.34), is directly proportional to  $\eta$  and  $\dot{\gamma}^2$ . The resulting temperature increase prevents the solidification of the melt in the barrel, allowing the computation to be successful.

In general, it can be stated that to properly blend PLA and PHBH, either with or without Cloisite, higher flow rates (3-5 kg/h) and screw speeds (100-600 rpm) are required. To have the certainty of avoiding freezing it is better to choose settings near the upper limits.

5.2. Residence Time Distribution (RTD)

After the DoE computation, it is also possible to evaluate the Residence Time Distribution (RTD) of the melt inside the extruder. In particular, the minimum or the average values of the RTD and its variance can be plotted as a function of the independent variables chosen while setting up the DoE. It is important to point out that only these discrete values are employed to draw the surfaces shown in the “Graphical Analysis” tab, since it would not be possible to do the same with the entire distributions.

As it has been reported for the “Case status” parameter, the observed trends are the same whatever the screw profile is. For this reason, in the present section are reported only the results related to the screw profile 2.

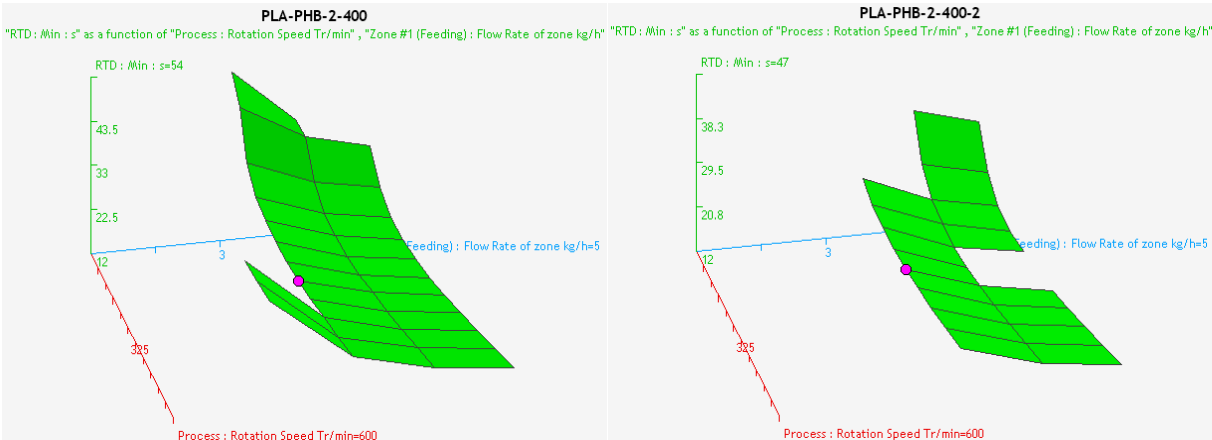
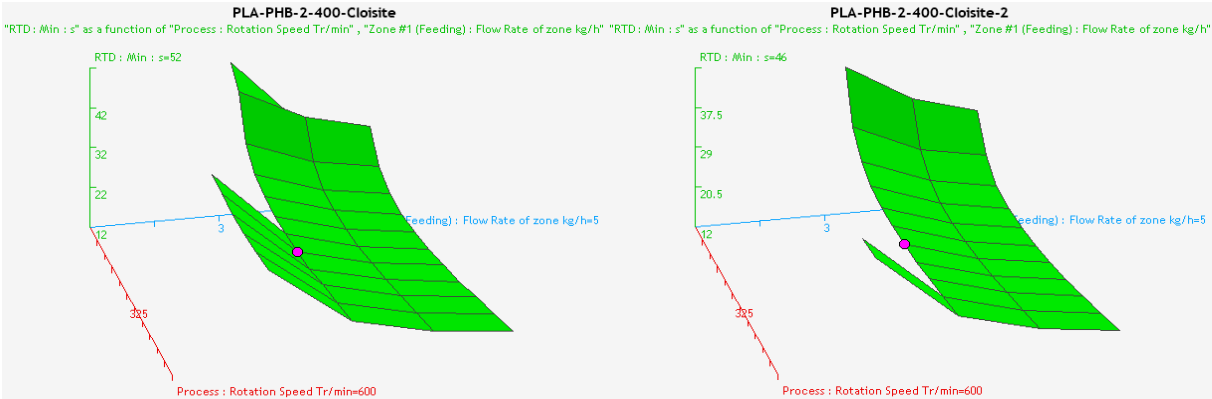


Figure 5.2 - RTD minimum values plotted as a function of screw speed and flow rate for the DoEs run in absence of Cloisite.

In Figure 5.2 it can be clearly seen that, as expected, the polymer requires a certain time before starting to flow through the die. This time is longer at lower flow rates and screw speeds, while it decreases moving along the bisector of the plane generated by the  $x$  and  $y$ -axis. The same can be observed in the case of the DoEs run with Cloisite (Figure 5.3). In this last case, it is interesting to notice how the minimum value of the RTD is generally lower of some tenths of a second, if compared to the Design of Experiments where the thermal settings are the same and the mineral filler is not employed. This phenomenon can be observed also when the heat transfer coefficient is raised from 1000 to 2500 W/m<sup>2</sup>K. A possible explanation can be found in the slightly higher viscosity reached in those situations, that makes the transport along the screw more effective. This hypothesis seems to be confirmed since the lowest values of the RTD minimum are registered when the mineral filler is added and more heat is dissipated.



**Figure 5.3** - RTD minimum values plotted as a function of screw speed and flow rate for the DoEs run with Cloisite.

The average value of the RTD (Figure 5.4) behaves in the same way as the minimum, but the surfaces are less steep, especially in the range 150-600 rpm at feed rates higher than 3 kg/h. It means that, as described by the equations (4.17) and (4.27), higher flow rates decrease the time needed by the melt to pass through the various elements. So does also the rotation speed of the screw, since it influences the axial velocity in the partially-filled sections<sup>[36]</sup>. However, if compared to what happens with the minimum values of the distribution, their effect is less pronounced, since the average takes into account the motion of the whole melt and not just of a little portion of it.

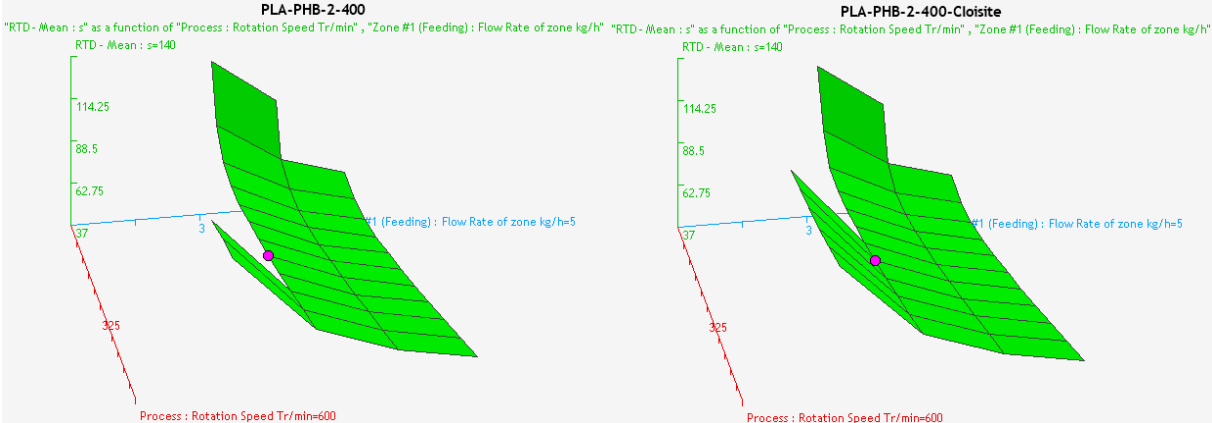


**Figure 5.4** - RTD average values. The chosen DoEs have the thermal exchange coefficient in the barrel set at 1000 W/m<sup>2</sup>K because the higher number of converging simulations make easier the trend analysis.

The last parameter of the RTD that has been analysed is its variance. Once again, it is expected that an increase of flow rate and screw speed would cause a decrease of this quantity, because the overall lower values of the residence time “squeeze” the distributions. The results computed by the DoEs (Figure 5.5) are in line with these assumptions.

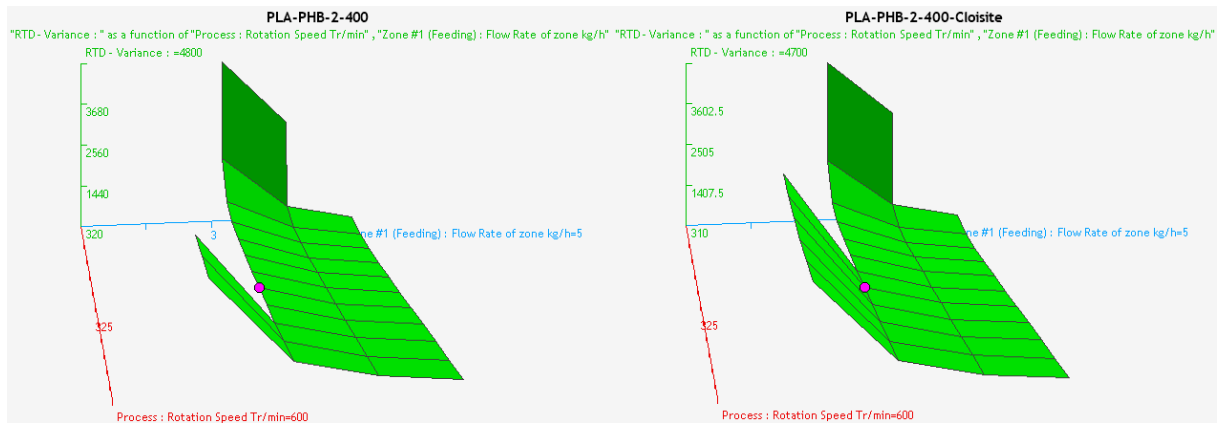


Figure 5.5 - RTD variance for the DoEs shown in Figure 5.4.

### 5.3. Temperature

A further result of the DoE of particular interest is the temperature registered inside the extruder, that is different in the various segments of the apparatus. As explained in the section dedicated to the RTD, it is not possible to plot surfaces using an entire distribution, so the average and maximum values of the temperature are studied. In particular, the maximum temperature is particularly important since if its value is too high the polymer can go through thermal degradation. This phenomenon is obviously undesired, first of all for its influence on mechanical properties, but also on functional ones, like the colour. In fact, an excessive heat can cause the formation of chromophores functional groups (like a double bond) that cause the yellowing of the material.

The observed trends are, also in this case, the same for the three screw profiles, so in this section only the results related to the screw profile 3 will be shown.

The mean temperature (Figure 5.6) increases while increasing the screw speed (more rapidly at faster rotations), but it is practically the same at any flow rate, although the highest temperature is registered for a feed rate of 5 kg/h. As it can be expected, when the thermal exchange coefficient of the barrel is set at 2500 W/m<sup>2</sup>K lower temperatures are computed, with a difference of about 13°C both with and without the mineral filler.

The addition of Cloisite (bottom of Figure 5.6) causes an increase of the viscosity and the amount of mechanical energy turned into heat. So does also the average temperature, which increases of about 3°C both at 1000 and 2500 W/m<sup>2</sup>K, meaning that the heat exchange at the barrel wall plays a more important role in the determination of this parameter.

The computed maximum temperature (Figure 5.7) follows the trends described above for its average. The plotted surfaces are steeper, meaning that much care must be taken while varying the rotation speed of the screw. In fact, in the filled sections of the extruder the temperature can increase sharply even just for a short time, which could be sufficient to induce polymer degradation.

Carneiro *et al.*<sup>[36]</sup>, state that during compounding the screw speed plays the most important role, since it determines the shear rate and so the heat lost due to mechanical dissipation. The

contribution of the flow rate is, instead, less significant. In fact, it is reported that the measured temperature profile during polypropylene compounding is substantially the same, irrespectively of the feed rate<sup>[36]</sup>. The same trend is observed by looking at the DoE results. A possible explanation is that if on one hand a lower volume of melt results in a higher energy density, on the other one also the surface-to-volume ratio is higher, leading to a greater heat loss.

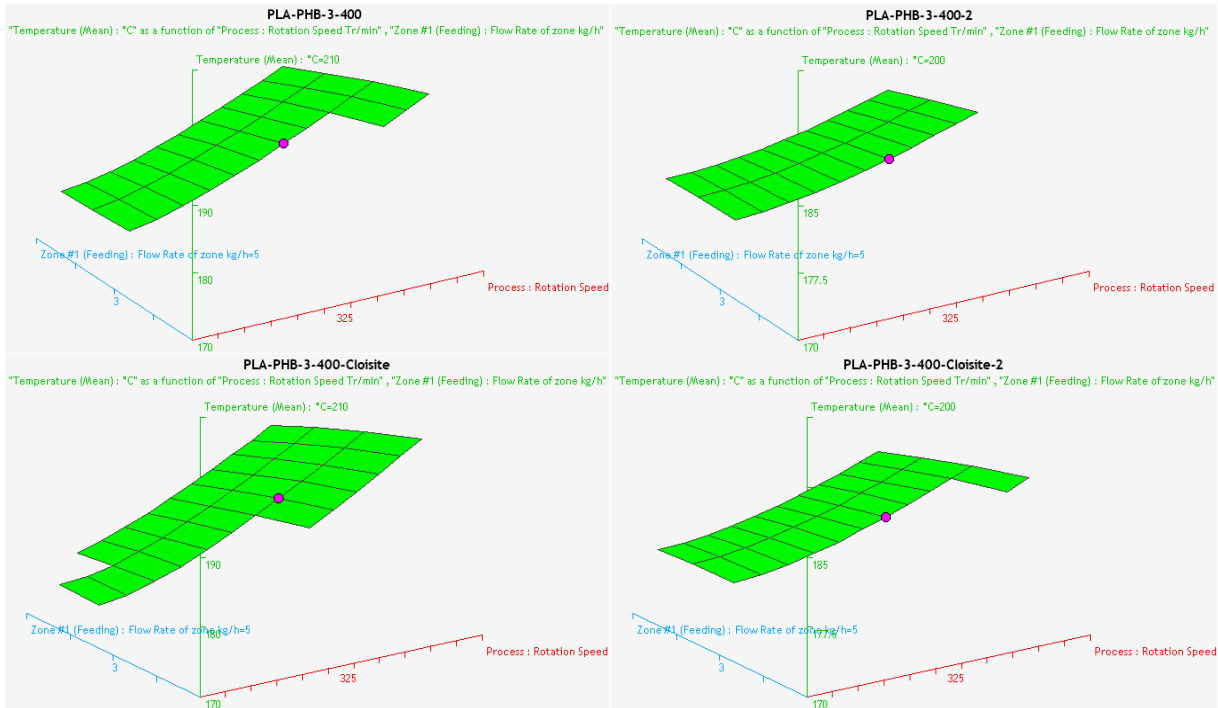


Figure 5.6 - Computed mean temperature for the screw profile 3 as a function of flow rate and rotation speed.

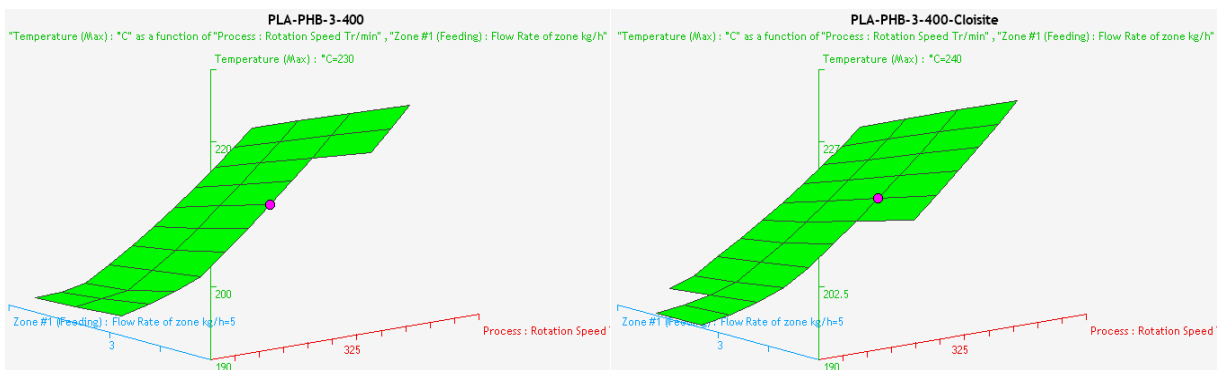


Figure 5.7 - Computed maximum temperatures with  $b_{barrel}=1000 \text{ W/m}^2\text{K}$ . Please note the greater slope of the surfaces if compared to the ones of Figure 5.6.

#### 5.4. Shear rate

Analysing the DoEs it is possible to observe how, for a same screw profile, the mean shear rate practically does not depend on the flow rate. This is true especially for values of this parameter over 3 kg/h, while the simulations having the feed rate set at 2 kg/h show an average shear rate that, with the same screw speed, is higher of 2-3%. This behaviour is observed also in those DoEs where the mineral filler is employed, and the results are the same of the case without Cloisite, except for the decimal part. On the other hand, the rotation speed of the screw is a key

parameter in determining the shear rate and a linear dependence between the two quantities is observed.

What is reported above reflects the technique employed by the software to compute  $\dot{\gamma}$  along the screw. In fact, as described in section 4.2.3, an initial value  $\dot{\gamma}_0$ , defined as

$$\dot{\gamma}_0 = \omega \frac{R_2}{H} \quad (5.1)$$

where  $\omega$  is the angular velocity, is adjusted according to the local velocity field. As it can be seen, this starting value depends only on the rotation speed and on some geometrical parameters of the screw. The flow rate has a role only in the following tuning operation of  $\dot{\gamma}_0$  and it can be reasonably presumed, by observing the plots, that its effect is only marginal. Since the viscosity does not participate in the determination of the shear rate, both the simulations run with and without Cloisite show the same values of this last parameter, because the operating conditions are the same (except for a slightly higher feed rate when the filler is employed). Also the effect of thermal exchange coefficients is negligible and, for this reason, in Figure 5.8 the chosen plots can be compared although the different value of  $b_{barrel}$ .

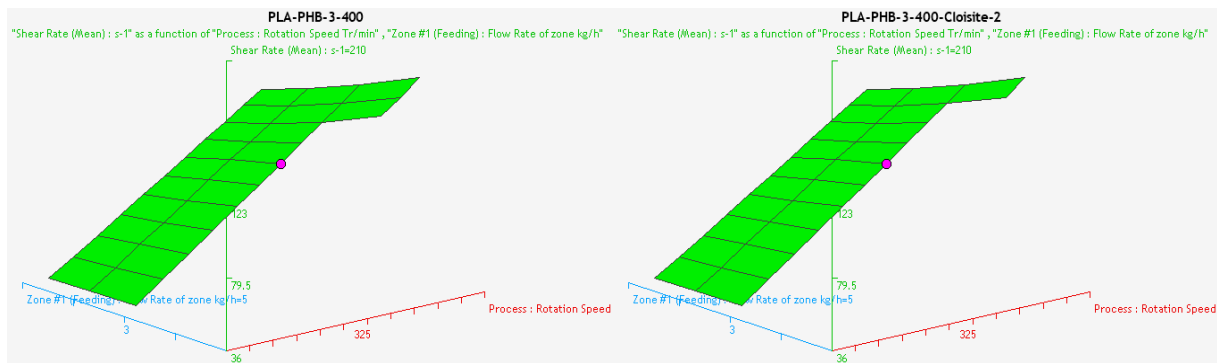


**Figure 5.8** - Comparison between the mean shear rates in the case of screw profile 3. Please note that the values are the same despite a different thermal exchange coefficient in the barrel and despite the addition of Cloisite.

Regarding the difference between the three screw profiles (see Figure 5.8 and Figure 5.9), the mean shear rates have the same order of magnitude. In particular, the lowest values (181,50 Pa·s at 600 rpm) are provided by the profile 2, while the highest ones (199,49 Pa·s at 600 rpm) are prerogative of the profile 3. Finally, the profile 1 shows intermediate values, with an average shear rate of 189,76 Pa·s at 600 rpm. This happens in the whole range of rotation speeds, although the difference of  $\dot{\gamma}$  between two simulations run with the same processing parameters but different screws is less pronounced at 50 rpm. In fact, the slope of the surfaces is not exactly the same in the three cases, but it is slightly higher for the profiles 3 and 1.

The above results confirm what was expected: in fact, keeping in mind that the first kneading section is the same for all the profiles, the screw number 2 has only another long kneading block, mainly composed of elements with low staggering angles. In contrast, the profiles 1 and 3 are characterised by two more completely-filled sections able to raise the mean shear rate.

Similarly to what has been observed for the average, also the maximum shear rate depends only on the rotation speed with a linear trend, as it can be seen in Figure 5.10. In particular, the results related to the screw profiles 1 and 2 are coincident (381,85 Pa·s at 600 rpm), since the TME blocks mounted on the profile 1 lead to lower shear rates, if compared to the kneading sections. Then, the maximum values are provided by this last type of elements, that can be found on both

the screws. Profile number 3 is instead characterized by a slightly higher maximum shear rate (397,27 Pa·s at 600 rpm), registered in correspondence of the back-flow element.

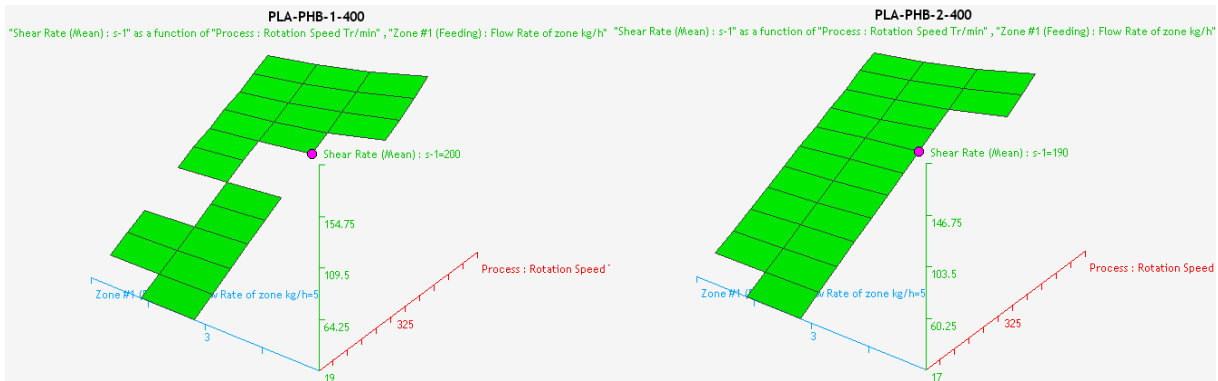


**Figure 5.9** - Mean shear rate for screw profiles 1 (left) and 2 (right) at  $h_{barrel}=1000 \text{ W/m}^2\text{K}$ .

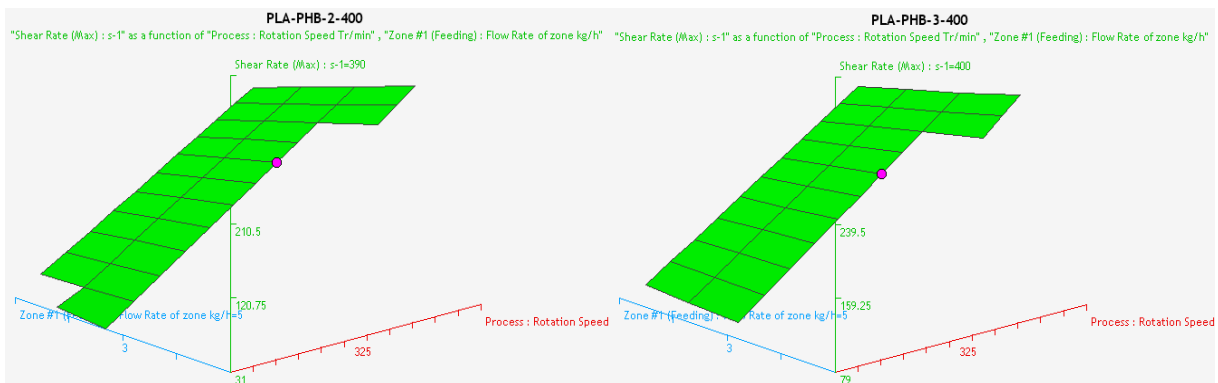


**Figure 5.10** - Maximum shear rate for screw profiles 2 and 3. Since the values do not vary after the addition of Cloisite or with different thermal exchange coefficients, the above plots are sufficient to describe the trends.

### 5.5. Viscosity

The DoEs have been run also to compute the maximum, minimum and mean viscosity of each simulation. Before proceeding with their analysis it is important to point out that the viscosity before the first restricting element, when the polymer is still solid, is considered by Ludovic as equal to 0 Pa·s (although, obviously, it does not correspond to the reality). Unfortunately, the software does not give the possibility to calculate the selected parameters only in a specific sector of the extruder, so the plots related to the minimum viscosity are practically useless, since its value is always null regardless of the operating condition. For this reason, only the results about maximum and mean viscosity will be reported and studied in this section.

As it can be expected, the average viscosity decreases while the rotation speed, and so the shear rate, increases. The same happens with an increasing flow rate, but this decrease does not reflect the correspondent temperature growth described in section 5.3. At first, that behaviour seems quite peculiar, but it reflects the trend shown also by the plots of the maximum viscosity (Figure 5.12). In fact, since the computation takes place considering the whole extruder, the very high values of  $\eta$  registered in the die greatly influence the average. It must be remembered that the computation in this part of the apparatus is done by a simplified model that is not as precise as the one employed in the barrel (see section 4.2.3), so also the final data can be less reliable.

Despite this drawback, the results respect the common knowledge about polymer melts when Cloisite is added and when the thermal exchange coefficient of the barrel is set at 2500 W/m<sup>2</sup>K. In fact, in both the cases higher viscosities are obtained, while the highest value is got when the mineral filler is added and contemporarily the thermal exchange becomes more effective, lowering the temperature in this way. As an example, for the profile number 3, the addition of the clay causes an increase of  $\eta_{mean}$  equal to 23 Pa·s, while the increase due to the higher  $h_{barrel}$  is of 48 Pa·s. Their combined effect raises the average viscosity of almost 90 Pa·s.

The trends and the orders of magnitude of mean viscosity are the same for all the screws, so the plots reported in Figure 5.11 are related only to the profile 3. Since the data are heavily influenced by the estimations made in the die, probably it makes no sense to rank the results correspondent to the different screw configurations.

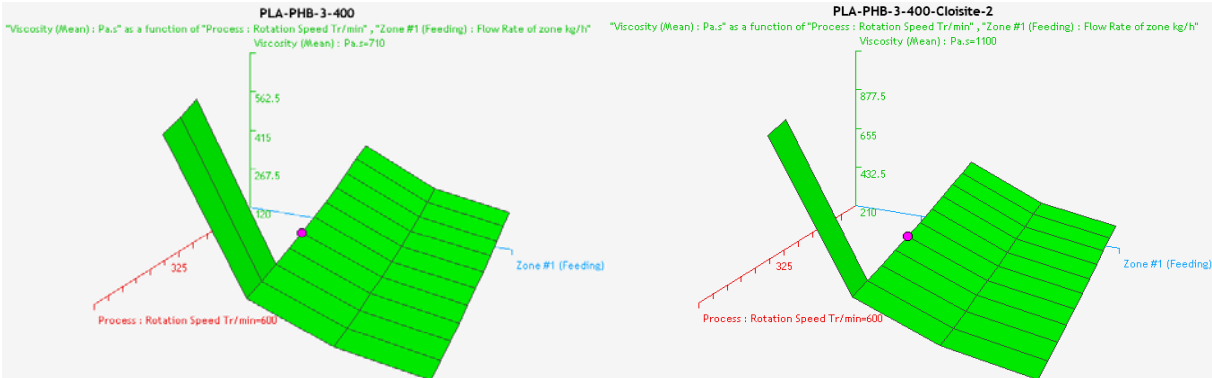


**Figure 5.11** - Mean viscosity for the screw profile 3. Please note (on the right) the higher values resulting from the addition of Cloisite and from the increase of  $h_{barrel}$ .

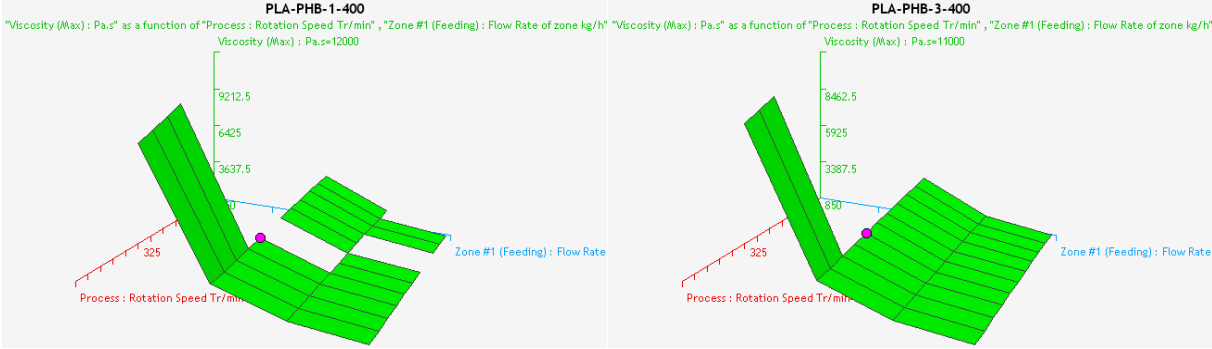


**Figure 5.12** - Maximum viscosity for screw profiles 1 (left) and 3 (right).

*5.6. Torque*

The last parameter that has been studied is the torque applied to the shaft. The plots show that the highest values can be found at high feed rates and low rotation speeds. In fact, for this last operating condition the shear rate decreases and, as reported in Figure 5.11, the viscosity is higher. Moreover, a greater torque is needed to move along the screw a higher quantity of material in the same interval of time.

These explanations are confirmed also by the user’s manual of the software<sup>[26]</sup>, where it is reported the following equation:

$$Tq = \frac{E_{mat} Q}{2\Omega} \quad (5.2)$$

where  $E_{mat}$  is the energy dissipated by a unitary mass of the material due to viscous dissipation, solid transport and melting,  $Q$  is the flow rate and  $\Omega$  is the rotation frequency. It can be clearly seen the linear dependence between torque and feed rate, while the lower  $\eta_{mean}$  obtained at higher shear rates reduces the viscous dissipation in the melt and so  $E_{mat}$ . The reduction of  $Tq$  is also an effect of the increase of  $\Omega$  resulting from higher screw speeds.

At low rotation speeds, the addition of Cloisite leads to a slight increase of the torque, but it is not true in case of a higher thermal exchange coefficient. This behaviour can be explained by the equations (4.34) and (5.2) and by the effect of viscous dissipation on the value of  $E_{mat}$ . In fact, under the above mentioned working conditions, the shear rate is lower and its decrease is compensated by the correspondent increase of viscosity, so  $E_{mat}$  substantially does not change. Instead, when the screw turns faster the effect of  $h_{barrel}$  can be observed through a little increase of the torque, because the higher shear rate is no more balanced by the decrease of viscosity. This results in a rise of the viscous dissipation and, consequently, in an increase of  $Tq$ .

The computed torque and the observed trends are almost coincident for all the screw configurations, so in Figure 5.13 only some results related to the profile number 2 are reported.

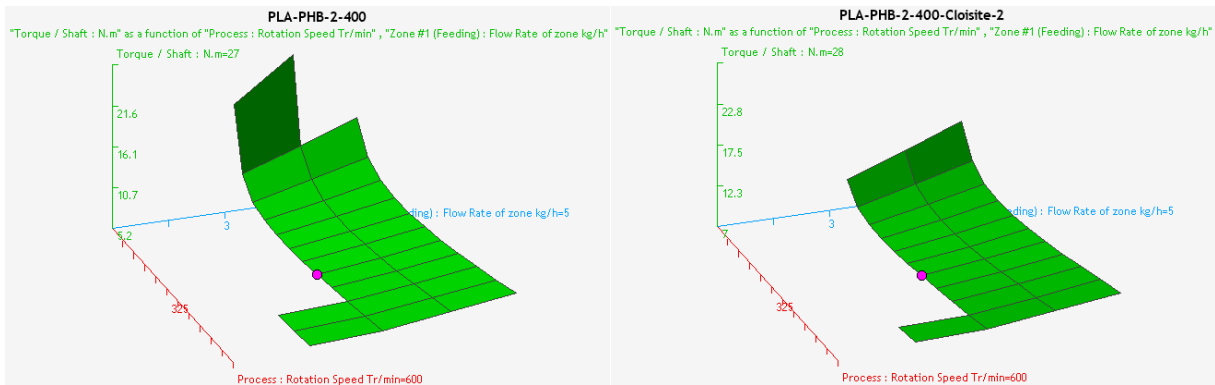


**Figure 5.13** - Computed torque values for the screw profile 2. On the left are reported the results of the simulations run without Cloisite and with a thermal exchange coefficient in the barrel of  $1000 \text{ W/m}^2\text{K}$ , while on the right the mineral filler is added and  $h_{barrel}=2500 \text{ W/m}^2\text{K}$ .

### 5.7. Effect of the composition

The effect of the composition has been evaluated in a different way, because Ludovic does not give the possibility to set a DoE in which the weight percentages of the polymers are varied. A different approach has been adopted, then. In particular, single simulations with different proportions of the components in the blend have been run and then the quantities of interest have been calculated with MS Excel and plotted as a function of the PLA fraction.

Since setting and elaborating the various simulations takes quite a long time, only the screw profile 3 has been considered, because in the previous section it can be observed that the DoEs have the same trends whatever the configuration is. The polymer flow rate has been kept at  $3 \text{ kg/h}$ ,  $h_{barrel}$  is equal to  $2500 \text{ W/m}^2\text{K}$  and Cloisite is always added, while the rotation speed has been set to 200, 400 and 550 rpm. For each value of this last parameter, 5 different compositions of the PLA/PHBH blend (50/50, 60/40, 70/30, 80/20 and 90/10) have been studied, with a total of 15 single simulations.

As far as the Residence Time Distribution is concerned, in Figure 5.14 it can be highlighted how the minimum values are substantially independent from the weight percentage of PLA. As it can be easily foreseen, higher rotation speeds result in a lower time required before the outflow of the melt from the die. The same trends are observed also for the average values (Figure 5.15), which show a slight decrease at 400 and 550 rpm along with the amount of PLA, while the plot at 200 rpm remains substantially constant. The width at half height (Figure 5.16) is almost constant at the lowest screw speed, while at 400 and 550 rpm it decreases as the PHBH percentage decreases. Then, at 200 rpm the distribution substantially retains its shape regardless of the blend composition. According to what is reported in the literature<sup>[27]</sup>, the RTD width reflects the effectiveness of the distributive mixing, so it is possible to hypothesise that better morphologies are obtained at 200 rpm for every composition of the blend, while at higher rotation speeds the extensive mixing could be less effective for higher amounts of PLA.

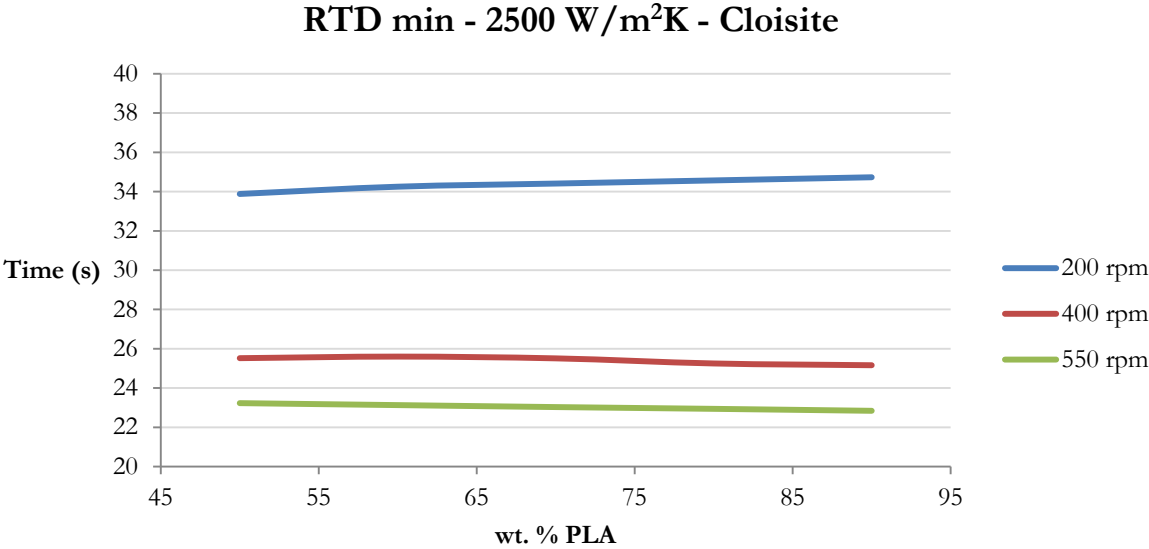


Figure 5.14 - RTD minimum values as a function of the amount of PLA.

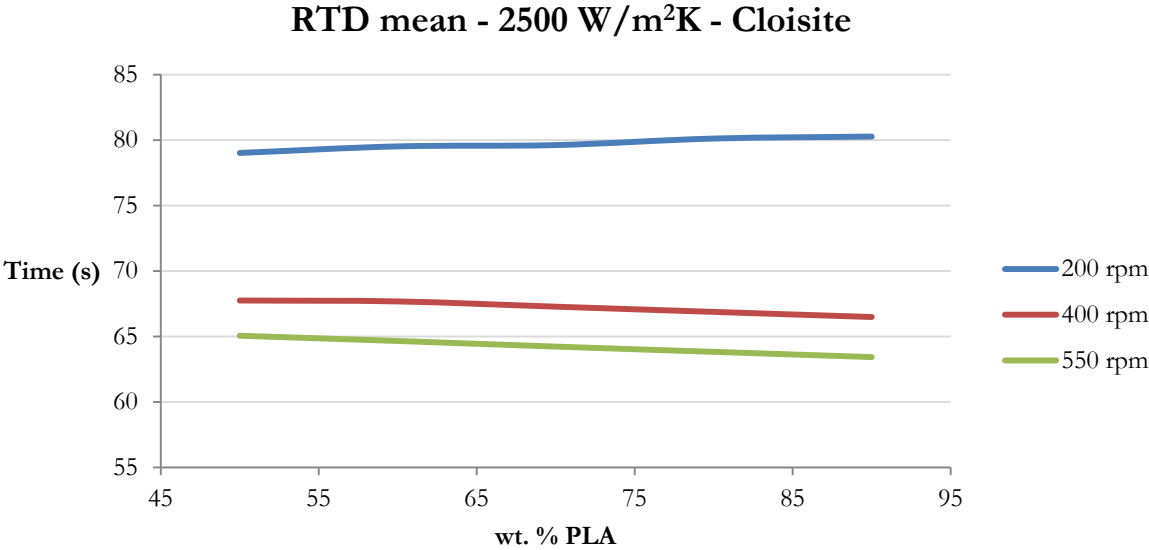
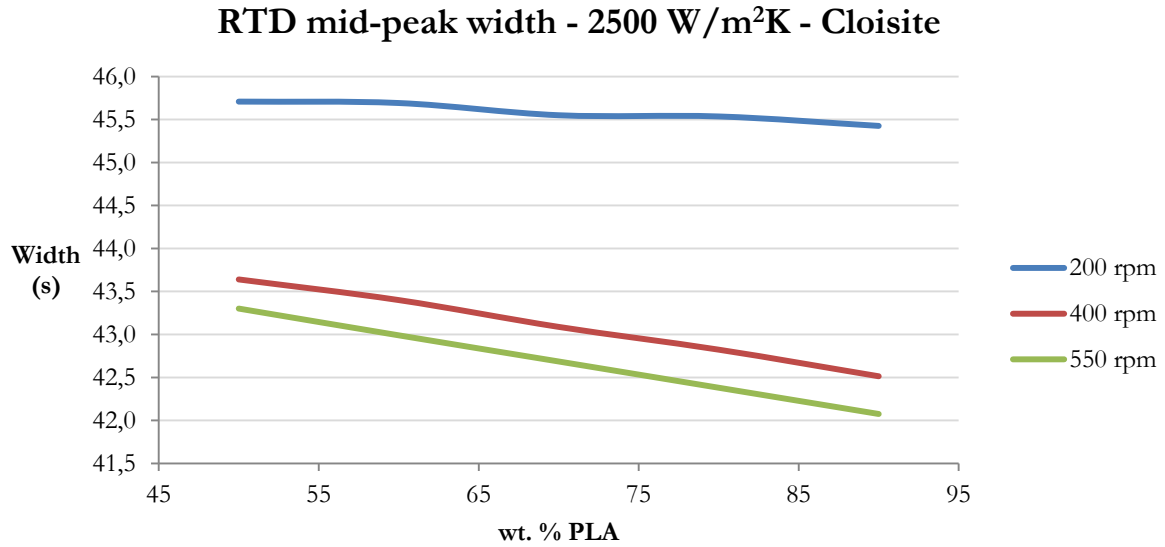
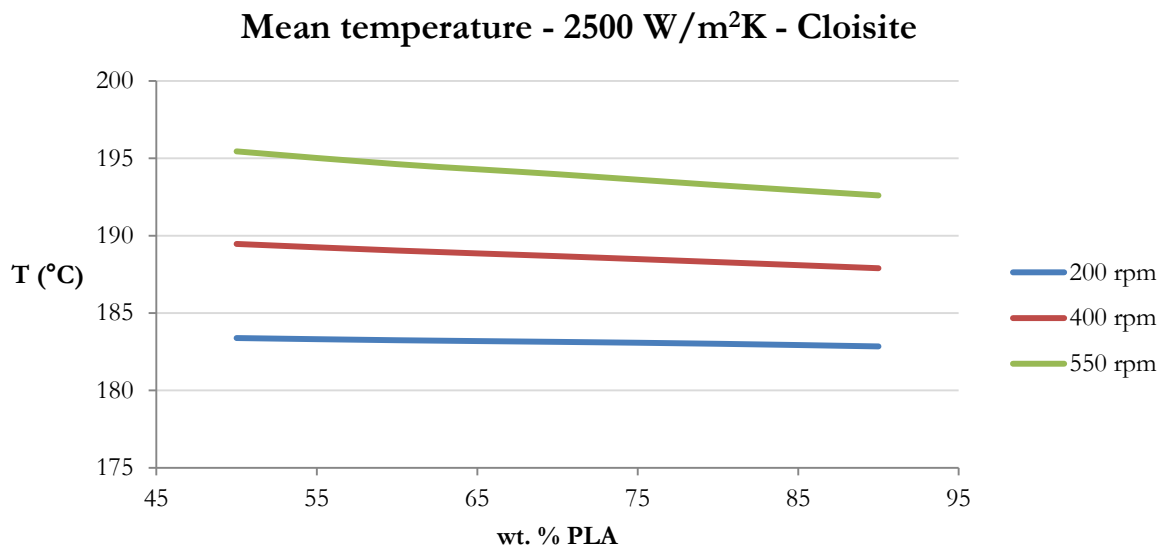


Figure 5.15 - RTD average values as a function of the amount of PLA.



**Figure 5.16** - Width of the distributions at half height as a function of the amount of PLA.

The other parameters that have been evaluated are the mean values of temperature, shear rate and viscosity. Since in this case the average has been computed using MS Excel, it has been possible to select specific sectors of the extruder in which this calculation has to take place. In particular, the mean temperature depends on the values related to the entire barrel, but not to the die section, while the other mean parameters are referred to that part of the apparatus located between the first restricting element (which is included in the calculation) and the die. This choice allows to achieve results referred only to those sectors of effective interest and to overcome the problems encountered in section 5.5 about the computation of the minimum, the maximum and the average values of the viscosity.



**Figure 5.17** - Mean temperature as a function of the amount of PLA.

Regarding the mean temperature, it is possible to observe that it decreases for increasing weight percentages of PLA, and this decrease is steeper at higher rotation speeds. These trends can be

explained in terms of dissipation of the mechanical energy, whose dependency on  $\eta_{melt}$  and shear rate is explained by eq. (4.34). As an example, at 200 rpm the lowest shear rate is reached and so also the resulting mean temperatures are the lowest of Figure 5.17. The decrease observed at higher amounts of PLA is due to its lower viscosity and so, one more time, to the lower energy dissipation.

The mean shear rate depends only on the rotation speed and on the geometry of the screw. Since this geometry does not vary because the profile is the same in the three cases,  $\dot{\gamma}_{mean}$  is only a function of the angular velocity. As expected, in Figure 5.18 it is possible to observe that the obtained trends are linear and parallel to the  $x$ -axis, meaning that the composition has no influence on the average values of the shear rate.

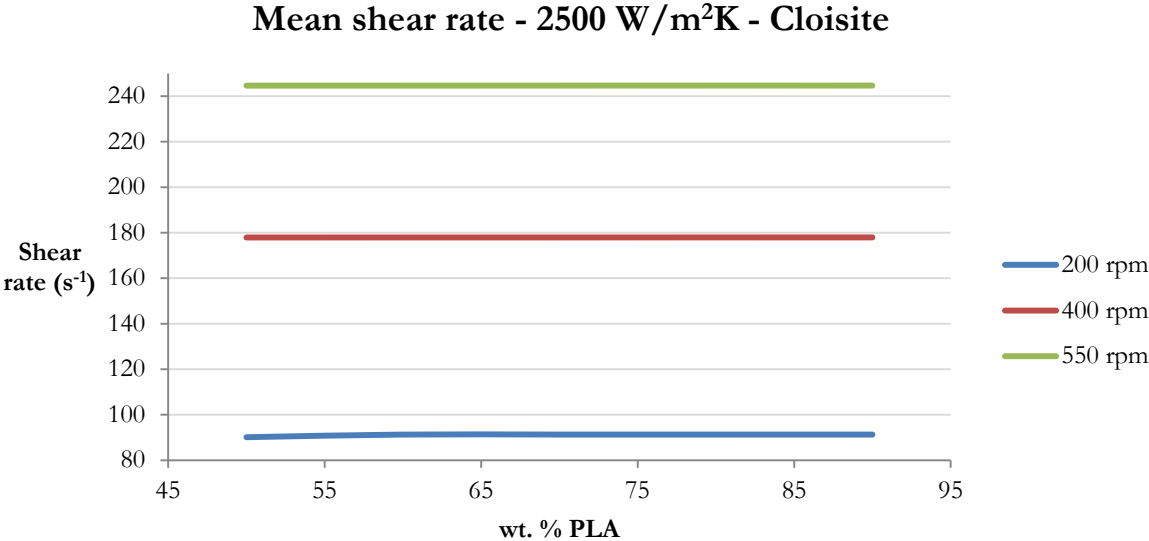


Figure 5.18 - Mean shear rate as a function of the amount of PLA.

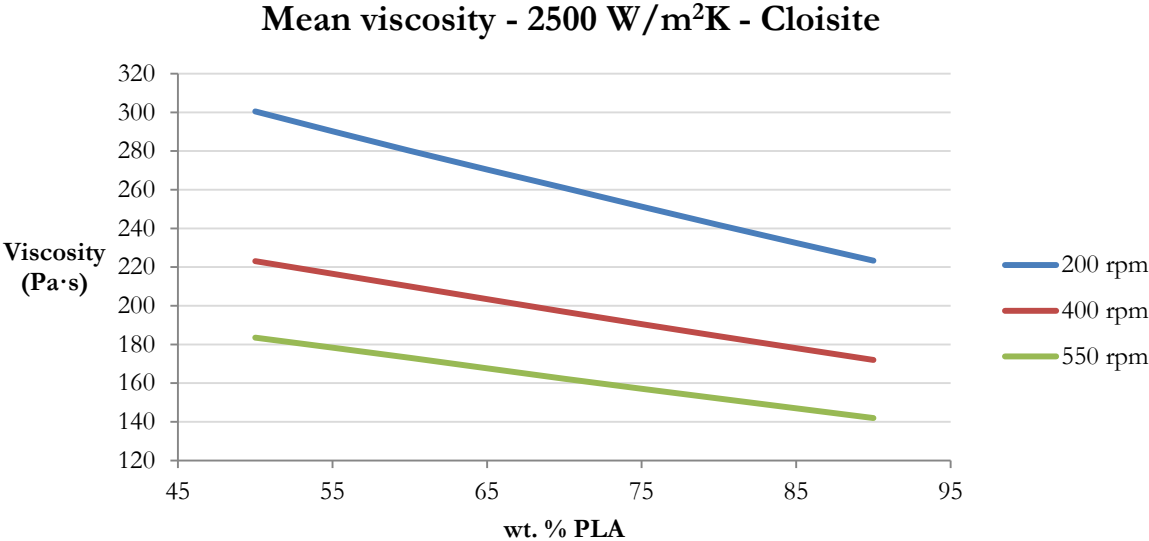


Figure 5.19 - Mean viscosity as a function of the amount of PLA.

### 5.8. *Conclusions about the DoE results*

From the analysis reported in this chapter it is possible to observe how, for all the trends shown by the DoE results, a logical explanation that is coherent with the knowledge about the behaviour of polymers can always be found. The only noteworthy drawback has been identified while trying to compute the viscosity in section 5.5, but it must be pointed out that the observed trends of maximum and average viscosities are anyway in line with what was expected. Moreover, in the following chapter the entire  $f(x)$  profiles of the aforementioned quantities will be evaluated. These profiles are surely more precise than a simple mean value and they do not depend on what happens in correspondence of the hopper or the die, so the problem is easily overcome.

In literature, it is reported<sup>[5]</sup> the possibility to simulate with a good precision the compounding operations of the most common polymers, like polyolefins, using Ludovic. The results of the DoEs reported in this section confirm that the software can be applied with an adequate degree of accuracy also to make predictions before blending biopolymers, even if a mineral filler is added and the thermal parameters are modified. Then, in the following chapter the software will be used to study the effect of the screw configuration on the morphology, and so on the properties of the final blend, while working with specific processing parameters that will not be changed.



## 6. Analysis of the simulations

After having proved the effectiveness of Ludovic to predict the compounding process of a bio-based PLA-PHBH blend under different working conditions, it is time to analyse the effect of the different screw configurations on the final characteristics of the blend. The quantities that have been studied are the same already seen in the previous chapter, but with a significantly difference: in fact, after a simulation the software plots the various parameters (except the RTD) as a function of the axial distance from the hopper. This allows to deepen what happens in particular sectors of the apparatus, while the same thing is harder to be done after a DoE. In fact, this last instrument should be used only to determine the proper settings, while the complete analysis has to be done through a simulation.

The results from many simulations run with the same processing parameters but different screws are necessary to determine the profile that leads to the blend with the best mechanical properties. Since these properties are related to the final morphology, the model of Vergnes and Delamare is employed to aid this selection. The various assumptions are then validated through a comparison with some specimens compounded under the same operating conditions. Since the objective of this work is to study the real process with the highest possible fidelity, only the simulations run with  $h_{barrel}$  set at 2500 W/m<sup>2</sup>K have been analysed. The codification explained at the beginning of Chapter 5 is still valid.

### 6.1. RTD

As previously stated, the Residence Time Distribution (RTD) is the only quantity analysed in this chapter that is not a function of the axial position along the screw. In fact, this distribution is built up by plotting the percentage of material that passes through the die as a function of time.

The minimum, mean and peak values are of great importance, along with the shape of the distribution, quantified by its width calculated at mid-height. If this value is low, the majority of the melt takes substantially the same time to pass through the extruder, while a broader distribution means that a certain delay is observed. In general, it can be said that the first situation is more favourable, since it makes possible a more effective control of the process, especially with materials that are more sensitive to the higher temperatures, or in the case of reactive extrusion.

The RTD is useful as a first instance, but it must be noted that it is an overall parameter, which does not give information about the residence time in the single elements. In fact, if on one hand higher residence times inside kneading blocks promote a more effective intensive mixing, on the other hand when the same occurs in a conveying element coalescence is no more balanced by the breakup of the PHBH nodules.

**Table 6.1** - RTD characteristic values for the simulations run without Cloisite.

	<b>PLA-PHB-1-400-2</b>	<b>PLA-PHB-2-400-2</b>	<b>PLA-PHB-3-400-2</b>
<b>Minimum value (s)</b>	36,01	22,03	26,15
<b>Average value (s)</b>	81,03	65,59	69,01
<b>Mid-peak width (s)</b>	40,77	47,69	44,12

Looking at the simulations run without Cloisite (Table 6.1 and Figure 6.1), it is possible to observe how the profile number 2 requires the shortest time in order to have the outflow from the die. This configuration, in fact, is characterized by only two sequences of restricting elements, with the one nearest to the die (distinctive of the profile) composed mainly of modules with staggering angles of  $30^\circ$  and  $60^\circ$ . For the same reason, also the mean time is the lowest that has been registered. The screw number 3 presents three kneading sections made of elements that are the same seen on the previous profile, but mounted with a different sequence and with the addition of a back-flow element. This leads to an increase of about 4 seconds of both the minimum and the average times. Finally, to process the blend with the screw configuration 1 the longest times are needed, likely because of the presence of two TME mixing elements, employed with the aim of getting a more effective dispersive mixing.

In this case, the width computed at half height is misleading, since this value do not take into account the “tails” at longer times of the RTDs, which have different shapes because different screws are employed. In fact, the profile 1 results in the broadest distribution, although the width at half height is the lowest, meaning that a certain percentage of the material spends very long times inside the extruder. The distributive mixing can be improved<sup>[27]</sup>, but there is also a greater chance for coalescence to occur. With the configurations 2 and 3 the “tails” are less pronounced, so the distribution is narrower. Then, the extensive mixing could be less effective, but it is possible to suppose that the greater  $RTD_{min}$  characteristic of the profile 3 can mitigate this drawback. At the same time, the coalescence phenomena should be reduced.

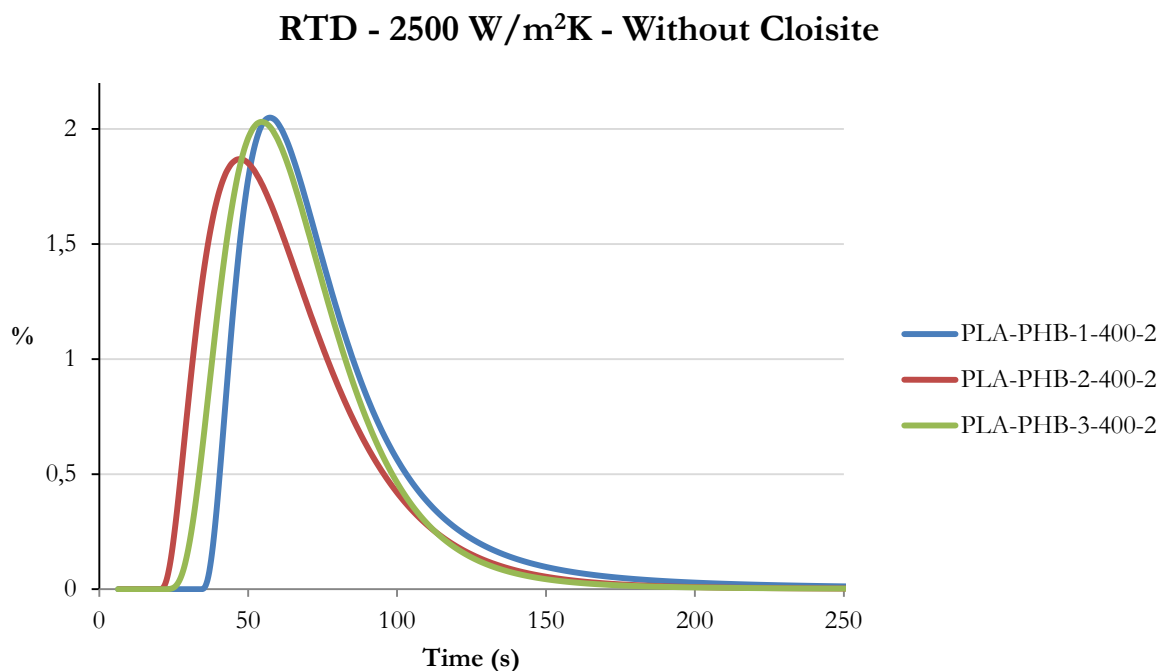


**Figure 6.1** - Residence Time Distribution plots for the simulations run in absence of the mineral filler.

It can be reasonably supposed that the 4 seconds of difference in minimum and mean residence times between the profiles 2 and 3 are fully spent in a restricting element, since the back-flow module is mounted right at the end of a kneading block. For what concerns the configuration 1, the major part of the same differences can be attributed to the presence of two mixing elements, whose disrupting effect on the axial flow is reflected also by the higher width of the correspondent RTD plot. Then, the odd-numbered profiles should lead to better morphologies

where the minor component is finely dispersed and well distributed in the matrix. The profile number 3 probably grants the best performances because it represents a good compromise between the need for high shear rates and long residence times in the restricting elements and the necessity of having a narrow peak. In fact, with the profile 1 a higher amount of the melt spends, if compared to the mean value, a longer time inside the extruder (not necessarily in a completely filled element) and so coalescence is more likely to occur without being balanced by an adequate breakup of the dispersed polymer nodules. To confirm the considerations reported above, a deepening on the residence time as a function of the axial position will be done in a further section of this chapter.

The RTD of those simulations run with the addition of Cloisite look in the same way as the ones where the filler is not added but, as already observed while analysing the DoEs, the characteristic values (Table 6.2) are about 1 s lower. This can be attributed to the slightly higher viscosity, which makes the transport more effective, as explained in section 5.2, coupled with the higher flow rate resulting from the addition of the clay. It is also possible to see how the peaks are a bit narrower, pointing out the effect of Cloisite, whose solid particles do not undergo deformation inside the barrel and force the motion of the melt in the direction of the die. A graphical comparison showing the consequence of adding a mineral filler is reported in Figure 6.2.

**Table 6.2** - RTD characteristic values for the simulations run with the addition of Cloisite.

	PLA-PHB-1-400- Cloisite-2	PLA-PHB-2-400- Cloisite-2	PLA-PHB-3-400- Cloisite-2
<b>Minimum value (s)</b>	35,04	21,52	25,51
<b>Average value (s)</b>	79,02	64,02	67,28
<b>Mid-peak width (s)</b>	40,01	46,63	43,09

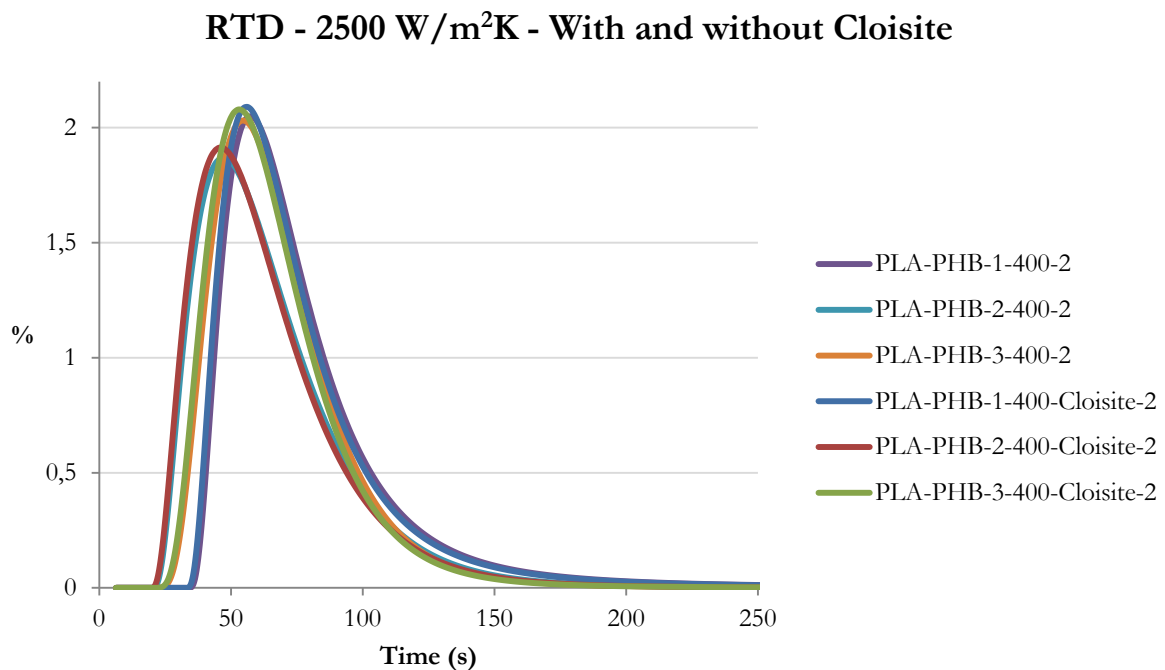


**Figure 6.2** - Comparison between the RTD plots of the simulations run in presence and in absence of Cloisite. It is possible to observe the superposition between the curves, that remarks the small difference existing between them.

## 6.2. Temperature

The temperature is the first quantity evaluated in this work as a function of the axial position. To correctly read the plots returned by Ludovic, it is important to point out that the  $x$ -axis reports the distance from the die, which is positive in the direction of the hopper and negative in the opposite direction. The origin of the reference frame is located at the interface between the barrel and the first element of the die.

The results of the simulations that do not involve the addition of Cloisite are reported in Figure 6.3. Since, according to what has been explained in section 4.2.5, melting is assumed to occur in the first restricting element, for all the screw profiles the temperature is computed as equal to  $168^{\circ}\text{C}$  (the  $T_m$  of PLA) in the conveying section prior to the first kneading block. Only when the polymers reach this last part of the screw the temperature raises and it worth noting that the plot describing that increase is the same whatever the profile is. In fact, the first sequence of kneading modules does not change, resulting in a superposition of the curves referred to the configurations 1 and 3, while in the case of the profile number 2 it can be observed a shift towards the left because the first conveying section is 30 mm longer. The temperature raise is explained through the dissipation of mechanical energy, that is more intense where the shear rate is higher. Contemporarily, a decrease of the viscosity is expected due to the combined effect of  $T$  and  $\dot{\gamma}$ .

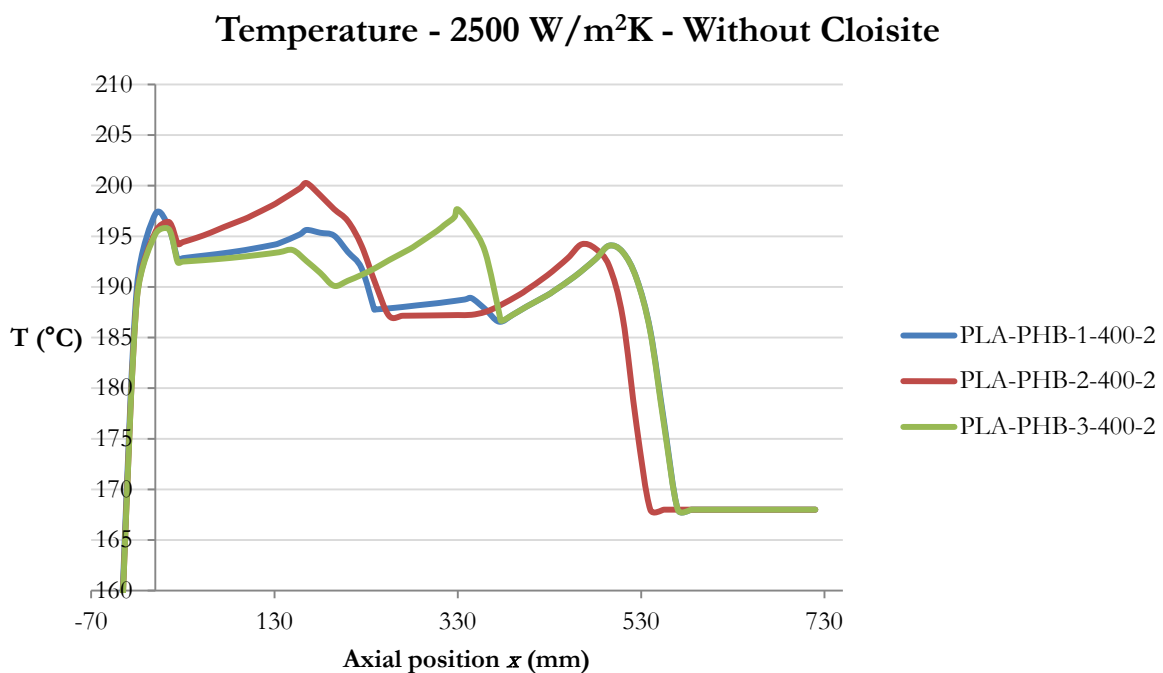


**Figure 6.3** - Temperature plots for the simulations that do not involve the addition of Cloisite.

After the first kneading block the plots are significantly different, so they will be analysed separately. In particular, with the profile number 1 it is possible to observe that the melt cools down in the transport section that precedes the second sequence of kneading elements (which starts at  $x=375$  mm), where another slight increase can be observed. A final raise, that follows a substantial isothermal plateau, can be noted in the TME mixing section ( $x=225$  mm), characterised by high shear rates. For what concerns the second profile it is possible to observe that once the melt has passed the first kneading block, it cools down until it almost reaches the temperature imposed by the heating elements of the barrel ( $187^{\circ}\text{C}$ ) and forms an isothermal

plateau. After this plateau, a long kneading section raises the temperature to the highest value computed for all the three simulations, prior to a cooling that occurs before entering in the die. Finally, with the profile 3 the maximum temperature is reached in correspondence of the second kneading section ( $x=375$  mm), thanks to the presence of the back-flow element. This last assumption is confirmed by looking at the last sequence of restricting elements ( $x=195$  mm), where the increase is lower although the staggering angle is greater.

Inside the die, the temperature follows practically the same trend for all the profiles, since this part does not change for all the simulations and the inflow has substantially the same temperature in all the cases. This happens because in the last conveying section the temperature drops closer to the values imposed by the thermoregulation system. In correspondence of  $x=-22$  mm the temperature is equal to  $185^{\circ}\text{C}$ , the same value measured with a thermocouple mounted on the first element of the die in the apparatus employed in laboratory. This element is 20 mm long, demonstrating a good accordance between the model and the reality.

Looking at those simulations that involve the addition of Cloisite (Figure 6.4) and comparing them with the simulations analysed above (Figure 6.5), it is possible to observe how before the addition of the clay the plots do not change. In fact, the filler enters in the barrel only after the first kneading block, which is employed to melt the polymers, so in the part of the apparatus nearer to the hopper the working conditions (materials, flow rate, screw speed) are exactly the same, both with and without the filler. When the clay ( $T=25^{\circ}\text{C}$ ) enters the extruder, it causes a drop of the temperature that is more pronounced for the profiles 1 and 3. It can be explained as an effect of the longer transport section, if compared to the one of the profile 2, that lays between the end of the first kneading sequence and the point where the filler is added. Then, the melt has more time to cool down.

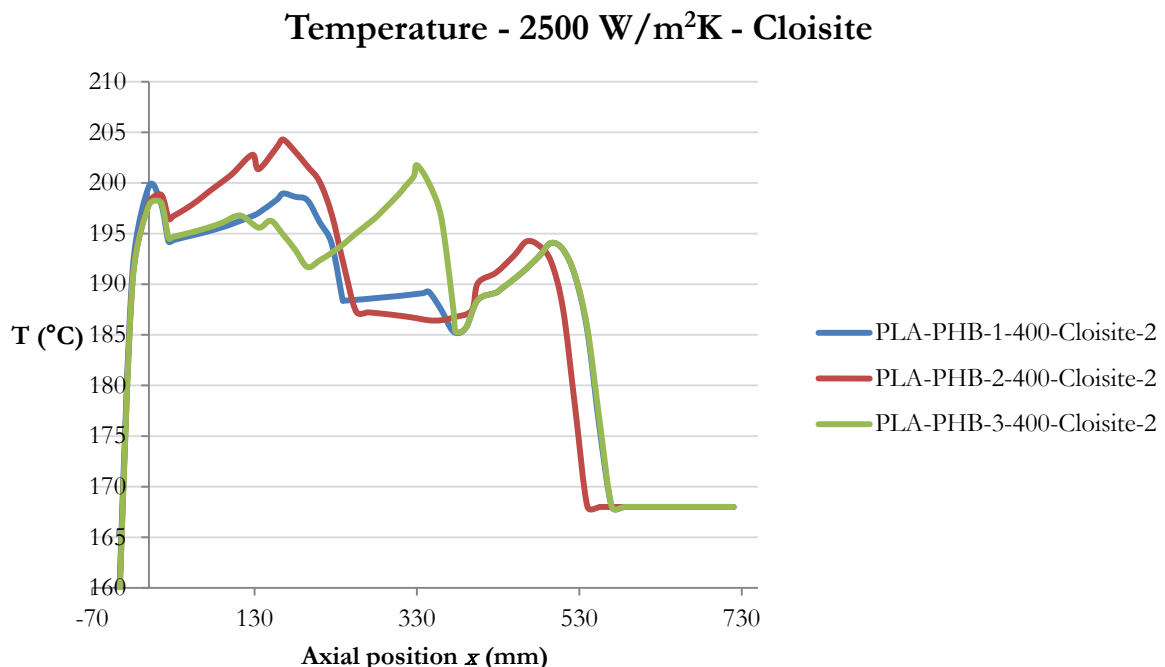


**Figure 6.4** - Temperature plots for the simulations that involve the addition of Cloisite.

After the insertion of the filler ( $x=405$  mm) the plots are significantly different so, also in this case, they will be analysed separately. In particular, with the profile 1 a considerable increase of  $T$  is reported in the two mixing elements, but practically no differences can be observed in the

kneading section. Here ( $x=375$  mm) the temperatures are substantially the same computed without the inclusion of Cloisite. For what concerns the screw configuration 2, it is possible to see how the raise in the second long kneading section ( $x=225$  mm) is more pronounced when the filler is added. This seems in contrast with what has just been reported for the same situation when the profile 1 is employed. Probably, this different behaviour is linked to a difference of residence time, so this topic has to be deepened in the following section. However, the assumption seems confirmed by what happens with the profile number 3, where a significant temperature increase is observed in the second kneading block ( $x=375$  mm), thanks to the presence of a back-flow module, while in the last kneading section the temperature increase is substantially equal to the same one reported for the simulations in which Cloisite is not employed. In fact, from  $x=195$  mm the plots run substantially parallel, meaning that the temperature raise is the same, despite the presence of the clay. Since this last kneading section is made of three 15 mm-long elements with a staggering angle of  $60^\circ$  (so it is similar to the kneading section of the profile 1), it is possible to conclude that after the addition of a mineral filler the temperature increase due to the mechanical energy dissipation is relevant only in case of an adequate residence time.

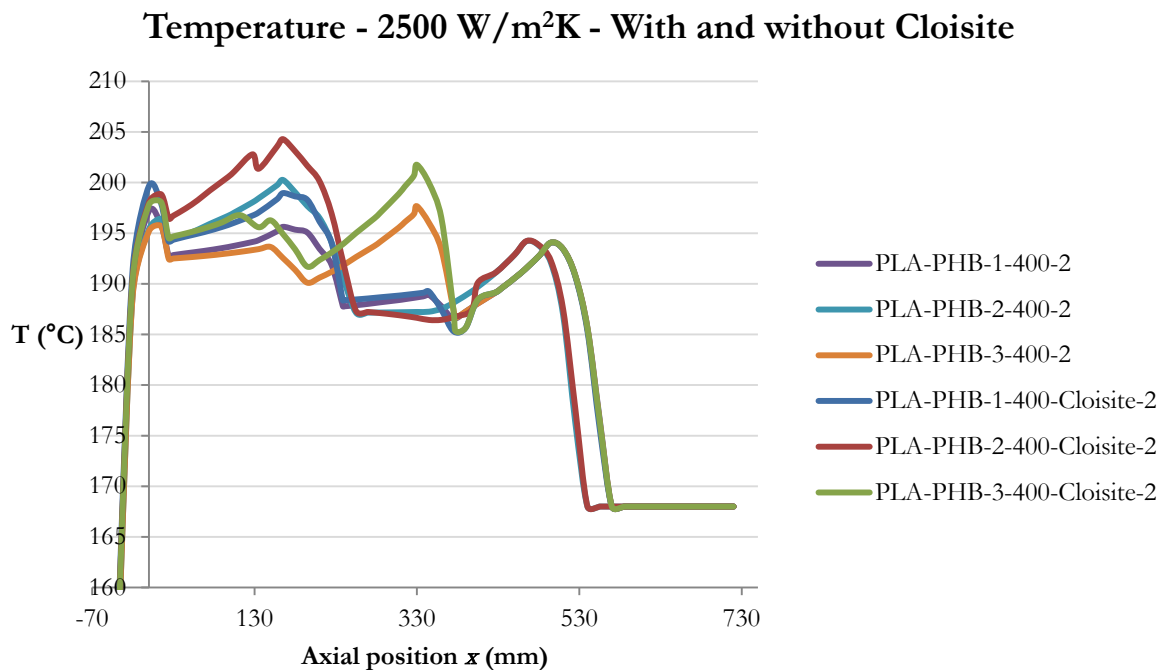


**Figure 6.5** - Comparison between the temperature plots of all the simulations.

In general, the profile number 2 provides the lowest temperatures in the middle of the extruder since no restricting elements are located in this part of the screw, while near the die  $T$  reaches the maximum value registered for all the simulations. On the other hand, with the odd-numbered configurations the changes in temperature are less intense, although with the profile 3 a consistent raise is observed just after the opening that allows the addition of the clay. This raise (observed also with the profile 1, but less significant) could have beneficial effects on the final morphology of the blend. In fact, the concurrent decrease of viscosity helps the distributive mixing of the filler<sup>[37]</sup>, which is exfoliated at the same time thanks to the elongational flow provided by the kneading discs.

### 6.3. Local and Total Residence Times

The Local Residence Time (LRT) in a particular element is measured by Ludovic in s/m, that is the time needed by the melt to pass through a 1 m-long element of the same type. So, the lower the value is, the faster the melt moves along the screw.

In all the simulations in which Cloisite is not added (Figure 6.6), it is possible to observe that the LRT depends only on the type of element that is considered, since the materials in the melt are the same and so they are also the rotation speed and the feed rate. In particular, the lowest values are reached in the conveying elements, while the highest one is provided by the mixing modules. For what concerns the transport segments, it worth noting that a difference of about 3 s/m is computed between the elements with a pitch of 20 mm (higher LRT) and the same ones where this value is equal to 30 mm. This reflects the current knowledge about polymers processing: in fact, screws with a shorter pitch grant a more effective transport, but they also result in a higher residence time. Unfortunately, the above-mentioned difference is quite hard to be seen in the plots because it is too small, so it comes from an analysis of the numerical results returned by the software.

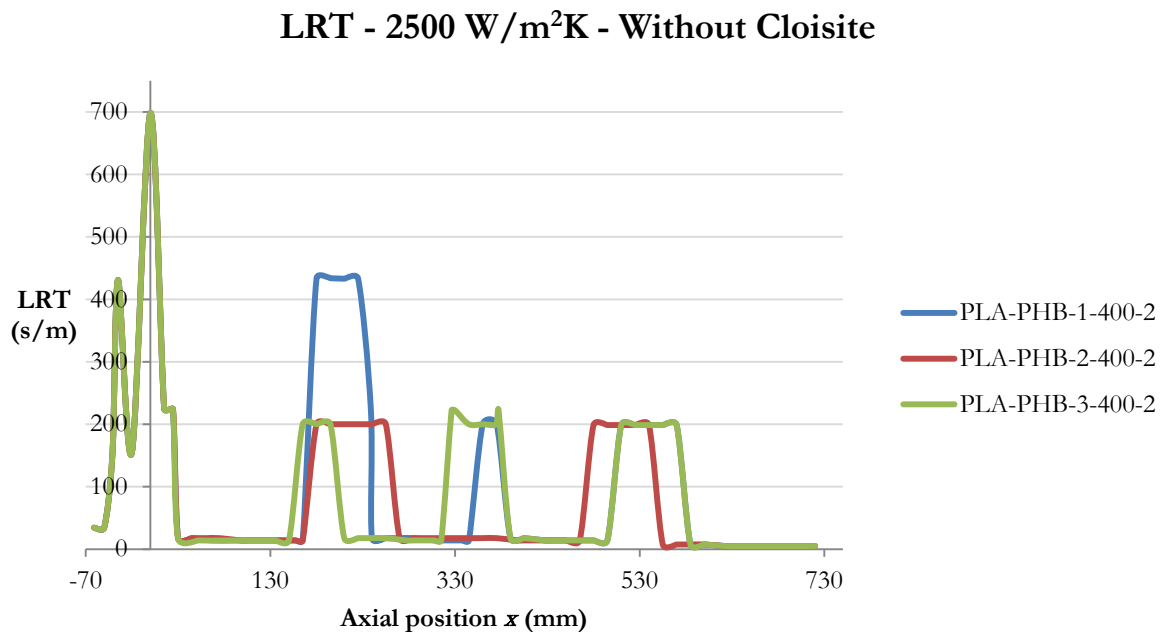


**Figure 6.6** - Local Residence Time as a function of the axial position for those simulation which do not involve the addition of Cloisite.

After a numerical analysis it is also possible to point out how the time spent by the melt in a kneading block does not depend on its staggering angle. Then, the returned value (200 s/m) is always the same and this is a consequence of the strategy employed by the software to compute the LRT. In fact, as reported by eq. (4.27), this parameter depends only on the free volume and the flow rate, that are both constant in all the lobed modules. In particular, the free volume is the same whatever the shift angle is, because the discs are geometrically identical, although they are arranged in a different way.

The reverse element on the profile number 3 raises the LRT to 222 s/m and causes an equal increase upstream the second kneading section. This last phenomenon can be reasonably

attributed to an accumulation of the melt in the part of the screw that precedes the sequence of lobed elements, confirming the action of the back-flow module in extending the residence time.

Finally, the highest LRT (434 s/m) is registered in correspondence of the TME mixing elements mounted on the profile 1, due to their effect of re-orientation of the flow along directions that are not the axial one. This result seems also to confirm the assumptions, made during the analysis of the RTD plots, concerning the longer times spent by the melt inside an extruder equipped with this particular screw configuration.

The addition of Cloisite (Figure 6.7) does not modify the residence time in the conveying elements, but results in a reduction of the LRT in those sections which restrict the flow. In particular, the computed values are 192, 214 and 418 s/m in the kneading, back-flow and TME modules, respectively. This behaviour confirms what has been reported in the RTD analysis (section 6.1): in that case the explanation was found in the higher viscosity and flow rate consequent to the inclusion of the filler. It was also suggested that the platelets of the clay, which do not melt at the operating temperatures, force the melt to move in the direction of the die. In the first kneading blocks of all the screw configurations the residence time does not vary (200 s/m), because Cloisite is added downstream and the operating conditions are the same of the simulations that do not involve the addition of the filler.

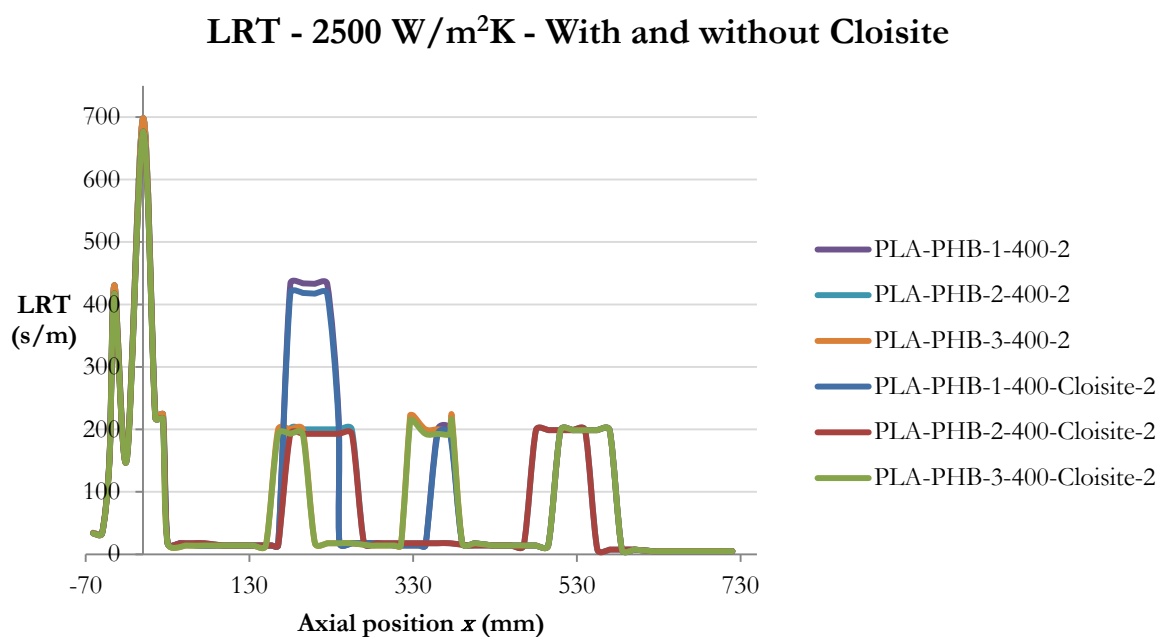


**Figure 6.7** – Comparison of the Local Residence Time as a function of the axial position for the simulations run in presence and in absence of the mineral filler.

The Total Residence Time (TRT), measured in seconds, describes how much time is spent by the melt inside the extruder, starting from the moment in which the solid polymer pellets are introduced inside the apparatus. This quantity is plotted as a function of the axial coordinate, so it is possible to analyse the contribution of each section of the screw. Since not all the melt exits from the die at the same time, as shown by the Residence Time Distributions, the TRT describes the evolution of the average values.

Looking at the plots of Figure 6.8, it is possible to see how, also in this case, the portions of the curves describing what happens in the first kneading sections, that are equal for all the profiles, are exactly the same. In particular, the ones referred to the configurations 1 and 3 are

superimposed, while with the profile 2 a shift through the left is observed, since the initial conveying section is 30 mm longer. In all the cases (also when the clay is added), the crossing of the first sequence of restricting elements takes about 17 s. Downstream this first kneading section significant differences can be noted, so the plots will be described separately from this point ( $x=405$  mm) on.

For what concerns the screw profile 1, it can be observed that the time spent inside the TME mixing element constitutes almost a half (30 s) of the Total Residence Time inside the barrel, while only 7 seconds are needed by the melt to cross the two kneading elements at  $x=375$  mm. The plot referred to the configuration 2 shows that the only significant increase is observed in the long kneading sequence that precedes the die, which causes the TRT to raise of 19 s. Comparing this last curve with the same one describing the Total Residence Time when the profile number 3 is employed, it becomes apparent the significant action of the reverse element. In fact, the sequence of three kneading modules followed by a back-flow one is able to raise the TRT of 13 s, more than a half of the increase provoked by the six kneading blocks mounted on the screw number 2.

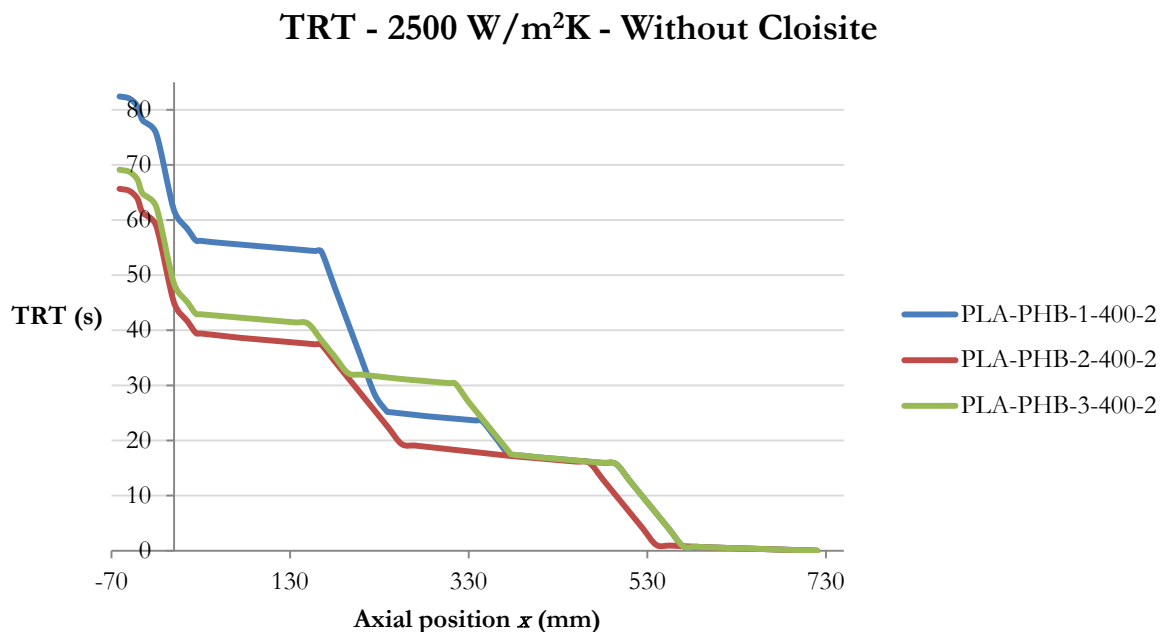


**Figure 6.8** - Total Residence Time as a function of the axial coordinate. The computation do not involve the inclusion of Cloisite.

As observed in the analysis of the LRT, also the Total Residence Times of the simulations that involve the inclusion of Cloisite are slightly lower for the same reasons explained above. The resulting plots (Figure 6.9) show that the trends are the same described previously.

Inside the die it is possible to observe how the plots of LRT and TRT are superimposed, since this part of the extruder does not change for all the simulations. Both the curves show that the melt spends some time (6 s, as quantified from the data of Total Residence Time) in the 30 mm of the barrel which precede the interface with the die. Then, it is possible to suppose a certain recirculation in this part of the apparatus, because there is a substantial difference between the cross-sections of barrel and die. Moreover, it can be also observed how the cooling of the molten polymers results in an increase of the Residence Times (Local and Total), due to the progressively higher viscosity which hinders the flow.

The LRT and TRT point out that with the odd-numbered profiles the melt spends a longer time inside the kneading or mixing elements. It means that these screw configurations should lead to better final morphologies, especially if compared with the ones returned by the profile number 2. In fact, in this last case the development of that morphology is totally demanded to only one long sequence of six kneading modules, while with the other configurations the same action is carried out by two sequences that are shorter, but characterised by a better spatial arrangement along the screw. Reducing the length of the conveying sections through the insertion of some restricting elements, indeed, can significantly reduce the size of the dispersed phase, since it has less time to coalesce. Moreover, an uniform distribution of the kneading or mixing elements increases the mean temperature of the melt, reducing in this way its viscosity and then helping the distribution of the clay when it is necessary to add Cloisite.

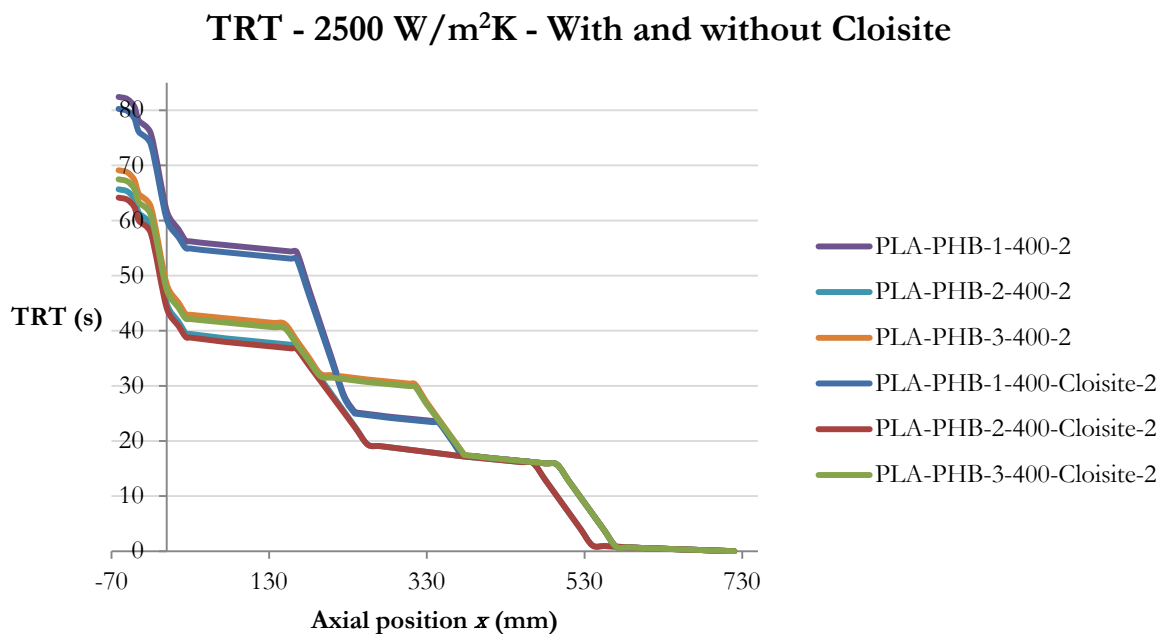


**Figure 6.9** - Comparison between the Total Residence Times of all the simulations.

#### 6.4. Shear rate

As explained in section 5.4, the shear rate depends on the geometrical parameters of the screw elements and on the rotation speed, quantities that Ludovic employs to calculate  $\dot{\gamma}_0$  according to eq. (5.1). This starting value is tuned taking into account the computed local velocity field but, as seen while analysing the DoEs, the final results do not differ significantly. It means that, once the screw speed is set, only the shape of the element is decisive to determine  $\dot{\gamma}$ . The last conclusion is confirmed by the plots returned by the software after the computation (Figure 6.10). In fact, for a same screw profile, no differences can be observed after the addition of Cloisite in both the graphical and the analytical results. Moreover, a certain type of module always provides the same shear rate, regardless of the profile number. Then,  $\dot{\gamma}$  will be analysed by looking at the peculiarities of the single elements and not of the entire profiles.

The lowest shear rate ( $133 \text{ s}^{-1}$ ) is provided by the conveying segments, practically the half of the contribution ( $263 \text{ s}^{-1}$ ) of the back-flow module. When the melt enters the TME elements mounted on the profile 1,  $\dot{\gamma}$  rapidly increases to  $236 \text{ s}^{-1}$ , while inside the kneading blocks a strange behaviour can be observed. In fact, according to the literature, higher staggering angles correspond to higher shear rates but, as it is possible to observe in the plots, it does not result in

the results of the simulations, which return a constant value of  $255 \text{ s}^{-1}$  in those sectors. Unfortunately, the manual of the software does not help to come to a valid conclusion, so a possible explanation has been found in the book of Hepperle *et al.*<sup>[14]</sup>, where it is reported that the highest value of  $\dot{\gamma}$  is registered in the tip area of each disc. Assuming that the shear rate computed in this particular zone has a significant influence on the final value reported in the  $f(x)$  plot, it is possible to justify the results. In fact, the discs which constitute the kneading blocks have the same shape, and so it is also possible to expect the same values of shear rate in the tip areas, regardless of the staggering angle.

Independently on the accuracy of the last supposition, the various plots show clearly how there is not a substantial difference in terms of shear rate between the different restricting elements. Then, when it is necessary to choose the types of segments that have to be used in order to get the best final morphology, mainly the Residence Times and the temperature profiles, rather than the shear rate, have to be exploited to guide the selection.

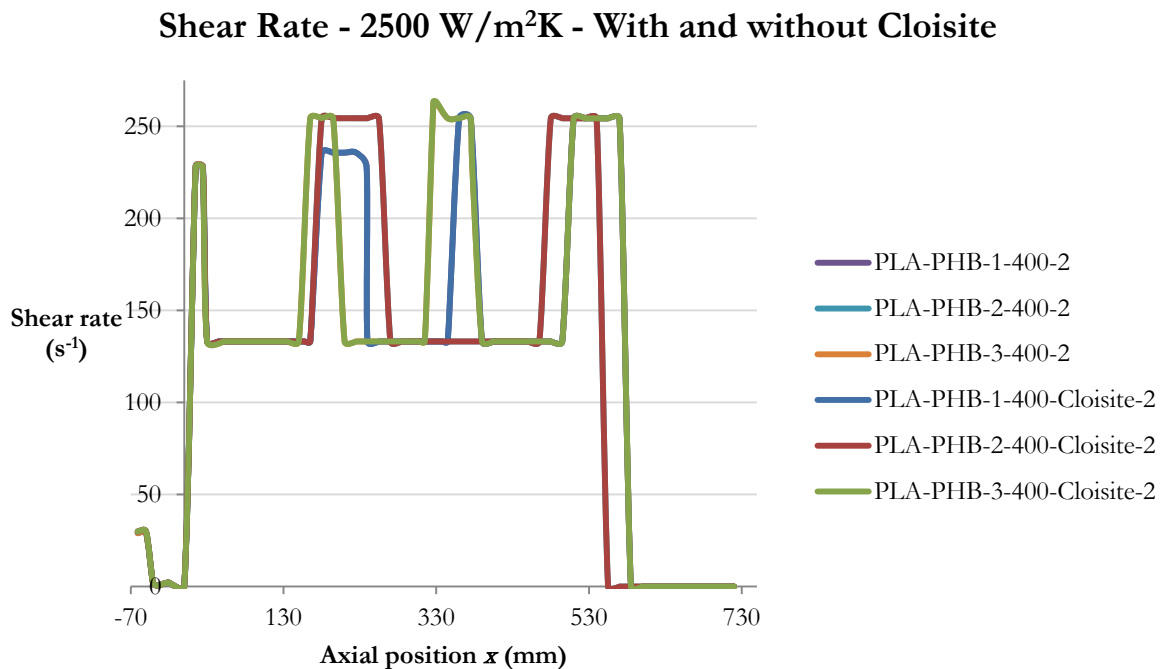


**Figure 6.10** - Shear rate as function of the axial position for all the simulations. The plots referred to a same screw are superimposed, since the addition of Cloisite has no impact on the shear rate.

The raise of  $\dot{\gamma}$  observed in the 30 mm which precede the barrel-die interface can be explained as a consequence of the smaller section of the die elements. It causes an increase of the local shear stresses undergone by the melt in this part of the extruder.

### 6.5. Viscosity

The last quantity returned by the simulations as a function of the axial coordinate is the viscosity, calculated, as explained in chapter 4, with a linear mixing law. The viscosity is a key parameter in the determination of the final morphology, since the arrangement of the minor component inside the matrix strongly depends on the ratio of  $\eta_{PHBH}$  and  $\eta_{PLA}$ , while low  $\eta_{melt}$  make the dispersion of a mineral filler more effective. Moreover, the  $f(x)$  diagrams showing the variations of the viscosity allow to confirm most of the hypothesis made in the previous paragraphs.

Since the materials and the operating conditions in the first kneading sequence are the same for all the simulations, also for the ones involving the addition of Cloisite, the initial portions of the curves coincide, so they are analysed only once. In particular, it is possible to observe that as long as the solid pellets of the polymers do not reach the first restricting element, Ludovic returns a viscosity equal to 0 Pa·s. Then, at  $x=585$  mm ( $x=555$  mm for the profile 2)  $\eta_{melt}$  starts to raise until the value of 210 Pa·s is reached in correspondence of the first kneading block of the sequence. From this point on, the melt becomes more and more fluid and  $\eta_{melt}$  in the outflow is reduced by almost one-quarter.

In those simulations run without adding Cloisite (Figure 6.11), once the melt exits from the first sequence of restricting elements, the viscosity raises in the subsequent conveying blocks in parallel to the cooling of the melt during transport. Employing the screw profile 1, it is possible to observe how the two kneading modules at  $x=375$  mm decrease  $\eta_{melt}$  to 152 Pa·s and then, in the following conveying segments, it raises to 175 Pa·s. This last value is slightly lower than what was computed upstream the lobed elements (190 Pa·s), because the temperature provided by the thermoregulation system progressively increase while moving towards the die. In the transport section prior to the mixing blocks, the viscosity is almost constant and when the melt passes through the TME modules it decreases again to 150 Pa·s. This value does not substantially vary in the last portion of the screw, although it is composed by transport segments, because there the heating elements are set in order to maintain the highest temperature (190°C). Similar trends, but more pronounced, are observed analysing the plot referred to the configuration number 3. In fact, the action of the back-flow element causes a significant drop of the viscosity to 125 Pa·s, followed by a slow increase in the subsequent conveying section. The last two kneading blocks provoke a reduction of  $\eta_{melt}$  that is more significant if compared to the effect of the TME modules. In the 150 mm which precede the die, the plots referred to the odd-numbered profiles are substantially superimposed.

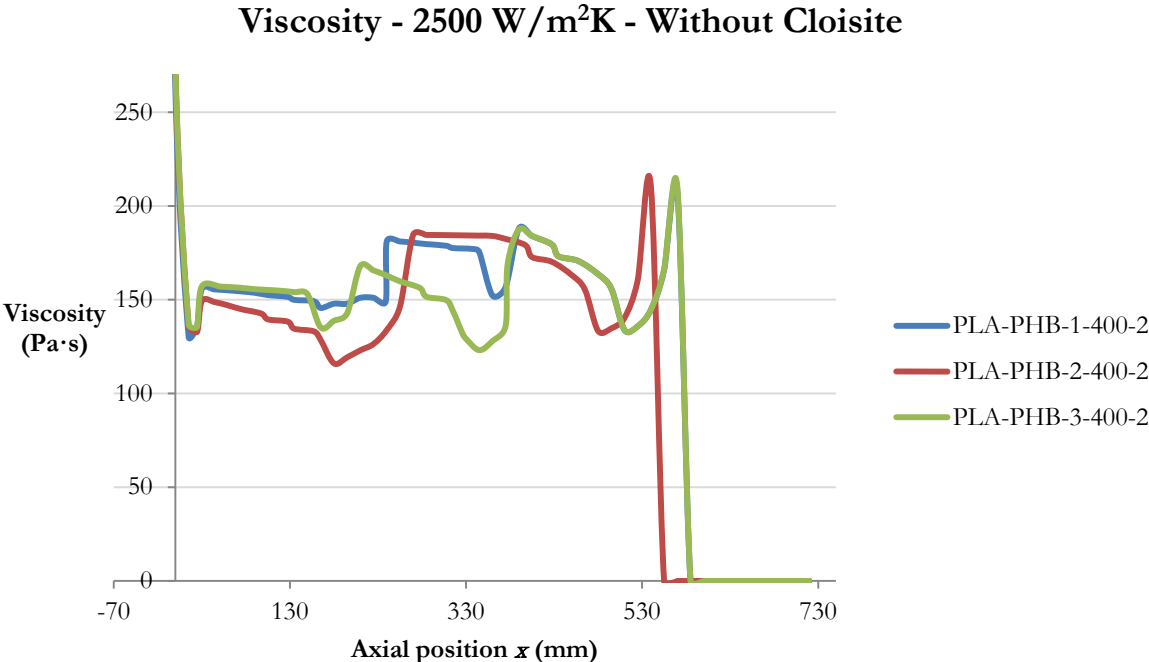


**Figure 6.11** - Viscosity as a function of the axial position for the simulations run in absence of the mineral filler.

For what concerns the profile 2, it can be seen that after the first kneading section the viscosity increases, at first rapidly and then more slowly, until the value of 180 Pa·s is reached. Then, it practically does not change until the melt enters the second sequence of lobed elements, where  $\eta_{melt}$  progressively drops to 120 Pa·s, the lowest value computed for all the simulations. Another slow increase is observed prior to the die.

After the addition of Cloisite at  $x=405$  mm the viscosity raises to 280 Pa·s (270 Pa·s with the profile 2) because the filler enters in the barrel at room temperature. According to the law of Krieger-Dougherty, the addition of the clay results in a general increase of  $\eta_{melt}$  and the plots appear “stretched”, not simply shifted. It means that if on one hand the viscosity of the melt in the conveying segments is 50-70 Pa·s higher if compared to the simulations run in absence of Cloisite, on the other one the increase of the minimum values is smaller. This behaviour can be explained one more time in terms of dissipated mechanical energy, which is higher for higher viscosities. Then, the temperature increases more, so  $\eta_{melt}$  undergoes a more pronounced reduction.

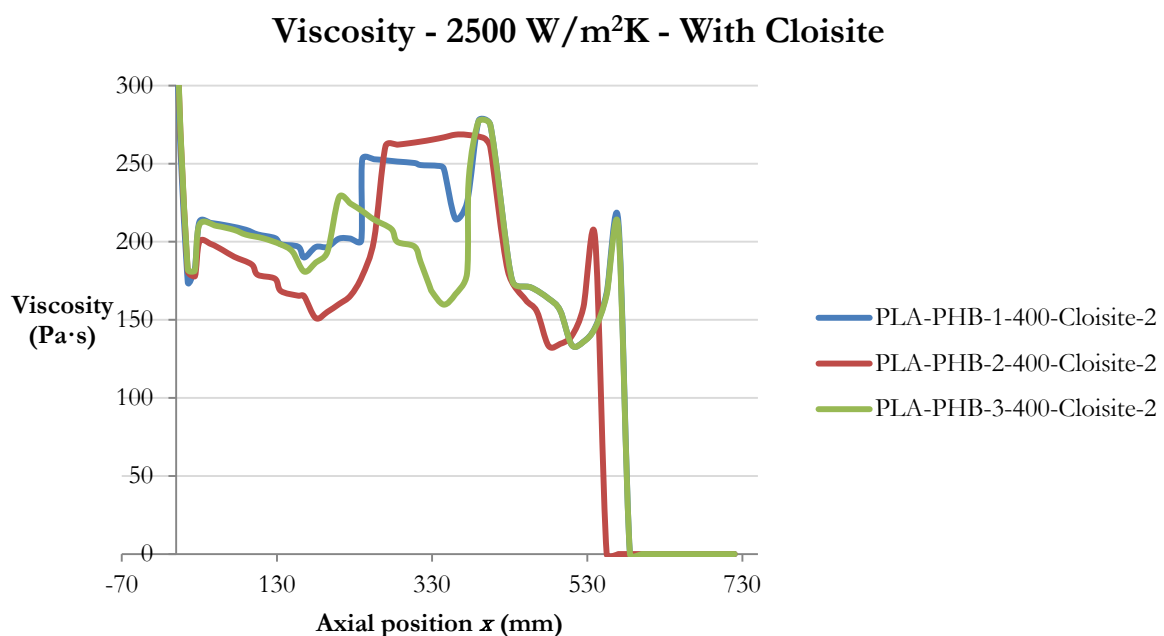


**Figure 6.12** - Viscosity as a function of the distance from the barrel-die interface for those simulations involving the addition of the clay.

Since the temperature profiles in the die follow the same path also when different screw configurations are employed, the viscosity raises sharply in this last part of the apparatus and the plots are superimposed. As predictable, slightly higher values of  $\eta_{melt}$  are attained when the clay is added.

The viscosity  $f(x)$  diagrams confirm the suppositions made in the previous sections about the higher effectiveness of the odd-numbered profile in the development of a satisfying morphology. In fact, for what concerns the simulations run in absence of Cloisite, Figure 6.11 shows how the resulting plots lay between the maximum and the minimum values computed when the configuration 2 is employed. Then, using the screw profiles 1 and 3 the viscosity variations are less significant. In contrast, the last long kneading segment of the screw number 2 lowers  $\eta_{melt}$  at a level for which coalescence is more likely to occur in the following conveying section. To prevent this last phenomenon, the distribution of the restricting elements in a higher number of

shorter sectors (as it happens in the odd-numbered profiles, if compared to the configuration 2) should have beneficial effects. In this way, in fact, the viscosity decreases less drastically, helping to reduce coalescence, while the different spatial distribution of those blocks along the axis leads to a constant size reduction of the PHBH domains.

The odd-numbered profiles, especially the number 3, should lead to better morphologies also when the clay is added. In fact, when Cloisite enters at room temperature inside the extruder, it provokes a sudden temperature decrease and a consequent viscosity increase that makes the dispersion more difficult (see Figure 6.12). With the configurations 1 and 3, the kneading elements next to the hole from which the clay is added lower the viscosity just after the filler enters in the melt. This reduction is more consistent with the profile 3, thanks to the presence of the back-flow element. Subsequently,  $\eta_{melt}$  is constantly kept about in the middle of the range defined by the minimum and maximum values computed with the configuration 2. Then, the screw number 3 represents the best compromise between the necessity of a low viscosity, which helps the dispersion of Cloisite, and the contemporary need for high values of the same quantity in order to counteract coalescence.

### 6.6. Application of Vergnes and Delamare's model to this case study

The model proposed by Vergnes and Delamare was originally employed, with a discrete success<sup>[5]</sup>, using a HDPE/ethylene-ethyl acrylate-maleic anhydride monodisperse blend. In that case, the starting point of the calculation was the data set returned by Ludovic after the simulation of the compounding operations and a good accordance between the computed results and the real case has been found. Then, in this section it will be tried to do the same using the PLA/PHBH blend, with the aim of confirming the conclusions, reported in the previous section of this chapter, about the choice of the screw profile which leads to the best performances in terms of final morphology.

In this work, the model is applied to the bio-based blend considering the system as monodispersed, in order to simplify the calculation. This condition is absolutely not linked to the reality, where the dispersed phase builds up an arrangement of domains with very different sizes. Moreover, due to some approximations done by Vergnes and Delamare (like the use of laws developed to describe the behaviour of Newtonian fluids), it is quite unlikely to have the exact description of the final blend morphology, even in the polydisperse case. Then, the main objective is to simply investigate the resulting trends, with the aim of choosing the screw profile that grants the best performances.

Before starting with the analysis of the results, it is very important to provide some information about the methodology that has been employed. In particular, the calculation of the capillary number  $Ca$ , according to eq. (3.12), requires the knowledge of  $\eta_{PLA}$  as a function of the axial coordinate, of the interfacial tension  $\Gamma_{12}$  and of the particle size  $D_d$  (at least its initial value).

For what concerns  $\eta_{PLA}$ , it has been simulated employing the same settings already used for the blend. The only difference can be found in the composition of the melt, completely constituted of polylactide, eventually with the addition of a 5 wt. % Cloisite if required. This approach has been employed also to compute  $\eta_{PHBH}$ , necessary to derive the viscosity ratio. It is assumed that the clay, after its addition, can be found in the bulk of both the major and the minor phases.

The interfacial tension between the two components of the melt has been calculated with the equation proposed by Mofokeng *et al.*<sup>[38]</sup>:

$$\Gamma_{12} = \Gamma_1 + \Gamma_2 - \sqrt{\Gamma_1^d \cdot \Gamma_2^d + \Gamma_1^p \cdot \Gamma_2^p} \quad (6.1)$$

with  $\Gamma_1$  and  $\Gamma_2$  total surface energies,  $\Gamma_1^d$  and  $\Gamma_2^d$  their dispersive components,  $\Gamma_1^p$  and  $\Gamma_2^p$  the polar ones. In the aforementioned study, it is possible to find these values (reported in Table 6.3) for what concerns PLA and PHBV, while in the current literature there is no information about the surface energies of PHBH. Then, considering the similarities in the chemical structure of the two PHA-based copolymers, it has been decided to employ the surface energy of PHBV and its components to describe also PHBH, obviously being aware of the possible consequences of this assumption on the accuracy of the results.

**Table 6.3** – Surface energies of PLA and PHBV as reported by Mofokeng<sup>[38]</sup>. All the values are expressed in mN/m.

	$\Gamma$	$\Gamma^d$	$\Gamma^p$
<b>PLA</b>	62,0	41,8	20,2
<b>PHBV (PHBH)</b>	56,3	41,7	14,6

According to eq. (6.1) and to the data reported in Table 6.3,  $\Gamma_{12}$  for the PLA/PHBH melt is equal to 73,2 mN/m. The initial diameter of the dispersed nodules  $D_d$  has been set to 1  $\mu\text{m}$ , as suggested by Vergnes and Delamare<sup>[5]</sup>.

Having defined these important parameters, it is now possible to describe how the evolution of the morphology has been computed using MS Excel. As explained before, the calculation of the capillary number as a function of the axial position is done using eq. (3.12), in which  $\Gamma_{12}$  is constant, while  $\eta_{PLA}$  and  $\dot{\gamma}$  vary along the screw. Then, these last two parameters are determined through simulations run by Ludovic. The value of  $Ca_{critical}$  has been derived from the plot reported by Grace<sup>[10]</sup>, where the critical capillary number is represented as a function of the viscosity ratio. Since the flow inside the apparatus is mainly extensional and since the viscosity ratio is equal to 1,7/1,8 in the whole barrel whatever the screw profile is,  $Ca_{critical}$  has been evaluated as equal to 0,1.

Comparing the computed values of  $Ca$  with  $Ca_{critical}$ , it can be observed that the ratio between these two parameters is lower than 2, except for few cases just after the polymers enter in the first kneading section. It means that the breakup originates two sister droplets with half of the original volume and that  $t_b$  can be determined according to eq. (3.15). To evaluate the dimensionless time, needed to compute the real time for this breakup, the plots proposed by Grace<sup>[10]</sup> have been employed again and, for a viscosity ratio of 1,7/1,8,  $t_b^*$  is equal to 0,10. It is then possible to compute  $t_b$  in each portion of the barrel as previously done with  $Ca$ . The local residence time  $t_{loc}$  along the  $x$ -axis, expressed in s and not in s/m, is necessary for a comparison with the breakup time, because this phenomenon occurs only if the particles spend a sufficient time in the portions of the extruder where the proper conditions exist. In particular,  $t_{loc}$  has been calculated by multiplying the LRT, computed by Ludovic as a function of the axial coordinate, for the length of each segment. Definitely, breakup occurs when  $Ca/Ca_{critical}$  is higher than 1 and contemporarily  $t_b$  is lower than  $t_{loc}$ .

To compute the probability of collision only quantities that have been already employed are required, so it has been simply applied the equation (3.18). Since the viscosity ratio is next to 1, the interface is partially mobile, so  $P_{exp}$  is evaluated by means of eq. (3.20) and  $b^*$  is computed through the eq. (3.22). In both the cases, the radius  $R$  is progressively assumed as equal to the value derived in the section of the barrel which lays just upstream the one that is considered. The probability of coalescence  $P_{coal}$  is obtained by multiplying  $P_{col}$  and  $P_{exp}$  and it is employed in the

relationship that allows to define the new particle size after coalescence (3.23). It is now possible to explain how the evolution of the morphology is computed.

The “IF” function of MS Excel is employed in this way:

- When the conditions for the breakup exist, a nodule originates two spherical sister droplets, whose radius is computed on the basis of volume conservation. The result is then multiplied for the expression which considers the effect of coalescence. The process can be resumed by the following equation:

$$R_n = R_{n-1}(2 - P_{coal})^{-\frac{1}{3}} \quad (6.2)$$

- If the requirement for the breakup are not met, only coalescence takes place and  $R_n$  is computed through eq. (3.23).

The computation process took place for the different profiles only in that part of the apparatus where the polymers are in the molten state, so in the portion which lays between the first kneading block and the die. In fact, it has been assumed that the cooling “freezes” the morphology in the last part of the extruder, while in the first conveying section (where the polymers is, at least partially, in the form of solid pellets) Ludovic does not provide some parameters which are useful for the calculation, like the viscosity.

Analysing the plots referred to the evolution of the droplet radius when the filler is not added (Figure 6.13), it is possible to observe how  $R$  correctly decreases in the same way for all the first kneading sequences of all the profiles.

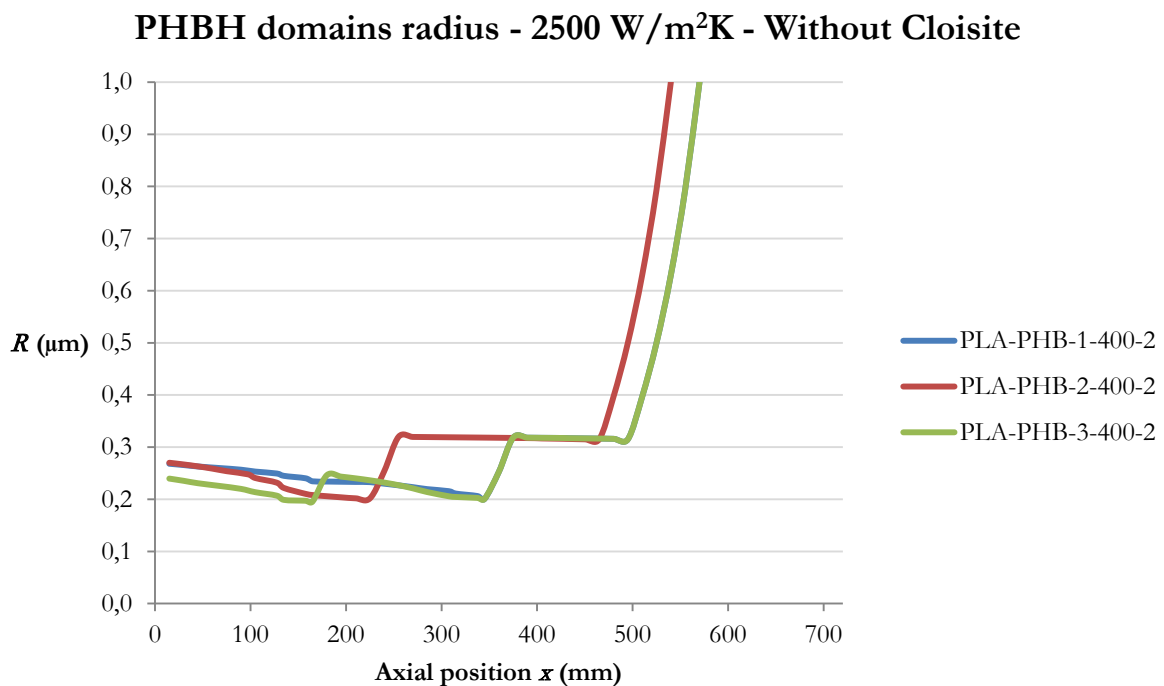


**Figure 6.13** - Radius of the PHBH domains as a function of the axial position in absence of Cloisite.

Looking at the curves concerning the screw configuration 1, it can be seen how, according to the model, only the second kneading section takes an active part in the size reduction, while the same cannot be said for the TME blocks. Regarding to the profile 2, the second kneading sequence causes a significant decrease of the radius, followed by a moderate increase in the conveying

modules prior to the die. As expected, the best performances are granted by the configuration number 3, which includes a back-flow module. The consequence is a reduction of  $R$  practically equal to the one observed in the long kneading block of the profile number 2, although in this case only the half of the elements is used. This consistent drop is followed by an increase of the particle size that is compensated by the action of a further kneading sequence just before the melt enters the die. Then, the model confirms that the best dispersion of PHBH is got with this last profile.

In general, the above analysis confirms the substantial effectiveness of the model, since, as reported by Vergnes and Delamare, the breakup must occur in a restricting element, while coalescence always takes place. This can be observed under another point of view in Figure 6.14, where the plots assume values greater than 1 in only in correspondence of the kneading sections. It is important to point out that the ratio between the capillary numbers is the only condition which determines the breakup, since in the present case study the time for breaking  $t_b$  is always significantly lower than  $t_{loc}$ . According to the results, when the profile number 2 is employed, less than a half of the second lobed sequence effectively reduces the particle size, because at  $x=240$  mm the ratio drops under the dashed line. The plot related to the screw configuration 1 can somehow explain why the TME elements seem not to have an effectiveness in the decrease of  $R$ . In fact, at about  $x=200$  mm the ratio is just under the unity but, considering all the assumptions made while setting up the model, it is quite likely that in the real process  $Ca/Ca_{critical}$  in correspondence of the mixing modules is higher than 1. This means that also these last elements have an active part in the size reduction.

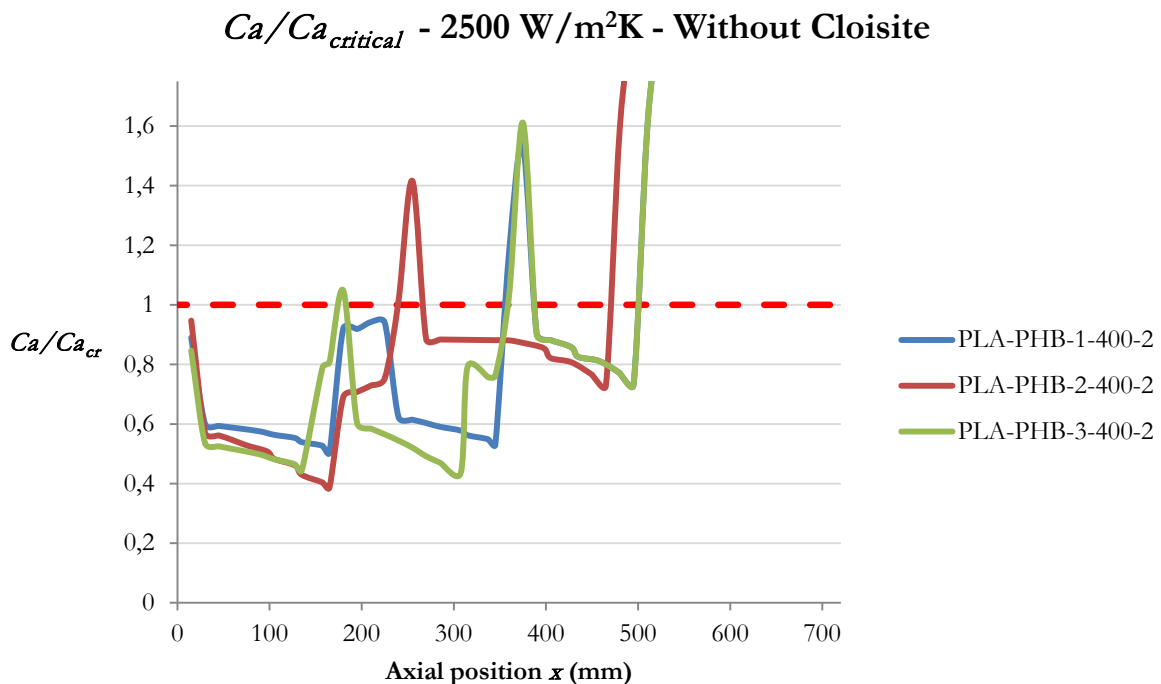


**Figure 6.14** -  $Ca/Ca_{critical}$  as a function of the axial position. Cloisite is not added.

Analysing the  $P_{coal}$  plots as a function of the axial coordinate (Figure 6.15), it is possible to observe how coalescence assumes a great importance especially in the half of the barrel prior to the die. This phenomenon can be put in relation with the high shear rates computed in this part of the apparatus. In fact, this condition results in an increase of the capillary number and then of

the probability of expelling the liquid film while, in contrast,  $P_{coal}$  is substantially constant along the whole screw.

Regarding the peculiarities of each screw, the overall low  $P_{coal}$  computed with the profile number 1 explains why, although the apparent lack of effect shown by the TME blocks, the final radius of the dispersed nodules is anyway low and comparable with the same one calculated with the screw number 2. This last configuration is, in contrast, the most prone to coalescence, frustrating in this way the important action of the second long kneading sequence. The plots related to the profile 3 lays in the middle, but (as it can be seen in Figure 6.13) the last lobed elements help in keeping  $R$  under control through a size reduction. In this way, it is avoided an excessive enlargement of the PHBH domains caused by the moderately high probability of coalescence.

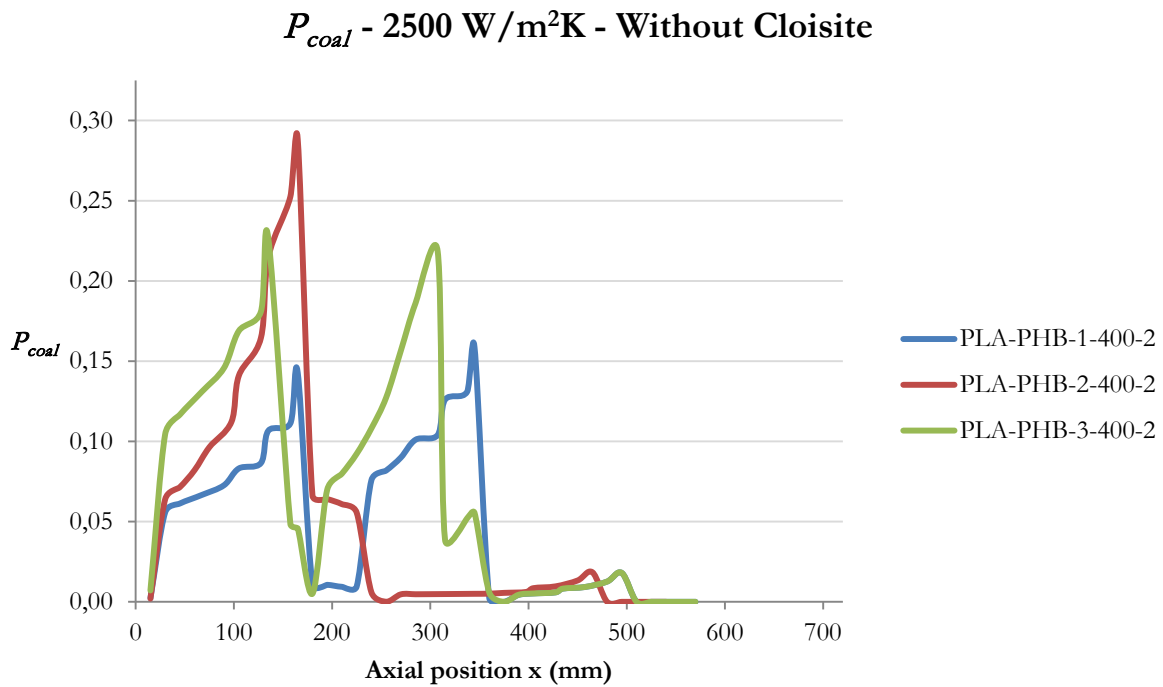


**Figure 6.15** -  $P_{coal}$  as a function of the distance from the barrel/die interface. Cloisite is not added.

It has been assumed that after the addition of Cloisite only the viscosities of the two components are varied according to the law of Maron and Pierce. It means that the mineral filler is equally distributed in the volume of PLA and PHBH, while at the interface only the two polymers can be found, so  $T_{12}$  does not change. These key hypothesis result in plots (Figure 6.16) which are quite similar to the ones observed when the clay is absent.

Looking in particular at the evolution of the radius, it is possible to see that, with the same screw profile, the final value of  $R$  is lower in presence of a mineral filler. Also in this case, the TME elements apparently do not have an effect in the size reduction, so the screw configuration 1 brings to the coarsest PHBH domains. In contrast to what it is observed in Figure 6.13, the profiles 1 and 2 lead to dispersed nodules with different sizes and the second one seems to grant better performances. Once again, the finest dispersion of the minor polymeric component is got with the configuration 3.

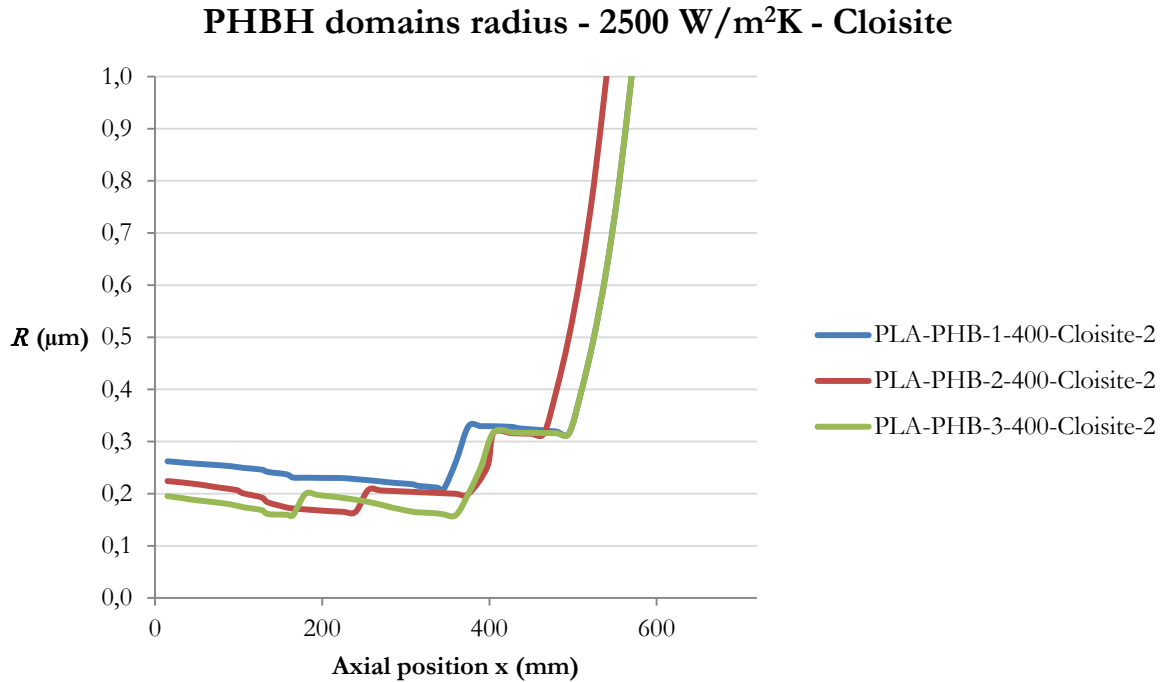


**Figure 6.16** - Radius of the PHBH domains as a function of the axial position in presence of Cloisite.

The ratio between the capillary numbers (Figure 6.17) is also in this case higher than the unity in all the restricting elements, except for the two TME modules of the configuration number 1. However, in this particular situation  $Ca$  assumes values really closer to  $Ca_{critical}$ , so it is plausible that a more rigorous application of the model would compute a size reduction also in the mixing sector of the profile 1.

The analysis of  $P_{coal}$  as a function of the axial position (Figure 6.18) can explain the difference in the final values of  $R$  between the profiles 1 and 2, observed in Figure 6.16. In fact, when the configuration number 2 is employed, the addition of Cloisite seems to partially hinder the expulsion of the liquid film along the conveying section which precedes the die. In contrast, the  $P_{coal}$  plots referred to the odd-numbered profiles do not significantly change. That can be considered as the reason why a slightly finer dispersion is computed when the screw number 2 is employed and the clay is added.

Ultimately, the model of Vergnes and Delamare applied to the data returned by Ludovic can greatly help the selection between different screw profiles on the basis of the performances they can grant. Obviously, the high number of assumptions made to simplify the calculation makes the results not so reliable, but the trends are generally in line with the hypothesis reported in the previous paragraphs, where the results of the simulations run at 400 rpm are analysed. According to the model, the best final morphology is got, as expected, employing the screw profile 3. As far as the screw number 1 is concerned, it can be reasonably thought that also this configuration is able to finely disperse the PHBH domains, because it is quite unlikely that no breakup phenomena occur in the TME modules. In contrast, the screw configuration 2 seems not to have the same good performances.

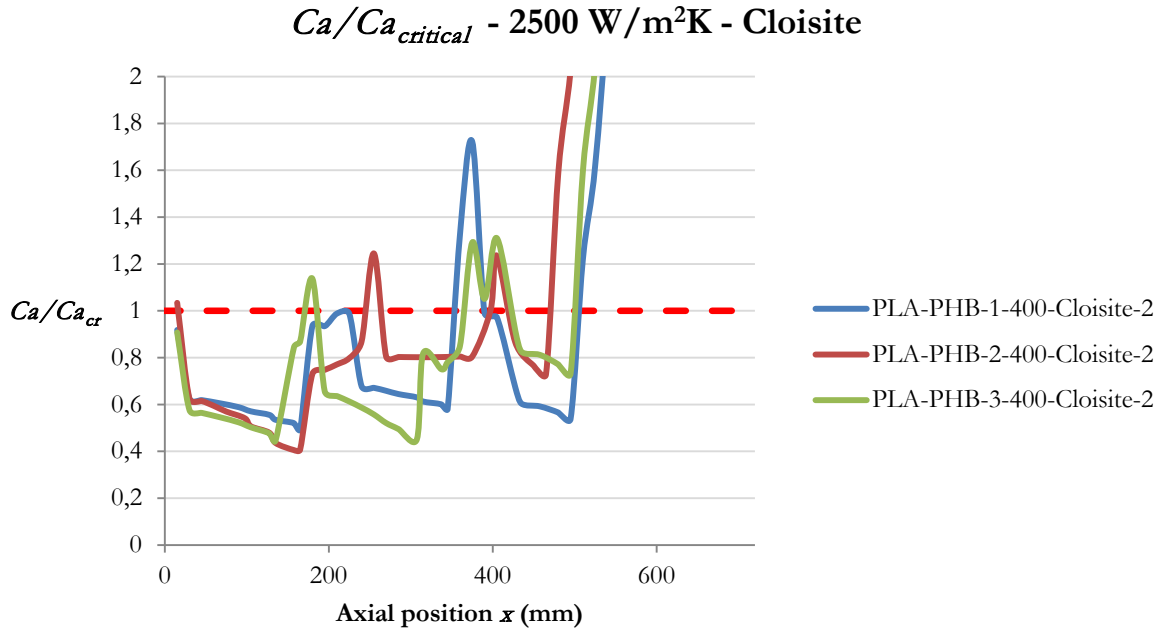


**Figure 6.17** -  $Ca/Ca_{critical}$  as a function of the axial position when Cloisite is added.

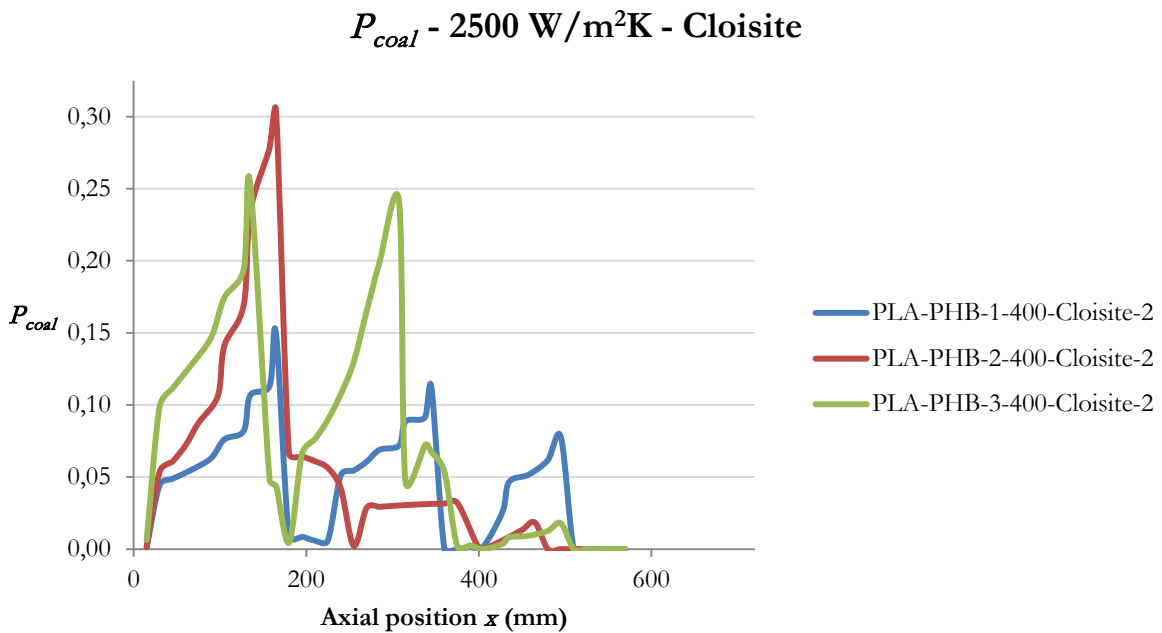


**Figure 6.18** -  $P_{coal}$  as a function of the distance from the barrel/die interface when Cloisite is added.

### 6.7. Effect of the screw speed on the simulations run with the profile 3

In the previous sections, it has been determined that the best final morphology is got with the screw configuration 3. Since one of the aims of this work is to evaluate the possibility of employing Ludovic to simulate the compounding process of blends containing a mineral filler, also the effect of the rotation speed is assessed. To do that, three simulations have been run at 200, 400 and 550 rpm with the addition of Cloisite. The resulting  $f(x)$  plots are then analysed and employed to model the morphology evolution.

Regarding the RTD, it is possible to observe (in Table 6.4 and Figure 6.19) how the highest minimum value is computed at 200 rpm, confirming the observations made in the DoE evaluation. Increasing the rotation speed, the reduction of  $RTD_{min}$  does not follow a linear trend and the computed values at 400 and 550 rpm are quite similar. This behaviour can be attributed to the decrease of viscosity, a consequence of the higher shear rates and temperatures, which makes the transport less effective due to stagnation<sup>[27]</sup>. A dissimilar evolution is observed looking at the mean values of the RTD. In fact, there is a larger difference between the averages at 400 and 550 rpm, since the distributions progressively narrow for higher rotation speeds, as confirmed by the width of the peak at half height. According to the conclusions reported in section 5.2, the increase of the screw speed should have a beneficial effect on the morphology, because the whole melt requires shorter times to pass through the extruder. Then, only a progressively lower fraction of the blend spends very long times inside the extruder, reducing coalescence. The slight difference between the mid-peak widths suggests that the effectiveness of the distributive mixing is not significantly affected.

**Table 6.4** - RTD characteristic times for different rotation speeds. The simulations involve the addition of Cloisite.

	PLA-PHB-3-200-2	PLA-PHB-3-400-2	PLA-PHB-3-550-2
<b>Minimum value (s)</b>	34,41	25,51	23,03
<b>Average value (s)</b>	79,62	67,28	64,23
<b>Mid-peak width (s)</b>	45,55	43,09	42,69

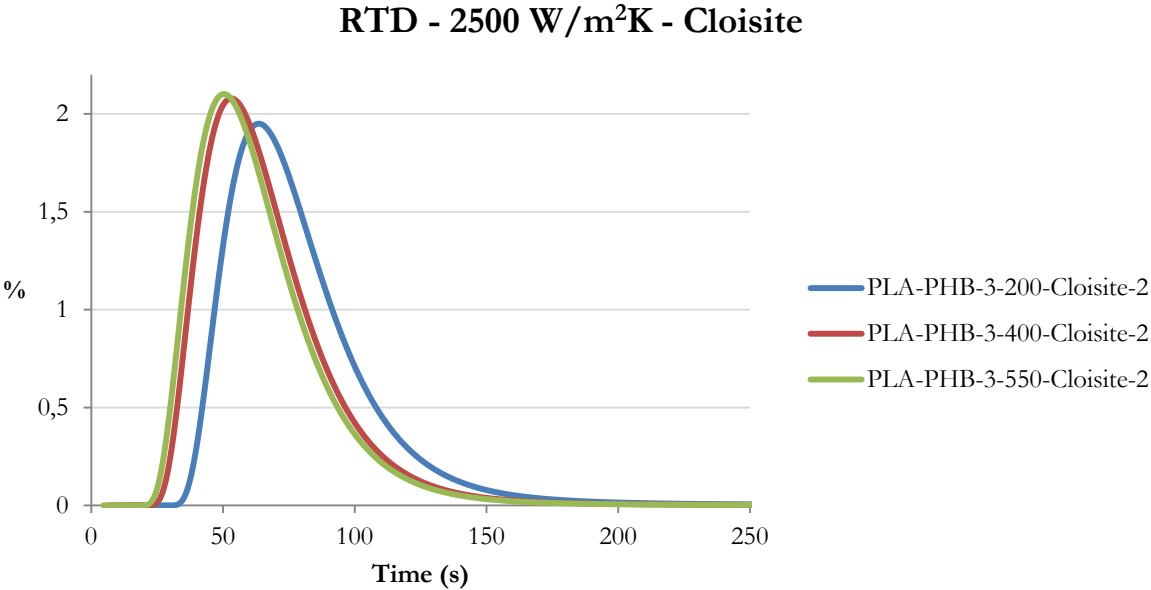


**Figure 6.19** - Residence Time Distributions at different rotation speeds for the screw profile 3 in presence of Cloisite.

The analysis of the LRT plots (Figure 6.20) helps to understand which are the elements that determine the different average times of the Residence Time Distribution. It is interesting to observe that the time required to pass through the kneading modules does not change at higher rpm, because this quantity depends only on the free volume and on the flow rate. In contrast, the time spent in the conveying sections is higher at low screw speeds, since the melt moves forward

of a shorter distance in the unit time. According to the interpretation given in section 6.3, at 200 rpm a significant recirculation can be observed in the 75 mm which precede the die, while at 400 and 550 rpm this phenomenon involves a shorter section of the apparatus (the 30 mm prior to the end of the barrel).

**Local Residence Time - 2800 W/m<sup>2</sup>K - Cloisite**

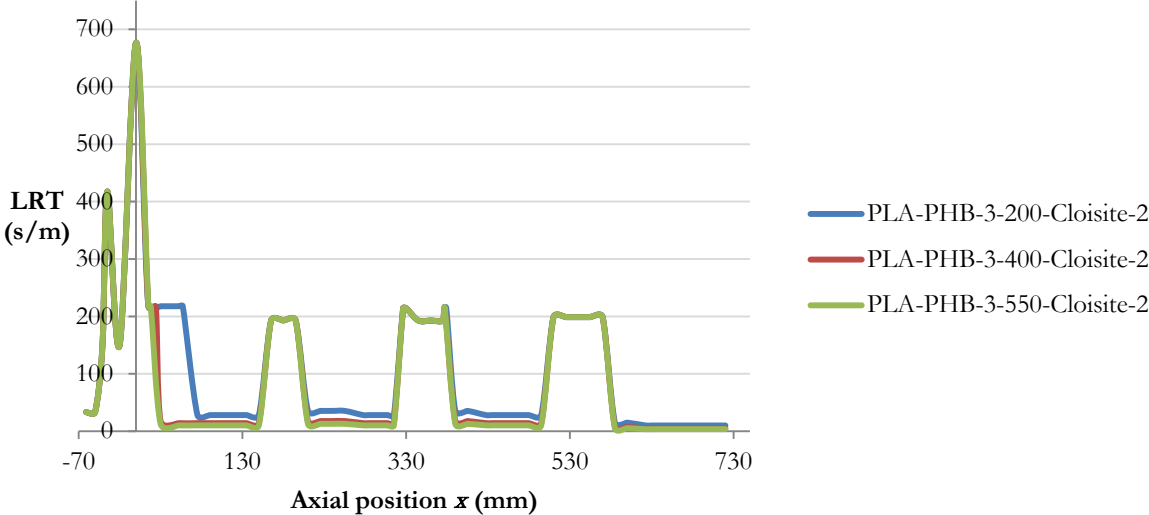


**Figure 6.20** - Local Residence Time as a function of the axial position. It is employed the screw profile 3 in presence of Cloisite.

**Total Residence Time - 2800 W/m<sup>2</sup>K - Cloisite**

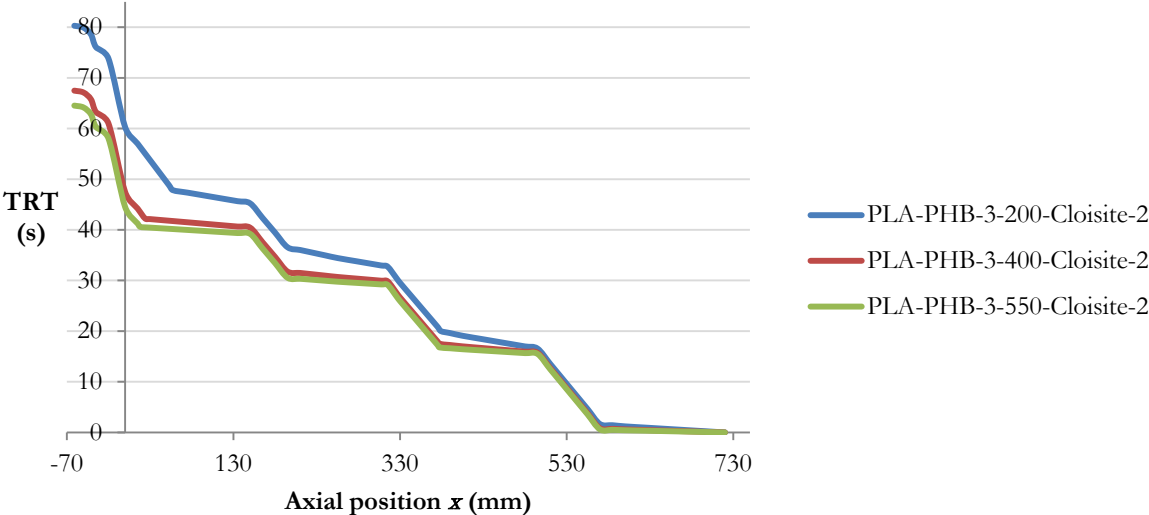


**Figure 6.21** - Total Residence Time as a function of the axial position for the screw profile 3 in presence of Cloisite.

What has been explained about the LRT can be observed also in the plots which represent the Total Residence Time (Figure 6.21). In fact, in correspondence of the restricting elements the

lines of the diagrams are parallel, due to the same residence time at any screw speed, while the TRT increase in the conveying segments is represented by lines with different slopes. In particular, they are less steep for faster rotations because less time is needed to pass through the transport elements.

The dissipation of the mechanical energy plays an important role in determining the temperature, as confirmed by the plots of Figure 6.22. In fact, the highest value is registered in correspondence of the back-flow element when the rotation speed is set at 550 rpm, that is where the highest shear rate is registered. In addition, observing all the diagrams it is possible to see that the most significant temperature increases occur in the kneading sections, while inside the conveying segments (where  $\dot{\gamma}$  is lower) the melt cools down. The correlation between the profiles of temperature and shear rate at different screw speeds is evident in Figure 6.23.

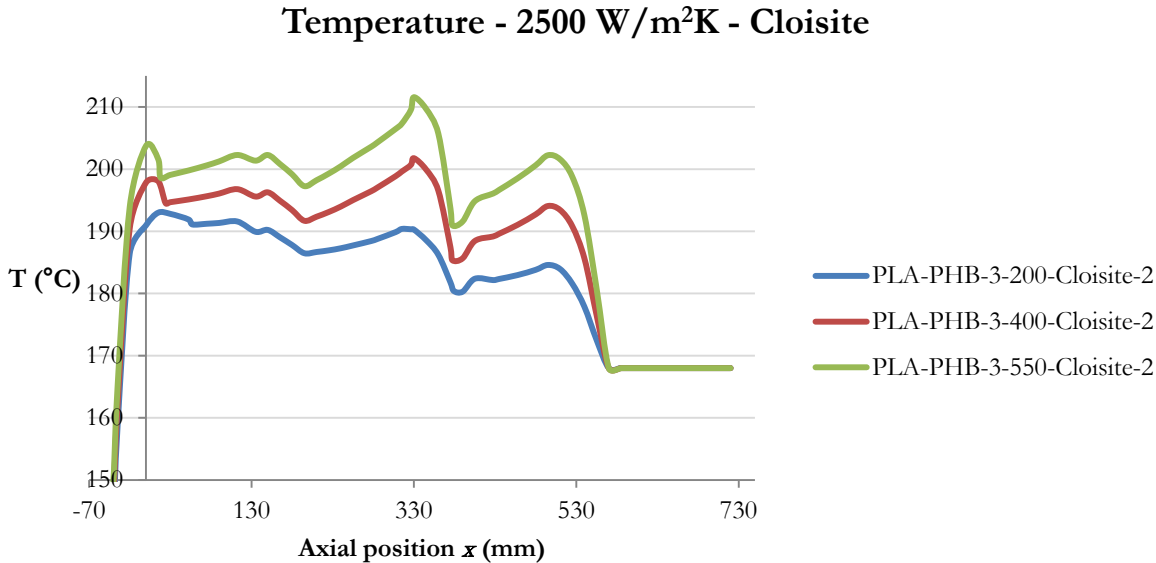


Figure 6.22 - Temperature profiles for the screw profile 3 at different rotations speed. Cloisite is added.

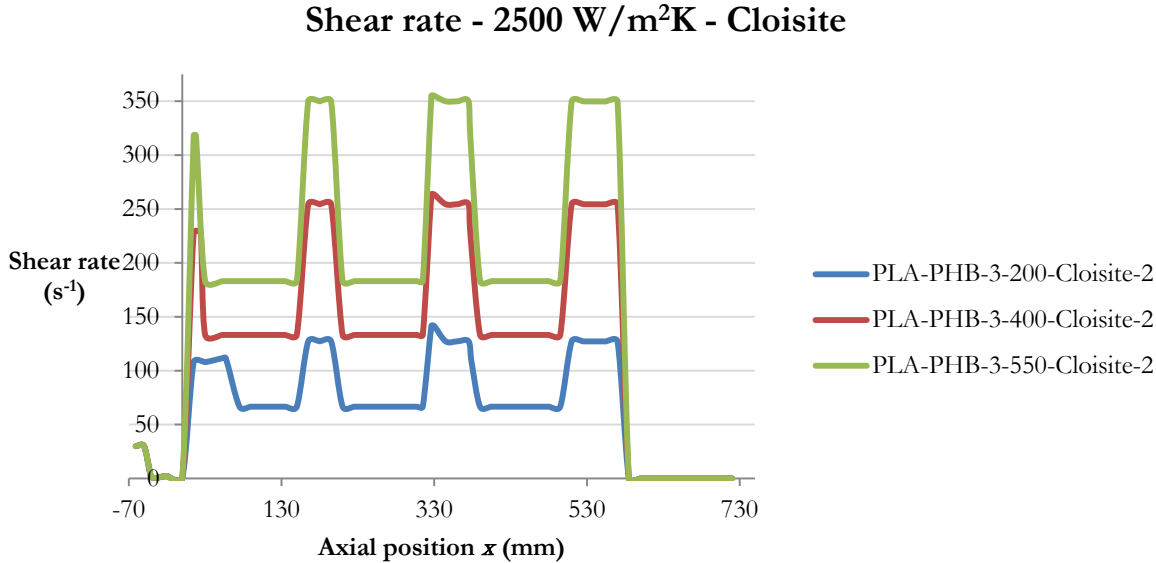
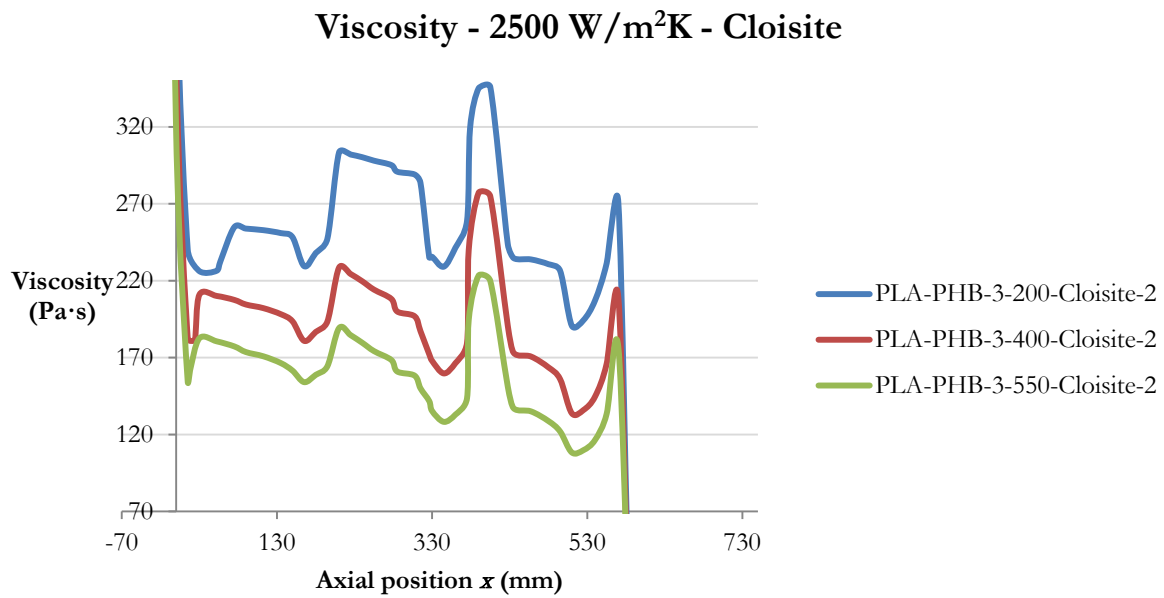


Figure 6.23 - Shear rate profiles at different rpm employing the screw profile 3. Cloisite is added.

The diagrams of temperature and shear rate are complementary to the one of viscosity (Figure 6.24), since it is possible to observe how the highest value is computed at 200 rpm in correspondence of the conveying element under the hole from which the clay is added. This happens due to the combination of low  $\dot{\gamma}$  (a consequence of the rotation speed and the type of element) and low temperatures resulting from the addition of the filler at 25°C. For the same reasons, the maximum overall fluidity is obtained at 550 rpm in correspondence of the back-flow module.



**Figure 6.24** - Viscosity as a function of the axial position. The screw profile 3 is employed and the simulations are run in presence of Cloisite.

Relying on the explanations reported in the previous sections of this chapter, it is possible to conclude that a better final morphology is obtained through an increase of the rotation speed. In fact, at high rpm the RTD width at half the peak is lower, meaning a better control on the process, and the LRT in the conveying elements (where coalescence is not balanced by the breakup) is lower. Moreover, the residence time in the restricting elements does not change, but the considerably greater shear rates help to obtain a finer dispersion of the dispersed polymeric domains. Since high  $\dot{\gamma}$  also result an increase of the capillary number, the probability of expelling the liquid film which lays between two PHBH nodules (and then  $P_{coal}$ ) becomes higher. The low viscosity registered at high rpm just after the point from which the clay is added remarks that the dispersion of the mineral filler should be simpler. To confirm these hypothesis, one more time it has been applied the model of Vergnes and Delamare to the results of the simulations run at different rotation speeds with the screw profile 3. All the considerations about the model reported in chapter 6.6 are still valid, especially the ones referred to the consequences of adding the clay and to the way in which this addition is numerically represented.

Looking at the evolution of  $R$  along the screw (Figure 6.25), it is substantially confirmed what has been supposed after the analysis of the various plots returned by the simulations, since the finest dispersion is obtained with the highest rotation speed. A significant difference is observed between the data computed at  $x=0$  mm and 200 rpm and the same ones obtained at 400 and 550 rpm, which are really similar. This behaviour can be explained by the analysis of the  $Ca/Ca_{critical}$  plots (Figure 6.26), which show how, according to the model, at 200 rpm only a little portion of

the second kneading section is effective in the size reduction. In contrast, with faster rotations the conditions for the breakup exist in the whole lobed sequence and the peaks resembles each other, so the computed final radius is smaller.

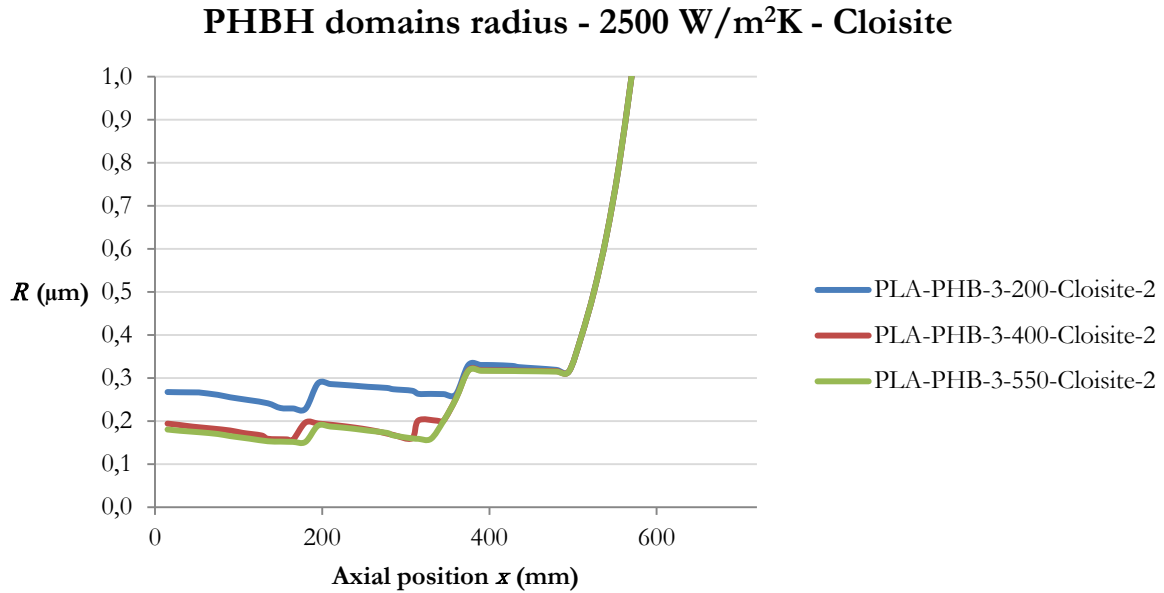


**Figure 6.25** - Radius of the PHBH domains as a function of the axial position in presence of Cloisite. The screw profile 3 is employed at different rotation speeds.

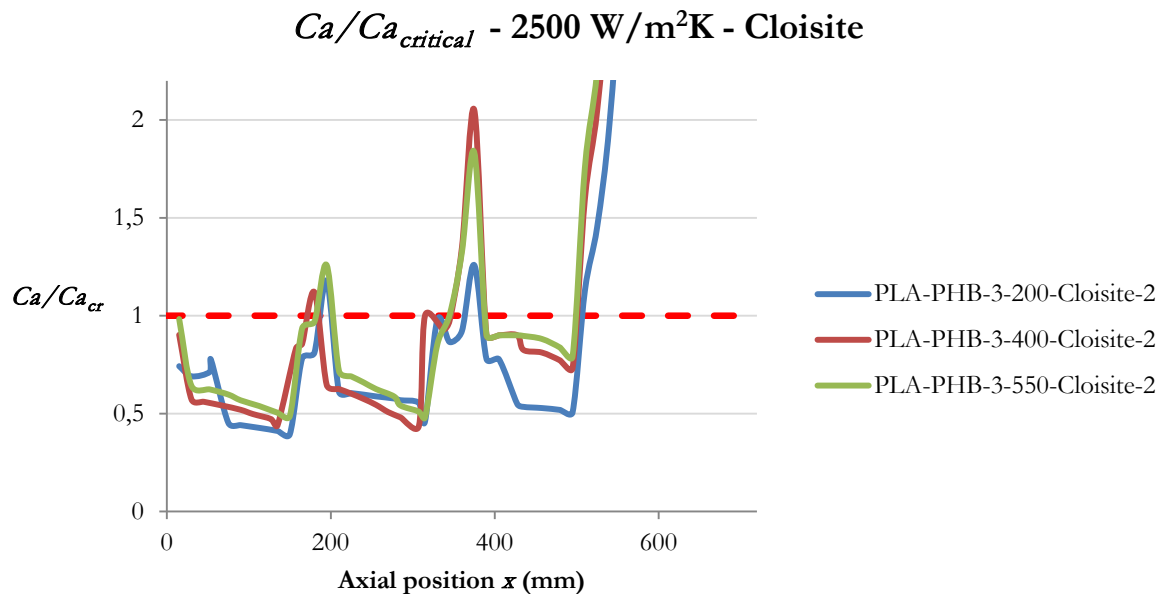


**Figure 6.26** -  $Ca/Ca_{critical}$  as a function of the axial position. The simulations are run at different rotation speeds in presence of Cloisite with the screw configuration 3.

Finally, the probability of coalescence (see Figure 6.27) is, once again, primarily determined by the value of  $P_{exp}$ , since  $P_{col}$  is practically constant. In contrast to what was expected prior to the application of the model, only in the conveying elements which follow the back-flow module  $P_{coal}$

is higher at higher rotation speeds and, then, shear rates. The situation in the other transport segments is a bit more complex due to the contemporary effect of the viscosity ratio, which shows some fluctuations especially at 200 rpm.

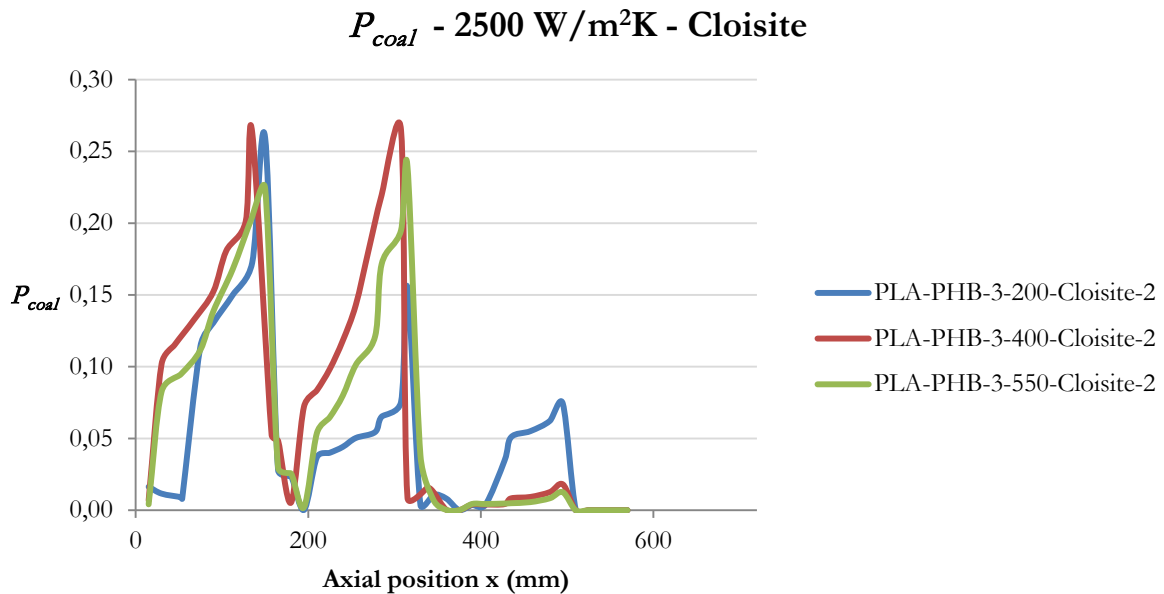


**Figure 6.27** -  $P_{coal}$  as a function of the distance from the barrel/die interface. Profile 3 is employed at different rotation speeds in presence of Cloisite.

### 6.8. Comparison of the computed results with SEM micrographs

Having defined from the simulations that the screw profile 3 leads to the best final morphology, it is now time to make a comparison between the computed results and the SEM micrographs of the blends obtained after the real compounding process. When Cloisite is not added (Figure 6.28), it is possible to observe that the screw configuration 1 produces a distribution of very big ( $R \approx 1,5 \mu\text{m}$ ) nodules alongside a great number of smaller ones, with a radius of about  $0,6-0,7 \mu\text{m}$ . Using the profile number 2, the largest PHBH domains are a bit smaller if compared to the previous case ( $R \approx 1,4 \mu\text{m}$ ), but the smallest ones are larger, with radii in the range  $0,8-0,9 \mu\text{m}$ .

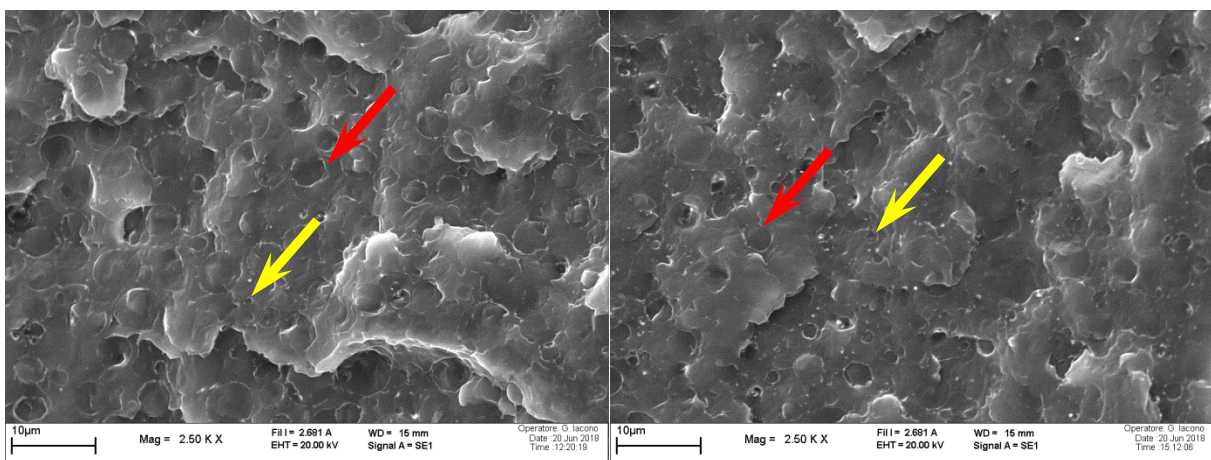


**Figure 6.28** - PLA/PHBH blends compounded without adding Cloisite with the screw profiles 1 (left) and 2 (right) at 400 rpm. The red arrows point out the domains with greater size, while the smaller ones are shown by the yellow arrows.

These observations confirm what was supposed in the RTD analysis, since the broader peak resulting from the action of the profile 1 was associated to a greater chance for coalescence to occur, leading to the large nodules that are observed. At the same time, a worse distribution of the minor phase is got when the melt is compounded with the screw number 2, since less time is spent inside the kneading modules.

The addition of Cloisite has a great influence on the final morphology (see Figure 6.29), since it causes a size reduction of the largest PHBH domains of about one order of magnitude and the system is close to be monodisperse. As expected after the analysis of the results returned by Ludovic, the worst result is obtained with the screw number 2, that leads to big ( $R \approx 0,7 \mu\text{m}$ ) and poorly distributed nodules of the minor component. In contrast, with the odd-numbered profiles (especially the number 3) a better morphology is got, and the radii lay in the range 0,3-0,4  $\mu\text{m}$ . The high shear rates and the consequent reduction of viscosity, provided by these last profiles just after Cloisite is added, aid also the distributive and dispersive mixing of the clay, which is found especially in the PLA matrix.

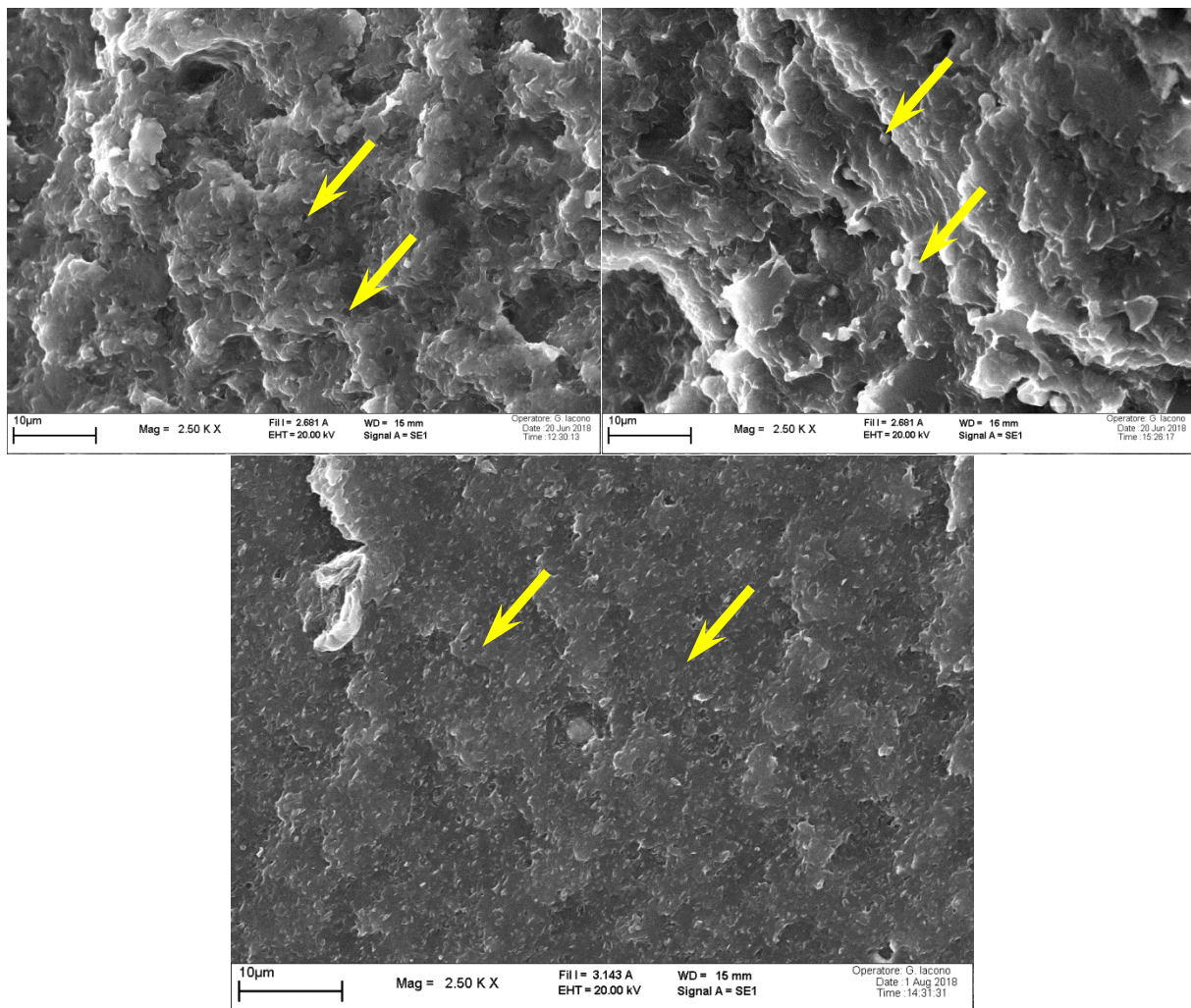


**Figure 6.29** - PLA/PHBH blends compounded in presence of Cloisite with the screw profiles 1 (top left), 2 (top right) and 3 (bottom) at 400 rpm. Since all the domains of the same blend have almost the same size, they are pointed out by the yellow arrows only.

As shown at the bottom of Figure 6.29 and in Figure 6.30, the progressively higher shear rates, which are a consequence of the increasing rotation speed, cause a gradual decrease of the PHBH

domain size. These domains are in general well-distributed inside the matrix and at 550 rpm they are quite hard to be observed due to their significantly small dimensions. The same can be said for the mineral filler, which is almost invisible at the highest screw speed.

The great difference of morphology observed between the blends in which Cloisite is added and the same ones without the clay, especially for what concerns the size distribution, is quite hard to be explained only on the basis of the data returned by Ludovic. In fact, the plots describing what happens when the filler is added or not do not show differences great enough to justify such a dissimilar behaviour, especially for what concerns coalescence. Since the software is designed to model only physical phenomena (temperature raises, residence times, shear rates and viscosity variations), probably the morphology that is got after the addition of the clay results from a different interfacial energy consequent to the presence of the platelets at the interface. In particular, the clay lowers  $T_{12}$  and the size of the domains decreases as observed.

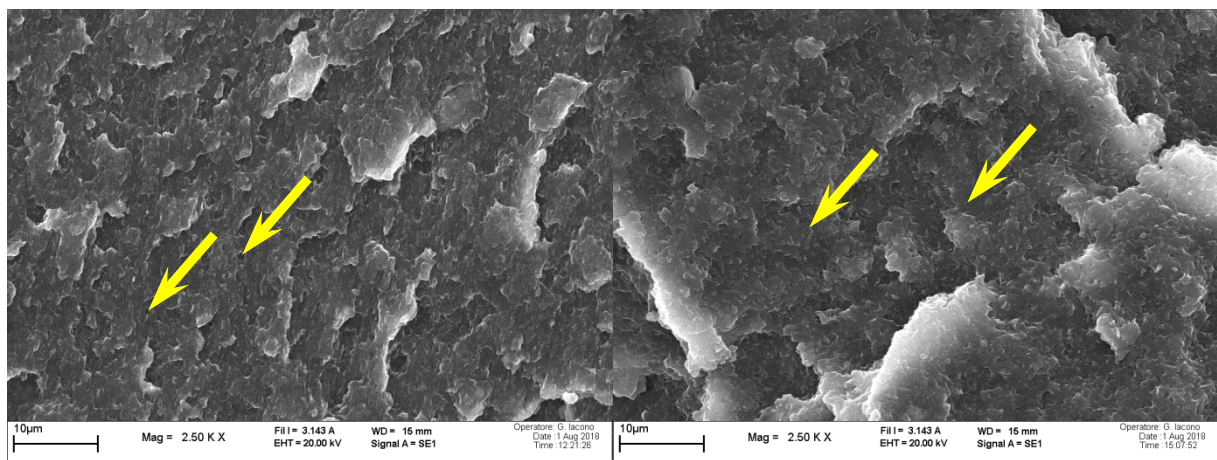


**Figure 6.30** - PLA/PHBH blends compounded in presence of Cloisite with the screw profiles 3 at 250 (left) and 550 rpm (right). Since all the domains of the same blend have almost the same size, they are pointed out by the yellow arrows only.

Finally, the effectiveness of the model proposed by Vergnes and Delamare when Cloisite is not added has to be assessed. Since the starting radius has been set to  $1 \mu\text{m}$  and the system has been modelled as a monodisperse one (an assumption that is very far from the reality), it is possible to think that the plots observed in section 6.6 describe the morphology evolution of the smallest classes of domains, pointed out by the yellow arrows in Figure 6.28. In fact, it is quite unlikely that, starting from such a small value of the initial radius, the droplets undergo only coalescence, which leads to the largest nodules, completely avoiding every kind of breakup phenomenon. Following this hypothesis, a satisfying accordance between the simulations and the reality can be found. Regarding the larger domains of the minor polymeric phase, it can be thought that they derive from nodules with a starting radius greater than  $1 \mu\text{m}$ . Unfortunately, the impossibility to know the exact value of  $D_0$  in the real extrusion process does not give the opportunity to completely rely on the numerical results. When Cloisite is added, the micrographs show that the clay nanoplatelets can be found especially in the PLA matrix and at the interface between the two polymers, so one of the assumptions used to simulate the morphology development is wrong. Despite that, the predictions of the model about the final radii are, especially in this case (with a system close to a monodisperse one), quite in line with what is observed in the reality. This is true also when the screw profile 3 is employed at different rotation speeds, because faster rotations actually reduce the size of the PHBH nodules. To conclude, for a PLA-PHBH blend the model of Vergnes and Delamare applied to the results returned by Ludovic is useful to compare the performances of different screw profiles, but the numerical results are not so trustworthy. In fact,

it will be possible to rely on them only after a rigorous evaluation of all the assumptions made under the theoretical and the empirical point of view.

### 6.9. Effect of the mixing law for the polymers

In this work the system has been modelled using a linear mixing law for the polymeric components. It has been supposed that, since the viscosities of PLA and PHBH are substantially similar in the range of temperatures and shear rates provided by the extruder, no significant differences should be observed between the values of  $\eta_{melt}$  calculated using the different relationships reported in section 4.2.1. Different simulations have been run employing only the screw profile 3 with the same settings already used to obtain the data reported in this chapter. In particular, the rotation speed has been set at 400 rpm and the effect of adding Cloisite is assessed.

For those simulations run without the filler (Figure 6.31), the only significant differences are observed in the profiles of viscosity. In particular, the highest values are obtained employing the linear relationship, while the lowest ones are computed with the harmonic law. The tree plots can be enclosed in a band that is 10 Pa·s wide. As a consequence, it is really difficult to appreciate substantial variations in the diagrams representing those quantities which are more or less linked with the viscosity (like the temperature), because the curves are practically superimposed.

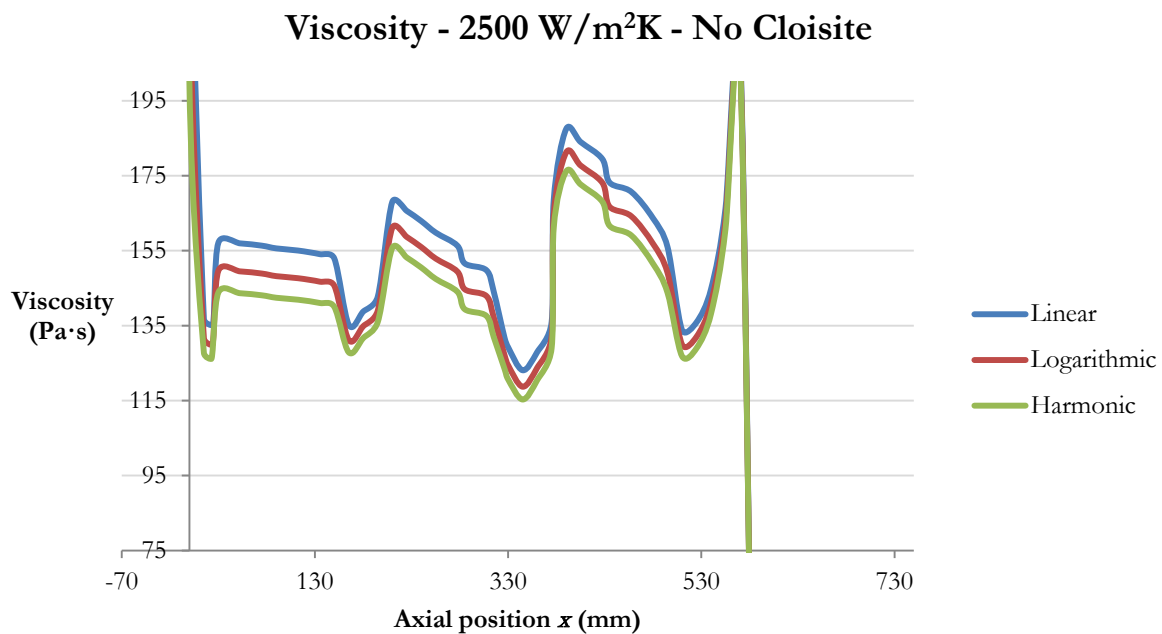


**Figure 6.31** - Viscosity as a function of the axial positions with different mixing laws. Cloisite is not added.

Some problems have been encountered while trying to run the simulations involving the addition of Cloisite, since with the logarithmic relationship convergence has not been reached. Similarly to the previous case, the most significant variations are observed in the diagrams referred to the viscosity and lower values of  $\eta_{melt}$  are obtained with the harmonic equation. However, in Figure 6.32 it can be clearly seen how after the addition of the filler the distance between the two plots increases of about 10 times and values of about 100 Pa·s are computed with the harmonic relationship. It means that employing this last law, the viscosity of the melt containing Cloisite is lower than what has been computed using the same mixing equation when the filler is not

present. This is in contrast with the behaviour of filled blends, so it is possible to conclude that something went wrong during the calculation. Probably, the underestimation of  $\eta_{melt}$  after the application of the Maron and Pierce equation can be linked to some problems in the derivation of the parameter  $B$  when the harmonic mixing law is employed. In fact, this last variable is automatically calculated by Ludovic. Moreover, despite the filler enters the barrel at room temperature, with the harmonic equation it is not observed a consequent increases of the viscosity. Then, it is possible to conclude that, when Cloisite is added and the harmonic relationship is employed, the predictions are not reliable. So, although the PLA/PHBH blend is immiscible, the linear mixing law between the polymers models the behaviour of the blend in the most effective way.

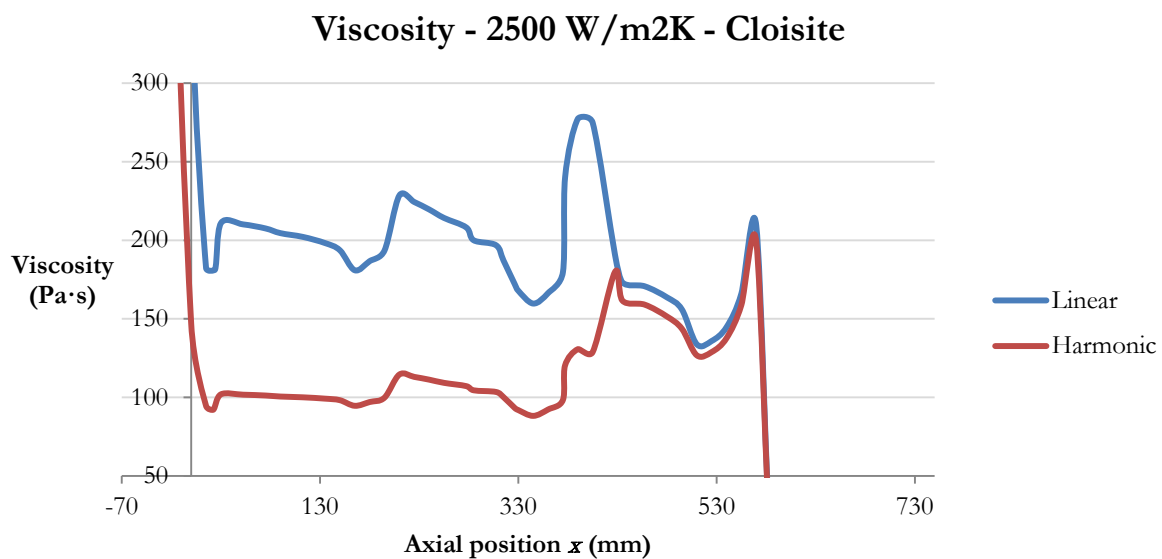


**Figure 6.32** - Viscosity as a function of the axial positions with different mixing laws when Cloisite is added.

### 6.10. Conclusions

After having determined through the DoE analysis that the predictions made by Ludovic are realistic, the possibility of using the software to select the most suitable screw profile for a specific application has been evaluated in the present chapter. The Residence Time Distribution has been put in relation with the probability of coalescence, while the LRT and TRT are useful to understand how much time is spent by the melt inside the various kinds of elements, especially in the kneading and mixing ones. Temperature and shear rate determine the viscosity, which is an important parameter in the distribution of all the minor components (mineral and organic, if added), because this action is made simpler by low values of  $\eta_{melt}$ . The results of the simulations alone allow to determine the screw profile which grants the best performances in the different situations, but the model of Vergnes and Delamare can further help this selection. In fact, after the analysis of the plots returned by the software at 400 rpm, the screw profile 3 was confirmed as the one able to lead to the best final morphology in all the situations. Moreover, it has also been speculated that an increase of the rotation speed would result in a finer dispersion of the minor components in the volume of the blend. All these hypothesis have been verified by the application of the model of Vergnes and Delamare and were confirmed by the observation of the SEM micrographs. The main drawback identified after this comparison is that the software only works on physical parameters, so the returned plots do not show significant differences when the

mineral filler is added. Then, it has been practically impossible to detect the substantial size reduction consequent to the action of the clay nanoplatelets.

For what concerns the effectiveness of the model in the determination of the PHBH domain sizes, on the basis of the images got with the microscope it is possible to conclude that the predictions about the morphology are only partially satisfying. In fact, the assumption of working on a monodisperse system is very far from the reality, especially when Cloisite is not added. Furthermore, some of the parameters which are needed have been derived from the existing literature and not, how it would have been better, from empirical results related to the bio-based blend object of this study. This is true especially for  $D_0$  which has a key role on the computed final values of  $R$ . Then, in order to successfully employ the model to predict the final morphology, a further deepening about this topic has to be carried out.

In conclusion, Ludovic is a valid instrument to simulate the blending operations also in the case of a PLA-PHBH blend containing Cloisite. Since the performances granted by a particular screw profile are evaluated only after the critical interpretation of the results, the operator has to be already familiar with the compounding process and with the properties of the employed materials. At present, the model proposed by Vergnes and Delamare can help the selection of the most suitable screw configuration (starting from the same key parameters for all the profiles). However, a significant improvement is needed if it is necessary to accurately simulate the final morphology employing the results returned by the software.



## 7. List of symbols

$x$ .....	Axial position along the screw	$M_w$ .....	Molecular weight
$\Delta G_m$ .....	Gibbs free energy for mixing	$K$ .....	Consistency
$\Delta H_m$ .....	Mixing enthalpy	$m$ .....	Pseudoplasticity index
$T$ .....	Temperature	$\tau_0$ .....	Yield stress
$\Delta S_m$ .....	Mixing entropy	$a$ .....	Carreau-Yasuda parameter
$\Phi$ .....	Volume Fraction	$\alpha, \beta$ .....	Empirical parameters
$N$ .....	Degree of polymerization	$R$ .....	Radius of the dispersed domains
$\chi$ .....	Flory-Huggins interaction parameter	$C_L$ .....	Centerline
$R$ .....	Gas constant	$R_1$ .....	Inner and outer radius of the screw
$V$ .....	Volume	$R_2$ .....	Outer radius of the screw
$\delta_1, \delta_2$ .....	Solubility parameters	$\delta$ .....	Leakage between screw and barrel
$\eta$ .....	Viscosity	$\psi$ .....	Intermeshing angle
$[\eta]$ .....	Intrinsic viscosity	$S$ .....	Cross-section
$X$ .....	Mass fraction	$H$ .....	Height of a screw channel
$MFI$ .....	Melt Flow Index	$v$ .....	Velocity
$\Gamma_{12}$ .....	Interfacial energy	$p$ .....	Pressure
$\Gamma$ .....	Surface energy	$F_r$ .....	Filling ratio
$\phi$ .....	Interaction parameter	$\alpha_m$ .....	Staggering angle
$\rho$ .....	Density	$Q$ .....	Mass flow rate
$F$ .....	Force	$Q_v$ .....	Volumetric flow rate
$\dot{\gamma}$ .....	Shear rate	$Rt$ .....	Residence time
$Ca$ .....	Capillary number	$u$ .....	Velocity field
$D$ .....	Diameter of the dispersed domains	$\omega$ .....	Angular velocity
$C$ .....	Frequency of collision	$Nu$ .....	Nusselt number
$P_{col}$ .....	Probability of collision	$h$ .....	Thermal exchange coefficient
$t_{loc}$ .....	Local residence time	$k$ .....	Thermal conductivity
$P_{exp}$ .....	Probability of expelling the liquid film	$\dot{Q}$ .....	Thermal power
$P_{coal}$ .....	Probability of coalescence	$C_p$ .....	Specific heat
$t_b$ .....	Time for breakup	$\dot{W}$ .....	Energy lost by viscous dissipation
$t_b^*$ .....	Dimensionless constant for breakup	$RT$ .....	“Room temperature” (25°C)
$\Omega_m$ .....	Dimensionless parameter	$Tq$ .....	Torque
$\alpha_0$ .....	Amplitude of the deformation	$E_{mat}$ .....	Energy dissipated by 1 kg of melt
$T_g$ .....	Glass transition temperature	$\Omega$ .....	Rotation frequency
$T_m$ .....	Melting temperature		



## 8. References

- [1] Arrieta, M.P., Samper, M.D., Aldas, M. and López, J., 2017, On the Use of PLA-PHB Blends for Sustainable Food Packaging Applications. *Materials* **10**(9), 1008/1-26. [DOI: 10.3390/ma10091008]
- [2] Gaspar-Cunha A., Poulesquen A., Vergnes B. and J. A. Covas, 2002, Optimization of Processing Conditions for Polymer Twin-Screw Extrusion. *Intern. Polymer Processing* **17**(3), 201-213. [DOI: 10.3139/217.1701]
- [3] Banu I., Puaux J.P., Bozga G. and Nagy I., 2010, Modeling of L-lactide Polymerization by Reactive Extrusion. *Macromol. Symp.* **289**, 108–118. [DOI: 10.1002/masy.200900012]
- [4] Rol F., Vergnes B., El Kissi N. and Bras J., 2020, Nanocellulose Production by Twin-Screw Extrusion: Simulation of the Screw Profile To Increase the Productivity. *ACS Sustainable Chem. Eng.* **8**(1), 50–59. [DOI: 10.1021/acssuschemeng.9b0191]
- [5] Delamare L. and Vergnes B., 1996, Computation of the Morphological Changes of a Polymer Blend Along a Twin-Screw Extruder. *Polymer Engineering & Science* **36**(12), 1685-1693. [DOI: 10.1002/pen.10565]
- [6] Morris B.A., 2017, Polymer Blending for Packaging Applications, in “*The Science and Technology of Flexible Packaging*”, Chap. 6. Elsevier, Amsterdam, pp. 149-177. [ISBN: 978-0-323-24273-8]
- [7] Coleman M., Graf J. and Painter P., 1991, *Specific interactions and the miscibility of polymer blends*. Technomic Publishing, Lancaster. [ISBN: 978-0-877-62823-1]
- [8] Deepak Selvakumar R. and Dhinakaran S., 2017, Effective viscosity of nanofluids - A modified Krieger-Dougherty model based on particle size distribution (PSD) analysis. *Journal of Molecular Liquids* **225**, 20–27. [DOI: 10.1016/j.molliq.2016.10.137]
- [9] Wu S., 1982, *Polymer interface and adhesion*. Marcel Dekker, Inc., New York. [ISBN: 978-0-203-74286-0]
- [10] Grace H.P., 1982, Dispersion phenomena in high viscosity immiscible fluid systems and application of static mixers as dispersion devices in such systems. *Chemical Engineering Communications* **14**(3-6), 225-277. [DOI: 10.1080/00986448208911047]
- [11] Utracki L.A. and Shi Z., 1992, Development of polymer blend morphology during compounding in a twin-screw extruder. Part I: droplet dispersion and coalescence - a review. *Poly. Eng. Sci.*, **32**(24), 1824-1833. [DOI: 10.1002/pen.760322405]
- [12] Pötschke P. and Paul D. R., 2003, Formation of Co-continuous Structures in Melt-Mixed Immiscible Polymer Blends. *Journal of Macromolecular Science, Part C: Polymer Reviews* **43**(1), 87-141. [DOI: 10.1081/MC-120018022]
- [13] Elmendorp J.J. and Van der Vegt A.K., 1986, A study on polymer blending microrheology: Part IV. The influence of coalescence on blend morphology origination. *Polymer Engineering and Science* **26**(19), 1332-1338. [DOI: 10.1002/pen.760261908]
- [14] Hepperle J., Flecke J., Thiele H., Geiger K. and Martin G.A., 2008, Material Properties of Polymers, in “*Co-Rotating Twin-Screw Extruders – Fundamentals, Technology, and Applications*”, (K. Kohlgrüber, Eds.), Chap. 3. Hanser Publishers, Munich, pp. 189-290. [ISBN: 978-1-56990-422-0]

- [15] Lim J.S., Park K., Chung G.S. and Kim J.H., 2013, Effect of composition ratio on the thermal and physical properties of semicrystalline PLA/PHB-HHx composites. *Materials Science and Engineering C* **33**(4), 2131–2137. [DOI: 10.1016/j.msec.2013.01.030]
- [16] Auras R., Harte B. and Selke S., 2004, An Overview of Polylactides as Packaging Materials. *Macromol. Biosci.* **4**(9), 835–864. [DOI: 10.1002/mabi.200400043]
- [17] D’Anna A., Arrigo R. and Frache A., 2019, PLA/PHB Blends: Biocompatibilizer Effects. *Polymers* **11**(9), 1416/1-11. [DOI: 10.3390/polym11091416]
- [18] Nampoothiri K.M., Nair N.R. and John R.P., 2010, An overview of the recent developments in polylactide (PLA) research. *Bioresource Technology* **101**(22), 8493–8501. [DOI: 10.1016/j.biortech.2010.05.092]
- [19] Chen C., Chueha J. Y., Tseng H., Huang H. and Lee S., 2003, Preparation and characterization of biodegradable PLA polymeric blends. *Biomaterials* **24**(7), 1167–1173. [DOI: 10.1016/s0142-9612(02)00466-0]
- [20] Sheth M., Kumar R.A., Davé V., Gross R.A. and McCarthy S.P., 1997, Biodegradable Polymer Blends of Poly (lactic acid) and Poly (ethylene glycol ). *Journal of Applied Polymer Science* **66**(8), 1495–1505. [DOI: 10.1002/(sici)1097-4628(19971121)66:8<1495::aid-app>3.0.co;2-3]
- [21] Amor A., Okhay N., Guinault A., Miquelard-Garnier G., Sollogoub C. and Gervais M., 2018, Combined compatibilization and plasticization effect of low molecular weight poly(lactic acid) in poly(lactic acid)/poly(3-hydroxybutyrate-co-3-hydroxyvalerate) blends. *eXPRESS Polymer Letters* **12**(2), 114–125. [DOI: 10.3144/expresspolymlett.2018.10]
- [22] Subramanian M.N., 2017, Polymer Blends, in “*Polymer Blends and Composites – Chemistry and Technology*”, Chap. 7. John Wiley & Sons, New York, pp. 169-211. [ISBN: 978-1-118-11889-4]
- [23] Zhou Y., Huang Z., Diao X., Weng Y., and Wang Y., 2015, Characterization of the effect of REC on the compatibility of PHBH and PLA. *Polymer Testing* **42**, 17-25. [DOI: 10.1016/j.polymertesting.2014.12.014]
- [24] Ravati S., Beaulieu C., Deschênes L., Cao V. and Favis B.D., 2012, Multi-Component Bio-Based Blends with Polylactic Acid and Polyhydroxybutyrate: Morphology and Physical Properties, in “*ANTEC 2012 Plastics: Annual Technical Conference Proceedings*” (Proc. 70th Annual Technical Conference of the Society of Plastics Engineers, Orlando, USA, 2-4 April 2012), Vol. 1, Nr. 43, pp. 219-224. [ISBN: 978-1-62276-083-1]
- [25] Zhang M. and Thomas N.L., 2011, Blending Polylactic Acid with Polyhydroxybutyrate: The Effect on Thermal, Mechanical, and Biodegradation Properties. *Advances in Polymer Technology* **30**(2), 67–79. [DOI: 10.1002/adv.20235]
- [26] SCC Consultants, Ludovic User's Manual - v7.0.
- [27] Jager T., 1992, Residence time distribution in twin-screw extruders. Ph.D. dissertation, Wageningen University, Wageningen, Netherlands.
- [28] Mahmood S.H., Ameli A., Hossieny N. and Park C.B., 2014, The interfacial tension of molten polylactide in supercritical carbon dioxide. *J. Chem. Thermodynamics* **75**, 69–76. [DOI: 10.1016/j.jct.2014.02.017]
- [29] Pyda M., Bopp R.C. and Wunderlich B., 2004, Heat capacity of poly(lactic acid). *J. Chem. Thermodynamics* **36**(9), 731–742. [DOI: 10.1016/j.jct.2004.05.003]
- [30] NatureWorks LLC, Ingeo™ Biopolymer 3251D Technical Data Sheet, <https://www.natureworkslc.com/Products/3-series-for-injection-molding>.

- [31] Tin Sin L. and Soo Tveen B., 2019, Thermal Properties of Poly(Lactic Acid), in “*Poly(lactic Acid) - A Practical Guide for the Processing, Manufacturing, and Applications of PLA (2<sup>nd</sup> edition)*”, Chap. 3. Elsevier, Amsterdam, pp 97-133. [ISBN: 978-0-12-814472-5]
- [32] Kaneka Corporation, PHBH Brochure, <http://www.kaneka.be/documents/PHBH-brochure-11-2017.pdf>.
- [33] Li Z., Kong J., Ju D., Cao Z., Han L. and Dong L., 2017, Thermal conductivity enhancement of poly(3-hydroxybutyrate) composites by constructing segregated structure with the aid of poly(ethylene oxide). *Composites Science and Technology* **149**, 185-191. [DOI: 10.1016/j.compscitech.2017.06.028]
- [34] Plötze M., Schärli U., Koch A. and Weber H., 2007, Thermophysical properties of bentonite. *Proceedings of the International Meeting on Clays in Natural & Engineered Barriers for Radioactive Waste Confinement*, Lille, France, September 17-20, pp. 579-580.
- [35] BYK, Cloisite 5 Technical Data Sheet, <https://www.byk.com/en/products/additives-by-name/cloisite-na>.
- [36] Carneiro O.S., Covas J.A. and Vergnes B., 2000, Experimental and Theoretical Study of Twin-Screw Extrusion of Polypropylene. *Journal of Applied Polymer Science* **78**(7), 1419–1430. [DOI: 10.1002/1097-4628(20001114)78:7<1419::AID-APP130>3.0.CO;2-B]
- [37] Thipmanee R., Lukubirac S., Ogale A.A. and Sane A., 2016, Enhancing distributive mixing of immiscible polyethylene/thermoplastic starch blend through zeolite ZSM-5 compounding sequence. *Carbohydrate Polymers* **136**, 812-819. [DOI: 10.1016/j.carbpol.2015.09.090]
- [38] Mofokeng J.P. and Luyt A.S., 2015, Morphology and thermal degradation studies of melt-mixed PLA/PHBV biodegradable polymer blend nanocomposites with TiO<sub>2</sub> as filler. *J. Appl. Polym. Sci.* **132**(25), 42138/1-11. [DOI: 10.1002/app.42138]
- [39] Brückner S., Allegra G., La Mantia F.P., Di Landro L., Malinconico M., Scaffaro R., Paoletti S. and Donati I., 2016, *Scienza e Tecnologia dei Materiali Polimerici*. EdISES, Napoli, Italy. [ISBN: 978-8-87-959919-1]



## 9. Instruments employed in the present work

- **Extruder**  
*ZSE 18 HP*, Leistritz AG (Nuremberg, Germany)
- **Polymer feeder**  
*ISC-CM DDW-MD2-DSR28-10*, Brabender Technologie (Duisburg, Germany)
- **Powder feeder**  
*ISC-CM DDW-MD1-MT-1*, Brabender Technologie (Duisburg, Germany)
- **Rheometer**  
*ARES*, TA Instruments (New Castle, DE, USA)
- **DSC module**  
*Q20*, TA Instruments (New Castle, DE, USA)  
The melting enthalpy has been derived by a sigmoidal integration of the correspondent DSC peak employing the *TA Universal Analysis* software.
- **Scanning Electron Microscope (SEM)**  
*LEO-1450VP*, Carl Zeiss GmbH (Oberkochen, Germany)



## 10. Breve manuale di Ludovic

### 10.1. Introduzione

Ludovic è un software in grado di simulare con notevole accuratezza il processo di estrusione all'interno di estrusori bivate al variare del materiale e delle condizioni iniziali. Siccome il programma analizza l'evoluzione in condizioni stazionarie delle grandezze di interesse lungo la sola direzione assiale, l'elaborazione è assai veloce e richiede pochi secondi per essere portata a termine.

Il programma può essere impiegato in un'ottica di affinamento delle condizioni di processo (ad esempio per massimizzare la produttività o limitare il più possibile la degradazione termica), ma anche per progettare da zero il profilo vite conoscendo in anticipo l'evoluzione di pressione, temperatura e tutto quello che può essere utile senza la necessità di verificarlo con prove di laboratorio più impegnative e costose.

La simulazione è effettuata scomponendo i canali in cui scorre il polimero fuso in un numero finito di elementi a forma di C, detti appunto *C-chambers*, e avviene con un processo iterativo basato sull'evoluzione della temperatura all'interno dell'estrusore. In particolare, Ludovic assume che il polimero fonda completamente all'altezza del primo elemento della vite che restringe il flusso, cioè in corrispondenza del primo elemento (iniziando dalla tramoggia) che non ha la semplice funzione di trasporto. Partendo dalla testa di estrusione, il software ricostruisce i valori di temperatura e di numerose altre grandezze muovendosi in senso opposto rispetto a quello del polimero. Se la temperatura in corrispondenza del primo elemento non di trasporto corrisponde alla temperatura di fusione del materiale e se a monte di tale elemento si ha un aumento di pressione, la simulazione viene interrotta, altrimenti il processo si ripete iterativamente finché queste condizioni non sono soddisfatte. Nonostante l'approssimazione introdotta sopra possa apparire piuttosto "drastica", anche se necessaria a causa della scarsa comprensione dei vari fenomeni che si verificano durante la fusione, l'accordo tra le previsioni e i risultati sperimentali è generalmente piuttosto soddisfacente e gli scarti sono quantificabili in pochi punti percentuali.

### 10.2. Database

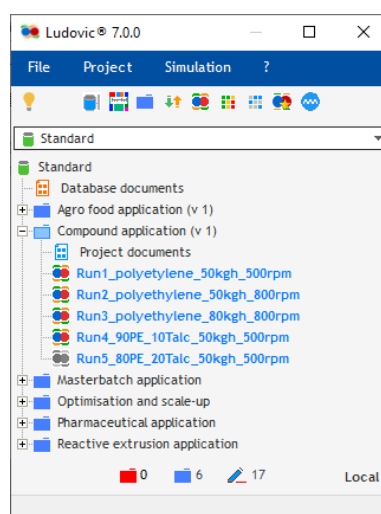


Figura 10.1 - Schermata principale di Ludovic.

Una volta aperto Ludovic ci si trova di fronte alla schermata rappresentata in Figura 10.1.

Il software organizza le varie simulazioni in progetti (le cartelle blu) a loro volta racchiusi in un database. Il numero di progetti e delle simulazioni in essi contenute è riassunto nella parte bassa della schermata e risulta utile conoscerlo in quanto, allo scopo di facilitare le operazioni periodiche di backup automatico, sarebbe meglio evitare di raccogliere tutte le simulazioni (soprattutto se in numero consistente) nello stesso database, radunandole invece sulla base di criteri comuni in database diversi.

### 10.2.1. Creazione di un database

Per creare un nuovo database si clicca sul menù a tendina in Figura 10.1 e poi sulla voce *Add a new database*. A questo punto si apre la seguente finestra di dialogo (Figura 10.2)

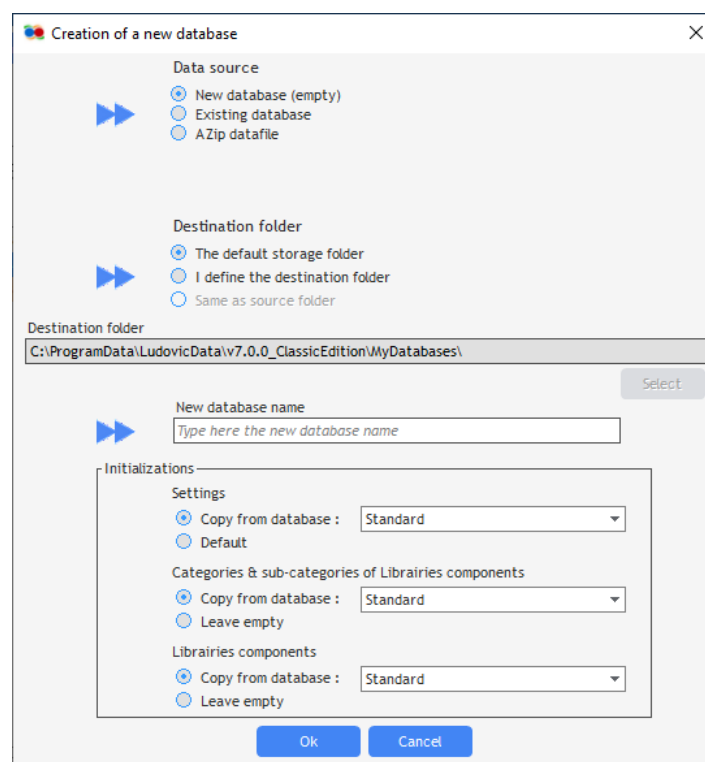


**Figura 10.2** - Finestra per la creazione di un nuovo database.

Nel menù *Data source* è possibile selezionare se si desidera creare un database vuoto o importare i dati da un database esistente oppure da un file .zip.

Il menù *Destination folder* permette di definire la cartella in cui il programma andrà a salvare i risultati delle simulazioni. Il consiglio è quello di utilizzare l'opzione di default salvo necessità specifiche. In questi casi sarà necessario indicare la cartella dove salvare i dati premendo sul pulsante *Select*.

Nella finestra *New database name* si inserisce il nome del database che si sta creando, mentre, principalmente per una questione di comodità, in tutte le voci del menù *Initializations* è bene copiare impostazioni, librerie e loro organizzazione dal database *Standard* che è installato con il software.

Successivamente si preme su *Ok* e si dà ulteriore conferma nella successiva finestra di dialogo.



### 10.3. Progetti e simulazioni

All'interno di un nuovo database è necessario creare un nuovo progetto cliccando sulla schermata principale con il tasto destro del mouse e poi selezionare la voce *New project*. Nella finestra che si apre è possibile definire, attraverso la scheda *Identification*, il nome del progetto per poi terminare l'operazione premendo sul pulsante *Add*.

Il nome del progetto può essere modificato successivamente cliccando su di esso con il tasto destro del mouse nella schermata principale e scegliendo *Modify project* nel menù che compare. È bene notare che si apre esattamente la stessa finestra vista nella fase di creazione in cui è possibile, attraverso le varie schede e se non lo si è effettuato in precedenza, modificare alcune impostazioni come ad esempio le grandezze che verranno visualizzate di default al termine delle simulazioni (*Preferred f(x) results*) o alcuni valori soglia (*Alarms settings*).

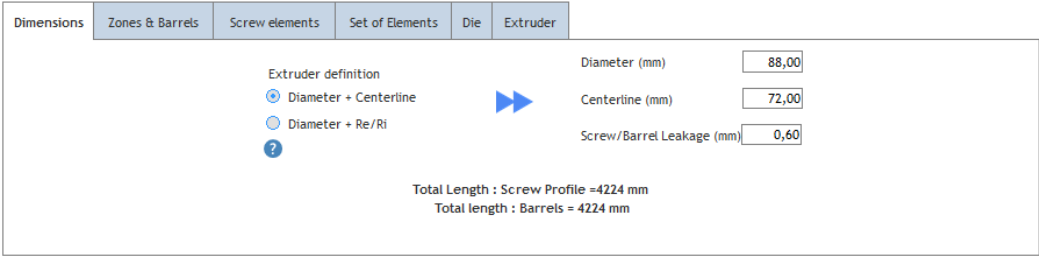
A questo punto è possibile creare una nuova simulazione premendo il pulsante  o attraverso il menù *Simulation>New simulation*. Si apre così la finestra in cui è possibile definire attraverso passaggi successivi i vari parametri che governano il processo di estrusione.

Nella prima scheda che si incontra (**Main**) è possibile scegliere il progetto di cui la simulazione farà parte attraverso l'apposito menù a tendina, mentre nella casella *Simulation* occorre specificare il nome che si vuole attribuire.

**ATTENZIONE!** Prima di passare ad una scheda successiva bisogna sempre salvare le modifiche cliccando su *File>Save*.

La scheda **Extruder** (Figura 10.5) è quella in cui si definiscono le caratteristiche geometriche della macchina e del die, il profilo vite e la presenza di elementi riscaldanti. Ciò è possibile attraverso le sotto-schede:

- *Dimensions* (Figura 10.4) – nelle apposite celle occorre specificare il diametro della vite (*Diameter*, in mm) e il gioco tra vite e cilindro (*Screw/Barrel Leakage*, in mm), mentre il terzo valore da inserire va scelto alla voce *Extruder definition* e può essere la distanza tra gli assi delle viti (*Centerline*, in mm) o il rapporto  $Re/Ri$  tra i diametri esterno e interno.



Dimensions	Zones & Barrels	Screw elements	Set of Elements	Die	Extruder
Extruder definition					
<input checked="" type="radio"/> Diameter + Centerline					
<input type="radio"/> Diameter + Re/Ri					
<input type="radio"/> ?					
			Diameter (mm) <input type="text" value="88,00"/>		
			Centerline (mm) <input type="text" value="72,00"/>		
			Screw/Barrel Leakage (mm) <input type="text" value="0,60"/>		
Total Length : Screw Profile = 4224 mm Total length : Barrels = 4224 mm					

Figura 10.4 - Sotto-scheda *Dimensions*.

- *Zones & barrel* – in questa scheda si definisce la geometria del cilindro. Inizialmente si posizionano le fasce riscaldanti trascinando la figura che sta sopra la voca *Barrel* nello spazio bianco sottostante. Si apre così una finestra in cui occorre specificare la lunghezza dell'elemento. L'operazione va ripetuta più volte finché non si arriva alla geometria desiderata.

Dopo la definizione del profilo vite occorre tornare su questa scheda per posizionare le zone di *Feed*, che possono anche essere più di una (ad esempio se si va ad aggiungere una carica) *Transition*, corrispondente ad un cambiamento nel materiale che si avrebbe ad esempio in caso di reactive extrusion, e *Extraction*, utile per le operazioni di degasaggio. Va notato che questa scheda permette di descrivere esclusivamente la geometria della macchina, mentre i parametri di temperatura dei cilindri e portata sono indicati successivamente nella scheda *Process*.

Per eliminare un elemento posizionato per errore occorre trascinarlo sull'icona  in alto a destra.

- *Screw elements* – con un'operazione di trascinamento simile a quanto spiegato prima si definisce anche il profilo vite. Gli elementi disponibili in libreria possono non essere gli

stessi realmente posseduti, perciò con un clic sull'icona  si apre una finestra dove sono riportate le varie tipologie dei segmenti (trasporto, masticazione, retroflusso ecc.). Selezionandone uno appaiono sulla destra alcune celle in cui, inserendo i valori richiesti, è possibile definire una specifica geometria.

È bene notare che gli elementi colorati in verde sono caratterizzati da spirale destra, quelli in rosso da spirale sinistra.

Anche in questo caso, per eliminare un elemento posizionato per errore occorre trascinarlo sull'icona  in alto a destra.

Una volta definito l'intero profilo vite è possibile esportarlo cliccando su di esso con il tasto destro del mouse e scegliendo la voce “*Export screw profile*”.

- *Set of elements* – permette di abbreviare il lavoro di costruzione del profilo vite attraverso l'uso di combinazioni di elementi anziché di parti singole.
- *Die* – questa scheda è utilizzata per posizionare il die e definirne la forma. Come nel caso degli elementi della vite, se nella libreria non è presente la geometria corretta è possibile

creare quella desiderata dalla finestra che si apre cliccando su . Ludovic permette di scegliere tra die cilindrici o convergenti di cui occorre specificare le dimensioni nelle apposite celle sulla destra. In alternative, è possibile impostare una certa caduta di pressione (il valore esatto sarà inserito nella scheda *Process*).

- *Extruder* – Permette di selezionare un intero estrusore dalla libreria (se disponibile).

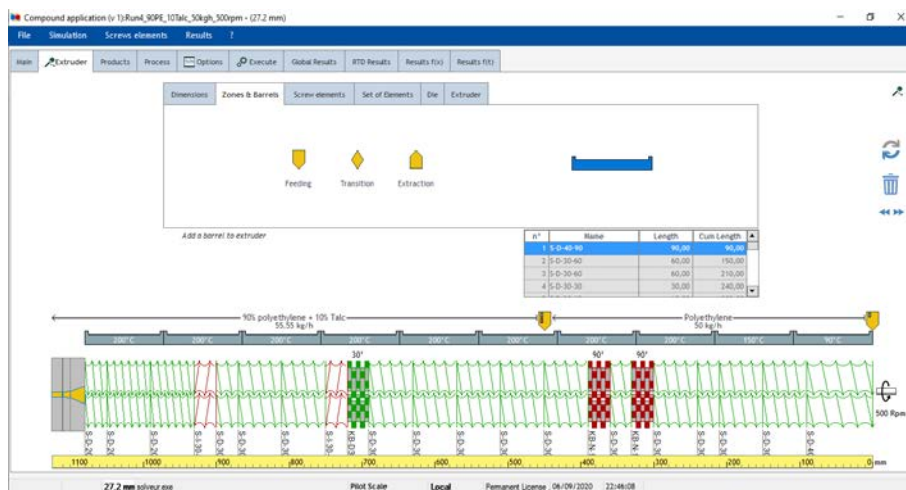


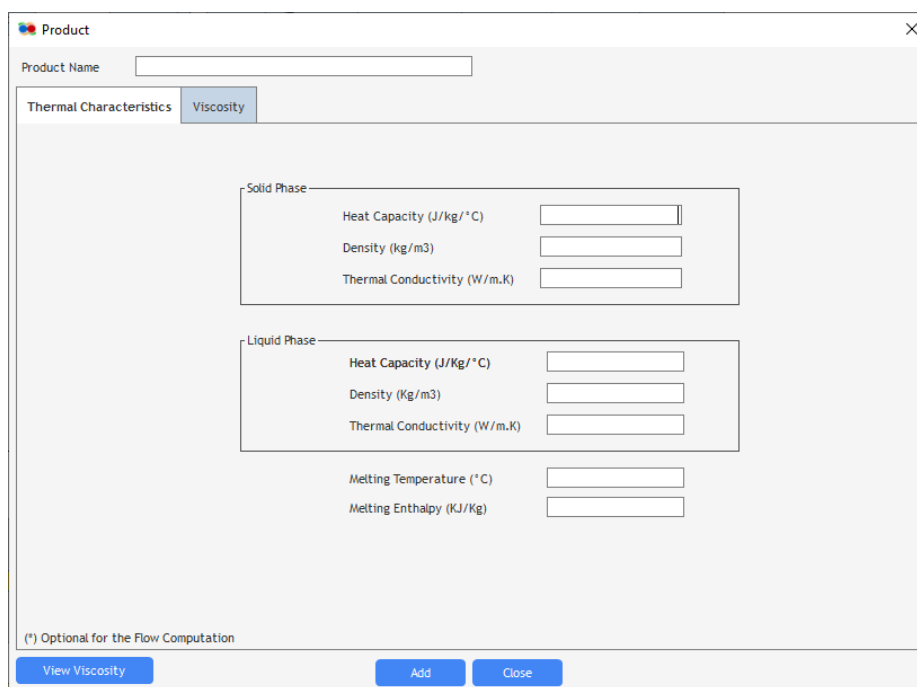
Figura 10.5 - Scheda *Extruder* al termine delle operazioni di creazione del profilo vite, del die e del cilindro.

Bisogna notare che l'estrusore viene visualizzato da destra (dove va posizionato il feed) a sinistra (dove si trova la testa di estrusione) dello schermo.

**ATTENZIONE!** Se le schede elencate sopra non sono visibili, ma appare un'unica finestra con più tabelle, bisogna cliccare sull'icona  in alto a destra.

Nella scheda **Products** (Figura 10.6) si specificano le caratteristiche del materiale da lavorare. Siccome l'estrusore bivate è usato comunemente per operazioni di compounding, Ludovic permette di inserire i dati relativi a più tipi di polimeri e cariche per poi miscelarli successivamente, creando la cosiddetta *Recipe*.

Se il polimero desiderato non è già presente nella libreria, è possibile impostarlo manualmente attraverso un clic sull'icona  per poi scegliere la voce *Add a product*. Si apre allora una finestra dove, nella scheda *Thermal characteristics*, è necessario digitare il nome del prodotto e i valori di capacità termica, conducibilità termica e densità per le fasi solida e liquida oltre che temperatura ed entalpia di fusione. Nella successiva scheda *Viscosity* va specificata la legge usata per modellizzare la viscosità, scegliendola dal menù a sinistra e digitando i parametri richiesti (temperature di riferimento, esponenti ecc.). La viscosità può anche essere definita attraverso un Set of Points (SoP), ovvero un insieme di terne di Temperatura, Shear rate e viscosità che risultano utili quando sono disponibili dati sperimentali. Infine si preme su *Add*.



La finestra "Product" mostra un campo "Product Name" e due schede: "Thermal Characteristics" (attiva) e "Viscosity".

**Thermal Characteristics**

**Solid Phase**

- Heat Capacity (J/kg/°C)
- Density (kg/m3)
- Thermal Conductivity (W/m.K)

**Liquid Phase**

- Heat Capacity (J/Kg/°C)
- Density (Kg/m3)
- Thermal Conductivity (W/m.K)
- Melting Temperature (°C)
- Melting Enthalpy (KJ/Kg)

(\*) Optional for the Flow Computation

View Viscosity  Add  Close

Figura 10.6 - Finestra *Product*.

L'aggiunta di una carica avviene nuovamente tramite un clic su  seguito da un altro su *Add an additive*. Nella finestra che si apre (Figura 10.7) vanno digitati i valori di densità, capacità termica e conducibilità termica oltre che il nome del filler, dopodiché bisogna premere sul pulsante *Add*.

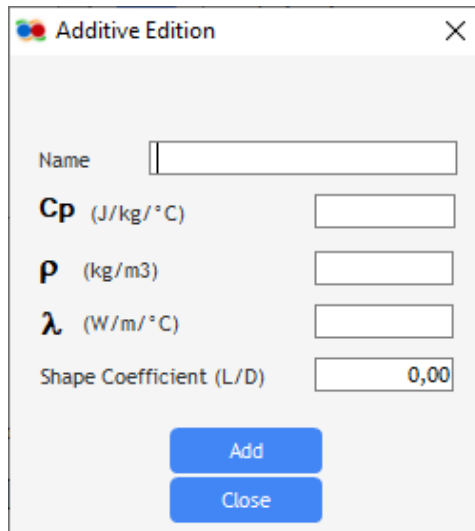


Figura 10.7 - Finestra *Additive Edition*.

Polimero e carica vengono combinati nella cosiddetta *Recipe* cliccando su  e poi sulla voce *Add a recipe*. La finestra che si apre (Figura 10.8) permette di scegliere il nome da assegnare al mix e le percentuali (in volume o massa, questo può essere scelto in alto a destra) dei vari componenti. Spuntando le voci sulla destra è possibile determinare il tipo di legge che governa la miscelazione tra polimeri e tra polimero e carica.

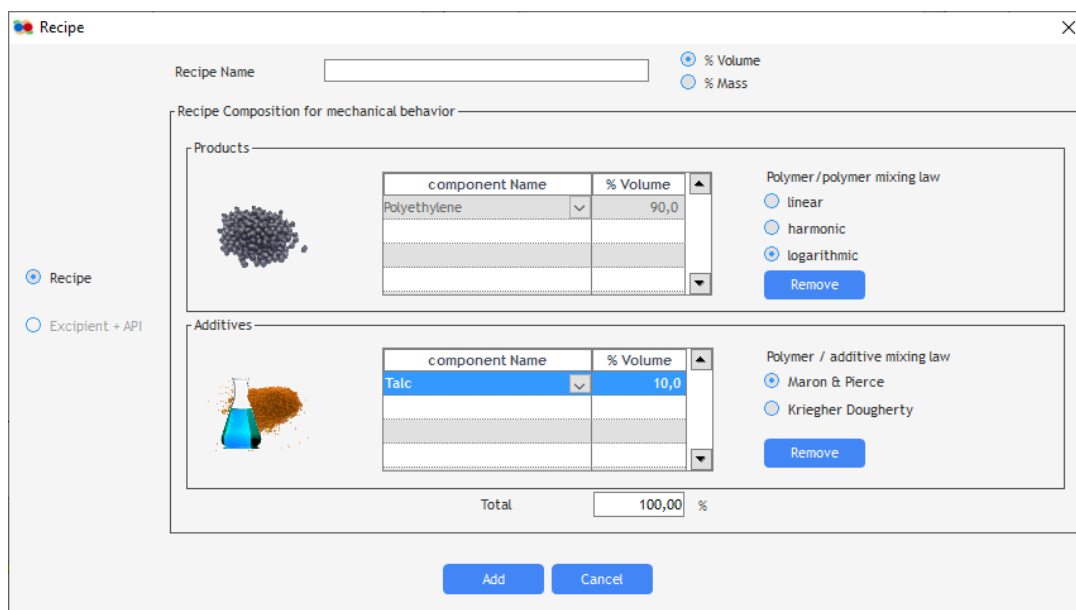


Figura 10.8 - Finestra *Recipe*.

Polimeri, cariche e recipes possono anche essere esportati o importati cliccando sul pulsante .

La scheda **Process** (Figura 10.9) permette di specificare le condizioni operative dell'estrusore.

Innanzitutto è necessario inserire la velocità di rotazione (in rpm) e la temperatura delle viti nelle apposite celle. Se la macchina non permette di controllare quest'ultimo parametro perché non

dispone di un apposito sistema di termoregolazione, la voce *Screw Temperature* va settata al valore 0.

Il menù *Thermal Exchange* permette di simulare l'effetto degli scambi termici in due modi:

- definendo i coefficienti di scambio termico di die, cilindro e vite (spunta sulla voce *Thermal Exchange Coefficients*). In caso di scambio termico efficace è consigliato il valore di  $1000 \text{ W/m}^2\text{K}$ ;
- definendo i valori del numero di Nusselt per la vite e lasciando che Ludovic calcoli quelli di cilindro e die (si elimina la spunta a fianco di *Thermal Exchange Coefficients*, mettendola invece alla voce *Auto Nusselt*);
- definendo i numeri di Nusselt per tutti gli elementi (eliminando le spunte sia a *Thermal Exchange Coefficients* che a *Auto Nusselt*).

The screenshot shows the 'Extruder Settings' window. At the top, 'Rotation Speed (Rpm)' is set to 500 and 'Screw Temperature (°C)' is set to 0. The 'Thermal Exchange' section has a checked box for 'Thermal Exchanges Coefficients' and three input fields: 'Thermal Exchange / Die (W/m2.K)' at 1,000.0, 'Thermal Exchange / Barrel (W/m2.K)' at 1,000.0, and 'Thermal Exchange / Screw (W/m2.K)' at 0.0. Below this are three tables: 'Zones Settings' with columns for Position (n° Screw elt), Added products Temp (°C), Total F Rate (kg/h), and Product / Recipe in extruder; 'Dies Temperature' with columns for n° and Temp (°C); and 'Barrels' with columns for n°, Temp (°C), and Thermal Exchange. The 'Barrels' table shows values for 10 barrels, with Temp (°C) ranging from 90 to 200 and Thermal Exchange values of 1,000.00.

Figura 10.9 - Scheda *Process*.

La tabella *Zones Settings* serve a specificare dove, a che temperatura e con quale portata polimeri e cariche entrano nella macchina (o escono nel caso in cui si abbia anche il degassaggio).

Nella tabella *Dies Temperature* si inseriscono invece le temperature dei vari elementi del die, numerati progressivamente secondo la direzione del flusso di materiale e quindi da destra a sinistra. Per elementi non riscaldati si inserisce il valore di  $0^{\circ}\text{C}$ .

Infine, la tabella *Barrels* permette di definire la temperatura delle varie sezioni del cilindro, controllate tramite le fasce riscaldanti, e i coefficienti di scambio termico, se questi sono diversi in diverse parti della macchina (altrimenti è più pratico utilizzare la cella *Thermal Exchange / Barrel* nella sezione *Thermal Exchange*). Anche in questo caso la numerazione aumenta progressivamente da destra a sinistra.

Nella scheda *Options* è possibile affinare ulteriormente le simulazioni. Ad esempio è possibile imporre il punto specifico in cui avviene la fusione del polimero, definire i dettagli del processo di reactive extrusion, modellizzare la rottura delle fibre di vetro usate come filler o ancora specificare i dettagli del riscaldamento tramite microonde.

Una volta caricati tutti i parametri richiesti, si può finalmente procedere a lanciare la simulazione dalla scheda *Execute*. Se necessario si possono modificare alcuni parametri numerici per migliorare la precisione della simulazione e si può accoppiare un terzo parametro per il calcolo della viscosità cliccando sul menù a fianco della voce *Coupling Mode* e scegliendo *Active Coupling*. Infatti, nella modalità *Without Coupling* la viscosità è valutata con la legge scelta nella scheda *Product* alla voce *Viscosity* basandosi esclusivamente sui valori di temperatura e shear rate.

La tabella *Alarms Settings* permette di specificare determinati intervalli di coppia, temperatura e pressione che è necessario rispettare (temperature o pressioni eccessivamente alte possono ad

esempio degradare il materiale o danneggiare la macchina). Se questo non avviene, un avviso compare in seguito alla simulazione.

A questo punto si preme sul pulsante *Compute* per avviare la simulazione.

La scheda **Global Results** riassume con un grafico a torta quanta energia (in percentuale ed in valore assoluto) viene utilizzata nella lavorazione del materiale e quanta è invece dissipata in attriti viscosi. In questa tabella è anche riportato il valore della coppia richiesta all'estrusore. I valori precisi si leggono scorrendo il menù sulla sinistra dello schermo.

Nella scheda successiva (**RTD results**) un grafico raffigura la distribuzione dei tempi di residenza, con una linea rossa che ne indica il valore medio. A sinistra dello schermo sono riportati anche il minimo, la varianza e il valore di picco, mentre spuntando la voce in alto a sinistra (*Integrated RTD*) si ottiene la curva integrale.

I risultati vengono rappresentati in funzione della coordinata  $x$  (orientata lungo l'asse della vite) nella scheda **Results  $f(x)$** . Con un clic sul pulsante *Results Selection* si apre una finestra (Figura 10.10) dove è possibile selezionare quali grandezze visualizzare e, di conseguenza, l'unità di misura degli assi. In uno stesso menù si possono selezionare più grandezze, a patto che l'unità di misura sia la stessa. Cliccando sul rettangolo colorato a destra delle varie grandezze è possibile selezionare, da un apposito menù, il colore da attribuire loro.

La scala degli assi può essere determinata dall'operatore cliccando sulla voce *Manual Scale* e digitando i valori massimo e minimo nelle celle che compaiono. In alternativa, si lascia fare al software con l'opzione *Automatic Scale*.

Nella parte in basso a sinistra della stessa finestra è anche possibile selezionare se visualizzare tra le grandezze da scegliere i cosiddetti *Advanced results*, ovvero informazioni più specifiche dei semplici valori di temperatura, pressione e tempo di residenza.

Cliccando infine su *Draw* si ottengono i grafici desiderati.

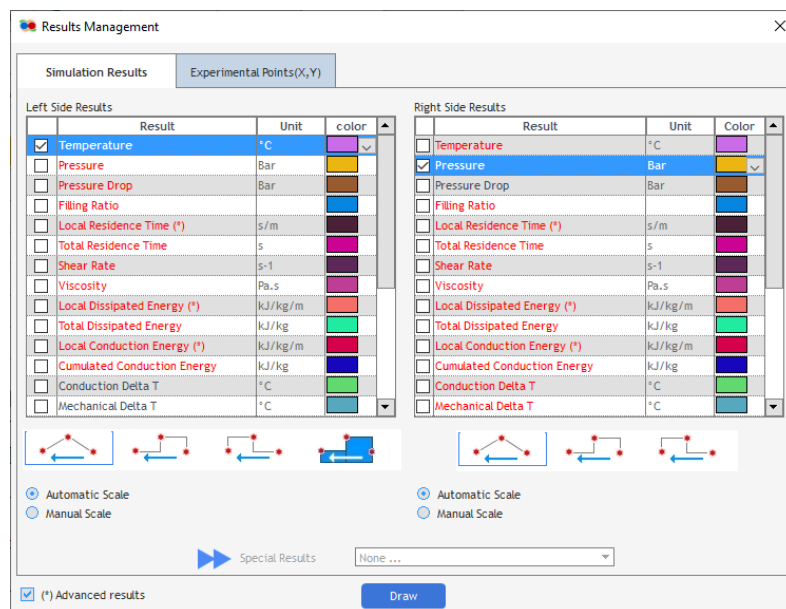
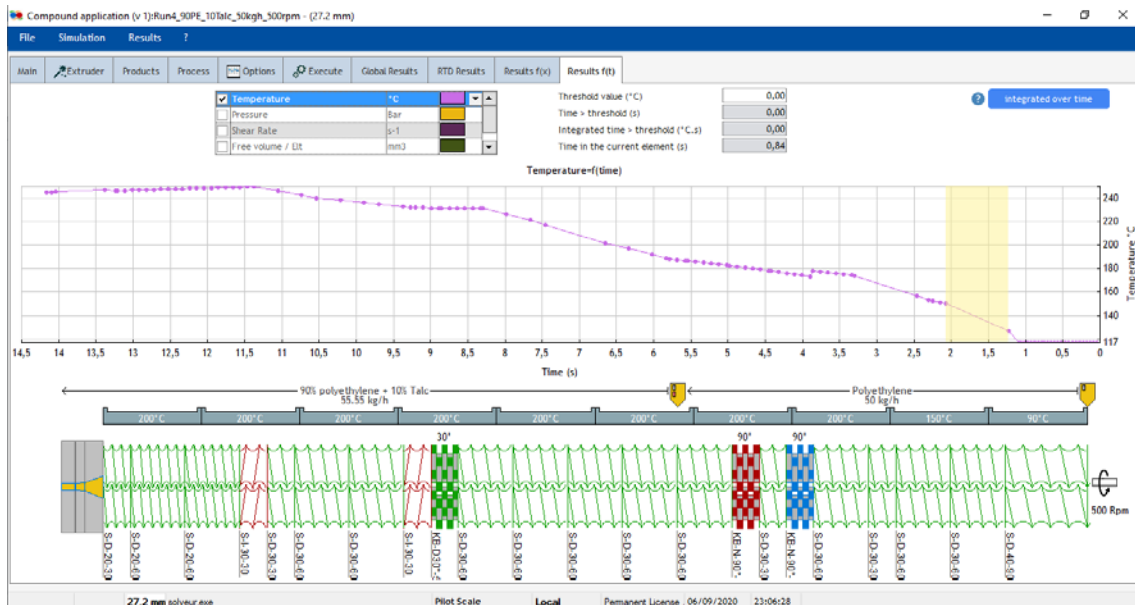


Figura 10.10 - Finestra *Results Management*.

L'ultima scheda, **Results  $f(t)$**  (Figura 10.11), permette di rappresentare i valori di temperatura, pressione, shear rate e volume libero (una grandezza per volta) in funzione del tempo inserendo un segno di spunta nella colonna di sinistra della tabella.

Nelle caselle a fianco della tabella si possono impostare determinati valori soglia e conoscere il tempo di residenza del fuso in un particolare elemento della vite, cliccando su di esso nello schema sottostante e leggendo il corrispondente valore nella cella *Time in the current element*.

Se anche la curva integrale è di interesse, questa viene calcolata premendo sul pulsante *Integrated over time* in alto a destra. Per tornare alla curva derivata si clicca sullo stesso pulsante, che ora reca la scritta *Result(t)*.



**Figura 10.11** - Grafico  $T(t)$ . In arancione è evidenziato il tempo di residenza nell'elemento di masticazione colorato di blu, il cui valore esatto può essere letto nella casella *Time in the current element*,

### 10.3.1. Esportare i risultati

Per esportare i risultati di una simulazione in un file Excel, così da elaborarli in seguito, occorre cliccare (una volta aperta la simulazione di interesse) sul menù *Results* e poi sulla voce *Export Results as .xls*. Una volta selezionati i dati di interesse occorre scegliere la posizione in cui salvare il file e cliccare su *Salva*.

### 10.3.2. Sbloccare una simulazione

In alcuni casi si può avere il bisogno di bloccare una simulazione per evitare modifiche accidentali o, al contrario, di sbloccarla. Per fare ciò basta cliccare su di essa con il tasto destro del mouse nella schermata principale e scegliere la voce *Lock/Unlock the Simulation*.

Una simulazione bloccata è caratterizzata dall'icona  a sinistra del titolo.

### 10.3.3. Raggruppare più simulazioni

Se si ha la necessità di raggruppare più simulazioni bisogna cliccare sull'icona  nella parte alta della schermata principale. Si apre così il Simulation Manager (Figura 10.12), ovvero una finestra dove è possibile spuntare le simulazioni che si desidera raggruppare per poi selezionare dal menù

a tendina in basso la voce *Group the Selected Simulations*. I titoli delle simulazioni raggruppate appaiono colorati in blu nella schermata principale di Ludovic.

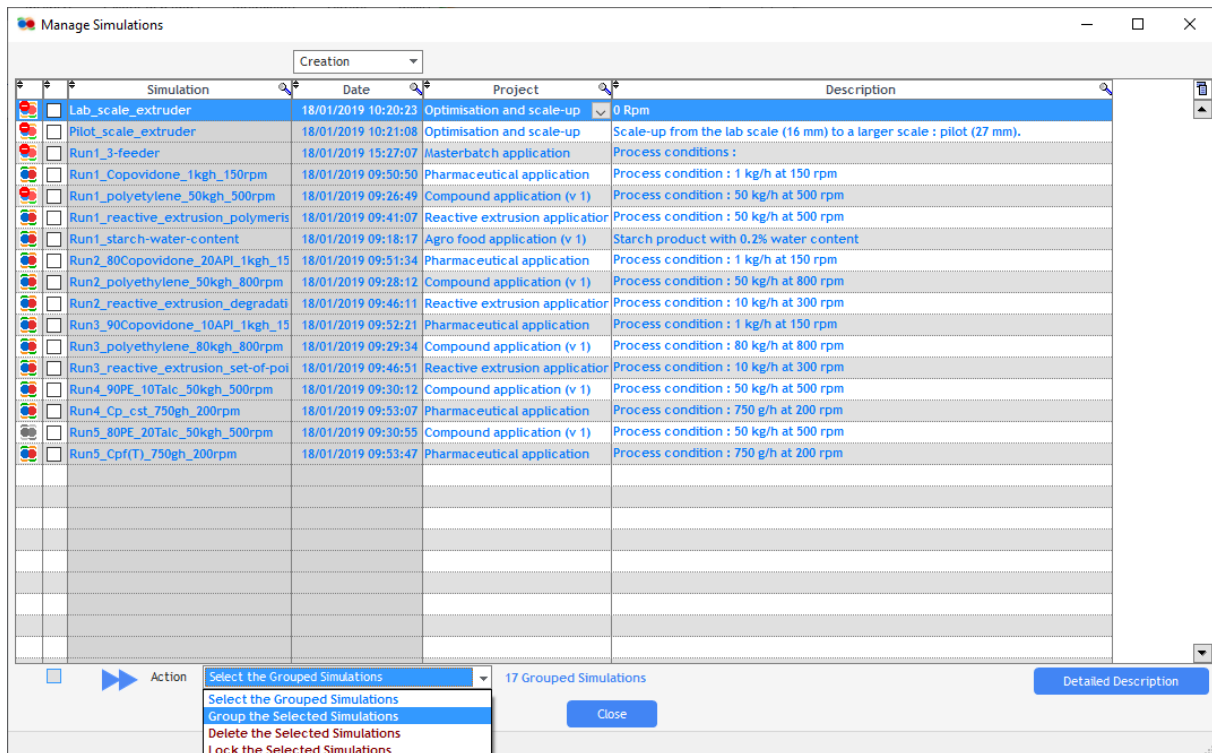


Figura 10.12 - Finestra del Simulation Manager.

#### 10.3.4. Confrontare più simulazioni

Spesso può risultare utile fare un confronto tra più simulazioni, che in Ludovic può essere svolto tra quelle appartenenti ad uno stesso progetto o tra quelle raggruppate. Nel primo caso, a partire dalla schermata principale, si clicca con il tasto destro del mouse sul titolo di una simulazione per poi scegliere la voce *Load all Project Results*. Nel secondo caso invece bisogna scegliere la voce *Load all Group Results* (colorata in blu come i titoli delle simulazioni raggruppate).

Nella parte sinistra della finestra che si apre (*Comparative Functions*) è possibile selezionare la simulazione di riferimento (attraverso un unico segno di spunta nella colonna sinistra) e quelle con cui la si vuole confrontare (aggiungendo una o più spunte nella colonna di destra).

La parte destra è invece divisa in schede, la prima delle quali (*Global results*) è costituita dalle tre sotto-schede:

- *Global Comparison* (Figura 10.13) – permette di effettuare una comparazione delle principali grandezze tra la simulazione di riferimento, rappresentata dal segmento orizzontale, e le altre che vanno a costituire il segmento verticale. Il tipo di visualizzazione può essere modificato cliccando sulle opzioni *Min/Max* e *Radar* in basso.
- *Comparison/Result* – concettualmente simile a *Global Comparison*, in questo caso il confronto avviene per mezzo di un istogramma. La grandezza di interesse è selezionabile dal menù in basso, dove sono riportate anche le medie.
- *Energy Comparison* – paragona, tramite istogrammi, il consumo e la distribuzione dell'energia.



sul pulsante *New DoE*, digitando successivamente nella casella *Name* il nome che si vuole impartire.

Fatto ciò, si passa alla scheda **Parameters Selection** (Figura 10.14) dove bisogna scegliere le grandezze che si vuole fare variare entro un certo intervallo per conoscerne il valore ottimale. Una volta selezionato con un clic nel menù a sinistra il parametro, è necessario definire nelle celle in basso a destra i valori massimo e minimo entro cui lo si vuole fare variare (*Start Value*, *Stop Value*) e il numero di step (*Steps Count*). La cella *Current Value* informa sul valore assunto dalla grandezza scelta nella simulazione di partenza.

Ludovic permette di scegliere solo due *Primary Parameters* (i cui valori vengono modificati in maniera indipendente) e quindi nel caso in cui se ne vogliono studiare un numero maggiore occorre impostarli, sempre in basso a destra, come *Secondary Parameters* e specificare da quale grandezza essi dipendono. In questo modo non è più possibile specificare il numero di step, che saranno gli stessi indicati in precedenza per il parametro primario.

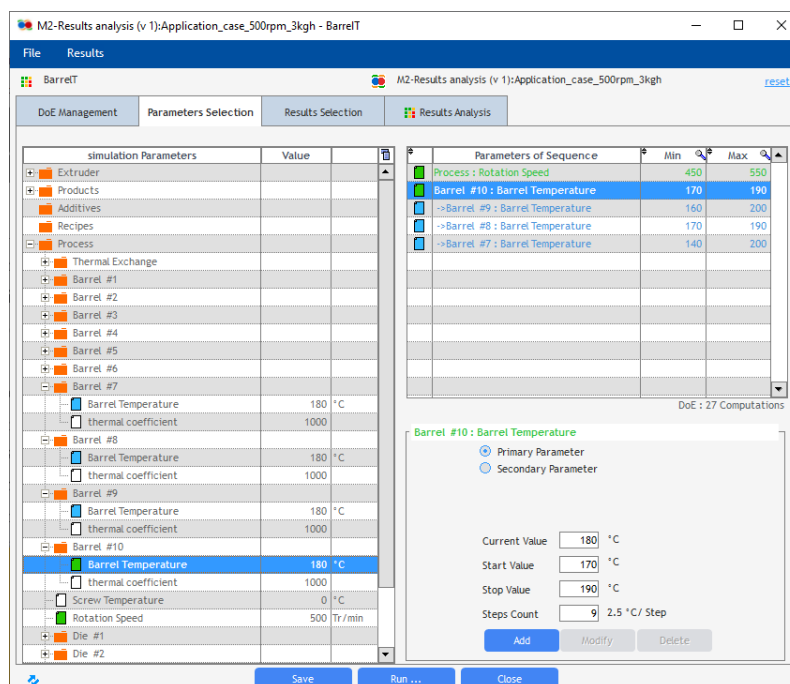


**Figura 10.14** - Scheda *Parameters Selection*. I parametri in verde nella tabella a destra sono i primari, quelli in blu sono i secondari.

Dalla scheda **Results Selection** bisogna invece scegliere le quantità di cui si vuole conoscere l'andamento al variare delle grandezze scelte in *Parameters Selection*.

A questo punto è bene salvare il DoE (clic sul pulsante *Save*), dopodiché si può dare il via alla fase di calcolo, che può durare alcuni minuti, con un clic sul pulsante *Run*.

La scheda **Results Analysis** permette di valutare i risultati ottenuti tramite diverse sotto-schede. Le più significative sono

- *Results Data* – una tabella che riassume i risultati del calcolo al variare dei parametri.
- *Graphical Analysis* – è essenzialmente una rappresentazione grafica, con i parametri primari sugli assi *x* e *y* e il risultato sull'asse *z*. I menù a tendina nella parte alta permettono di scegliere un preciso valore lungo l'asse *x* o *y* (si ottiene un grafico 2D) e quale grandezza visualizzare lungo *z*.

- *Trends* – come nella comparazione di più simulazioni, anche in questo caso è possibile richiedere al software di ricercare eventuali trend significativi. Vale quanto spiegato in precedenza nella stessa sezione del paragrafo 10.3.4.

#### 10.4.1. Esportare i risultati

Per esportare i risultati di un DoE, un volta aperto si clicca sul menù Results, poi sulla voce Export Results as .xls. A questo punto si procede come descritto nella sezione 10.3.1.

## Acknowledgements

I would like to express my gratitude to all the people who supported me while writing this thesis.

First of all, I would like to thank my supervisors Professor Alberto Frache and Professor Rossella Arrigo for the precious assistance given in every aspect of this work and for the patient review of all the contents. A big thanks goes also to Alessandra D'Anna, who provided all the experimental data about the materials.

I would like to remember every wise counsel provided by my grandparents, every encouragement from my parents, the technical support given by my brother (also when it was not required) and the tremendous understanding of Elisa. Without them this would not have been possible.

I would also like to thank my nearly sisters Lucia and Giulia, but also Andrea, Claudia, Davide, Giulia, Ivan, Luca, Milva, and Stefano. They shared with me the forgettable daily inefficiencies of the railway system, but also many unforgettable moments. Finally, I would like to extend my sincere thanks to Edoardo, Federico, the two Alessandro, Luca, Lorenzo and Eugenia, who made happier the long days at Politecnico.